Modeling Navigation System Performance of a Satellite-Observing
Star Tracker Tightly Integrated with an Inertial Measurement Unit

DISSERTATION

Scott J. Pierce, Major, USAF

AFIT-ENG-DS-15-M-260

DEPARTMENT OF THE AIR FORCE
AIR UNIVERSITY

AIR FORCE INSTITUTE OF TECHNOLOGY

Wright-Patterson Air Force Base, Ohio

AFIT-ENG-DS-15-M-260

Modeling Navigation System Performance of a Satellite-Observing Star Tracker Tightly Integrated with an Inertial Measurement Unit

DISSERTATION

Presented to the Faculty

Graduate School of Engineering and Management

Air Force Institute of Technology

Air University

Air Education and Training Command

In Partial Fulfillment of the Requirements for the

Degree of Doctor of Philosophy

Scott J. Pierce, B.S.E.E., M.S.E.E.

Major, USAF

March 2015

AFIT-ENG-DS-15-M-260

MODELING NAVIGATION SYSTEM PERFORMANCE OF A SATELLITE-OBSERVING
STAR TRACKER TIGHTLY INTEGRATED WITH AN INERTIAL MEASUREMENT UNIT

Scott J. Pierce, B.S.E.E., M.S.E.E.
Major, USAF

Committee Membership:

John F. Raquet, PhD
Chair

Bryan Dorland, PhD
Member

Kyle Kauffman, PhD
Member

ADEDEJI B. BADIRU, PhD
Dean, Graduate School of Engineering
and Management

AFIT-ENG-DS-15-M-260

Abstract

As Global Positioning System (GPS) and similar systems have been developed, less emphasis has been placed on the use of celestial navigation, or star sighting for position determination. Celestial navigation has been used previously for heading correction in aircraft by observing known stars and the local horizon [9]. An emerging technique [93] is to determine a position by observing satellites in addition to stars, which satellites allow for local position estimation.

This dissertation defines the navigation system using this satellite-observing method to tightly integrate a star tracker, an Inertial Measurement Unit (IMU), and a barometric altimeter using an Extended Kalman Filter (EKF). Models of each of these components are described with emphasis added to the accuracy of the star tracker measurement of a satellite. Several system configurations are simulated comparing the performance of the estimate with respect to IMU grade, star tracker measurement accuracy, satellite orbit height, and measurement time interval parameters. In addition to system component parameters, two other variables are introduced: ephemeris error correction from a remote sensor and satellite selection algorithm.

Experimental observations, using a visible band star tracker integrated with a navigation grade IMU, showed that the observer's position can be estimated with a median distance root mean square (drms) position error of test cases of 39 m when observing satellites in Medium Earth Orbit (MEO) orbit. The drms position error was less than 65 m for 90% of test cases and was less than 21 m in 10% of the cases.

Additionally, power requirements were calculated for a satellite signal operating in imaging bands, such that a Low Earth Orbit (LEO) orbiting satellite constellation could be detected during the day. This type of signal would make it possible to operate the star tracker integrated navigation system in GPS-degraded environments with similar duration and comparable accuracy of GPS.

iv

Acknowledgements

Table of Contents

List of Figures

List of Tables

Modeling Navigation System Performance of a Satellite-Observing Star Tracker Tightly Integrated with an Inertial Measurement Unit

I. Introduction

THE Department of Defense (DoD) relies heavily on the Global Positioning System (GPS) as the workhorse of precise positioning, navigation, and timing (PNT). GPS enables military applications of accurate positioning, precision engagement, and synchronization. Commercial uses of GPS include similar applications such as accurate navigation and coordinated timing, which subsequently impact geography, surveying, communications, banking, and recreational activities. Additionally, GPS has caused a reliance on very precise PNT. As adversaries began to develop anti-GPS technologies and as warfighter missions adapt to new environments, a strict reliance on GPS comes into question.

Many research areas seek to compensate for perceived GPS vulnerabilities. Some of those are video-aided navigation [87], [86], [88], [90], [11], more precise accelerometers and gyroscopes [79], [68], [21], [10], novel sensors that use reliable, globally available sources [75], [76], [34], [55], and processing algorithms that incorporate measurement data in a navigation estimate [85], [35], [54].

With such a reliance on GPS for the past two decades the development of star trackers for navigation dwindled [43]. This lack of development leaves some room for improvement in using celestial navigation techniques in the field of precision navigation.

Celestial navigation has been used by mariners for centuries to measure the angle of stars with respect to the horizon, refer to almanacs, and plot lines of position, thereby calculating a position estimate in an otherwise featureless environment [9]. In 1957, when the first man-made earth satellite, Sputnik, launched, Dr. William H.

Guier and Dr. George C. Wieffenbach noted a distinct Doppler shift of the satellite's signal [27]. They determined that it is possible to predict the orbit of the satellite by measuring that Doppler shift from a fixed known location. Soon after, Dr. Frank T. McClure turned the method around [28]. If the satellite orbit is known, measuring the satellite signal would provide information to determine the observer's position.

From this concept many early satellite navigational systems were designed including the Navy Navigation Satellite System (NAVSAT), also called TRANSIT, Sequential Collation of Range (SECOR), Mobile System for Accurate ICBM Control (MOSAIC), Time and Navigation (TIMATION), and GPS. Other systems more recently are being developed and deployed for navigation purposes such as Globalnaya navigatsionnaya sputnikovaya sistema (GLONASS), Beidou, and Galileo. All of these Global Navigation Satellite Systems (GNSS) operate with radio-frequency signals and require knowledge of the signal design to decode navigation information. Hence, they aren't necessarily celestial navigation aids in the sense of using stars for reference.

This dissertation seeks to investigate the pertinent parameter space and anticipated performance of a alternative (to GNSS) navigation system that images light from a satellite on a background field of stars. From this image, the observer-satellite line-of-sight angle can be calculated. If the satellite ephemeris is known, the observer's position can be calculated. This method relies on the stars and their highly-precise catalogued positions to measure the pointing angle to a satellite observed by an imaging system. By measuring angles independent of the horizon or local horizontal plane, this proposed method is distinct from traditional celestial navigation. How those angle measurements of stars and earth satellites are made, and the application of modern sensors and data processing algorithms to calculate an observer's navigational state is distinct. One advantage of this satellite-observing method is that the reference sources (stars) are globally available and unjammable through human intervention. Some additional properties of such a system are that by observing sun-illuminated satellites, any satellite with a known orbit in the field of view potentially has valu-

able information regardless of which "named" system it belongs to. By observing it passively, the observer's position is not broadcast to other entities.

1.1 Objective

This research intended to determine the performance capability of an inertial navigation system Inertial Navigation System (INS) tightly integrated with a star tracker that observes illuminated satellites for terrestrial-based operations. The contributions of this research include

- **Use of light-emitting satellites to enable day/night capability.** This research investigated the requirements of a satellite, star tracker, and navigation algorithm in order to perform adequately in day and night conditions. The properties of the signal generated at the satellite was evaluated to determine nominal system requirements for detection and navigation.

- **Development of rigorous performance model.** This research defines the tightly-integrated INS-Star tracker system model. System error sources are identified and defined for a star tracker measurement model. These models are compared against real data collected using a representative star tracker sensor.

- **Trade study to identify key performance parameters.** The model was used to perform a trade study to identify the key performance parameters of the system. System performance was evaluated varying system specifications.

1.2 Dissertation Overview

Chapter II of this document describes background subject matter and previous related research. Chapter III details the problem of creating a man-made constellation of satellites for PNT applications and the parameter space involved in defining an approach using star trackers as the primary detectors. Chapter IV develops the tightly-integrated model of the objective Inertial Measurement Unit (IMU), describing the system components, their contributing noise sources, and algorithms used to

calculate vehicle navigation estimates. Chapter V describes the analysis of the expected performance as a function of system parameters, identifying key performance parameters. Chapter VI compares the model performance to navigation performance using real star tracker imagery. Chapter VII explains conclusions drawn from the results of this research and identifies additional work of interest on this topic.

Several Appendices are provided as a matter of reference. Appendix A derives the linearized measurement equations as applied to the position error states in the Kalman filter. Appendix B defines the conversion of the measurement uncertainty from the image frame of the differential site to that of the main observer. Finally, Appendix C describes the procedures used in collecting imagery at the United States Naval Observatory (USNO) Celestial Navigation Testbed (CNTB), which generated the imagery used in Chapter VI.

II. Background

THIS chapter describes the current approaches to using star trackers for position navigation and background topics relevant to the development of this new approach.

In presenting current research, an overview of star trackers is provided in Section 2.1. Section 2.2 reviews several reports regarding daytime detection of stars. Section 2.3 summarizes several key reports of using star trackers for earth navigation. Finally, Sections 2.4 and 2.5 discuss ancillary research regarding hardware and processing improvements to star trackers, and the application of star trackers for satellite attitude determination, respectively.

An introduction of several concepts involved in this research are presented in Sections xx-xx. properties of radiometry, constellation geometry, detector properties, and coordinate reference frames are described in this chapter as they are relevant to this dissertation's discussion of satellite light source requirements and star tracker integration with IMUs.

2.1   Star Tracker Properties

Liebe [49] introduces to the properties of a star tracker. He describes how they operate, their major components, and performance parameters. Star trackers detect the light from stars or other radiant sources, determine the positions of those stars in a desired reference frame, compare the star positions to published catalogs of stars and output a value indicative of the pointing angle in the celestial sphere, or inertial reference frame.

He introduces an estimator of the average number of stars in the field of view (FOV), N_{FOV} derived from the Positions and Proper Motions (PPM) Star Cata-

logue [49].

$$N_{FOV} = 6.57e^{1.08M} \left(\frac{1 - \cos\left(\frac{FOV}{2}\right)}{2} \right) \tag{2.1}$$

where the FOV is assumed to be circular in degrees and M is the limiting visual star magnitude of the detector. This method of estimating the number of stars in the field of view assumes that the stars are distributed homogeneously across the sky. It is known, however, that the density of the number of stars varies at different locations in the celestial sphere [20]. Despite this simplification, Liebe's estimator is used to evaluate a general performance result that doesn't require specific vehicle trajectories and subsequent specific pointing angles.

Liebe also introduces the application of star centroiding to get subpixel accuracy of an observed star. If the detector is placed at the focus of the optical system, all stars will be collected as point sources on individual pixels; however, if the system is defocused, the collected signal is spread across many pixels, which through weighed averaging can determine a center location (x_{cen}, y_{cen}) with subpixel accuracy. Using background-subtracted pixels in an image, $I(x, y)$, in a region of interest (ROI), the brightness, DN, is calculated as [49]

$$DN = \sum_{x=ROIstart+1}^{ROIend-1} \sum_{y=ROIstart+1}^{ROIend-1} I(x, y) \tag{2.2}$$

The centroid locations are then determined by [49]

$$x_{cen} = \sum_{x=ROIstart+1}^{ROIend-1} \sum_{y=ROIstart+1}^{ROIend-1} \frac{xI(x, y)}{DN} \tag{2.3}$$

$$y_{cen} = \sum_{x=ROIstart+1}^{ROIend-1} \sum_{y=ROIstart+1}^{ROIend-1} \frac{yI(x, y)}{DN} \tag{2.4}$$

He also states that the standard deviation of the centroiding error σ_{cen} in pixels is [49]

$$\sigma_{cen} \propto \sqrt{\frac{DN}{G}} \tag{2.5}$$

where G is the gain converting collected photoelectrons to stored pixel values. Alternatively, sources can be modeled to determine the expected number of incident photoelectrons in addition to detected noise to determine this value.

Liebe also discusses the noise equivalent angle (NEA) performance measure, which describes the amount of angle that would be measured by an ideal noise-free system given the values generated by typical noise sources. He states, "this error exclusively reflects the hardware (it is independent of software, algorithms, and calibration). It consists of photon noise, dark current noise, read/amplifier noise, limited resolution of the analog-to-digital (A/D) converter, and random error on the timestamp of the attitude estimate." He mentions that the error can be estimated in two ways, across the boresight of the camera, σ_{cb}, and around the boresight, σ_{roll} [49].

$$\sigma_{cb} = \frac{FOV \sigma_{cen}}{N_{pixel}\sqrt{N_{stars}}} \tag{2.6}$$

$$\sigma_{roll} = \tan^{-1}\left(\frac{\sigma_{cen}}{0.3825 N_{pixel}}\right)\left(\frac{1}{\sqrt{N_{stars}}}\right) \tag{2.7}$$

where N_{pixel} is the number of pixels in a square focal plane array, and N_{stars} is the average number of detected stars in an image. These error equivalencies are valuable when further applying the angle estimated by the star tracker to a navigation solution.

Given these basic functions of a star tracker, one avenue of research in the field is that of determining the star tracker capability to detect stars during the day.

2.2   Daytime Star Detection

Part of evaluating a global satellite navigation system available in day and night is determining the signal required from the satellite. The development and results of

defining the signal as a function of star tracker specifications and operating environments are presented in Chapter III. Funge [24] and Truesdale [82] have performed studies on detecting stars during daytime operations and their work is summarized below.

Funge [24] describes his process of modeling the sun reflections from satellites to an observer according to known structure and material of the satellites. Additionally, he compared the simulated intensity of the satellite reflection to modeled background radiance to calculate a Signal-to-Noise Ratio (SNR) as compared to a variety of sensor FOVs. He uses an *SNR* derivation from Dereniak [18], which applies when a sensor is in Background Limited Infrared Photodetector (BLIP) mode, or "when the background photon flux is much larger than the signal flux and is the dominant noise source". [24] He then simulated reflected "flares" of Iridium satellites in multiple bands and reported a night-time 90 second SNR range of approximately 145-188 dB. The daytime flares had an SNR range of approximately 0-70 dB, but also depended on a varying sensor FOV and the space object geometry. He noted that better SNR could be achieved if the signal were detected in an Infrared (IR) band rather than in the visible band [24].

Truesdale, et al., [82] tested in September 2012 a prototype star tracker in a high altitude balloon to validate the changes they made to a ST5000 star tracker in order for it to be capable of collecting images during daytime. Their adaptations included using a Complementary Metal-Oxide-Semiconductors (CMOS) sensor and longpass filter at 620 nm. Daytime collection of stars was demonstrated and their test results show cross-boresight accuracies of 0.22-0.26 arcseconds and a roll accuracy of 5.5 arcseconds.

The application of interest in this dissertation is the measurement of satellites using a star tracker for position determination. The following section discusses related work in this application.

2.3   Satellite Tracking for Position Determination

Star tracker hardware is traditionally used for satellite attitude correction. However, some effort has been done in adapting those techniques to lower altitudes such as in aircraft or ships by incorporating observations of satellites to determine the navigation state.

Crassidis, Alonso, and Junkins present the use of line-of-sight measurements to determine vehicle attitude and position [16]. The application of their research was in using the Vision Navigation System (VISNAV) [38] to perform relative position and attitude navigation between two spacecraft [2]. They describe the novel design of a Position Sensing Diode (PSD) that uses 4 leads (one on each each side of the square diode) on a single silicon photodiode to determine the centroid of incident light by comparing the levels of current through each lead. Combining this sensor with specific satellite beacon configurations and signals, the imaging and emitting satellites can perform relative navigation [16]. In [16] they also propose a non-linear predictive filter that estimates the position and attitude of the imaging vehicle with an attitude and position covariance matrix that achieves the Cramér-Rao lower bound.

Northrop Grumman developed the LN-120G Stellar-Inertial-GPS system that uses a star tracker to aid aircraft navigation [26]. This device is mounted on an aircraft and provides angular measurements of a catalog of 57 stars to provide a heading correction to the navigation solution of the aircraft. This application of a star tracker corrects for gyroscope errors due to drift; however the star tracker does not directly compute a position. Other methods have demonstrated position calculation as described next.

Willhite [93] described the use of sighting satellites in conjunction with a star to triangulate an observer's position using several measured angles. The satellite sighting, or Skymark, was used to improve a vehicle trajectory by providing a position update to an IMU. Willhite's thesis also used satellite availability analysis by Kaptuch [41]. He showed that the use of Skymark integrated with an IMU could

achieve a final position circular error probability (CEP) of 100 m, making the navigation solution 50% more accurate. Willhite's method uses these Skymark sightings to loosely-couple with an INS to improve position estimation. This dissertation will define the tight-coupling of the same measurement with an INS.

2.3.1 Angles-Only Navigation.   George Kaplan derived a 3-dimensional closed-form solution to determining an observer's position given a known satellite position on an identifiable star background [40]. With several observations, a least-squared solution of the observer's position is of the form $Ax = b$, where A is determined from n observations, the 3-dimensional (3-D) pointing vector to observed object i, $\mathbf{d}_i$, which object is known to have position, $\mathbf{P}_i$.

$$\begin{pmatrix} x_1 \\ x_2 \\ x_3 \end{pmatrix} = \begin{pmatrix} n - [d_{i_1}^2] & -[d_{i_1}d_{i_2}] & -[d_{i_1}d_{i_3}] \\ -[d_{i_1}d_{i_2}] & n - [d_{i_2}^2] & -[d_{i_2}d_{i_3}] \\ -[d_{i_1}d_{i_3}] & -[d_{i_2}d_{i_3}] & n - [d_{i_3}^2] \end{pmatrix}^{-1} \begin{pmatrix} [P_{i_1} - (\mathbf{d}_i \cdot \mathbf{P}_i)d_{i_1}] \\ [P_{i_2} - (\mathbf{d}_i \cdot \mathbf{P}_i)d_{i_2}] \\ [P_{i_3} - (\mathbf{d}_i \cdot \mathbf{P}_i)d_{i_3}] \end{pmatrix} \qquad (2.8)$$

The $[\cdot]$ operator represents a summation over n values, $\sum_{i=1}^{n} \cdots$. Kaplan describes the measurement errors associated with this approach as defined by

$$\sigma_X^2 = \sigma_P^2 + r^2 \sigma_d^2 \qquad (2.9)$$

where the σ_X represents the average ellipsoid radius of uncertainty around the determined position, σ_P represents the average ellipsoid radius of uncertainty around the observed satellite position, r is the distance to the observed satellite, and σ_d is the angular uncertainty. For a sensor with imaging resolution $\Delta\theta$ and observing an earth satellite with a star background, whose distances from the observer are relatively near and infinitely far, the angular uncertainty is found by [40]

$$\sigma_d = \frac{\Delta\theta}{2} \qquad (2.10)$$

Figure 2.1 visually describes the geometry of observation.
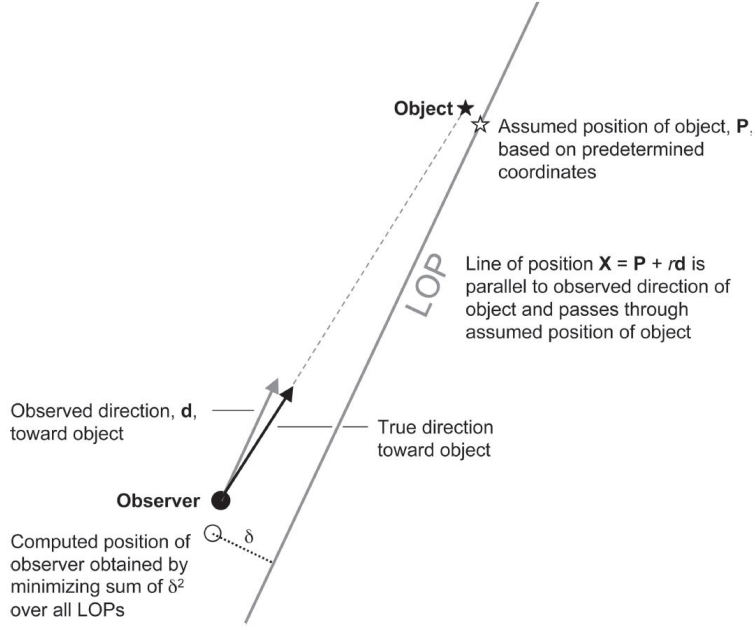
Figure 2.1:   Observation Geometry of Viewer and Satellite, reproduced with Author's permission [40].

This approach was tested against simulated GPS measurements and known GPS positions, where during approximately 30 minutes, 9 observations where made resulting in median positional errors of 70 m. The least-squares method inherent in the angles-only method minimizes the error of the observer's position. However, since it computes the residual update as a batch process, it doesn't account for the movement of the observer. The research presented in this dissertation uses a dynamic error estimate model of the observer's position. Therefore, a Kalman filter approach to integrating the measurements is an estimation method much better suited to the simulated scenario because the Kalman filter optimally estimates desired states as they change in time due to both dynamics and random processes, while maintaining all prior measurement information such that batch processes are not required when new measurements of the state are available.

2.4 Star Trackers for Satellite Navigation

Star tracker hardware is primarily used for determination of instrument and satellite orientation as part of the guidance, navigation, and control system [61], [69], [70], [37], [80], [47], [22]. Star trackers have also been proposed for use to measure satellite position as a function of refraction of observed stars [91]. Research related to the use of star trackers for these purposes are presented in this section. These summaries provide a sample of research of the application of star trackers.

Mortari, et al., [61] describe the results of a study done for the Italian Space Agency to determine the feasibility of imaging 3 FOVs on a single Charge-Coupled Device (CCD)s. They describe a variety of optical designs and an analysis of methods to distinguish the individual FOVs from each other using chromatic, monochromatic, and point spread function methods with a recommendation to use the latter. The authors introduce an iterative pyramid algorithm [59], Pyramid III, which is based on the k-vector method [58]- [60] to identify the stars in each FOV. The authors describe methods to improve both the speed and accuracy of calculating the centroid of imaged stars. Regarding improving the speed, one method maintains two vectors, which contain the indices of the maximum pixel intensity according to columns and rows. The other method, called "Run Length Encode" clusters adjacent high-intensity pixels in each row, then merges adjacent clusters over column space. Regarding improving the accuracy, they first proposed applying varying masks to the region of interest, reducing the weights of the values of pixels that are further from the center of the imaged star. Second, they proposed using recursive functions to reevaluate the centroid under different point spread function (PSF) assumptions to identify a best case. They showed a 40% improvement in centroiding accuracy, decreasing the mean error from 0.138 to 0.080 [61]. Lastly, the authors develop the mathematics to calculate large and small misalignments of the system, where small refers to the misalignments that can be determined using all three FOVs, and large refers to misalignments that only use a single FOV.

Rousseau, et al., [69] propose a new algorithm for finding attitude by reducing the star catalog from right ascension, declination, and magnitude values to oriented triangles. The oriented triangle is represented by a single value calculated as the norm of the cross product between the longest segment and the shortest segment of a three star triangle, where there is no other star internal to the triangle. The value is also signed as positive or negative depending on the direction from small to large segment. Upon collection, the oriented triangle value is calculated for each star in the image and compared to the catalog value within some threshold. The list of triangles should contain common stars, which are then used as a candidate reference or supposed reference star. The QUEST algorithm [12] is then used to express both the measured stars and the supposed stars as vectors in the reference frame creating matrices, M_1 and M_2. The catalog match is found by finding the index j of the max value of row i in $M(i, j) = M_1 M_2^T$. $M_2(j)$ is then the vector corresponding to the best match. To validate the star identification result, the angles of the measured stars, $M_i = \cos^{-1}(M_1, M_1^T)$ are compared to the resultant identified star list, M_3 angles, $M_c = \cos^{-1}(M_3, M_3^T)$. Those values in $M_c - M_i$ must therefore be within a threshold to validate the measured and identified lists. As such the stars are either confirmed or labeled unrecognized/incorrectly identified. This method reduces the overall size of the catalog and also removes the dimension of star magnitude from the profile. It reduces the processing time, making fewer comparisons between measurements and catalog. It also provides some robustness to errors in the measurements as more image wide comparisons are made beyond single triangle to triangle comparisons [69].

Rufino and Accardo [70] approached reducing the error in the calculated centroid of a star in an image by describing the amount of error due to the irradiance distribution on a pixel (systematic error) and that amount due to randomness associated with irradiance amplitude on the pixel. To test the effects of each, the authors defined two PSF models. One model incorporates only error due to defocusing and the other model incorporates both defocusing and diffraction. Point sources representing stars produced a PSF from which a centroid is determined by averaging pixel

locations weighted by irradiance amplitudes. The errors associated with defocusing and diffraction were on the order of 0.01 pixels. Additionally, the authors developed a neural network to identify and correct for systematic error, which could be done through calibration, resulting in a centroid accuracy of 0.005 pixels [70]. These results give some indication of possible star tracker measurement accuracy, which later is modeled in this dissertation.

Jørgensen [37] reports the performance of the Advanced Stellar Compass (ASC) star tracker in-orbit as compared to the preliminary lab results. The results show that the star tracker maintained an NEA of < 3 arcseconds (compared to the 1.2 arcseconds produced in the lab), that all autonomous functions to include automatic dark-level tracking, automatic gain, and gain degradation, as well as radiation defect buildup and mapping worked well, and that the camera controls correctly pointed such that sunlight did not impact image collection [37].

Tappe, et al., [80] describe the development of an indoor Three Axis Spacecraft Simulator (TASS) used for testing of attitude estimation algorithms. They present the use of angle methods (measuring the angles between stars in an image) to identify stars in their catalog and calculating the sensor attitude using a least squares solution (originally presented in [15]), the TRIAD algorithm [48], and the QUEST algorithm [92] [80].

Lee, et al., [47] discuss the use of a star tracker to align a distant spacecraft with the earth for optical communication. They propose that by fusing an INS, a star tracker, and a ground station, which determines the satellite's position, the satellite pointing angle can be known to 150 nanoradians or 30.9 milliarcseconds. They use a Kalman filter to fuse the measurements from the sensors thereby correcting for gyro drift and reducing pointing error of the satellite. Though they integrate an INS and star tracker with a Kalman filter, which is what this dissertation also presents, the application is different.

Enright, et al., [22] seek to develop a star tracker for small satellites that relies solely on the attitude estimate for satellite navigation to reduce payload size by removing all other navigation instruments. They review several of the challenges posed by this approach and present nominal designs of such a star tracker. In contrast, this dissertation doesn't want to remove all other sensors, but integrate the star tracker with an IMU for position estimation.

2.4.1 Refraction Measurement for Satellite Positioning. White and Gounley [91] proposed that a satellite could receive information about its position in orbit by observing stars near the Earth's horizon and calculating the refraction of the stars. This method is referred to as Stellar Horizon Atmospheric Dispersion (SHAD). Star catalogs provide highly accurate angles to the stars and the refraction causes deviations of those angles for stars close to the horizon. Additionally, the difference in refraction at different wavelengths can be used to inform the observer's position. Satellite navigation performance was simulated at Medium Earth Orbit (MEO) and Geostationary Orbit (GEO) orbits as well as with varying numbers of star sightings. They reported that steady state position error standard deviations were between 10 and 40 m, depending on the satellite orbit and number of stars observed, improving contemporary satellite navigation systems.

2.5 Detector Device Improvement

Another popular area of research in star tracker development is the improvement of the detector. CCDs have long been used in star trackers because they were easily and cheaply produced and have been available for some time. As the CMOS-type focal plane arrays have become more readily available, the community proposes advances that are possible by using them in star trackers.

Yadid-Pecht, et al., [95] discuss the development of the Automatic Wide Accepted Range Detector (AWARD), which in its first phase improved a CMOS Active Pixel Sensor (APS) to allow electronic shuttering of individual pixel elements. This

is done by adding both a column and row reset capacitor to each pixel element's electronics such that the controller can perform individual addressing, rather than complete row or column resets as done previously. What this also allows is control of individual pixel integration times, which subsequently allows for a wider dynamic range in image capture. Their experimental results showed improved performance in those areas over CCD cameras and other APS devices [95].

Another effort is the Defense Production Act Title III Advanced CMOS focal plane array (FPA) for Visible Sensors for Star Trackers (VSST) Project that invests money in capabilities that design, manufacture, and test products exclusively in the United States. This program was started in an effort to motivate and revitalize the United States (US)' capabilities to produce star trackers. The specifications for such a sensor was released in a Broad Agency Announcement (BAA), known as the Staring Technology for Enhanced Line-of-sight Angular Recognition (STELLAR) Technical Goals, in 2010 [17].

Liebe, et al., report the testing of an APS system in a star tracker application. They characterized their system to have a readout noise of 94 electrons, a full well capacity of 450,000 electrons, centroiding accuracy of 0.1 pixels, and greater dynamic range than CCDs, concluding that CMOS technology could be used in a star tracker [52].

Liebe, et al., also propose in [51] to reduce by at least an order of magnitude the mass and power required for the star tracker while increasing the update rate by an order of magnitude without loss of performance compared to larger versions.

Saint-Pe, et al., review the advantages of CMOS sensors to CCD sensors such as lower power consumption, higher frame rates, read-out flexibility (windowing), simple electrical interfaces, anti-blooming capability, and intrinsic radiation hardening, and on-chip signal processing. They also introduced a few applications that CMOS sensors would enhance such as star trackers and optical terminals, earth observation of satellites, and smart sensors that allow for event detection and processing.

Their recommendation is that CMOS image sensors are fully qualified for space-type applications [72].

Shucker reports the development of a prototype CMOS star tracker for use on small satellites. He discusses the focal plane specs, the star catalog used, the method to identify star pairs, simulation results, and experimental results. The simulations resulted in 82.8 arcseconds in cross-boresight error and 140.4 arcseconds in roll error. Testing an uncooled 1280 x 1024 FPA operating in the spectral range of 400-1000 nm, the author demonstrated an ability to image a star but didn't report pointing accuracy information [77].

2.6 *Kalman Filter*

The Kalman filter is an optimal, recursive data processing algorithm that models random processes in order to estimate system states and the uncertainties associated those states as a function of time. Maybeck [54] describes the process in detail, elements of which will be discussed in the following section regarding the Extended Kalman Filter (EKF). The algorithm is divided into two steps, a propagation step and an update step. The state of the system is represented by a vector of random variables, $\mathbf{x}$. In the propagation step, the system dynamics, $\mathbf{F}$, control inputs, $\mathbf{u}$, and dynamic driving noise, $\mathbf{w}$ are used to model the change of the state over time. During the update step, measurements of the state, $\mathbf{z}$, that have associated measurement noise, $\mathbf{v}$, are compared to estimated measurements generated from the system state. In a Kalman filter, system dynamics and measurements are linear combinations of the system state. When either the dynamics equations or the measurement equations are nonlinear, a different filter must be used. An EKF uses a first-order linear approximation of the dynamics and measurement equations to estimate the system state and is described in more detail below.

2.6.1 Extended Kalman Filter.   The EKF has the same mathematical structure of a Kalman filter with propagation and update steps. Non-linear dynamics and

measurement equations can be linearized using a perturbation model and a Taylor series expansion. The EKF uses this method to adapt the Kalman filter to non-linear systems by truncating all but the first-order terms of the dynamics and measurement equations in order to calculate a state estimate. A summary based on the derivation by Maybeck [53] follows.

A system with non-linear dynamics and additive noise can be described as

$$\dot{\mathbf{x}}(t) = \mathbf{f}[\mathbf{x}(t), \mathbf{u}(t), t] + \mathbf{G}(t)\mathbf{w}(t) \tag{2.11}$$

where the superscript dot, $(\dot{\cdot})$, signifies the first derivative of the variable with respect to time, $\mathbf{x}(t)$ is an n-dimensional Gaussian random vector describing the state of the system at time t, $\mathbf{u}(t)$ is the system input, $\mathbf{G}(t)$ maps $\mathbf{w}(t)$ into state space and $\mathbf{w}(t)$ is a zero-mean white Gaussian noise process with covariance

$$E\{\mathbf{w}(t)\mathbf{w}^T(t + \tau)\} = \mathbf{Q}(t)\delta(\tau) \tag{2.12}$$

where $E\{\}$ is the expectation operator and $\delta(\tau)$ is a Dirac delta function.

Given the state dynamics in Eqn. (2.11), the state transition matrix, $\mathbf{\Phi}$, which describes the deterministic propagation of the state from the current state over an increment of time, is defined by the matrix exponential

$$\mathbf{\Phi}[t_{i+1}, t_i; \hat{\mathbf{x}}(t_i)] = e^{\mathbf{F}\Delta t} \tag{2.13}$$

where Δt is the time interval from t_i to t_{i+1}, and the state transition matrix is evaluated at an estimate of the state at time t_i, given by

$$\hat{\mathbf{x}}(t_i) = E\{\mathbf{x}(t_i)\} \tag{2.14}$$

18

and $\mathbf{F}$ is the Jacobian of the non-linear $\mathbf{f}()$ matrix evaluated at the current estimate.

$$\mathbf{F}[t_i; \mathbf{x}(t_i)] \triangleq \left. \frac{\partial \mathbf{f}[\mathbf{x}, t_i]}{\partial \mathbf{x}} \right|_{\mathbf{x}=\hat{\mathbf{x}}(t_i)} \tag{2.15}$$

The estimate mean and covariance are propagated from t_i to t_{i+1} by

$$\hat{\mathbf{x}}(t_{i+1}^-) = \mathbf{\Phi}[t_{i+1}, t_i; \hat{\mathbf{x}}(t_i)]\hat{\mathbf{x}}(t_i^+) \tag{2.16}$$

$$\mathbf{P}(t_{i+1}^-) = \mathbf{\Phi}[t_{i+1}, t_i; \hat{\mathbf{x}}(t_i)]\mathbf{P}(t_i^+)\mathbf{\Phi}^T[t_{i+1}, t_i; \hat{\mathbf{x}}(t_i)]$$
$$+ \int_{t_i}^{t_{i+1}} \mathbf{\Phi}[t_{i+1}, i; \hat{\mathbf{x}}(t_i)]\mathbf{G}(t)\mathbf{Q}(t)\mathbf{G}^T(t)\mathbf{\Phi}^T[t_{i+1}, t; \hat{\mathbf{x}}(t_i)]dt \tag{2.17}$$

The uncertainty in the system state will grow in relation to the process noise and time as shown in Eqn. (2.17). At some time, the state is observed through a discrete measurement, $\mathbf{z}_{i+1}$, and the information contained in that measurement will update the state estimate to more closely reflect the true state of the system, reducing the uncertainty in the estimate. The "+" and "−" characters associated with the time variable indicate at the given time, whether the measurement at that time has been incorporated into the estimate by the filter. The "+" character signifies after the measurement has been incorporated giving an *a posteriori* estimate of the state, and the "−" character signifies the *a priori* estimate of the state or just before incorporating the measurement.

Discrete-time measurements are modeled by

$$\mathbf{z}(t_i) = \mathbf{h}[\mathbf{x}(t_i), t_i] + \boldsymbol{\nu}(t_i) \tag{2.18}$$

where the measurement function $\mathbf{h}[\cdot]$ may be non-linear, and $\boldsymbol{\nu}(t_i)$ is zero-mean additive white Gaussian noise (AWGN) with covariance

$$E\{\boldsymbol{\nu}(t_i)\boldsymbol{\nu}^T(t_j)\} = \begin{cases} \mathbf{R}(t_i), & t_i = t_j \\ 0, & t_i \neq t_j \end{cases} \tag{2.19}$$

The state estimate and estimate covariance are updated by

$$\hat{\mathbf{x}}(t_{i+1}^+) = \hat{\mathbf{x}}(t_{i+1}^-) + \mathbf{K}(t_{i+1})\{\mathbf{z}_{i+1} - \mathbf{h}[\hat{\mathbf{x}}(t_{i+1}^-), t_{i+1}]\} \tag{2.20}$$

$$\mathbf{P}(t_{i+1}^+) = \mathbf{P}(t_{i+1}^-) - \mathbf{K}(t_{i+1})\mathbf{H}[t_{i+1}; \hat{\mathbf{x}}(t_{i+1}^-)]\mathbf{P}(t_{i+1}^-) \tag{2.21}$$

where the measurement residual, described by the difference between the actual measurement, $\mathbf{z}$, and the estimated measurement, $\mathbf{h}[\hat{\mathbf{x}}]$, is distributed to the states through the Kalman gain, $\mathbf{K}$ given by

$$\mathbf{K}(t_{i+1}) = \mathbf{P}(t_{i+1}^-)\mathbf{H}^T[t_{i+1}; \hat{\mathbf{x}}(t_{i+1}^-)]\cdot$$
$$\{\mathbf{H}[t_{i+1}; \hat{\mathbf{x}}(t_{i+1}^-)]\mathbf{P}(t_{i+1}^-)\mathbf{H}^T[t_{i+1}; \hat{\mathbf{x}}(t_{i+1}^-)] + \mathbf{R}(t_{i+1})\}^{-1} \tag{2.22}$$

In Eqns. (2.21) and (2.22), the $\mathbf{H}[\cdot]$ matrix is calculated by linearizing $\mathbf{h}[\cdot]$ through Taylor series expansion and truncation of 2nd- and higher-order terms. This results in the Jacobian of $\mathbf{h}[\cdot]$ evaluated at a nominal value $\hat{\mathbf{x}}(t_{i+1}^-)$ given by

$$\mathbf{H}[t_{i+1}; \mathbf{x}(t_{i+1}^-)] \triangleq \left.\frac{\partial \mathbf{h}[\mathbf{x}, t_{i+1}]}{\partial \mathbf{x}}\right|_{\mathbf{x}=\hat{\mathbf{x}}(t_{i+1}^-)} \tag{2.23}$$

This summary of the EKF is generic to any modeled system. The EKF specific to the system in this dissertation is defined in Chapter IV.

2.7 System Properties

As the elements of the system are described, there are mathematical properties that govern the signal transmission, the geometry of the satellite-observer-earth configuration, and the processing of digital images for signal detection. This section describes these elements and how they apply to the proposed research. The system will detect a signal from the satellite and measure the angle that satellite makes with the observer and the earth. First, the properties of satellite-sun reflections will be discussed. Next, properties of the detector itself will be presented. Finally, geometrical calculations are given for the earth-satellite-observer system.

2.8 Sun Exitance

Spectral exitance, M_e of a blackbody source is given by Planck's law [65]

$$M_e(\lambda) = \frac{2\pi h c^2}{\lambda^5 (e^{\frac{hc}{k\lambda T}} - 1)} \tag{2.24}$$

where $h = 6.626 \times 10^{-34}$ watt·sec^2 is Planck's constant, c is the speed of light in a vacuum, $k = 1.381 \times 10^{-23}$ watt·sec/°K is Boltzmann's constant, T is the temperature of the blackbody in Kelvin, and λ is the wavelength in meters. In the case of the Earth's sun, which has an accepted temperature of 5778° K, implementation of Eqn. (2.24) results in the exitance curve shown in Figure 2.2. The blackbody curve is an approximation of the solar radiance rather than a true measurement as it doesn't account for solar atmospheric conditions that result in absorption in the spectrum.

The sun's energy reflects off of Earth satellites and to the Earth's surface. Approximating the satellite as a sphere and a lambertian surface, the magnitude, M_v, of these reflections can be modeled by [30]

$$M_v = -26.74 - 2.5 \log\left(\frac{2}{3\pi^2} A\rho\left[(\pi - \phi)\cos\phi + \sin\phi\right]\right) + 5\log(R) \tag{2.25}$$
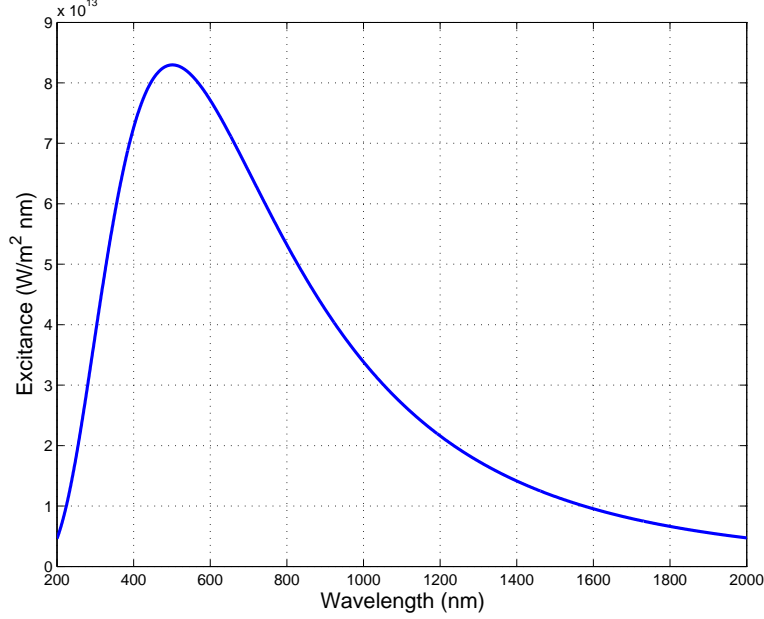
Figure 2.2:   Exitance of the Sun over the wavelengths 1-2000 nm

where A is the cross-section of a spherical representation of the satellite, ρ is the bond albedo, ϕ is the solar phase (sun-satellite-sensor) angle, and R is the line-of-sight distance from the satellite to the observer.

Thus the "signal" from the satellite can be simply the reflected light. Measuring this light is the primary source for determining the observer-earth-satellite angle. Therefore, it must be detected using a star tracker. Properties of a star-tracker as a generic detector are presented in the next section.

2.9   Detector Properties

When observing the sky to collect star light or satellite-sun reflections, the detector collects the energy on a focal plane array of detector elements. These elements receive both the signal energy and the alternative energy source of scattered background radiance. When observing the satellites and stars from the earth, molecules in the atmosphere absorb and radiate energy in processes called Mie and Rayleigh scattering [45]. This scattered energy becomes a radiant source that is collected in the detector as noise, and in this study is referred to as background radiance, L_b.

22

Similarly, the actual signal energy from a star or a satellite is transmitted through the atmosphere and partially scattered. The effects of the signal scatter can be summarized in an atmospheric transmission term, $\tau_{atm} \in [0, 1]$, used linearly to reduce the detected signal power.

As may be obvious, the amount of energy scatter due to the atmosphere is therefore dependent on the molecular makeup of the atmosphere along the line of sight from the observer in the direction of observation. This introduces parameters such as air density, humidity, aerosol composition, and others that when measured could reasonably predict the anticipated background radiance in the image as well as the atmospheric transmission of the signal. The derivation of the radiance and transmission terms has previously been documented [45] and will not be described here. This research will leverage tools developed for performing the radiance and transmission modeling. Specifically, this research will use the Phillips Laboratory EXpert-assisted User Software (PLEXUS) software, version 3.0, which is an interface for the user input parameters and generate data using Moderate Resolution Atmospheric Radiance and Transmittance Model (MODTRAN) 4.0 modeling software. Samples of background radiance and atmospheric transmission values are shown in Figures 2.3 and 2.4.

As the signal and background energy reaches the star tracker it is focused through one or more optical element onto the focal plane. Though each optical element, e.g., a lens or mirror, transmits or reflects the incident energy, they are not ideal and therefore introduce an optical transmission term, $\tau_{opt} \in [0, 1]$, that reduces the amount of energy collected on the detector. The optical elements are generally placed in series, so that the overall optical transmission is the product of the transmissions of each of the n elements. Additionally, the optical path transmission is a function of the wavelength due to numerous materials from which the optical elements can be made.

$$\tau_{opt}\left(\lambda\right) = \prod_{i=1}^{n} \tau_{opt_i}\left(\lambda\right) \tag{2.26}$$

23
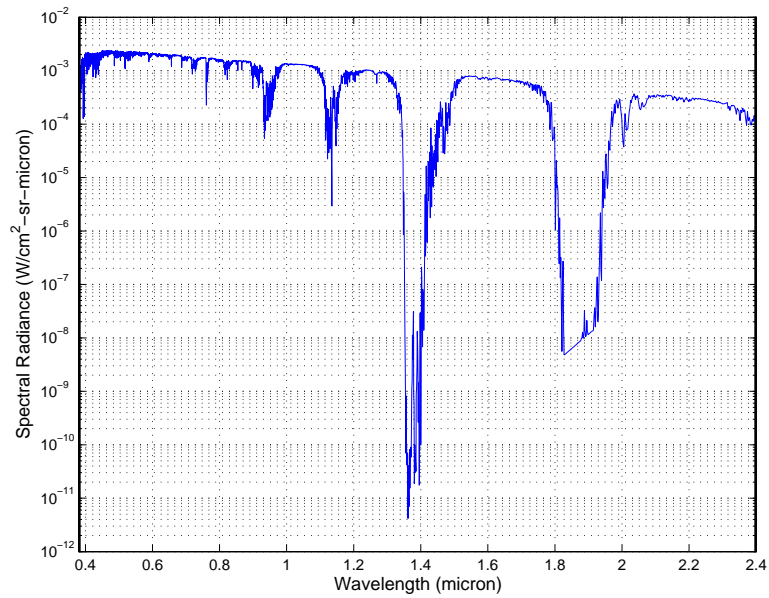
Figure 2.3: Sample PLEXUS Results for Spectral Radiance. Radiance of scattered sunlight from 0.38 to 2.4 microns at sea level.
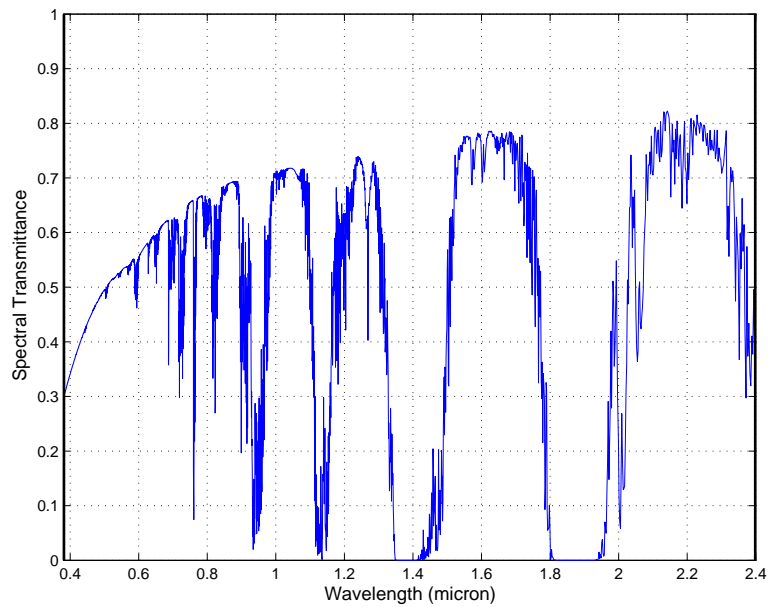
Figure 2.4: Sample PLEXUS Results for Atmospheric Transmission from 0.38 to 2.4 microns at sea level.
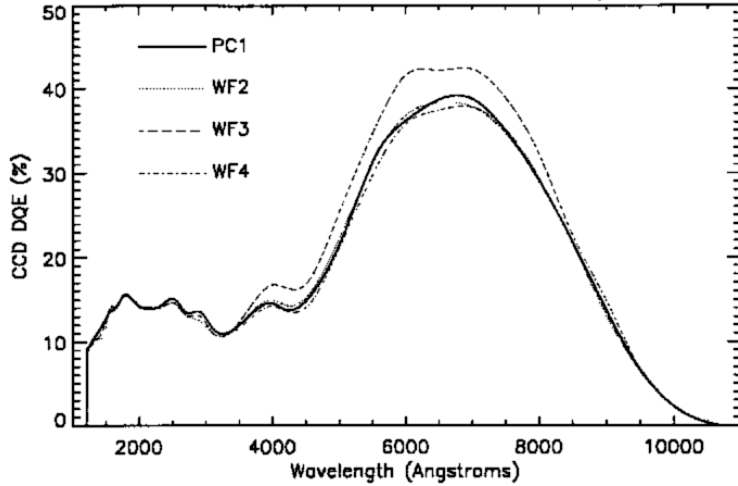
Figure 2.5:   Quantum Efficiency of Hubble Wide Field and Planetary Camera 2 [7]

Energy has finally arrived at the detector elements and is now converted to a discrete level of charge. Due to the photoelectric effect, the number of incident photons can be calculated given the incident energy and the wavelength of the light by [73]

$$E_p(\lambda) = \frac{hc}{\lambda} \tag{2.27}$$

Though a number of photons are incident on a detector, the number of photons collected by the detector is a function of the focal plane array's quantum efficiency, $Q_e \in [0, 1]$. Figure 2.5 shows the Q_e response to signal wavelength for one of the Hubble space telescope focal plane arrays [7].

Given an incident number of photons, N_p, and the quantum efficiency, the number of photoelectrons detected, N_{det}, is the product of the two.

$$N_{det}(\lambda) = N_p(\lambda)Q_e(\lambda) \tag{2.28}$$

25

However, the detector elements collect the charge contributed by all wavelengths, therefore, the detected number of photons is

$$N_{det} = \sum_{\lambda} N_p(\lambda) Q_e(\lambda) \qquad (2.29)$$

The charge that has been collected in each detector element must now be "read" to process the data in a usable form. CCDs and CMOSs read the values from the elements in different manners, but both require the same electronics that first convert the charge to a voltage, second, convert that analog voltage to a quantized voltage level, and third, convert the signal again through an A/D converter into computer memory. The first step, where a capacitor receives the transferred charge from detector elements, contributes a noise referred to as readout noise or read noise. This noise can be characterized by comparing short- or no-duration integration time frames.

To determine the read noise of an image, first the frame bias or detector element offset values must be found. After a detector element is read, it is reset to an ideal zero-charge level. However, after the reset there is some residual charge left in the potential well. This residual charge is the initial value or charge offset on top of which photons are collected. A bias frame, $I_{bias}(x, y, t_{int})$, is characterized by taking an image over a short integration time, t_{int}. Since read and to-be-discussed dark current noises may be affecting the values of that bias frame, N bias frames may be averaged to determine the characteristic bias frame, $I_{bias}(x, y)$.

$$I_{bias}(x, y) = \frac{1}{N} \sum_{i=1}^{N} I_{bias_i}(x, y, t_{int,i}) \qquad (2.30)$$

A sample bias frame and the associated histogram of pixel values is shown in Figure 2.6, and an average bias frame and associated histogram of pixel values is shown in Figure 2.7.

Note that the distribution of values for the bias frames are nearly Gaussian and that the average bias frame has a smaller standard deviation than a single bias
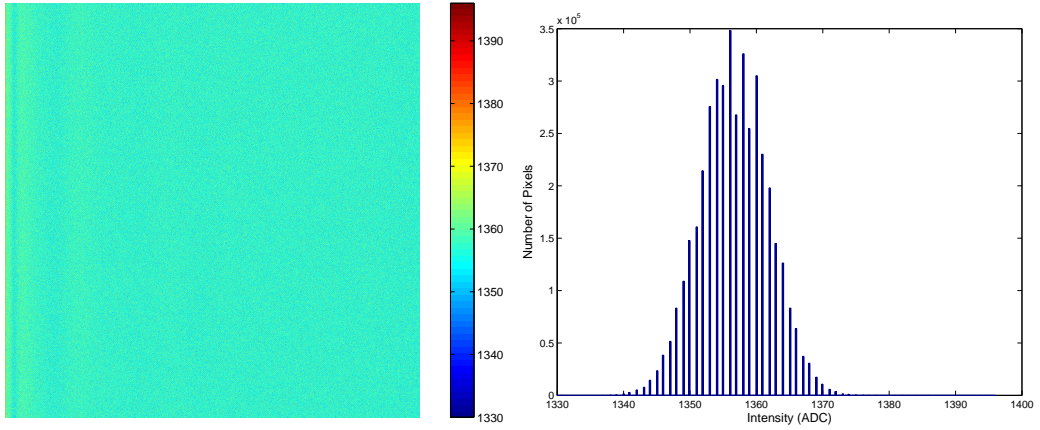
Figure 2.6: Sample bias frame and histogram of pixel intensities of the bias frame.
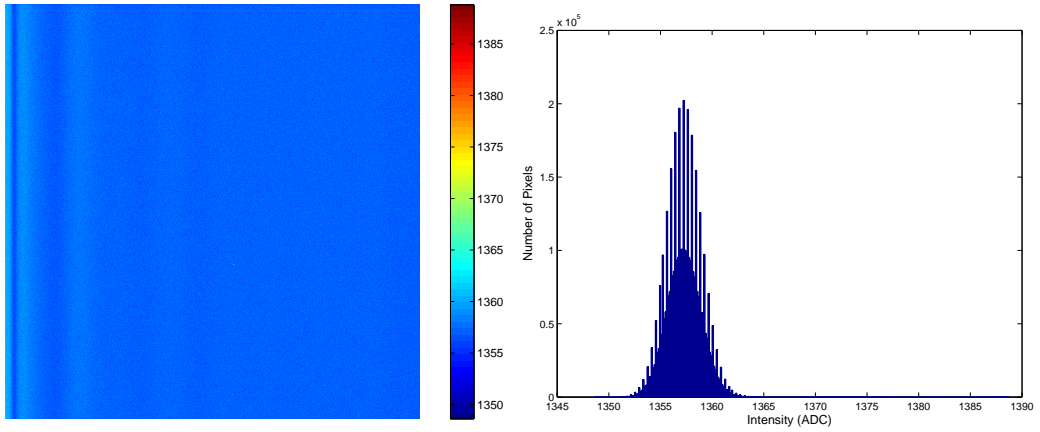
Figure 2.7: Sample average bias frame and histogram of pixel intensities of the average bias frame.

frame. This change in standard deviation of bias frames can indicate the impact of read noise. Specifically the read noise σ_{read} can be estimated by [36]

$$\sigma_{read} = \frac{\sigma_b}{\sqrt{2}} \tag{2.31}$$

where σ_b is the standard deviation of the difference of two bias frames,

$$\sigma_b = \sqrt{\frac{1}{M_x M_y} \sum_{x=1}^{M_x} \sum_{y=1}^{M_y} [(I_{b1}(x,y) - I_{b2}(x,y)) - \mu_{I_{12}}]^2} \tag{2.32}$$

and $\mu_{I_{12}}$ is the mean value of the difference of two bias images. Note that σ_{read} is in units of Analog to Digital Unit (ADU)s, but typically are represented in units of electrons (e$^-$). To make the conversion back to electrons from ADUs requires knowledge of the system gain, but this parameter will not be derived here. In the application discussed in Chapter III, background-induced noise is typically the dominant noise source rather than detector read noise. In Chapter III, typical star tracker read noise parameters are given, however the impact to the overall system performance is negligible.

One final noise term contributes to the overall collected signal value. Operating a detector at any temperature above zero Kelvin, electrons are emitted within the system and collected by the detector elements. Because the temperature of the system causes the electrons to be emitted, but not an external light source, this is often referred to as thermal noise or dark current. Once the offset values of the elements have been characterized, the dark current can be similarly characterized and stored as a dark image, I_{dark}. The element-by-element effect of dark current $I_{dark}(x,y)$ can be determined for a specific integration time by averaging N dark frames, which have had the offset values subtracted.

$$I_{dark}(x,y,t_{int}) = \frac{1}{N} \sum_{i=1}^{N} I_{dark_i}(x,y,t_{int,i}) - I_{bias}(x,y) \tag{2.33}$$

The bias frame is not dependent on the integration time, but on the initiation of collecting data and therefore applicable to any dark frames. By subtracting the offset values, the average dark frame characterizes the values due only to the thermally-generated electrons with some read noise.

After characterizing the noise in the detector, a detected image, $I_n(x, y)$ can be corrected for these noise terms by subtracting them element-wise to produce an image of the true sources $I(x, y)$. Though a dark image rate could be found by dividing by the integration time, a dedicated dark, or dark image dedicated to the specific integration time of the detected image is more appropriate to use.

$$I(x, y, t_{int}) = I_n(x, y) - I_{dark}(x, y, t_{int}) - I_{bias}(x, y) \qquad (2.34)$$

The amount of light that falls on a detector element in the FPA is dependent on the geometry of the optical system and the fact that it is collecting photons from two sources. The background is a broad radiant source and the signal of interest is a point source. The amount of background energy collected is a function of the angular field of view of the detector elements. A single element has an angular field of view, in radians, called the Instantaneous Field of View (IFOV), that is calculated geometrically as a function of the focal length, f, and the element pitch size or physical width, d_{pixel}, [66]

$$IFOV = 2\tan^{-1}\left(\frac{d_{pixel}}{2f}\right) \qquad (2.35)$$

or alternatively by the detector field of view, θ_{FOV} and, assuming a square FPA, the number of detector elements in one axis, N_{FPA} [66].

$$IFOV = \frac{\theta_{FOV}}{N_{FPA}} \qquad (2.36)$$

The circular aperture, through which the light enters the optical system, causes a Fraunhofer diffraction. Because of radial symmetry, this causes a large peak of

intensity at the focal point on the image plane surrounded by a dark ring. The **2D!** (**2D!**) circle of imaged light is the Airy disk, with a radius of r_{airy}. The size of the disk refers to the distance from the center of the signal to the first null of the pattern, driven by a first-order Bessel function, the focal length, and the diameter of the detector aperture, d_{ap}. This is approximated by [29]

$$r_{airy} = 1.22 \frac{f\lambda}{d_{ap}} \tag{2.37}$$

which is given in units of length and can be converted to units of pixels, n_{airy}, or number of elements, by

$$n_{airy} = \frac{2 r_{airy}}{d_{pixel}} \tag{2.38}$$

This diffraction pattern introduces a spreading of the point source power to a certain number of detectors. Shanks [74] uses an Energy on Detector (EOD) term that describes the amount of signal power collected on a single (central) element. Assuming 100% fill-factor, describing how much physical space the semiconductor element uses within its allotted space in the array, Shanks defines the $EOD(x) \in (0, 1]$ as

$$EOD(x) = \mathrm{Erf}\left[\frac{x}{2\sqrt{2}}\right]^2 \tag{2.39}$$

where

$$x = \frac{IFOV}{r_{airy}} \tag{2.40}$$

and the error function is the integral of a normal distribution

$$\mathrm{Erf}[\gamma] = \frac{2}{\sqrt{\pi}} \int_0^\gamma e^{-t^2} dt \tag{2.41}$$
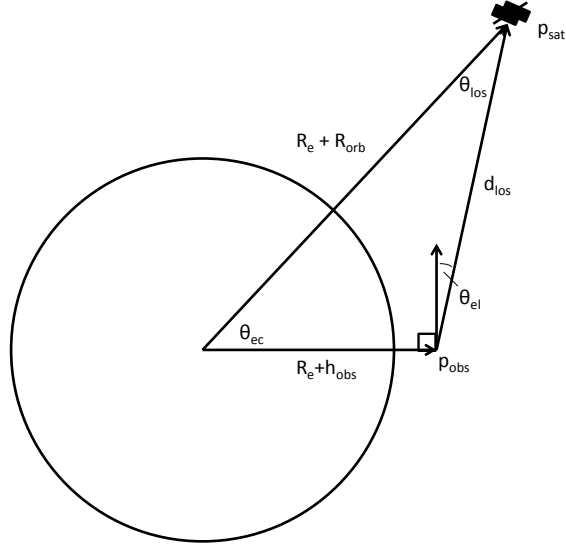
Figure 2.8:   Geometry of Satellite and Detector

Having defined the pertinent noise sources and the amount of signal power incident on the detector, the ability to detect the signal in the noise is evaluated according to the SNR. Generally, it is computed by [19]

$$SNR = \frac{\text{Signal Power}}{\sqrt{\text{Detector Noise} + \text{Background Noise} + \text{Signal Noise}}} \qquad (2.42)$$

Chapter III will describe in more detail several versions of the SNR that were compared specific to the task of detecting a satellite signal in daylight.

2.10   Geometry of Satellite-Earth-Observer System

Observing a satellite allows an observer to measure both the magnitude of the source and an angle with respect to his local reference frame. The geometry associated with the satellite-earth-observer system is presented here with additional discussion of satellite constellation development.

2.10.1   Observer Geometry.   The geometry of this system is shown simplistically in Figure 2.8.

Chobotov describes the following relationships between the observer-earth center-satellite angle, or earth central angle, θ_{ec}, the local horizontal to satellite observer elevation angle, θ_{el}, the satellite orbit height, R_{orb}, the observer-satellite-earth center angle, or nadir angle, θ_{los}, and the line of sight distance, or slant range from observer to satellite, d_{los} [13].

$$\cos(\theta_{ec} + \theta_{el}) = \frac{\cos\theta_{el}}{1 + (R_{orb}/R_e)} = \sin\theta_{los} \qquad (2.43)$$

$$\tan\theta_{el} = \frac{\cos\theta_{ec} - (R_e/(R_e + R_{orb}))}{\sin\theta_{ec}} \qquad (2.44)$$

$$d_{los}^2 = R_e^2 + (R_e + R_{orb})^2 - 2R_e(R_e + R_{orb})\cos\theta_{ec} \qquad (2.45)$$

By including an observer height, h_{obs}, multiplying Eqn. (2.43) by an identity R_e/R_e, and similarly multiplying Eqn. (2.44) by an identity $(R_e + R_{orb})/(R_e + R_{orb})$ the equations become [13]

$$\cos(\theta_{ec} + \theta_{el}) = \frac{(R_e + h_{obs})\cos\theta_{el}}{R_e + R_{orb}} = \sin\theta_{los} \qquad (2.46)$$

$$\tan\theta_{el} = \frac{(R_e + R_{orb})\cos\theta_{ec} - R_e}{(R_e + R_{orb})\sin\theta_{ec}} \qquad (2.47)$$

$$d_{los}^2 = (R_e + h_{obs})^2 + (R_e + R_{orb})^2 - 2(R_e + h_{obs})(R_e + R_{orb})\cos\theta_{ec} \qquad (2.48)$$

Given that the satellite orbit height, and the observer elevation and height are known, the earth central angle can be found from Eqn. (2.46) by [13]

$$\theta_{ec} = \cos^{-1}\left[\frac{(R_e + h_{obs})\cos(\theta_{el})}{R_e + R_{orb}}\right] - \theta_{el} \qquad (2.49)$$

Similarly, the nadir angle can be solved using Eqn. (2.46) as [13]

$$\theta_{los} = \sin^{-1}\left[\frac{(R_e + h_{obs})\cos(\theta_{el})}{R_e + R_{orb}}\right] \qquad (2.50)$$

Assuming the observer is positioned at the edge of the detectable signal, the total broadcast angle, or dispersion angle, of the satellite signal in radians is double the nadir angle.

$$\theta_{disp} = 2\theta_{los} \tag{2.51}$$

Finally, the slant range between the observer and the satellite is the square root of Eqn. (2.48),

$$d_{los} = \sqrt{(R_e + R_{orb})^2 + (R_e + h_{obs})^2 - 2(R_e + R_{orb})(R_e + h_{obs})\cos^2(\theta_{ec})} \tag{2.52}$$

2.10.2 Satellite and Constellation Properties. When multiple satellites are used, it's necessary to define the constellation size according to the number of orbital planes, p and number of satellites in each plane, s. Chobotov [13] describes the process of global coverage of a constellation assuming circular orbits of the satellites. Satellites that orbit in the same plane with overlapping coverage form a band or street of coverage on the Earth's surface. In a constellation of such satellites the half-street width, c, must be known, which determines the distance of the sides of non-overlapping regions of satellite coverage as shown in Fig. 2.9.

The radius of the circle of signal coverage, θ, the half-street width, c, and the number of satellites in the same orbital plane are related by [13]

$$\cos\theta = (\cos c)\cos\left(\frac{\pi}{s}\right) \tag{2.53}$$

Therefore, the number of satellites, s, can be solved recognizing that the Earth central angle, θ_{ec} is the same as the radius of the circle of signal coverage,

$$s = \frac{\pi}{\cos^{-1}\left(\dfrac{\cos\theta_{ec}}{\cos c}\right)} \tag{2.54}$$

33
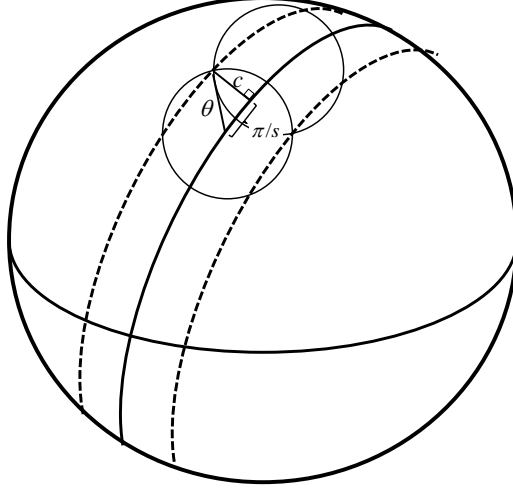
Figure 2.9:   Satellite Coverage in Orbital Plane

The earth central angle has previously been determined, but the half-street width is also required. Therefore, orbital plane properties separating co-rotating planes and counter-rotating planes must be used. Co-rotating planes are planes who have adjacent ascending nodes, whereas counter-rotating planes are planes that are adjacent, but one of whom has their ascending node on the opposite side of the Earth. The angle separating co-rotating planes, α, the angle separating counter-rotating planes, β, are related by [13]

$$\alpha = c + \theta_{ec} \tag{2.55}$$

$$\beta = 2c \tag{2.56}$$

$$(p - 1)\alpha + \beta = \pi \tag{2.57}$$

Combining Eqns. (2.55) and (2.56) in Eqn. (2.57), and estimating the number of orbital planes needed allows us to solve for the half-street width [13].

$$c = \frac{\pi - (p - 1)\theta_{ec}}{p + 1} \tag{2.58}$$

34
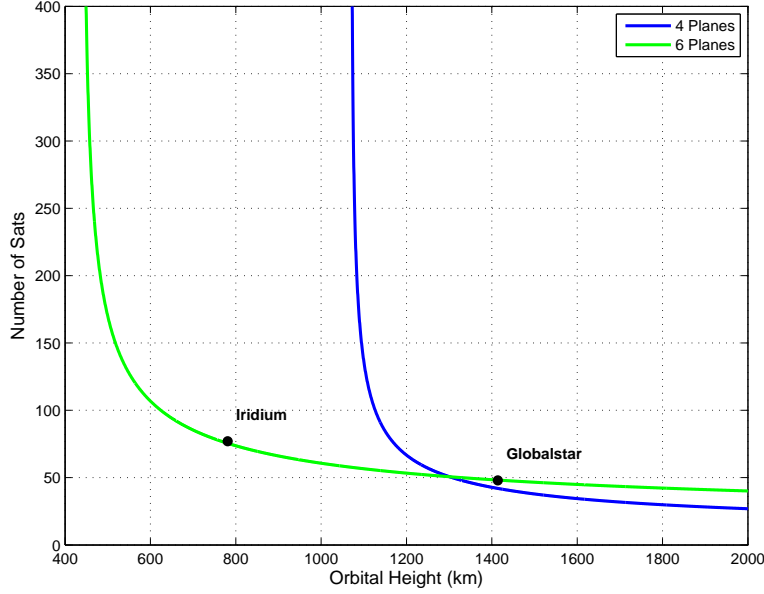
Figure 2.10:   Number of satellites required for global coverage with 10 degree elevation minimum observability. Two sample LEO constellations are also included.

Finally, the total number of satellites required, n_{sats} for global coverage is given by the product of the number of planes and the number of satellites in each plane.

$$n_{sats} = ps \tag{2.59}$$

For example, two LEO satellite constellations that require global coverage are the Iridium and Globalstar systems. Both of these networks provide global communication by providing at least one satellite visible on the ground at all times. Initial plans for the Iridium constellation called for 11 satellites in 7 orbital planes for a total of 77 satellites (77 being the atomic number of the Iridium element), but in operation consists of 11 satellites in 6 orbital planes for a total of 66 satellites at a height of 781 km. Figure 2.10 shows the plots for the number of satellites required for constellations of 4 and 6 orbital planes as a function of the orbit height. The specific Iridium constellation falls on the 6 orbital plane curve where expected. The Globalstar constellation consists of 48 satellites orbit orbiting in 4 planes at 1414 km. The plot shows the Globalstar constellation lies near the 4 orbital plane curve.

35

2.11 Reference Frames

Generally, navigation relates a location with respect to a point of reference. Many different frames of reference are used in this research and they are described in this section. Of interest to this research are Earth-Centered Inertial (ECI), Earth-Centered Earth-Fixed (ECEF), Hill's, and navigation frames of reference.

2.11.1 Earth-centered Inertial Frame. The ECI frame of reference has its origin at the Earth's center. Two axes lie in the plane of the Earth's equator and the third axis is orthogonal to the equatorial plane, in the direction of the North pole. Of the two axes in the equatorial plane, the first axis points in the direction where the equator and the ecliptic cross during the vernal equinox. The ecliptic is the plane defined by the apparent motion of the sun across the celestial sphere. Furthermore, the celestial sphere is the projection of the stars onto an Earth-centered large-radius sphere depicting the angles to each star. Figure 2.11 shows the axes with respect to the Earth, the equator and the ecliptic. Positions are represented as a vector of $[x, y, z]^{eci}$.

2.11.2 Earth-centered Earth-fixed Frame. The ECEF reference frame has an origin at the center of the Earth, similar to the ECI frame. In contrast, however, the axes in the equatorial plane are fixed to specific locations on the Earth, with the first axis in the direction of the Prime Meridian, the second axis orthogonal to the first and within the equatorial plane, and the third axis orthogonal to the equatorial plane in the direction of the North pole. Locations are often expressed as $[x, y, z]^{ecef}$ vectors.

2.11.3 Hill's Frame. The Hill's reference frame is often used in satellite rendezvous applications, where a target satellite is referenced with respect to an intercepting satellite. The Hill's coordinate frame is centered on the intercept satellite position with the first axis, $\mathbf{r}_1$, extending along the radius line from the Earth, the second axis, $\mathbf{r}_2$, is in the direction of the satellite velocity but aligned with local hori-
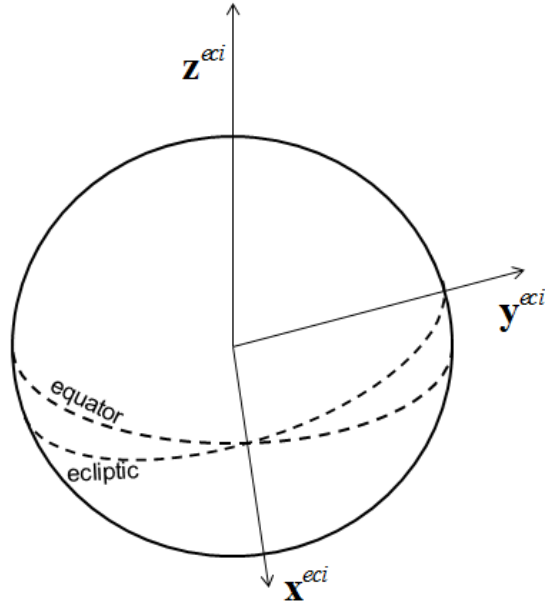
Figure 2.11: Earth-centered inertial reference frame depicted Earth's equator and ecliptic, where the first axis points in the direction of the Vernal equinox.
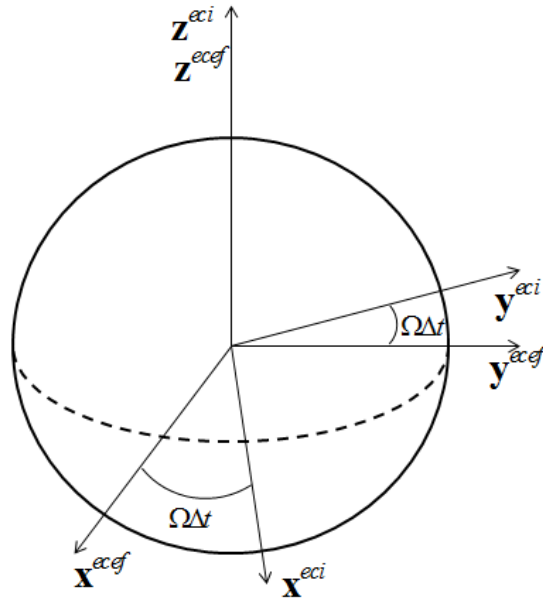
Figure 2.12: Earth-centered Earth-fixed reference frame depicted Earth's equator and the difference from the Earth-centered inertial frame as a function of the Earth's rotation and time.
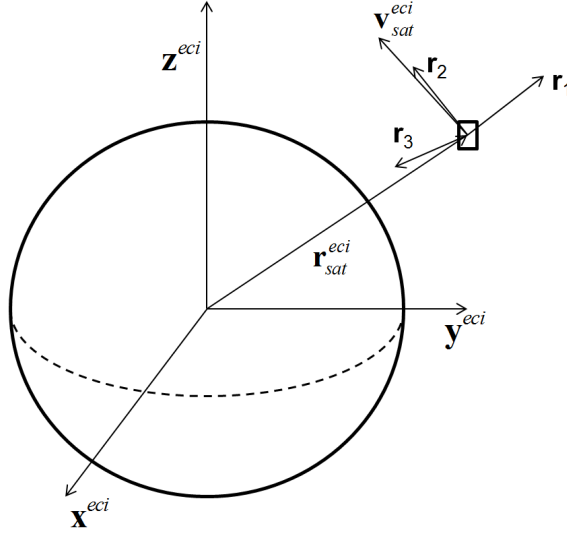
Figure 2.13:   Hill's reference frame depicted with Earth-orbiting satellite

zontal, and the third axis $\mathbf{r}_3$ is orthogonal to the first two axes. Figure 2.13 depicts the Hill's frame as defined above. Section 4.2.4 shows how this frame is used in modeling the satellite ephemeris errors in the system model.

2.11.4   Navigation Frame.   The final frame of interest is the navigation reference frame. It is used to reference direction with respect to a specific vehicle, or body, but is in relation to the surface of the Earth. Centered in the vehicle body it has axes in the north, east, and down directions with respect to the Earth geoid. The first axis points in the direction of North from the vehicle's position. The second axis points in the direction East from the vehicle's position. The third axis points in the local vertical direction of down. Figure 2.14 depicts the local navigation frame of a point mass at a specific latitude and longitude.

2.12   Summary

This chapter described previous research relevant to the advancement of star tracking capabilities as well as several studies that describe methods for using star trackers to navigate on the earth. In addition, detector properties, satellite constellation properties and the derivation of the Kalman Filter for this application were
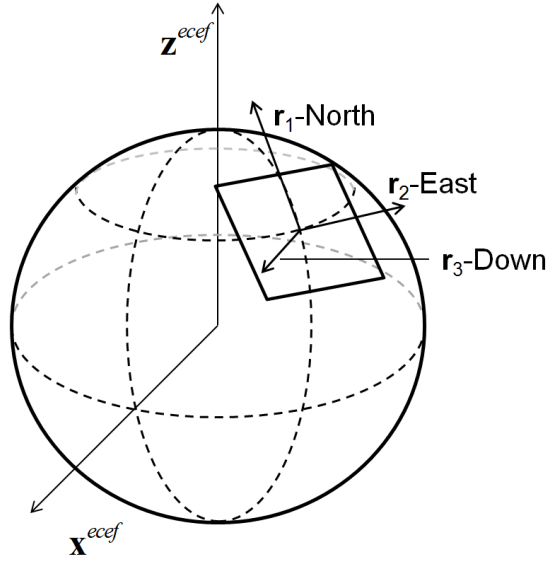
Figure 2.14:   Navigation reference frame

introduced. Finally, useful reference frames were explained with respect to their use in this research.

III.   Man-Made Star Navigation

THIS chapter describes the feasibility of creating a constellation of earth-orbiting satellites that emit a light signal capable of being detected on earth using a star tracking system. Such a satellite is referred to as a Man-Made Star (MMS).

This idea was initially introduced in August 2012 as a "back of the envelope" study into the feasibility of using man-made satellites to emit a light from Low Earth Orbit (LEO) in order to determine a navigation solution by a vehicle on or near the surface of the earth (such as a car or a plane). In further discussions, the end-goal was described as determining if navigation is feasible in this manner and if not, to describe the limiting technologies that would need to be invested in or developed to realize such a capability. This chapter discusses the approach to determining the feasibility of the capability using "back of the envelope" calculations. Specifically, the system requirements according to properties of the detector, the emitting source, and the navigation solution are presented.

The detector has limiting factors which drive the amount of light needed to be emitted from orbit. Information regarding the satellite emitting the signal is also needed, such as position, to calculate the ground vehicle position. A full trade study of the space in which an optimal solution exists was not performed nor presented here. Since the driving question is feasibility rather than system design, the authors present only some limiting factors to provide a framework from which to determine specific system requirements and/or technology investment.

3.1   Concept of Operations

The utility of having a navigation system based on optical measurements of a MMS is that it is independent of GPS, it is veritably un-spoofable and un-jammable by others, and it can potentially provide accuracies somewhat comparable to GPS solutions. A simple illustration of the **CONOPs!** (**CONOPs!**) is shown in Figure 3.1. As an alternative to GPS, it must be operational in day or night conditions, and at any location on the earth. For this specific system to operate, the sensor, or
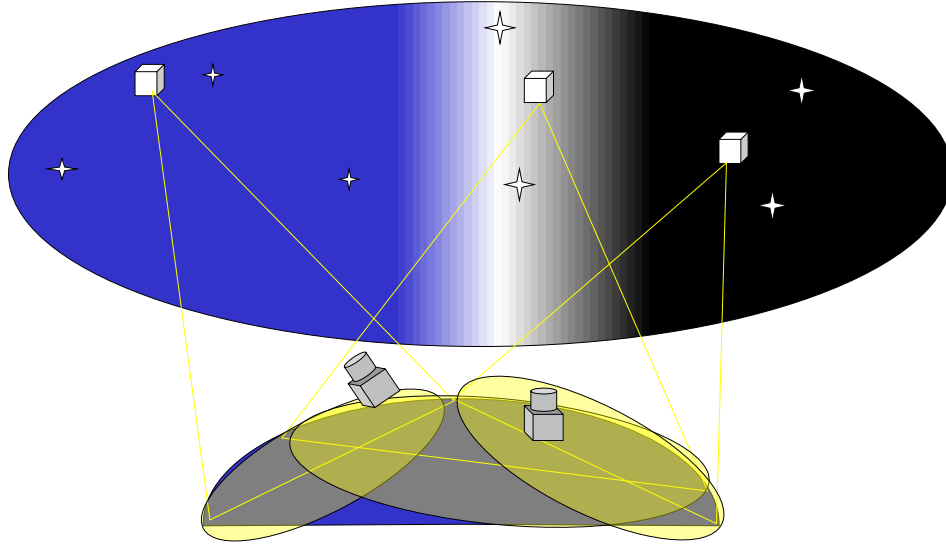
Figure 3.1:   Concept of Operations for Satellite Detection

star tracker, on the ground or in the air must be able to detect the satellite signal, assumed to be operating at optical or near optical wavelengths, in those conditions. The star tracker must detect and identify the background stars in the image. The position of the satellite detected must also be known to a certain accuracy as discussed in Section 3.5.2. For the purposes of this study, the satellite orbits are confined to LEO orbits.

3.2   System Components

The system that implements a navigation solution using a MMS as the earth-satellite source has the following components of interest: a signal from the satellite of sufficient power, a star tracker capable of detecting the satellite signal, a constellation of satellites to provide global coverage, a method to determine the ephemerides of the satellites, and the navigation algorithm that interprets the measured data.

Some discussion of each of these components is presented in this chapter. First, the signal power required for collection on the earth is derived from the star tracker detection capabilities as a function of SNR.

3.3 Required Power of Detected Signal

The signal power required of a MMS to broadcast over a swath of the Earth and be detected by a star tracker is represented by Figure 3.2. The satellite emits a signal at a specific wavelength and solid angle, determined by either capability or operational desires. The signal is transmitted through the atmosphere where some scattering or absorption occurs represented by an atmospheric efficiency. A portion of that signal is collected through the aperture of the telescope, or star tracker. This portion as compared to the overall signal area of coverage determines an angular efficiency. The star tracker optical elements (e.g. lenses, mirrors) incur an optical efficiency. The signal distance traveled maximum range is depicted as the edge of the signal FOV. The collected power focuses on a FPA where quantum efficiency reduces the power detected and where the navigation algorithm can measure to the angular location of the satellite. In addition to the signal strength detected, the background sky field contributes a radiant noise source, which is maximum during local daylight time and drives the signal power level according to a desired SNR.

3.3.1 SNR Comparison.   The *SNR* of a MMS against a day sky background can be calculated as a function of N_{sig}, which represents both the number of photons incident on the detector aperture from a MMS (numerator) and the variance of that signal (denominator), and the number of incident photons from the sky background, N_{back}.

$$SNR = \frac{N_{sig}t_{int}\tau_{opt}Q_e\tau_e}{\sqrt{N_{back}t_{int}\tau_{opt}Q_e + N_{sig}t_{int}\tau_{opt}Q_e\tau_e + N_{read}}} \tag{3.1}$$

where t_{int} is the integration time of the detector, τ_{opt} is the efficiency of the optical elements of the detector, Q_e is the quantum efficiency of the detector at the wavelength of the signal, τ_e is the *EOD* factor describing the amount of signal power focused on a single detector and N_{read} is the number of photoelectrons detected due to the read noise.
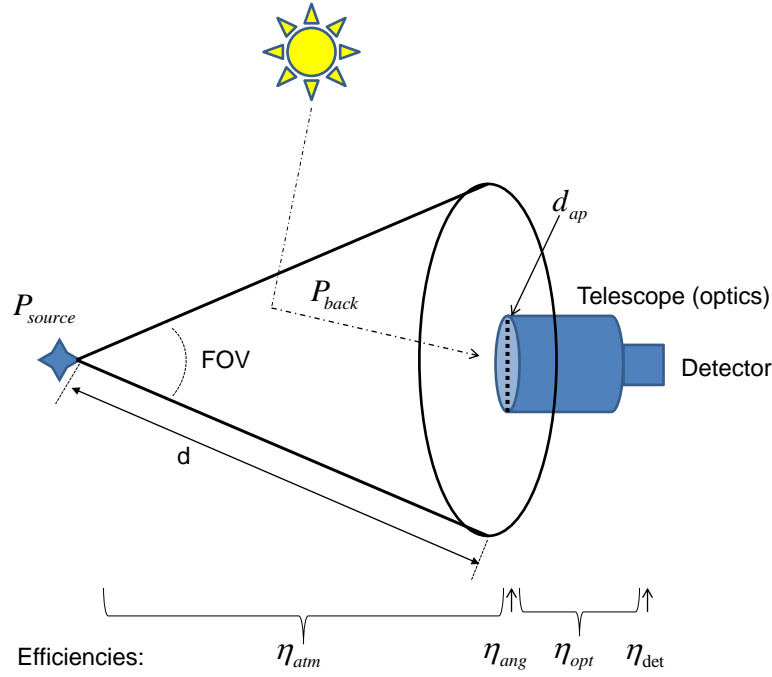
Figure 3.2:   Celestial Navigation Signal Components

Given a desired SNR, the number of signal photons can be calculated from Eqn. (3.1) algebraically and by using the quadratic equation as

$$SNR^{-2}(t_{int}\tau_{opt}Q_e\tau_e)^2 N_{sig}^2 - t_{int}\tau_{opt}Q_e\tau_e N_{sig} - N_{back}t_{int}\tau_{opt}Q_e - N_{read} = 0$$

(3.2)

$$N_{sig} = \frac{t_{int}\tau_{opt}Q_e\tau_e + \sqrt{(t_{int}\tau_{opt}Q_e)^2 - 4(t_{int}\tau_{opt}Q_e\tau_e)^2 SNR^{-2}(t_{int}\tau_{opt}Q_e N_{back} + N_{read})}}{2(t_{int}\tau_{opt}Q_e\tau_e)^2 SNR^{-2}}$$

(3.3)

Once the number of incident photons is determined, the amount of signal power can be calculated as the reverse application of the angular and atmospheric efficiencies as well as converting photons to units of watts.

$$P_{source} = \frac{N_{sig}\left(\frac{hc}{\lambda}\right)}{\tau_{atm}\tau_{ang}}$$

(3.4)

43

Funge [24] uses the SNR calculation to determine if a star can be detected in daylight, while Shanks' [74] sensor model is a generic SNR calculation for any signal against a background. Funge's version of the SNR with minor notation variation is [24]

$$\frac{S}{N} = \frac{\eta E_{q,signal} A_d q}{[2q^2 \eta E_{q,background} A_d \Delta f]^{\frac{1}{2}}} \tag{3.5}$$

where η is the quantum efficiency, E_q is the signal and background irradiance, A_d is the sensor area, q is the charge of an electron, and Δf is the noise-equivalent bandwidth. This result is similar to Eqn. (3.1), except that Funge does not include the noise associated with the signal itself, but only that from the background. In addition the author calls the background contribution an irradiance, which infers a point source, rather than the sky radiance, which represents a distributed source and contributes noise as a function of the incident area as well as the angular FOV of the detector. This version of the SNR was not used in the final calculation of the signal power.

A final comparative version of calculating the SNR comes from Shanks [74] and is given by

$$SNR = \frac{\dfrac{J_{Tgt}^{(source)} \tau_{atm} EOD \left[\frac{IFOV}{\sigma_{blur}}\right]}{(d_{los} IFOV)^2}}{\sqrt{\dfrac{\langle L \rangle}{Gain} + \left(\dfrac{\sigma_{e^-}}{Gain}\right)^2}} \tag{3.6}$$

where J_{Tgt} is the intensity of the target in units of W/sr, $\dfrac{IFOV}{\sigma_{blur}}$ is the ratio of the detector element field of view to the standard deviation along one dimension of the PSF, or Airy disk, $EOD[\cdot]$ is defined in Section 2.9, $\langle L \rangle$ is the average of the signal radiance across the detector spectral band, σ_{e^-} is the contribution of detector and background noise sources, which in daylight collection is dominated by the background radiance shot noise. The $Gain$ is the concatenation of detector and range attenuation

terms given by [74]

$$Gain = \pi \left(\frac{d_a}{2} \right)^2 IFOV^2 \left(\frac{\langle \lambda \tau_{opt} Q_e \rangle}{hc} \right) t_{int} \qquad (3.7)$$

where $\langle \cdot \rangle$ is the average value over the detector spectral band. The $Gain$ is in units of $\frac{e^-}{\text{W/sr m}^2}$. By assigning a variable, l to the system configuration terms in Eqn. (3.6), and by arguing that the number of photons due to the signal represented by $\langle L \rangle$ in the denominator of Eqn. (3.6) is equivalent to the value of the numerator, or the number of incident photons on the area of an aperture for a single detector element, then using a desired SNR value, the target, or source, intensity is calculated as [74]

$$J_{tgt} = \frac{\frac{l}{Gain} + \sqrt{\left(\frac{l}{Gain} \right)^2 + 4 \left(\frac{l}{SNR} \right)^2 \left(\frac{\sigma_e}{Gain} \right)^2}}{2 \left(\frac{l}{SNR} \right)^2} \qquad (3.8)$$

This results in the satellite signal intensity in units of $\frac{\text{W}}{sr}$, therefore, to find the total signal power required, J_{tgt} must be integrated over the MMS emitted field of view, FOV_{sat},

$$P_{source} = J_{tgt} FOV_{sat} \qquad (3.9)$$

A comparison of the methods by their steps of operation is summarized in Table 3.1.

Before presenting the results of comparing these methods and the expected MMS signal power, some discussion is required regarding the effects of the system components as well as a description of nominal system specifications. The contribution of the components to the signal power calculation is introduced in the next section.

3.3.2 System Parameter Contributions. The required power of the satellite signal is a function of many parameters as shown in Eqns. (3.3) and (3.4). Some of

Table 3.1:   Comparison of SNR Calculation Methods

Step	Pierce	Funge [24]	Shanks [74]
1	Determine number of background photons incident on detector	Determine the background irradiance	Calculate background photons per pixel
2	Calculate number of signal photons incident on aperture given system parameters	Calculate the background noise on detector	Calculate signal (and background*) gain
3	Convert signal photons to power, integrate over ground swath and compensate for atmospheric effects	Calculate the signal irradiance at the detector aperture from the SNR	Calculate signal irradiance from SNR in photons
4		Integrate the irradiance over ground swath and compensate for atmospheric effects* (not implemented)	Apply angular efficiency and calculate signal power*

* - indicates steps added to referenced research for final result

these parameters are sensor dependent, such as the optical efficiency, the quantum efficiency and the EOD term. Some of these parameters are operationally dependent, such as the integration time, the desired SNR, the angular efficiency and the desired spectral band. The remaining parameters are external-to-system, though operational parameters, such as the atmospheric transmission and the background radiance. The effects of each of these types of parameters are discussed in this section beginning with the last of the three.

3.3.3   *External Operational Parameters.*   Two parameters of the MMS system involve modeling external influences to the satellite signal and detection capability. These are the the background radiance of a daylight detected signal and the

atmospheric attenuation due to scattering of that signal. PLEXUS, as described in Section 2.9, models the atmospheric effects driven by other operational parameters. Several parameters of interest were chosen to coincide with nominal operating parameters. The parameters set other than the default settings are summarized in Table 3.2. PLEXUS then reports the atmospheric transmission values and the radiance at the

Table 3.2:   Plexus Atmospheric Model Parameters

Parameter	Setting	Unit
Spectral Limits	.380 − 2.4	micron
Spectral Resolution	5	cm^{-1}
Sensor Altitude	[0, 5k, 10k, 15k, 30k]	ft
Sensor Lat/Lon	(38.89, -150)	deg N, E
Sensor Geometry (Zenith)	45	deg
Range to Path End	Infinity	n/a
Date/Time	7 July 2012, 1300 hrs*	local time
Scale Factor for Solar Irradiance	1	none
Boundary Layer Aerosol	clear, high visibility (23 km), maritime environment	n/a

observer position over the desired spectrum. Figure 3.3 depicts the transmission values given by PLEXUS. The model indicates that around certain bands, such as near .8, 1.6, and 2.2 microns, the transmission values are relatively high and therefore good candidates to propose a transmitted signal.

Figure 3.4 shows average transmission values around several wavelengths and evaluates their change as a function of zenith angle. The shape of these modeled results are similar to those reported in [6], but do not coincide in actual values. The report concludes that operational limits should be set below 60 degrees to avoid the drastic reduction in transmission values. In the study presented here, the zenith angle is fixed at 45 degrees and therefore allows for a broader signal from the satellite, yet avoids too much loss of the signal through the atmosphere.

The model results for a minimum elevation angle of 45 degrees at varying observer altitudes is shown in Figure 3.5. The separate plots allow the results by altitude
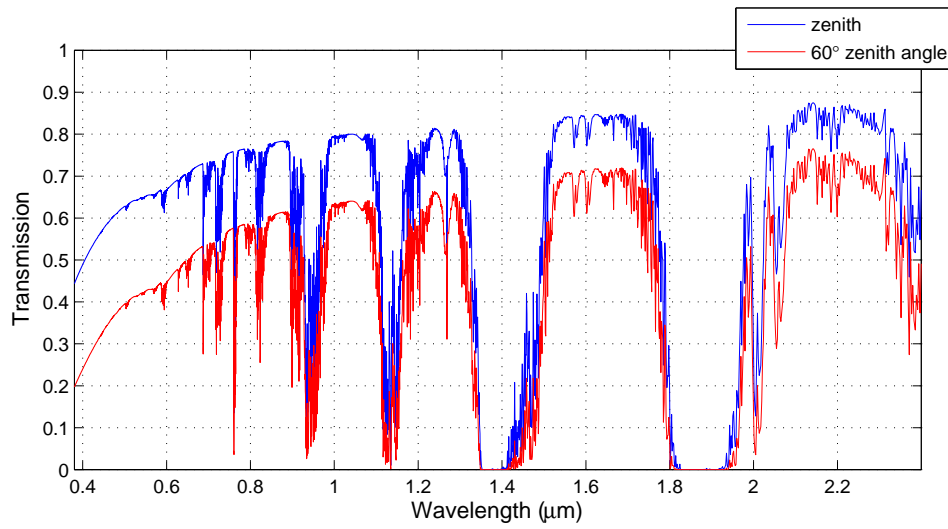
Figure 3.3:   Atmospheric transmission values reported by PLEXUS using Table3.2 values, unless specified in plot
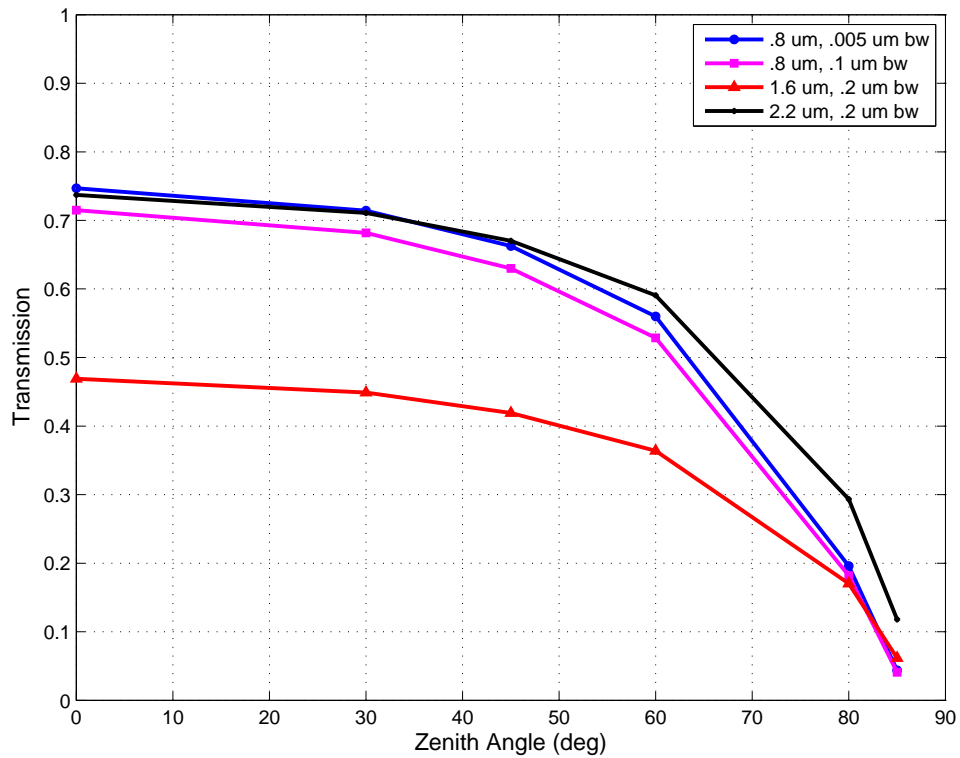
Figure 3.4:   Average atmospheric transmission values in windows defined in legend. Reported by PLEXUS using Table 3.2 values, unless specified in plot.
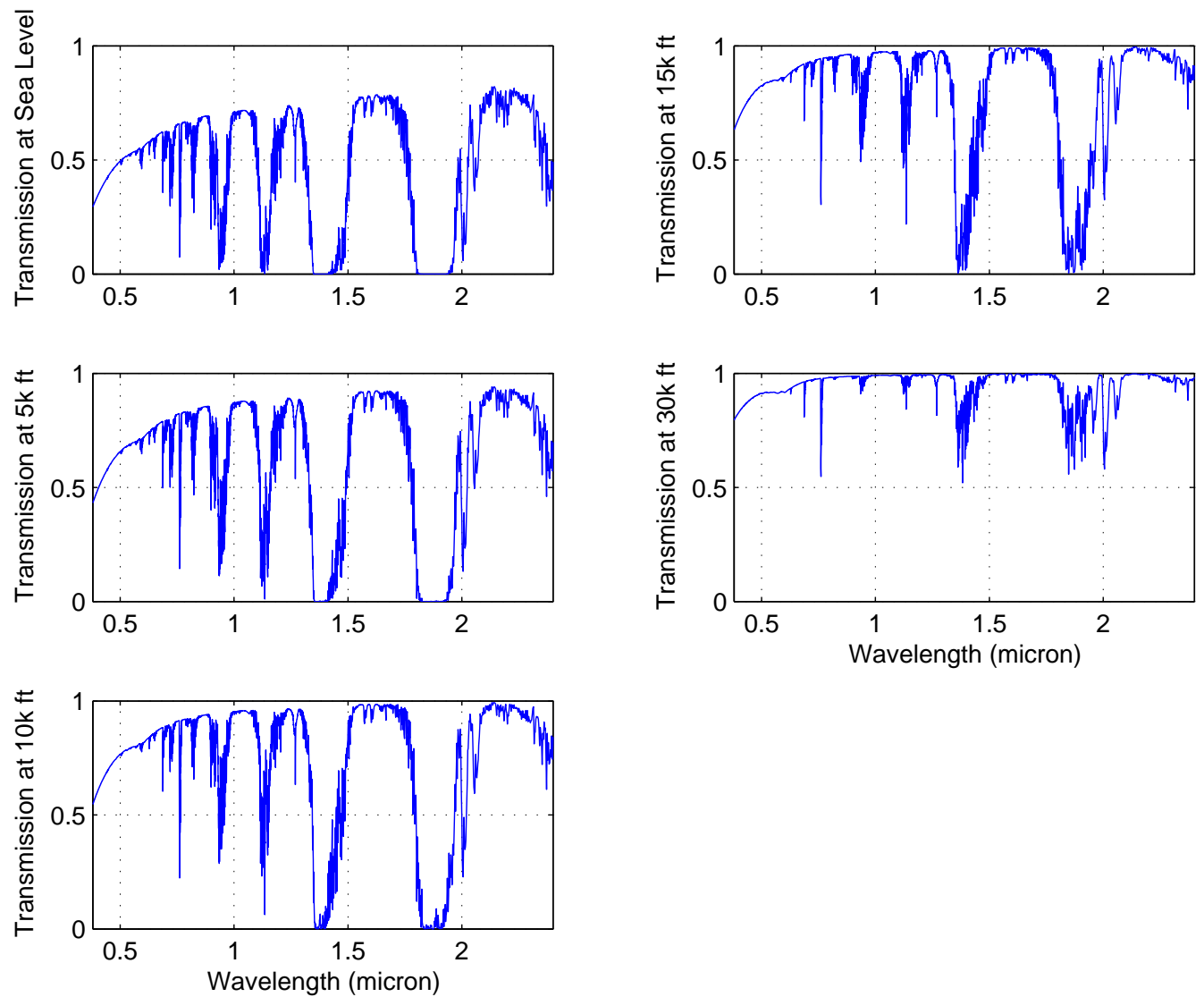
Figure 3.5:   Atmospheric transmission reported by PLEXUS using Table 3.2 values at five different operating altitudes.

to be visually distinguished. As expected, at higher altitudes, the signal propagates through less atmosphere therefore and the transmission values increase respective to lower altitudes for the same wavelength. Since the signal is expected to operate in a very narrow band, the transmission efficiency becomes that associated with the operating altitude and the nearest modeled wavelength to the signal wavelength rather than an average transmission value over the bandwidth. The bandwidth of the detector is associated with the background radiance, also modeled by PLEXUS.

PLEXUS reports the solar radiance at the observer's position given the same operational and atmospheric conditions as the atmospheric transmission. For the operating altitudes of interest, PLEXUS models the radiance as shown in Figure 3.6. The curves of all the plots resemble the blackbody curve depicted in Chapter II over the wavelength window shown with the addition of absorption bands at specific wavelengths associated with specific atmospheric particles. In each plot the higher wavelengths have a lower amount of radiance due to the sun generating less power at those wavelengths. As the altitude increases, because the atmospheric transmission increases, less light scattering occurs, which also leads to less sky radiance. Thus, the plots show a decreasing amount of radiance between plots from sea level to 30k feet. The contribution of the sky or background radiance is not in the value itself, but how it contributes as a noise term to the signal detection.

The SNR as calculated in Eqn. (3.1) refers to a background noise number of photons, N_{back}. The background noise is a shot noise generated by the variance of arrive of the incident photons from sky radiance on the detector. Since the process is a Poisson random process the variance is also the mean and therefore, if the number of incident photons, N_{sky} can be calculated, the amount of noise is known. Given a nominal background radiance, L_{back}, from the atmospheric model, the number of
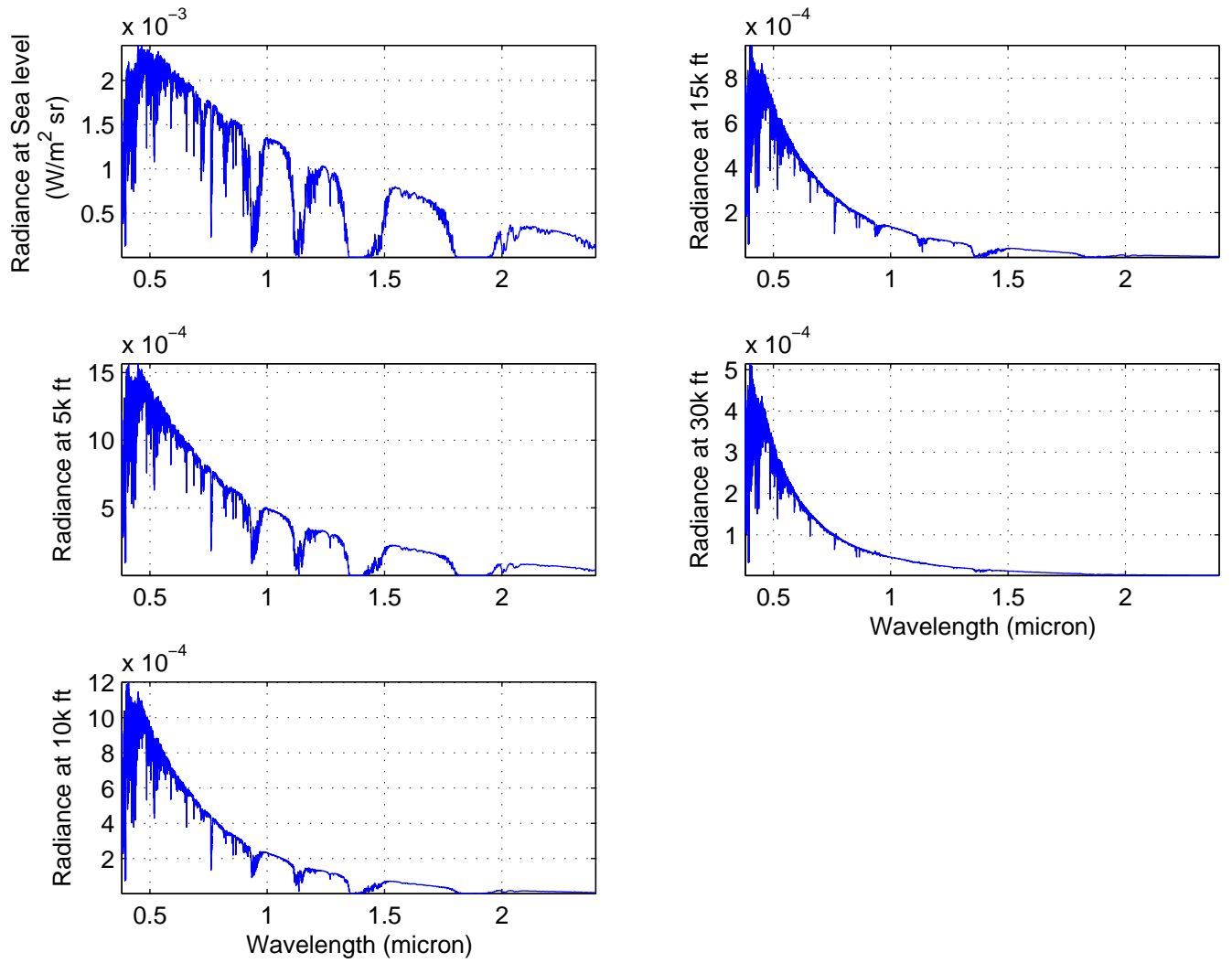
Figure 3.6:   Radiance reported by PLEXUS using Table 3.2 values at five different operating altitudes.

incident photons per detector element is found by

$$N_{sky} = \sum_{\Delta\lambda} L_{back}(\lambda)\frac{\lambda}{hc}A_{det}IFOV^2 \qquad (3.10)$$

$$= N_{back}$$

where $\frac{\lambda}{hc}$ is the wavelength-specific number of photons per watt, A_{det} is the area of the detector aperture, and $\Delta\lambda$ is the band over which the detector operates. Eqn. (3.1) identifies two other noise terms, the shot noise of the satellite signal itself, N_{sig} and the read noise of the detector, N_{read}. The satellite signal is not known and must be solved for, therefore the only other noise to discuss as evaluated here is the read noise.

A detector's read noise is not derived from other operational elements, but is intrinsic to it's design and manufacturing. As such it is characterized uniquely during testing and in operation. However, for the purposes of this study, and since the read noise is identified as being significantly lower than the noise contributed by other sources, it can be nominally represented by an expected value. In discussion with USNO, three different qualities of detectors can be modeled with different amounts of read noise. In the work presented here, the three qualities of detector are referred to as typical, advanced, and future versions. The typical detector reflects what can be purchases commercially today on the market, or what is common in current star trackers. The advanced detector reflects values at the leading edge of development or available in the best available star trackers. The future detector reflects values that could be achieved with significant investment or development beyond what is currently available: a next-generation star tracker. The read noise values associated with each type are

$$N_{read} = \begin{cases} 60 & e^- \text{ /pix/read, typical,} \\ 10 & e^- \text{ /pix/read, advanced,} \\ 5 & e^- \text{ /pix/read, future} \end{cases} \qquad (3.11)$$

The background and signal noise terms are modified by parameters specific to the detector. These are previously referred to as sensor dependent parameters.

3.3.4   Detector Parameters.   The background radiance and signal irradiance incident on the detector aperture are further modified by characteristics of the star tracker. Chapter II introduced the topics of a detector element quantum efficiency, IFOV and EOD. A detector's quantum efficiency can vary depending on the band over which it operates and the materials used. For the purposes of a feasibility study, this value is given nominally, similar to the read noise as a single value associated with the quality of detector used.

$$Q_e = \begin{cases} 0.4 & \text{typical,} \\ 0.9 & \text{advanced,} \\ 0.9 & \text{future} \end{cases} \tag{3.12}$$

The values for the IFOV and the EOD, however are derived from other detector parameter as described in Section 2.11, such as the sensor field of view, size of detector elements and size of the focal plane array. Establishing these three sensor specifications, the IFOV, focal length, and Airy disk size can be derived. For example, given a star tracker with a $10° \times 10°$ field of view and 1024×1024 pixels in the FPA with each detector element 13.5 micron square, the sensor aperture diameter of 10 cm, and a signal wavelength of 0.55 micron, several other system parameters can be determined. The IFOV, or angle subtended by an individual pixel element, is calculated as

$$IFOV = \frac{\theta_{FOV}}{N_{FPA}} \tag{3.13}$$

$$= \frac{10}{1024} \text{ deg/pix} \tag{3.14}$$

$$= 35.16 \text{ arcsec/pix} \tag{3.15}$$

The focal length of the system is

$$f = \frac{d_{pixel}}{IFOV} \tag{3.16}$$

$$= 13.5\,\mu\text{m/pix} \left(\frac{(35.16 \text{ arcsec/pix})(\pi)}{(3600 \text{ arcsec/deg})(180 \text{ deg})} \right)^{-1} \tag{3.17}$$

$$= 79.2 \text{ mm} \tag{3.18}$$

Diffraction causes the light to have interference and produce intensity nulls on the focal plane. The Airy disk radius is the distance from the center of the focused point source to the first null and is calculated as

$$r_{airy} = \frac{f}{d_{ap}}(1.22\lambda) \tag{3.19}$$

$$= \frac{79.2 \text{ mm}}{10 \text{ cm}}(1.22)(.550\,\mu\text{m}) \tag{3.20}$$

$$= 0.53\,\mu\text{m} \tag{3.21}$$

The number of pixels over which the energy will be detected is a function of the radius of the Airy disk, given as

$$n_{airy} = \frac{2r_{airy}}{d_{pixel}} \tag{3.22}$$

$$= \frac{2(0.53\,\mu\text{m})}{13.5\,\mu\text{m}} \tag{3.23}$$

$$= 0.079 \text{ pixels} \tag{3.24}$$

The full results of the derived values from the system specifications are detailed in Section 3.3.6.

In addition to the system parameters determined by external influences and detector characteristics, the signal detection depends on operating parameters.

3.3.5 Operational Parameters. A few of the operational parameters have already been discussed, such as the observer's altitude and the signal's operating

wavelength. Aside from these values, the system depends on the geometry of how the earth, satellite and observer are configured. This configuration takes into account not only the observer's altitude, but the satellite orbit height, the minimum required elevation for observation, and the field of view of the satellite signal. These effects appear in Eqn. (3.4), in the angular efficiency term. The angular efficiency is the ratio of the size of the detector aperture to the size of the satellite area of coverage. Since the detector is obviously going to be small in comparison to a relatively widely broadcast signal, it's evident that this term is very small. Given the minimum elevation, observer altitude, and satellite orbit, the required signal field of view, θ_{los} can be found using Eqn. (2.50), from which the signal solid angle becomes

$$\Omega_{sig} = 4\pi \sin^2(\theta_{los}/2) \text{ sr} \tag{3.25}$$

and the size of the spherical wavefront of the signal at the edge of its range is

$$S_{sig} = d_{los}^2 \Omega_{sig} \text{ m}^2 \tag{3.26}$$

Then the ratio of the detector to the signal area is

$$\tau_{ang} = \frac{\pi(d_a p/2)^2}{S_{sig}} \tag{3.27}$$

For a ground level observer, a satellite orbiting at 780 km, a star tracker with an aperture of 10 cm and a minimum elevation angle of 45°, the angular efficiency is

$$\tau_{ang} = \frac{\pi(.10/2)^2}{(1048.6 \text{ km})^2(1.404 \text{ sr})} \tag{3.28}$$

$$= \frac{.0079 \text{ m}^2}{1.544 \times 10^{12} \text{ m}^2} \tag{3.29}$$

$$= 5.116 \times 10^{-15} \tag{3.30}$$

The parameters affecting the MMS system performance in detecting the signal have been discussed. A further summary of how those parameters differ according to the quality of the star tracker are given next.

3.3.6 Description of Nominal System Values. In discussion with USNO, and as mentioned previously, three types of star trackers are categorized to provide nominal characteristics of detectors in order to calculate the required signal power. A summary of those values are listed in Table 3.3. The parameters are divided into specified detector parameters, parameters derived from the specifications, and parameters pertinent to the signal transmitted in orbit. Additionally, each parameter is designated according to typical, advanced, or future values of star trackers. The units of each parameter is given as well as a reference to their symbols as used in this document. From these system parameter values, the required signal power can be calculated.

3.3.7 Signal Power Results. Using each type of star tracker (typical, advanced, and future) operating at each of the desired observer altitudes, the required signal power to detect is calculated using the equations found in Section 3.3.1. Figure 3.7 shows the signal power required to detect that signal at each of the indicated altitudes and with the parameters associated with each type of star tracker. The highest required signal occurs when observing a signal at a wavelength of 0.550 micron with a typical detector from the ground. At this operational condition almost 98 W of output signal power is needed to detect it with an SNR of 7. Using the same detector the signal power decreases substantially as the operating altitude increases, such that at 30k ft, only 20 W of power is required. This change is expected due to the decrease in background noise from the sky radiance as well as the increased atmospheric transmission values. As the design elements improve between detectors, the required signal power decreases. The signal using an advanced star tracker, observing a signal at a wavelength of 0.780 micron requires at most approximately 11.5 W when observed on the ground and at the least approximately 2 W when observed
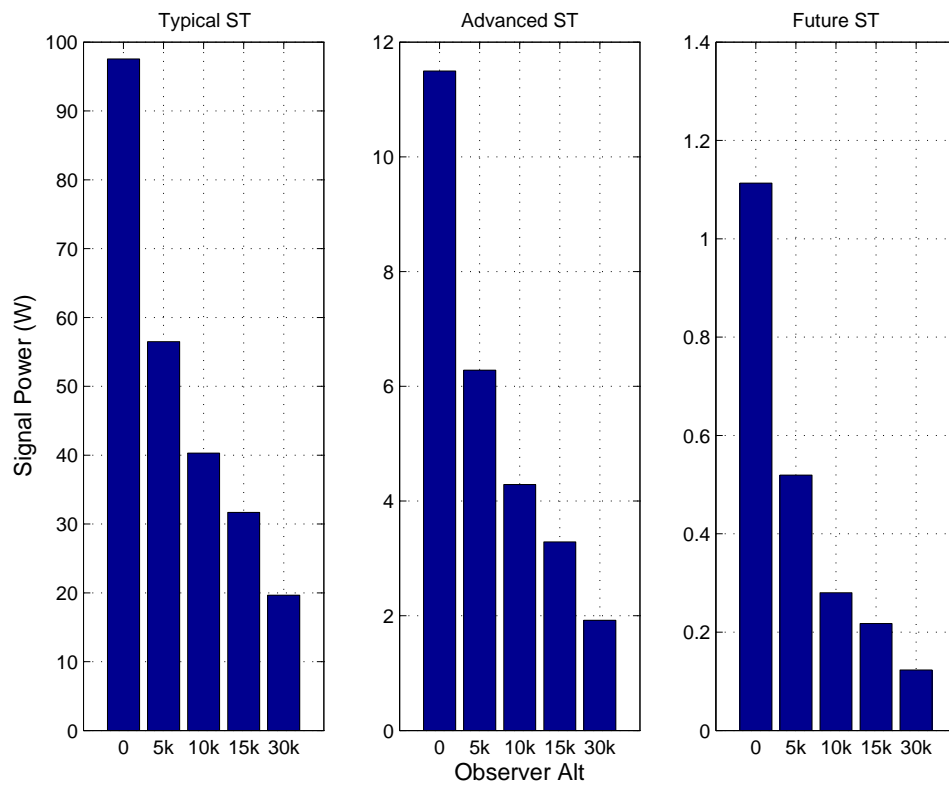
Figure 3.7:   Signal power required according to Pierce calculation

Table 3.3:   Summary of MMS Parameters for Signal Detection

Parameter	Typical Value	Advanced Value	Future Value	Unit	Symbol
Detector					
Integration Time	1	1	1	sec	t_{int}
Aperture Diameter	10	10	10	cm	d_{ap}
Quantum Efficiency	0.4	0.9	0.9	none	Q_e
Optical Transmission	0.5	0.7	0.8	none	τ_{opt}
Field of View	10	10	10	deg	θ_{FOV}
Number of FPA Pixels	1024	2048	4096	pixels	N_{FPA}
Size of Pixels	13.5	10	10	micron	d_{pixel}
Read Noise	60	10	5	e$^-$/pixel	N_{read}
Optical Bandwidth	0.25	0.25	0.25	micron	$\Delta\lambda$
Operating Altitude	[0, 5k, 10k, 15k, 30k]			ft	h_{obs}
Derived					
Pixel Resolution	35	17.6	8.8	arcsec	$IFOV$
Focal Length	79	117	235	mm	f
Airy Disk Radius	0.53	1.12	4.44	micron	r_{airy}
Airy Disk Radius	0.079	0.22	0.89	pixel	n_{airy}
Signal					
SNR	7	7	7	none	SNR
Signal Center Wavelength	0.550	0.780	1.550	micron	λ
Minimum Elevation	45	45	45	deg	θ_{el}
Satellite Orbit Height	780	780	780	km	R_{orb}
Number of Orbital Planes	18	18	18	none	p

at 30k ft. The signal using a future, to-be-developed star tracker, observing as signal at a wavelength of 1.55 micron requires approximately 1.1 W when observed on the ground and at least approximately .12 W when observed at 30k ft.

The required signal power as calculated using the Shanks equations are shown in Figure 3.8. The results using the Shanks method have the same trend as the Pierce method in that with increasing altitude lower signal power is required and as the detector parameters improve the required signal power decreases. The power calculated using the Shanks method is slightly higher than the Pierce method in
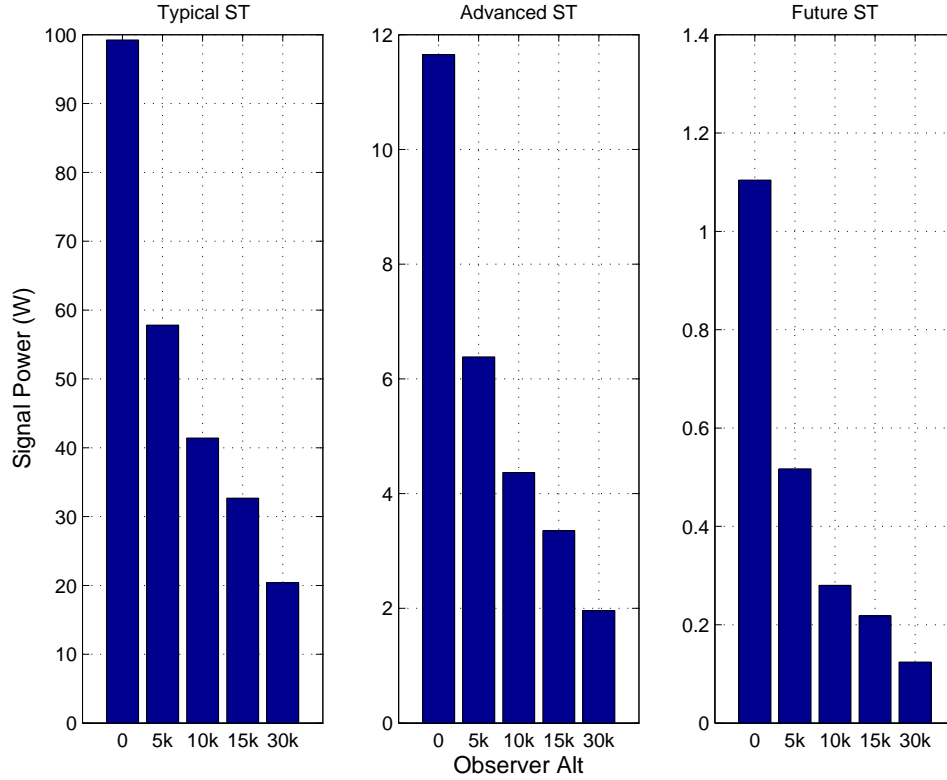
Figure 3.8: Signal power required according to Shanks calculation

most operational circumstances with a difference in calculation from 1.7 W to 0.1 milliwatts. This shows very good agreement between the distinct approaches in the matter of determining the feasibility of a MMS system.

By showing consistency in the results despite different approaches to viewing the problem, the three methods give a consistent picture that the creation of a MMS signal is feasible. Specifically, as the operating parameters push the signal wavelength higher the lower power signal become more feasible than the high-power signal. The original idea for the MMS platform is a very small satellite, such as a cubesat. Because of the small size and reduced power available, in addition to the general concept that low power hardware is preferred in the austere space environment, the desire would be for the lowest power signal feasible. There is additional trade for when the system would need to be available and whether a detector of sufficient capability could be developed in the appropriate time or become available in the marketplace.

Assuming a MMS is built, in order to provide a GPS-like navigation solution more information is required than just a single image of the satellite on a background of stars. There must be multiple satellites providing near-constant updates to the INS thereby requiring the design of a constellation.

3.4   Constellation Design

At the most simple approach, the global coverage equations found in Section 2.10.2 can determine the number of satellites required such that at least one satellite is visible at any time, in any location, according to the previously determined operating parameters. The constellation design is somewhat arbitrary in the sense that it is needed to ensure feasibility, yet has no guiding restrictions. Therefore, what is presented here consists of what could be considered a worst-case scenario as relates to the number of satellites.

Given the minimum elevation to detect the signal and the nominal satellite orbits, the Earth central angle of the satellite is found to be

$$\theta_{ec} = \cos^{-1}\left[\frac{(R_e + h_{obs})\cos(\theta_{el})}{R_e + R_{orb}}\right] - \theta_{el} \tag{3.31}$$

$$= \cos^{-1}\left[\frac{(6378\text{ km} + 0)\cos(\pi/4)}{6378\text{ km} + 780\text{ km}}\right] - \left(\frac{\pi}{4}\right) \tag{3.32}$$

$$= 0.1038\text{ rad} \tag{3.33}$$

To exercise Eqn. (2.54), choosing an estimated number of orbital planes of 18 and using the Earth central angle above, the number of satellites per orbital plane is

calculated as

$$s = \frac{\pi}{\cos^{-1}\left(\dfrac{\cos\theta_{ec}}{\cos c}\right)} \tag{3.34}$$

$$= \frac{\pi}{\cos^{-1}\left(\dfrac{\cos\theta_{ec}}{\cos\left(\dfrac{\pi - (p-1)\theta_{ec}}{p+1}\right)}\right)} \tag{3.35}$$

$$= \frac{\pi}{\cos^{-1}\left(\dfrac{\cos(0.1038)}{\cos\left(\dfrac{\pi - (17)(0.1038)}{19}\right)}\right)} \tag{3.36}$$

$$= \frac{\pi}{\cos^{-1}\left(\dfrac{.9946}{\cos(.0725)}\right)} \tag{3.37}$$

$$= \frac{\pi}{\cos^{-1}\left(\dfrac{.9946}{.9974}\right)} \tag{3.38}$$

$$= \frac{\pi}{0.0743} \tag{3.39}$$

$$= 42.27 \approx 43 \tag{3.40}$$

Since there can't be a partial number of satellites, the number per orbit is rounded
up. Then the total number of satellites is

$$n_{sats} = ps \tag{3.41}$$

$$= 18(43) = 774 \tag{3.42}$$

Therefore, for global coverage, one solution is to have 18 orbital planes with 43 satellite
in each orbit for a total number of 774 satellites. Some additional trades may need to
occur such as reducing the areas of coverage to desired latitudes as well as padding
time between satellite visibility times in lieu of a constant availability. However,
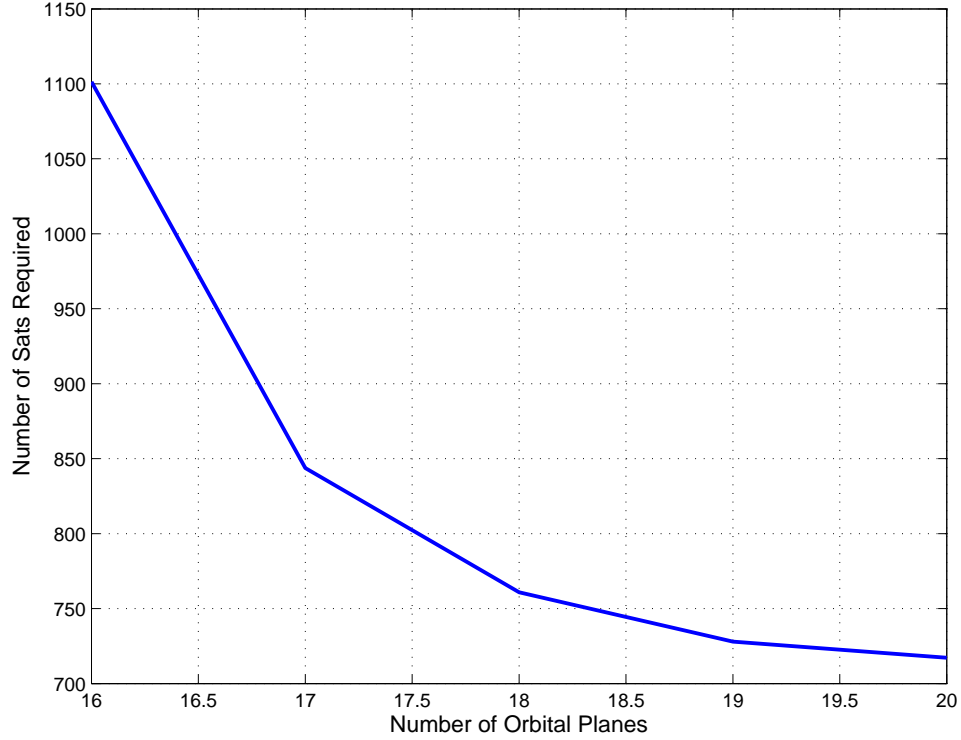
Figure 3.9: Number of satellites required for global coverage of MMS signal with 45 deg elevation and 780 km orbit height

assuming unlimited budget and access to launch facilities, the MMS system may be feasible.

This study did not thoroughly investigate an optimal solution to the satellite constellation problem. Through trial and error a sample of several orbital plane values yielded the results shown in Figure 3.9. A a detectable signal from a constellation of satellites must then be measured to determine the pointing angle to the satellite as compared to a known satellite position. This measurement will provide a value with which to update the Kalman filter estimating the navigation state.

3.5   Navigation Accuracy

As a 'back-of-the-envelope' approach to determining the feasibility of using the MMS signal for navigation accuracy, extensive modeling of the system dynamics was not accomplished. However, this section discusses some of the known attributes of

the navigation solution, namely, the possible accuracy of the measurements and some known issues regarding implementation of the MMS system.

3.5.1 *Position Accuracy.* The position accuracy of the MMS navigation system is dependent on the accuracy of the measurements made by the star tracker. Kaplan [40] describes the possible positional standard deviation, σ_X and expected results of this system as governed by Eqn. (2.9) and reiterated here

$$\sigma_X^2 = \sigma_P^2 + r^2 \sigma_d^2 \tag{3.43}$$

where σ_P is the standard deviation of the position of observed satellite, r is the distance to the satellite and σ_d is the standard deviation of the measured angle. The sensor image resolution, $IFOV$, determines the size of σ_d as

$$\sigma_d = \frac{IFOV}{2} \tag{3.44}$$

One approach to evaluate the navigation accuracy is to compare the required angle and satellite position accuracy according to a desired GPS-like position accuracy. Figures 3.10, 3.11 and 3.12 show the required system performance curves for 3 different satellite orbits and for a desired position accuracy of 3 m, 10 m and 20 m, respectively. Note that the plots show that there's a direct correlation between the satellite position accuracy and the observer's position accuracy in that the satellite position must be at least as good as the desired navigation solution. For example, if the observer desires a 20 m navigation solution accuracy, with an ideal sensor that had almost no angle uncertainty, the satellite position must be known to 20 m or better.

Another approach is to compare the three types of star trackers that are proposed according to their achievable accuracy. Using Eqn. (3.43) the minimum navigation position accuracy is shown in Figure 3.13. The satellite orbital height used in those calculations are from the proposed height of 780 km. The results shown indicate the accuracy at the nearest distance of the satellite. As the geometry changes such
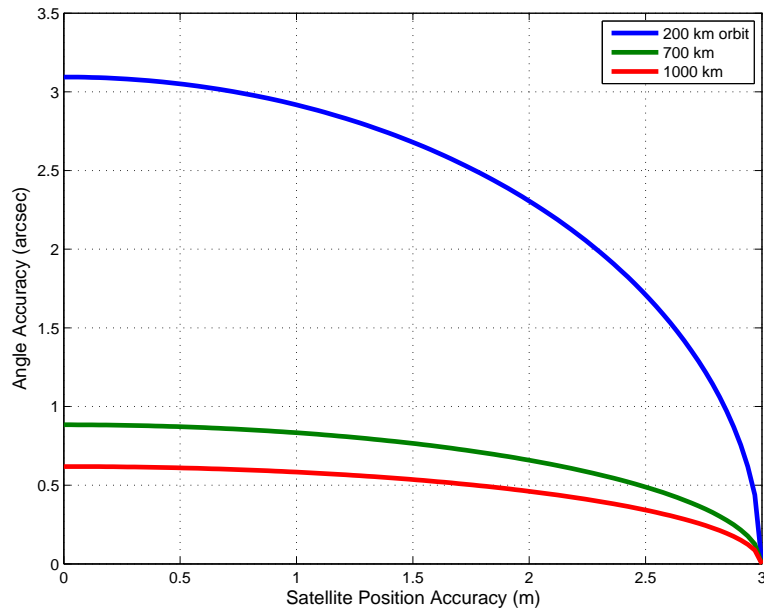
Figure 3.10:   Detector angular resolution and satellite position accuracy for 3 m position navigation solution accuracy
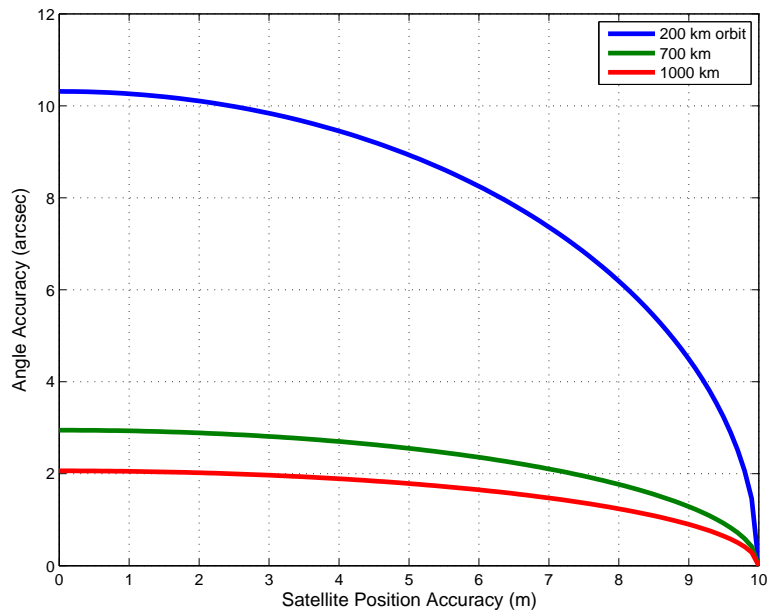
Figure 3.11:   Detector angular resolution and satellite position accuracy for 10 m position navigation solution accuracy
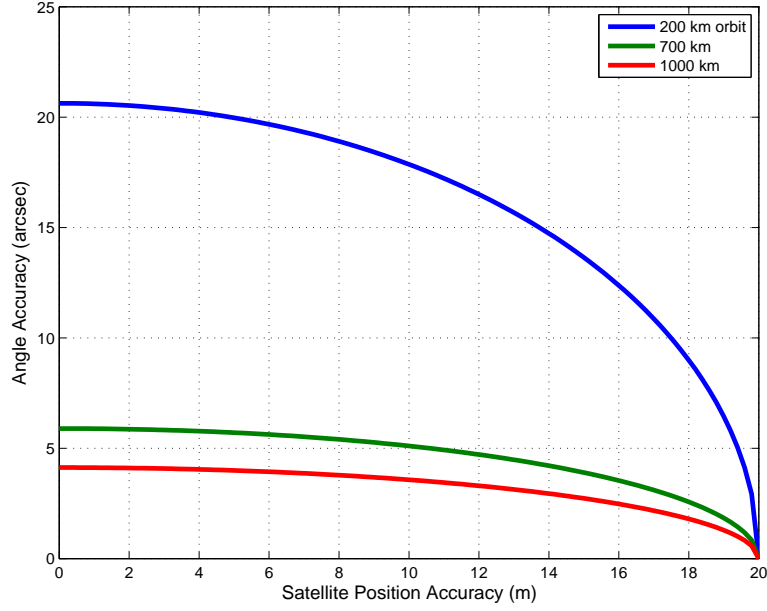
Figure 3.12: Detector angular resolution and satellite position accuracy for 20 m position navigation solution accuracy

that the satellite moves further away, yet is still detectable, the observer's position uncertainty will increase. The results also indicate the the typical star tracker, with a relatively large angular resolution will not achieve as good a navigation solution as the other types. Regardless of the ability to detect the signal, the typical star tracker would need improvements in the size of the FPA, or a redesign of the aperture or FOV in order to achieve comparable navigation solutions. The uncertainty due to pointing errors or angular resolution can be resolved by design considerations, however the other component is the accuracy of the satellite position.

    3.5.2 Ephemeris Accuracy.   Scientist researching Space Situational Aware-
ness (SSA) measure data from Earth satellites to estimate the orbital elements gov-
erning their ephemerides. GPS updates the ephemerides within the signal itself in
order to use the psuedorange measurements for navigation. Those coded ephemerides
are updated by a network of ground stations that continually update the orbital ele-
ments and provide a window of time, or epoch, in which the elements are valid, or will
estimate the satellite position to within a specified accuracy. In a single MMS system,

65
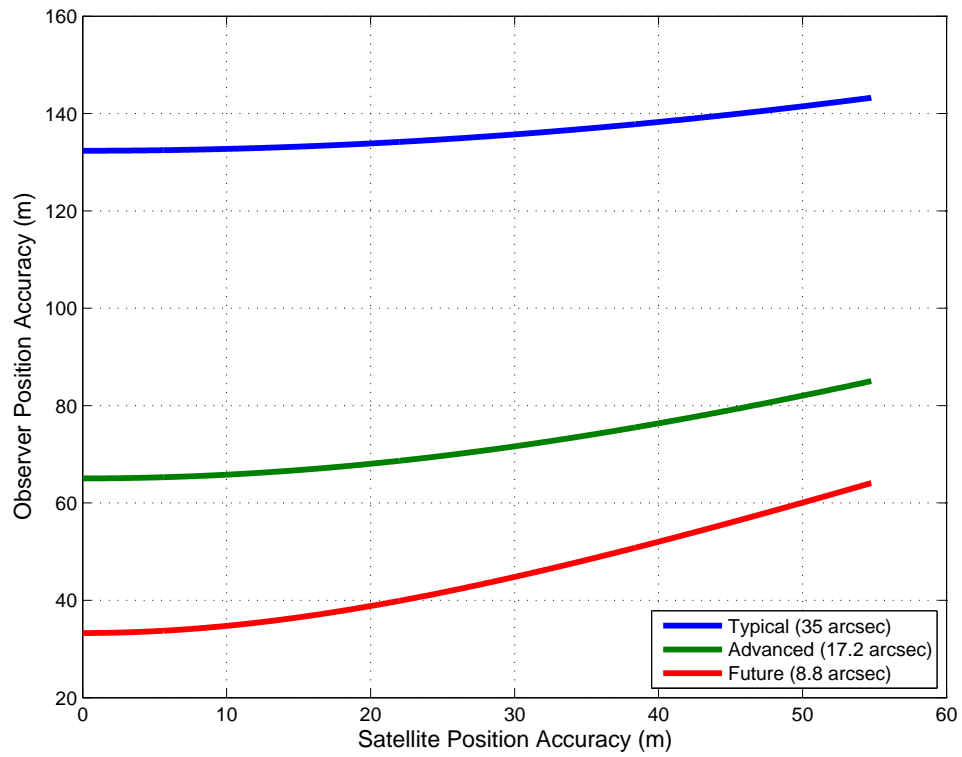
Figure 3.13:   Navigation solution accuracy given the nominal star tracker values of angular resolution and estimated satellite position accuracy observing a LEO satellite

the signal will not be encoded with a message in order to transmit the ephemerides to the observer. An observer will have to receive the ephemerides prior to operation and have frequent updates to that information driven by the ability of the MMS network to maintain accurate orbital estimates. Three solutions are proposed to obtain the required ephemeris information.

First, GPS receivers can be installed on the MMSs. The advantages of this approach is that the satellite position can be known to a high accuracy (<1 m), the technology and hardware is currently developed, mature, and understood, and the support system currently exists. The disadvantage of this approach is that the MMS system becomes dependent on another system, assuming some of its vulnerabilities. In addition, this would introduce another signal to be sent by the satellite for the purpose of receiving ephemeris information, which may be vulnerable to spoofing or jamming. Considering a similar approach where GNSS receivers are used rather than just GPS, the availability of external references increases and the risk of losing all ability to determine ephemerides decreases through redundancy. If GPS or another single system goes out entirely, then the other available global navigation systems may still be available. Ultimately, the MMS system doesn't become an entirely non-GPS solution to navigating on Earth, which may be a criteria for implementation.

Second, a network of ground receivers with high accuracy star trackers can be deployed across the Earth. These ground stations would measure the satellites from known locations and determine each satellite's ephemeris accordingly. This new network is independent of the GPS system and can use existing technology to maintain the database of ephemerides. However, this network would incur a large support footprint with multiple locations and the solution is yet untested as a viable option.

Third, during an operation in an area of interest, local differential references could be deployed that provide timely updates to the satellite ephemeris. This is a smaller local network avoiding the need for global coverage of a ground station net-

work. The ground system architecture becomes significantly smaller and adaptable. As this deployment would be of interest to areas where GPS is denied or unavailable, the deployment of the references becomes a precursor task or mission to accomplish in a likely hazardous environment increasing the risk to operators.

Since a solution to determine the satellite ephemeris does exist using GPS this provides justification to say that the MMS system is still feasible. Depending on the specific operating environment, additional research and development may be necessary to prove feasibility under those conditions.

3.6 Conclusion

This chapter presented the results of a MMS navigation system feasibility study. The initial Concept of Operations (CONOPS) introduce likely operation of the system from the standpoint of three components: the satellite signal, the star tracker/detector, and the navigation algorithm. Several signal to noise ratios discuss the impact of detector parameters, operational parameters and external influences. Those parameters, including a desired SNR value, indicate the required signal strength. The three approaches to calculating signal strength result in similar values. Those values decrease as the operational altitude increases, the signal wavelength increases, and the detector properties improve. This comparison of signal values uniquely justifies the feasibility of building a MMS capable of serving as a navigational aid.

The chapter also examined the constellation requirements for a system of MMSs. The constellation proves to be large in number and therefore difficult to implement, yet not infeasible. The navigation solution illustrates that a "typical" star tracker requires improvements to achieve GPS-like accuracy. In addition to the advancing star tracker capabilities, the navigation accuracy results indicated that the satellite ephemerides present a likely challenge. GPS-like accuracy is possible by leveraging the GPS system to determine MMS ephemerides. However, if the MMS system must be entirely independent from GPS, then feasibility of that system requires additional research and development to alternative ground networks.

In summary, a navigation system using MMSs can provide a GPS-like navigation accuracy (to within tens of meters). Satellite, signal, detector and operational parameters provide initial indication to its feasibility. However, the entire parameter space was not investigated to develop the envelope in which this system is operational. The envelope could be further defined by researching a broader range of atmospheric model conditions, the change in required power in daytime versus nighttime collection, the effect of a moving platform on the detection capability, the optimal satellite constellation configuration for maximum coverage with minimal loss of navigation accuracy, and the performance of such as system in simulation.

IV. Modeling Approach

THIS chapter explains the development of the model to simulate a star tracker integrated with an IMU and a barometric altimeter. A simple block diagram describes the overall system model. The satellite trajectory and associated ephemeris error model is presented. A review of star tracker properties leads to defining expected angular noise according to a variety of parameters. The IMU model is described and two sensor grades are defined. A model of the barometric altimeter allows for vertical component stabilization in the system. Finally, a description of the noise sources in the system components and how those components are integrated using an EKF is presented. Simulation results of each component are presented to demonstrate model functionality.

4.1   Model Description

The simulation models a moving vehicle whose navigation solution is determined by an IMU integrated with a barometric altimeter and a star tracker using an EKF. By imaging a satellite on a star background, the star tracker measures two angles. Those angles, when associated with a time, describe a 3-D line of sight vector that from the observer's position to the satellite. This research determines the component error sources to such measurements and the expected performance of a navigation system that corrects the observer's position given the measurements.

The navigation model consists of four major system components: an IMU, a barometric altimeter, a satellite constellation, and a star tracker. The IMU measures specific force due to trajectory changes in velocity and attitude of the observer. The velocity and attitude changes are integrated to calculate a trajectory based on dead-reckoning. The barometric altimeter provides a measurement of the observer's altitude. To measure the horizontal dimensions of the observer's position, a star tracker observes satellites against a field of stars, where the pointing angles to the satellites provide position information of the observer. The observed satellites are in LEO, MEO, and GEO orbits.

To model this system, aspects of each of these components are accounted for. IMUs are modeled as having random noise inputs affecting velocity and attitude data. Several types of IMU quality are evaluated for navigation performance, which quality defines the strength of the modeled random noise. The barometric altimeter model includes a bias, which itself is modeled as a first order Gauss-Markov (FOGM) process. When modeling the satellites, a nominal satellite constellation defines the true satellite positions. However, to simulate satellite ephemeris error, those satellites' positions and velocities are perturbed by a random error and the error is propagated using Hill's equations.

The star tracker model describes three types of star trackers with varying parameters, which include focal plane array size, aperture size, field of view, and others. From the given star tracker parameters, additional model parameters are derived, such as the average number of stars viewed in an image and the accuracy of the star tracker to find the center of an imaged star or satellite. These sensor parameters define the accuracy of the measured angle from the observing vehicle to the satellite. Simulations vary all these components' parameters and estimate the navigation state using a Kalman filter.

An EKF algorithm estimates the vehicle navigation error state from the IMU, star tracker and altimeter random processes. The dynamics of the position, velocity and tilt errors are modeled using a Pinson error model. Velocity and attitude bias models are augmented to the navigation state, described by FOGM stochastic processes with appropriately selected time constants and white noise strengths. Similarly, a state is added to estimate the time-correlated bias in the barometric altimeter. A linearization of the star tracker measurements of a satellite position with respect to the error states determines the distribution of measurement information to the states. The following section describes how the components are integrated.

4.1.1 Overall Model Approach. Figure 4.1 depicts the flow of data as simulated in this model. Beginning at the top and working down, the model set the

simulation parameters, which included specifications for each system component as well as simulation data management functions. After this initialization, satellite trajectories were generated from desired methods. Both a 'true' satellite trajectory and a 'nominal' satellite trajectory were generated to model the propagation of error in the known satellite position. Next, a candidate vehicle trajectory was generated to describe the vehicle motion over the desired simulation timeframe, labeled as the true navigation state. From that trajectory, changes in velocity and attitude were calculated, which with the addition of appropriate noise represent IMU data. Given the true navigation state, satellite trajectories and a model of the star tracker sensor, measurements of the angle from the vehicle, or observer, to the visible satellites were calculated. To complete the suite of sensors, a modeled barometric altimeter measured the altitude of the observer. These data from the IMU, the star tracker and altimeter were then integrated using an EKF. A nominal navigation state was calculated by integrating the IMU data and a navigation error state mean and covariance was estimated using a Pinson error model with measurement updates from the star tracker and altimeter. The error between the estimated navigation state and the true navigation state described the system performance with the given system parameters. The following sections describe each of these steps in more detail.

4.2   Satellite Trajectory Model

The satellite trajectory model has two initialization approaches. One method accepts a random number of satellites, uniformly distributed between 1 and N_{sats}. These satellites have initial positions calculated at any Earth-centered azimuth and elevation, but at a desired orbital height. Given the initial positions, velocities are calculated psuedo-randomly in that the satellites can orbit in any direction in the plane tangent to the vector from the Earth's center to the satellite, but with appropriate magnitude to create a circular orbit. A second method initializes the satellites according to a specified Walker Delta Pattern constellation [89]. The notation for a Walker Delta Pattern constellation describes the number of satellites in a constella-
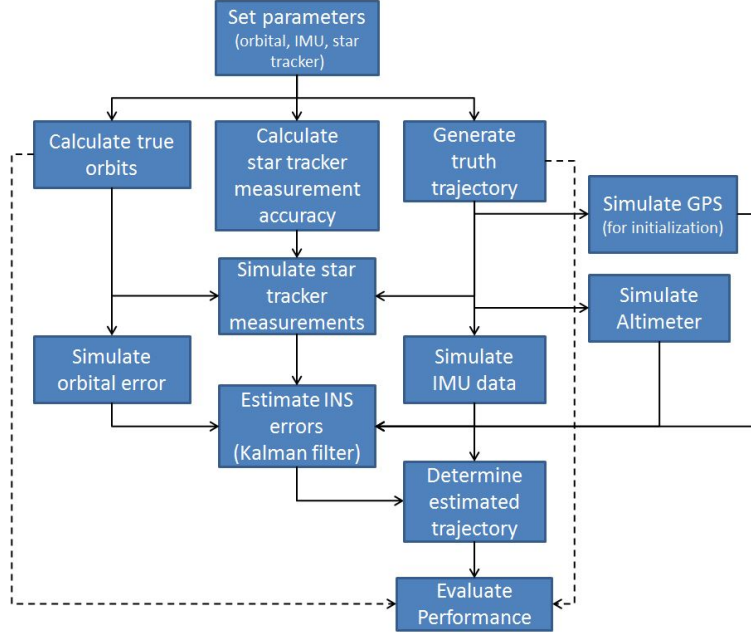
Figure 4.1:   Model of Estimating Navigation Solution using Images of Satellites
Integrated with IMU

tion and how those satellites orbit the Earth in coordination with each other. These
two approaches will be described in the sections that follow.

4.2.1   Random Orbits.   In lieu of looking at a coordinated constellation of
satellites, the satellites can be generated to have unique orbits at a specified orbital
height. Given the orbital height above the Earth, h_{sat}, and the desired number of
satellites to be generated, which are drawn from a uniform distribution $\sim U[1, N_{sats}]$,
where the maximum number of satellites N_{sats} is specified by the user, the procedure
for each satellite's initial position and velocity is the same. First, the unit direction
of the satellite in an ECEF frame is determined randomly by drawing three random
values from a uniform distribution $\sim U[-1, 1]$, one value for each axis, and normalizing
the vector. The actual satellite position can be calculated by extending the unit vector

to be the length of the adjusted orbit height.

$$[d_{s1}, \ d_{s2}, \ d_{s3}] \sim U[-1, 1] \tag{4.1}$$

$$\mathbf{u}_s = \frac{[d_{s1}, \ d_{s2}, \ d_{s3}]}{\sqrt{\sum_{i=1}^{3} d_{si}^2}} \tag{4.2}$$

$$\mathbf{r}_s = (R_E + h_{sat}) \, \mathbf{u}_s \tag{4.3}$$

In determining the orbital velocity, some randomness in direction is allowable, yet not all three axes' values can be random or the satellite motion will not be a circular orbit around the Earth. At most, two directions can be randomly drawn and the third follows the physical limitations of the system. To solve the system, the magnitude of the velocity in the direction of the radial vector from the satellite to the Earth is 0, yet the direction is known. Complementing that fact, the directions of the velocity in the plane tangent the radial vector can be random, yet the magnitude is known [84].

$$[d_{v1}, \ d_{v2}] \sim U[-1, 1] \tag{4.4}$$

$$\mathbf{b} = [d_{v1}, \ d_{v2}, \ 0] \tag{4.5}$$

$$\text{Let } \mathbf{A} = \begin{bmatrix} \mathbf{r}_s \\ 1 & 0 & 0 \\ 0 & 1 & 0 \end{bmatrix} \tag{4.6}$$

$$\mathbf{x}_v = \mathbf{A}^{-1} \mathbf{b} \tag{4.7}$$

$$\mathbf{u}_v = \frac{\mathbf{x}}{||\mathbf{x}||} \tag{4.8}$$

$$\mathbf{v}_s = \left(\frac{\sqrt{\mu}}{R_E + h_{sat}} \right) \mathbf{u}_v \tag{4.9}$$

This method of initialization allowed for "random" orbits, or orbits of a random number of satellites in random directions that follow circular paths and are uncorrelated. This method was used mostly for testing purposes of the rest of the model, but wasn't used in analysis of the system performance since this method also generated orbits that may not represent actual satellite systems.

74

4.2.2 Walker Constellation.   Having a constellation of satellites described in the Walker format, the satellites can be initialized by selecting a single satellite's initial position, then referencing all subsequent satellites in the same plane and the first satellite in adjacent planes to it. The description of a Walker Delta Pattern constellation that follows has been adapted from [84].

The Walker format describes the inclination of the planes with respect to the equator, i, the number of satellites in the constellation, N_{sats}, the number of planes in the constellation, N_{planes}, and the number of increments of true anomaly angle separation units between satellites in adjacent planes, s. These are often referred to as a vector of variables $(i/\ N_{sats}/\ N_{planes}/\ s)$. From these data the number of satellites in each plane, n_{sats} is

$$n_{sats} = \frac{N_{sats}}{N_{planes}} \qquad (4.10)$$

The angular spacing in degrees between each satellite in a single plane, or change in planar anomaly, is

$$\Delta\omega = \frac{360}{n_{sats}} \qquad (4.11)$$

The angular spacing in degrees between one satellite and its respective satellite in an adjacent plane is

$$\Delta\omega_{s0} = \left(\frac{360}{N_{sats}}\right) s \qquad (4.12)$$

The angular spacing in degrees between one plane and its adjacent plane, or change in longitude of ascending node, is

$$\Delta\Omega = \left(\frac{180}{N_{planes}}\right) \qquad (4.13)$$

Since this data is all determined with respect to the orbital planes, the simplest way to implement them is to define the Perifocal reference frame, calculate the angular rotations in that frame, then apply a rotation matrix from the Perifocal frame to an ECEF frame. The Perifocal frame is centered on the orbit center of a satellite. In simulating a constellation, a nominal satellite position is initialized after which orbital plane separations can be applied. The first axis in the Perifocal plane, P, points towards the satellite position. The second axis, Q, is perpendicular to the first and within the plane of orbit. The third axis, W, is orthogonal to the orbital plane. The rotation matrix from the PQW frame to the ECEF frame is defined by [4]

$$
\mathbf{R}_{PQW}^{ecef} = \begin{bmatrix} \cos\Omega\cos\omega - \sin\Omega\sin\omega\cos i & -\cos\Omega\sin\omega - \sin\Omega\cos\omega\cos i & \sin\Omega\sin i \\ \sin\Omega\cos\omega + \cos\Omega\sin\omega\cos i & \sin\Omega\sin\omega + \cos\Omega\cos\omega\cos i & -\cos\Omega\sin i \\ \sin\omega\sin i & \cos\omega\sin i & \cos i \end{bmatrix}
$$
(4.14)

As state previously, an initial position of one satellite must be chosen. This can be described in angular terms of anomaly within the plane, ω_0, and right ascension of the ascending node of that plane, Ω_0. Other satellites within that same plane have an anomaly described by

$$
\omega_{s_i} = \omega_0 + n_i \Delta\omega
$$
(4.15)

where n_i refers to the index of the satellite in the plane. The first satellite of the adjacent plane has an anomaly and longitude of ascending node of

$$
\omega_{s0_j} = \omega_0 + \Delta\omega_{s0}
$$
(4.16)

$$
\Omega_{s0_j} = \Omega_0 + n_j \Delta\Omega
$$
(4.17)

where n_j refers to the index of the plane in the constellation. This can be summarized by the following formula for positioning satellite n_i in plane n_j in the Perifocal frame.

$$[\omega_{ij},\ \Omega_{ij}] = [\omega_0 + n_i\Delta\omega + n_j\Delta\omega_{s0},\ \Omega_0 + n_j\Delta\Omega] \begin{cases} \text{for } n_i = 0 \text{ to } (n_{sats} - 1) \\ \text{for } n_j = 0 \text{ to } (N_{planes} - 1) \end{cases}$$

(4.18)

The position and velocity of a satellite in the PQW frame is calculated as [4]

$$\mathbf{p}_{s_{ij}}^{PQW} = [r_{sat}\cos(\omega_{ij}),\ r_{sat}\sin(\omega_{ij}),\ 0]$$

(4.19)

$$\mathbf{v}_{s_{ij}}^{PQW} = \frac{\sqrt{\mu}}{r_{sat}}[\sin(\omega_{ij}),\ \cos(\omega_{ij}),\ 0]$$

(4.20)

where r_{sat} is the radial distance of the satellite from the center of orbit, or the orbital height from Earth's center. This calculation assumes a circular orbit.

The final step in initializing the satellites is given by applying the rotation matrix between frames.

$$\mathbf{p}_{s_{ij}}^{ecef} = \mathbf{R}_{PQW}^{ecef}\mathbf{p}_{s_{ij}}^{PQW}$$

(4.21)

$$\mathbf{v}_{s_{ij}}^{ecef} = \mathbf{R}_{PQW}^{ecef}\mathbf{v}_{s_{ij}}^{PQW}$$

(4.22)

In this way, the satellites in the constellation are given initial positions and velocities such that they move in a set number of planes at the correct inclination and with proper separation between satellites to be distributed evenly. After initializing the satellites, their positions as a function of time are propagated.

4.2.3 Satellite Propagation. Once initialized, the satellite trajectories are propagated using Kepler's equations of two-body dynamics [84]. To use the two body equations described here, 4 assumptions must hold true [84].

1. The mass of the satellite is very small compared to the Earth.

2. The calculations are performed in an inertial coordinate frame.

3. The two bodies (satellite and Earth) are modeled as point masses. They are uniformly dense.

4. There are no other forces in the system affecting motion.

The algorithm presented here is given by Vallado [84], which calculates the position, $\mathbf{r}_s$ and velocity, $\mathbf{v}_s$, vectors of a satellite in inertial coordinate frame given an initial position, $\mathbf{r}_{s0}$, velocity, $\mathbf{v}_{s0}$, and the time, Δt, at which to calculate new positions and velocities.

$$\alpha = \frac{-||\mathbf{v}_{s0}||^2}{\mu} + \frac{2}{||\mathbf{r}_{s0}||} \tag{4.23}$$

$$\chi_0 = \alpha \Delta t \sqrt{\mu} \tag{4.24}$$

where μ is Earth's gravitational constant, $\mu = 398.6004418 \times 10^{12}$ m^3/s^2 and χ_0 is the initial guess at the universal variable used in this formulation to replace time as the independent variable.

$$\text{LOOP} \tag{4.25}$$

$$\psi = \chi_n^2 \alpha \tag{4.26}$$

$$\text{Find } c_2, c_3(\psi) \tag{4.27}$$

$$r_s = \chi_n^2 c_2 + \frac{\mathbf{r}_{s0} \cdot \mathbf{v}_{s0}}{\sqrt{\mu}} \chi_n (1 - \psi c_3) + ||\mathbf{r}_{s0}||(1 - \psi c_2) \tag{4.28}$$

$$\chi_{n+1} = \chi_n + \frac{\sqrt{\mu} \Delta t - \chi_n^3 c_3 - \frac{\mathbf{r}_{s0} \cdot \mathbf{v}_{s0}}{\sqrt{\mu}} \chi_n^2 c_2 - ||\mathbf{r}_{s0}||\chi_n (1 - \psi c_2)}{r_s} \tag{4.29}$$

$$\chi_n \Leftarrow \chi_{n+1} \tag{4.30}$$

$$\text{UNTIL } |\chi_n - \chi_{n-1}| < 1 \times 10^{-6} \tag{4.31}$$

where ψ is an intermediate variable used to find coefficients to the satellite range, r_s in Eqn. 4.28. The final position and velocity of the satellite is defined by a linear combination of the initial position and velocity using state transition functions

f and g.

$$f = 1 - \frac{\chi_n^2}{||\mathbf{r}_{s0}||}c_2 \qquad g = \Delta t - \frac{\chi_n^3}{\sqrt{\mu}}c_3$$
$$\dot{g} = 1 - \frac{\chi_n^2}{r_s}c_2 \qquad \dot{f} = \frac{\sqrt{\mu}}{r_s||\mathbf{r}_{s0}||}\chi_n(\psi c_3 - 1) \tag{4.32}$$

$$\mathbf{r}_s = f\mathbf{r}_{s0} + g\mathbf{v}_{s0} \tag{4.33}$$

$$\mathbf{v}_s = \dot{f}\mathbf{r}_{s0} + \dot{g}\mathbf{v}_{s0} \tag{4.34}$$

This algorithm uses the Newton method to converge to a correct answer and uses the coefficients c_2 and c_3, which are derived from the universal formulation of Kepler's equation and defined by [5] and calculated using this algorithm [84].

$$\text{IF} \quad \psi > 1 \times 10^{-6} \tag{4.35}$$

$$c_2 = \frac{1 - \cos(\sqrt{\psi})}{\psi} \quad c_3 = \frac{\sqrt{\psi} - \sin(\sqrt{\psi})}{\sqrt{\psi^3}} \tag{4.36}$$

$$\text{ELSE IF} \quad \psi < -1 \times 10^{-6} \tag{4.37}$$

$$c_2 = \frac{1 - \cosh(\sqrt{-\psi})}{\psi} \quad c_3 = \frac{\sinh(\sqrt{-\psi}) - \sqrt{-\psi}}{\sqrt{(-\psi)^3}} \tag{4.38}$$

$$\text{ELSE} \tag{4.39}$$

$$c_2 = \frac{1}{2} \quad c_3 = \frac{1}{6} \tag{4.40}$$

4.2.4 Satellite Ephemeris Error Model. Having established the trajectories of the satellites, the satellite ephemeris errors were modeled. These ephemeris errors represent the change from what would be the expected satellite position calculated using the Kepler two-body approach just described caused by perturbations in the orbit. These perturbations could be implemented in simulation by adding uncorrelated noise to the position data or a fixed bias. However, neither of those methods would capture the change in the perturbation in time. The ephemeris error would likely be correlated in time and therefore the approach taken in this research was to introduce a position and velocity error at the beginning of the simulated satellite availability

and propagate the error according to the dynamics introduced by Clohessy and Wilt-shire [14], or also by Hill [31]. In this manner, the ephemeris error is both accounted for and will change in time appropriate to the orbit that is being simulated.

From an estimated initial offset in position and velocity of a satellite the error becomes time-correlated due to the orbital dynamics. These dynamic errors can be modeled by propagating initial errors in a Hill's frame of reference. New satellite positions and velocities were defined by slightly offsetting the known initial satellite values. Random values drawn from a uniform distribution with a mean of zero and several different boundaries for the offset positions. Random values were drawn from a similar uniform distribution for the offset velocities. The true and offset satellite positions were established in the Hill's coordinate frame, which describes the relative relationship from one satellite to another. This reference frame was introduced in Section 2.11.3. The transformation of the position and velocity vectors of the two satellites were performed using the algorithm described by Vallado [84].

First, a matrix transforming vectors from an ECI frame to a satellite coordinate system, referred to as the RSW frame, $\mathbf{T}_{eci}^{rsw}$, can be calculated from the true satellite position and velocity in an ECI frame, $\mathbf{r}_{s1}^{eci}$ and $\mathbf{v}_{s1}^{eci}$, respectively. The RSW frame is centered on the satellite and the R axis points in the radial direction from the Earth center to the satellite. The S axis points in the direction of the velocity and in the local horizontal plane. The W axis is orthogonal to the first two axes.

$$\mathbf{T}_{eci}^{rsw} = \begin{bmatrix} \mathbf{r}_1 & \mathbf{r}_2 & \mathbf{r}_3 \end{bmatrix} \tag{4.41}$$

$$\mathbf{r}_1 = \frac{\mathbf{r}_{s1}^{eci}}{||\mathbf{r}_{s1}^{eci}||} \tag{4.42}$$

$$\mathbf{r}_2 = \frac{\mathbf{r}_{s1}^{eci} \times \mathbf{v}_{s1}^{eci}}{||\mathbf{r}_{s1}^{eci} \times \mathbf{v}_{s1}^{eci}||} \tag{4.43}$$

$$\mathbf{r}_3 = \frac{\mathbf{r}_1 \times \mathbf{r}_2}{||\mathbf{r}_1 \times \mathbf{r}_2||} \tag{4.44}$$

The positions and velocities of the true satellite and the offset satellite, $\mathbf{r}_{s2}^{eci}$ and $\mathbf{v}_{s2}^{eci}$, are transformed to the RSW frame by

$$\mathbf{r}_{s1}^{rsw} = [\mathbf{T}_{eci}^{rsw}]^T \, \mathbf{r}_{s1}^{eci} \tag{4.45}$$

$$\mathbf{r}_{s2}^{rsw} = [\mathbf{T}_{eci}^{rsw}]^T \, \mathbf{r}_{s2}^{eci} \tag{4.46}$$

$$\mathbf{v}_{s1}^{rsw} = [\mathbf{T}_{eci}^{rsw}]^T \, \mathbf{v}_{s1}^{eci} \tag{4.47}$$

$$\mathbf{v}_{s2}^{rsw} = [\mathbf{T}_{eci}^{rsw}]^T \, \mathbf{v}_{s2}^{eci} \tag{4.48}$$

In order to calculate the Hill's frame vectors, the geocentric angles from the first satellite to the second due to the offset in the z and y directions, $\Delta\Lambda_z$ and $\Delta\Lambda_y$, respectively are calculated. From those angles, the position vector of the first satellite can be rotated to incorporate these effects.

$$\Delta\Lambda_z = \tan^{-1}\left(\frac{r_{s2_w}^{rsw}}{||\mathbf{r}_{s1}^{rsw}||}\right) \tag{4.49}$$

$$\mathbf{r}_{s2_{temp1}} = \text{ROT2}\left(-\Delta\Lambda_z\right)\mathbf{r}_{s1}^{rsw} \tag{4.50}$$

$$\Delta\Lambda_y = \tan^{-1}\left(\frac{r_{s2_s}^{rsw}}{||\mathbf{r}_{s1}^{rsw}||}\right) \tag{4.51}$$

$$\mathbf{r}_{s2_{temp2}} = \text{ROT3}\left(-\Delta\Lambda_y\right)\mathbf{r}_{s2_{temp1}} \tag{4.52}$$

where $r_{s2_s}^{rsw}$ and $r_{s2_w}^{rsw}$ are the second and third components of the $\mathbf{r}_{s2}^{rsw}$ vector. ROT2($\cdot$) and ROT3($\cdot$) are rotation matrices defined as

$$\text{ROT2}\left(\zeta\right) = \begin{bmatrix} \cos\zeta & 0 & -\sin\zeta \\ 0 & 1 & 0 \\ \sin\zeta & 0 & \cos\zeta \end{bmatrix} \tag{4.53}$$

$$\text{ROT3}\left(\zeta\right) = \begin{bmatrix} \cos\zeta & \sin\zeta & 0 \\ -\sin\zeta & \cos\zeta & 0 \\ 0 & 0 & 1 \end{bmatrix} \tag{4.54}$$

where ζ represents the angle of rotation.

81

Finally, the Hill's frame representation of the true position and velocity, $\mathbf{r}_{s1}^{Hill}$ and $\mathbf{v}_{s2}^{Hill}$, and the offset position and velocity, $\mathbf{r}_{s2}^{Hill}$ and $\mathbf{v}_{s2}^{Hill}$, are calculated as

$$\mathbf{r}_{s2}^{Hill} = \begin{bmatrix} \mathbf{r}_{s2_{temp2}} - \mathbf{r}_{s1}^{rsw} \\ \Delta\Lambda_y ||\mathbf{r}_{s2}|| \\ \Delta\Lambda_z ||\mathbf{r}_{s2}|| \end{bmatrix} \tag{4.55}$$

$$\mathbf{v}_{s2}^{Hill} = \mathbf{v}_{s2}^{rsw} - \mathbf{r}_{s1}^{rsw} - \boldsymbol{\omega}_{\frac{rsw}{Hill}} \times \mathbf{r}_{s2}^{Hill} \tag{4.56}$$

$$\mathbf{r}_{s1}^{Hill} = \mathbf{0} \tag{4.57}$$

$$\mathbf{v}_{s1}^{Hill} = \mathbf{0} \tag{4.58}$$

where $\boldsymbol{\omega}_{\frac{rsw}{Hill}}$ is the angular rate of the RSW frame with respect to the Hill's frame calculated as

$$\boldsymbol{\omega}_{\frac{rsw}{Hill}} = \frac{\mathbf{r}_{s1}^{rsw} \times \mathbf{v}_{s1}^{rsw}}{|\mathbf{r}_{s1}^{rsw}|^2} \tag{4.59}$$

In the Hill's coordinate frame the motion of the second satellite in relation to the first satellite can be approximated using Hill's equations [31], also known as the Clohessy-Wiltshire equations [14]. In order to use Hill's equations, it must be assumed that the orbit is circular, no external forces are acting on the satellite and that the mass of the satellite is negligible with respect to the body being orbited. The position, $[x, y, z]$, and velocity, $[\dot{x}, \dot{y}, \dot{z}]$, of the second satellite follows the behavior described by

Vallado [84], where ω is the satellite's angular rate.

$$x(t) = \frac{\dot{x}_0}{\omega} \sin(\omega t) - \left(3x_0 + \frac{2\dot{y}_0}{\omega}\right) \cos(\omega t) + \left(4x_0 + \frac{2\dot{y}_0}{\omega}\right) \tag{4.60}$$

$$y(t) = \left(6x_0 + \frac{4\dot{y}_0}{\omega}\right) \sin(\omega t) + \frac{2\dot{x}_0}{\omega} \cos(\omega t) - (6\omega x_0 + 3\dot{y}_0) t + \left(y_0 - \frac{2\dot{x}_0}{\omega}\right) \tag{4.61}$$

$$z(t) = z_0 \cos(\omega t) + \frac{\dot{z}_0}{\omega} \sin(\omega t) \tag{4.62}$$

$$\dot{x}(t) = \dot{x}_0 \cos(\omega t) + (3\omega x_0 + 2\dot{y}_0) \sin(\omega t) \tag{4.63}$$

$$\dot{y}(t) = (6\omega x_0 + 4\dot{y}_0) \cos(\omega t) - 2\dot{x}_0 \sin(\omega t) - (6\omega x_0 + 3\dot{y}_0) \tag{4.64}$$

$$\dot{z}(t) = -z_0 \omega \sin(\omega t) + \dot{z}_0 \cos(\omega t) \tag{4.65}$$

The trajectory of the relative satellite, indicating the propagation of satellite error can be transformed back to an inertial frame using this algorithm [84]. First, the first satellite's position in the inertial frame can be used to determine it's position in the RSW frame using the transformation matrix in Eqn. 4.41. The position of the second satellite takes into account the first satellite's position.

$$\mathbf{r}_{s2_{temp1}} = \mathbf{r}_{s1}^{rsw} + \left[x_{s2}^{Hill}, 0, 0\right]^T \tag{4.66}$$

$$\Delta\Lambda_y = \frac{y_{s2}^{Hill}}{||\mathbf{r}_{s1}||} \tag{4.67}$$

$$\mathbf{r}_{s2_{temp2}} = \text{ROT3}\left(-\Delta\Lambda_y\right) \mathbf{r}_{s2_{temp1}} \tag{4.68}$$

$$\Delta\Lambda_z = \frac{y_{s2}^{Hill}}{||\mathbf{r}_{s1}||} \tag{4.69}$$

$$\mathbf{r}_{s2}^{rsw} = \text{ROT2}\left(-\Delta\Lambda_z\right) \mathbf{r}_{s2_{temp2}} \tag{4.70}$$

$$\mathbf{r}_{s2}^{eci} = \mathbf{T}_{eci}^{rsw} \mathbf{r}_{s2}^{rsw} \tag{4.71}$$

where x_{s2}^{Hill} and y_{s2}^{Hill} are the first and second components of the second satellite's position in the Hill's frame.

$$\mathbf{v}_{s2}^{rsw} = \mathbf{v}_{s1}^{rsw} + \mathbf{v}_{s2}^{Hill} + \frac{\mathbf{r}_{s1}^{eci} \times \mathbf{v}_{s1}^{eci}}{|\mathbf{r}_{s1}^{eci}|^2} \times \mathbf{r}_{s2}^{Hill} \qquad (4.72)$$

$$\mathbf{v}_{s2}^{eci} = \mathbf{T}_{eci}^{rsw} \mathbf{v}_{s2}^{rsw} \qquad (4.73)$$

These two trajectories represent true satellite positions and expected satellite position. From these two types of trajectories angle measurements can be simulated and nominal angle measurements can be estimated, respectively.

The effect of the initial satellite position and velocity offset were evaluated over a time frame relative to the orbital height of the satellite. For satellites orbiting at a LEO height, the satellite ephemeris error was evaluated over a period of 12 minutes, which is consistent with the time a satellite at a 100 km orbital height would be above the horizon. For MEO and GEO height satellites, their orbits allow for much longer visibility times, yet the simulation time is reduced to a period of 3 hours, which is the maximum length of time that the overall system is modeled. An example of the ephemeris error growth for a LEO satellite is shown in Figure 4.2. In this figure, each axis has independent initial position error drawn from a uniform distribution with absolute maximum values of 100 m. Each axis' initial velocity error is similarly drawn randomly from a uniform distribution with absolute maximum values of 1 m/s. With these initial conditions, the errors follow the dynamics of the Clohessy-Whiltshire equations, given in Eqns. 4.60-4.65.

For each orbital height, 200 Monte Carlo iterations of the ephemeris error were evaluated to determine the statistics of expected ephemeris error growth over the simulation time period. The results of these simulations are shown in Figure 4.3. Figure 4.3 shows the standard deviation of the satellite position error as a function of initial position maximum error along the horizontal axis and the color-coded initial velocity maximum error. In all three plots, the case when there's no initial position or velocity error is not displayed as it results in approximately 0 m of ephemeris error

84
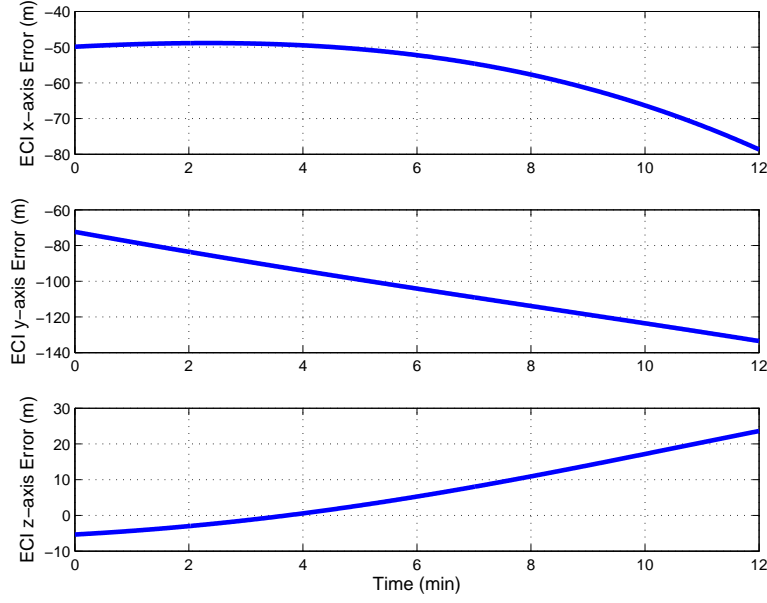
Figure 4.2:   LEO Satellite Position Error Simulation with 100 m position and 1 m/s velocity initial absolute error max

after 12 minutes of a LEO satellite and after 3 hours of a MEO and GEO satellite. This result is expected in that with no error the path of the second satellite will be identical to the first. As the initial position error increases from 0 m to 100 m with no initial velocity error, the error grows to approximately 100 m in a LEO orbit. In contrast, the MEO ephemeris error reaches approximately 200 m under the same initial conditions. This is due to the longer time period over which the simulation is run. The GEO orbital error increases to approximately 100 m after 3 hours with up to 100 m initial position error and 0 m/s initial velocity error. Despite having the same simulation time as the MEO orbit, the growth is smaller than that seen by the MEO case because both the orbital rate and the velocity at GEO is much less than at MEO. This should cause a slower growth of error between orbit heights under the same initial conditions.

In the LEO orbits, the impact of the initial velocity error varies. When there is no initial position error the effect of the initial velocity error is distinct. From 1 mm/s to 100 mm/s, the standard deviation grows from less than 1 m to approximately 70 m. This indicates that the initial velocity error can dominate the ephemeris error results.

85
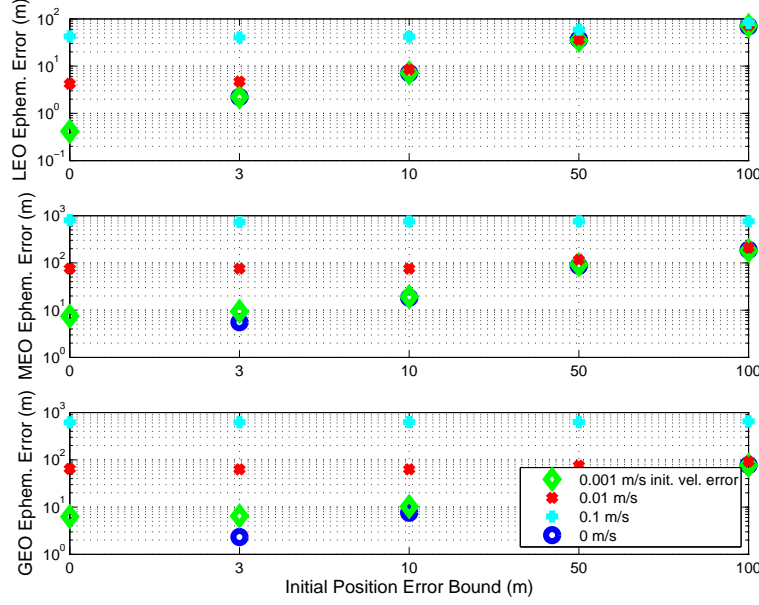
Figure 4.3:   Growth of Satellite Position Error. LEO orbit results are after 12 minutes and MEO and GEO orbits' results are after 3 hours.

However, as the initial position error increases, the impact of the initial velocity error decreases, such that at an initial position error of 100 m the initial velocity error seems to make little difference. This is likely due to a short duration of simulation for LEO orbits. Since the LEO orbits are only simulated over 7 minutes, the rate of position change doesn't grow the ephemeris error larger than the initial position error is already set. In contrast, for the MEO and GEO orbits, the longer simulation time does make a difference. Over a period of 3 hours, the largest initial velocity error dominates the ephemeris error at all initial position error values.

In performing these simulations, a reference table can be built, depending on the desired orbit height and allowable satellite ephemeris error, to initiate ephemeris error conditions. These conditions will be used in simulating the full system and the random ephemeris errors for observed satellites.

4.3   Star Tracker Model

To model the measurement of a star tracker, the angle uncertainty must be defined. The angle uncertainty is determined by the star tracker's physical properties.

The measurement uncertainty of the star tracker must be derived as a function of the sensor's specifications. The star tracker boresight error is the accuracy of the sensor to detect one star, σ_{star}, divided by the square root of the expected number of stars in an image, N_{stars} [50].

$$\sigma_{st} = \frac{\sigma_{star}}{\sqrt{N_{stars}}} \tag{4.74}$$

It should be noted that, as with any measurement process, Eqn. (4.74) isn't valid for an arbitrarily large N. At some point, the error will meet the star tracker's systematic error floor, at which point, observing mores stars in the image doesn't decrease the boresight error further. The accuracy of detecting a single star is further a function of the sensor's ability to find the center of the star, $\sigma_{centroid}$, and the angular resolution of the focal plane array [50].

$$\sigma_{star} = \frac{\text{FOV}}{N_{pix}} \sigma_{centroid} \tag{4.75}$$

where FOV is the angular field of view of the star tracker in radians, N_{pix} is the number of pixels in one dimension of a square focal plane array and the centroiding accuracy is in units of pixels. The centroiding accuracy can vary according to the algorithm used to sample the image, but it can be estimated by the ratio of the PSF of the sensor to the signal to noise ratio of the source.

$$\sigma_{centroid} = \frac{\text{PSF}}{\text{SNR}} \tag{4.76}$$

The number of stars visible in an image is approximated using the Bright Star catalog [32] for magnitudes up to 6 and Allen [1] for dimmer stars. The number of stars visible as a function of the minimum detectable star magnitude of the star tracker is shown in Figure 4.4. Alternatively, the number of stars can be approximated using least-squares fit to that data using a function up to order 3. This results in an equation
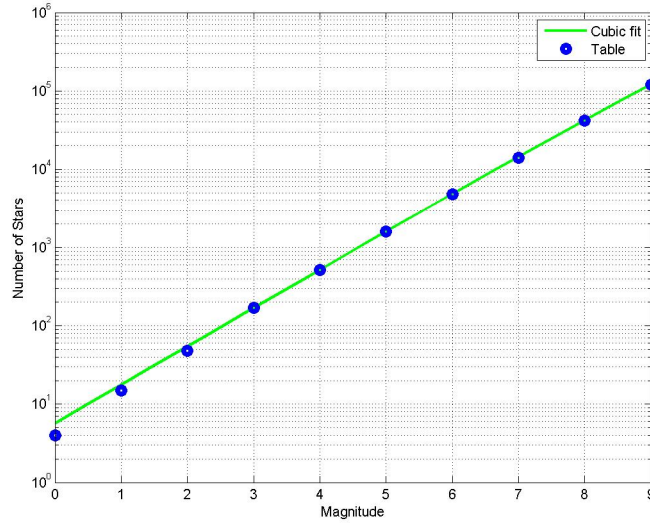
Figure 4.4: Number of Visible Stars in Star Tracker Catalog based on Minimum Magnitude of Detectability

describing the number of stars in the catalog of a given minimum magnitude [63].

$$\log(n) = 0.754 + 0.4896 M_{min} + 0.001159 M_{min}^2 - 0.000235 M_{min}^3 \tag{4.77}$$

$$N_{cat} = 10^{\log(n)} \tag{4.78}$$

After the number of eligible stars in the catalog are determined, the estimated number of stars in the field of view are calculated as [49]

$$N_{stars} = \left(\frac{1 - \frac{d_{ap}}{2}}{2} \right) N_{cat} \tag{4.79}$$

This calculation assumes a uniform distribution of stars in the celestial sphere. A higher fidelity estimate of the number of stars imaged would adapt the number of imaged stars according to the observer-satellite geometry.

Three types of star trackers were evaluated, based on nominal operating characteristics of currently available star trackers and possible future developments. The pertinent sensor parameters for each are shown in Table 4.1.

Table 4.1:   Star tracker parameters

Parameter	Star Tracker Type			Units
	1	2	3	
FOV	10	10	10	deg
SNR	7	7	7	none
PSF	0.0787	0.2233	0.8876	pixels
N_{pix}	1024	2048	4096	n/a
σ_{st}	0.116	0.164	0.327	arcsec

4.4   IMU Model

The IMU is modeled as returning changes in velocity, Δv, and attitude, $\Delta \theta$, given the true position along a vehicle's trajectory. The model is configurable to commercial, tactical, and navigation grade IMUs. These different grades describe the noise associated with each type affecting the error growth. This IMU error growth can be modeled by running Monte Carlo simulations and calculating statistics at each time step or by calculating the expected error growth directly using a Pinson error model [81]. A description of the trajectory calculation and the simulation of IMU noise is described in the next two sections. The error growth of the IMU is described in Section 4.6.1.

4.4.1   Trajectory Description.   Before simulating measurements, the observer's trajectory must be determined. In these simulations, the observer initializes at a known latitude, longitude and altitude and has a constant velocity. From these parameters, a time series of observer positions is calculated. Subsequently, IMU Δv and $\Delta \theta$ values are generated from the position values using [81] such that when integrated, the Δv and $\Delta \theta$ values result in the desired trajectory.

89

First, the Earth is modeled as an ellipsoid with the meridian radius of curvature, R_N, and the transverse radius of curvature, R_E, at a given latitude, L, are calculated as

$$R_N = R_e \frac{1 - e^2}{(1 - e^2 \sin^2(L(t)))^{\frac{3}{2}}} \tag{4.80}$$

$$R_E = \frac{R_e}{\sqrt{1 - e^2 \sin^2(L(t))}} \tag{4.81}$$

where e is the eccentricity of the Earth and R_e is the Earth radius. Next, the rate of change of the latitude, $\dot{L}$, and longitude, $\dot{l}$, are calculated from the known velocity, $\mathbf{v}$, expressed in the navigation frame with components, $[v_N, v_E, v_D]$.

$$\dot{L} = \frac{v_N}{R_N + h(t)} \tag{4.82}$$

$$\dot{l} = v_E \frac{\sec(L(t))}{R_E + h(t)} \tag{4.83}$$

$$\tag{4.84}$$

In order to find the acceleration, the change in position, Δx is calculated as

$$\Delta\mathbf{x} = \begin{bmatrix} (L(t + \Delta t) - L(t))(R_N + h(t)) \\ (l(t + \Delta t) - l(t))(R_E + h(t))\cos(L(t)) \\ -(h(t + \Delta t) - h(t)) \end{bmatrix} \tag{4.85}$$

where Δt is the time interval. From the change in position and the velocity, the acceleration, $\mathbf{a}$, and the forces in the navigation frame, $\mathbf{f}_{NED}$, that cause that acceleration are calculated as

$$\mathbf{a} = \dot{\mathbf{v}} = 2\frac{\Delta\mathbf{x} - \mathbf{v}\Delta t}{\Delta t^2} \tag{4.86}$$

$$\mathbf{f}_{NED} = \begin{bmatrix} \mathbf{a}_N + v_E(2\Omega_E + \dot{l})\sin(L) - v_D\dot{L} \\ \mathbf{a}_E - v_N(2\Omega_E + \dot{l})\sin(L) - v_D(2\Omega_E + \dot{l})\cos(L) \\ \mathbf{a}_z + v_y(2\Omega_E + \dot{l})\cos(L) - v_N\dot{L} - g \end{bmatrix} \tag{4.87}$$

where it's assumed that there are no gravitational field variations, such that $g = 9.80665$ m/s^2 is constant, and Ω_E is the Earth's rotation rate in radians per second. The change in velocity over the time interval, $\Delta\mathbf{v}$ can now be calculated as

$$\Delta\mathbf{v} = \frac{\mathbf{C}_b^n(t) + \mathbf{C}_b^n(t + \Delta t)}{2}\mathbf{f}_{NED}\Delta t \tag{4.88}$$

where $\mathbf{C}_b^n$ is the direction cosine matrix (DCM) describing the transformation from the body frame to the navigation frame, and $\mathbf{C}_n^b$ is DCM describing the transformation from the navigation frame to the body frame.

To calculate the change in attitude over the same time interval, the transport rate, $\boldsymbol{\omega}_{en}^N$, which describes the turn rate of the navigation frame with respect to the ECEF frame

$$\boldsymbol{\omega}_{en}^n = \left[\begin{array}{ccc} \dfrac{v_y}{R_E + h(t)} & -\dfrac{v_x}{R_N + h(t)} & -v_y\dfrac{\tan(L(t))}{R_E + h(t)} \end{array}\right]^T \tag{4.89}$$

The turn rate of the navigation frame expressed in the ECI frame, ω_{ie}^n, takes into account the Earth rate and is calculated as

$$\boldsymbol{\omega}_{ie}^n = \left[\begin{array}{ccc} \Omega_E\cos(L(t)) & 0 & -\Omega_E\sin(L(t)) \end{array}\right]^T \tag{4.90}$$

$$\tag{4.91}$$

Additionally, the attitude is known at the beginning and the end of the time interval, expressed as DCMs, and are used to calculate the rotation angle, *sigma* through which the attitude changes.

$$\boldsymbol{\sigma}\times = \log\left(\mathbf{C}_b^n(t)\mathbf{C}_n^b(t + \Delta t)\right) \tag{4.92}$$

$$\boldsymbol{\sigma} = \frac{1}{2}\left[\begin{array}{c} \boldsymbol{\sigma}\times(3,2) - \boldsymbol{\sigma}\times(2,3) \\ \boldsymbol{\sigma}\times(1,3) - \boldsymbol{\sigma}\times(3,1) \\ \boldsymbol{\sigma}\times(2,1) - \boldsymbol{\sigma}\times(1,2) \end{array}\right] \tag{4.93}$$

where the matrix $\boldsymbol{\sigma}\times$ is indexed by the parenthetical numbers. Then, the change in attitude the gyroscopes would measure, $\Delta\theta$, is calculated from the body to navigation frame DCM, the affecting rotation rates, and the rotation angle.

$$\Delta\boldsymbol{\theta} = \boldsymbol{\sigma} + \Delta t \left(\mathbf{C}_b^n(t) \left(\boldsymbol{\omega}_{ie}^n + \boldsymbol{\omega}_{en}^n \right) \right)^T \tag{4.94}$$

From these equations, a known trajectory is converted to the change in velocity and angle values that an IMU would report in the absence of noise. To account for the noise in an IMU, the following section describes the models used.

4.4.2 IMU Noise Model. The IMU values calculated using Eqns. 4.88 and 4.94 establish the true Δv and $\Delta\theta$ values. But IMUs contain noise sources due to a variety of factors including spurious magnetic fields, temperature gradients, mass unbalance, vibro-pendulous errors, non-orthogonal axes, and others, which introduce error into the values [81]. For this research, IMU accelerometers are modeled to include a first-order Gauss-Markov bias, b_a, and AWGN, w_a according to

$$\Delta\mathbf{v} = \Delta\mathbf{v}_{true} + \mathbf{b}_a + \mathbf{w}_a \tag{4.95}$$

where the bias and white noise are uncorrelated and the noise inputs between each axis' accelerometer is uncorrelated.

$$E[\mathbf{w}_a(t)\mathbf{w}_a(t+\tau)] = q_a \mathbf{I}_{3\times3}\delta(\tau) \tag{4.96}$$

$$E[\mathbf{w}_a(t)\mathbf{b}_a(t+\tau)] = \mathbf{0}_{3\times3} \tag{4.97}$$

The bias noise is modeled as

$$\dot{\mathbf{b}}_a(t) = -\frac{1}{\tau_a}\mathbf{b}_a(t) + \mathbf{w}_{b_a} \tag{4.98}$$

where τ_a describes the time constant and $\mathbf{w}_{b_a}$ is zero-mean AWGN with a covariance given by

$$E[\mathbf{w}_{b_a}(t)\mathbf{w}_{b_a}(t+\tau)] = \frac{2\sigma_a^2}{\tau_a}\mathbf{I}_{3\times3}\delta(\tau) \tag{4.99}$$

Similarly, the IMU gyroscopes are modeled to include a first-order Gauss Markov bias, b_g, and AWGN, w_g according to

$$\boldsymbol{\Delta\theta} = \boldsymbol{\Delta\theta}_{true} + \mathbf{b}_g + \mathbf{w}_g \tag{4.100}$$

where the bias and white noise are uncorrelated and the noise inputs between each axis' gyroscope is uncorrelated.

$$\mathbf{E}[\mathbf{w}_g(t)\mathbf{w}_g(t+\tau)] = q_g\mathbf{I}_{3\times3}\delta(\tau) \tag{4.101}$$

$$\mathbf{E}[\mathbf{w}_g(t)\mathbf{b}_g(t+\tau)] = \mathbf{0}_{3\times3} \tag{4.102}$$

The bias noise is modeled as

$$\dot{\mathbf{b}}_g(t) = -\frac{1}{\tau_g}\mathbf{b}_g(t) + \mathbf{w}_{b_g} \tag{4.103}$$

where τ_g describes the time constant and w_{b_g} is zero-mean AWGN with a noise strength given by

$$E[\mathbf{w}_{b_g}(t)\mathbf{w}_{b_g}(t+\tau)] = \frac{2\sigma_g^2}{\tau_g}\mathbf{I}_{3\times3}\delta(\tau) \tag{4.104}$$

Table 4.2 lists the values used for each grade IMU [42].

Table 4.2:   IMU parameters used for IMU grades.

IMU Grade	σ_a $(\mathrm{m/s}/\sqrt{s})$	σ_g $(\mathrm{rad}/\sqrt{s})$	σ_{b_a} $(\mathrm{m/s})$	σ_{b_g} $(\mathrm{rad/s})$	τ (s)
Tactical (HG1700)	8.7×10^{-5}	9.5×10^{-3}	4.8×10^{-6}	9.8×10^{-3}	3600
Navigation (HG9900 - H764G)	5.8×10^{-7}	2.3×10^{-4}	7.2×10^{-9}	2.45×10^{-4}	3600

4.5   Barometric Altimeter Model

The barometric altimeter measures the altitude of the sensor. It can be modeled as the sum of the true altitude, a time-correlated bias (first-order Gauss Markov process) and additive white Gaussian noise.

$$h_{baro}(t) = h_{true}(t) + b_b(t) + w_b(t) \tag{4.105}$$

where the Gaussian noise is defined by

$$E[w_b] = 0 \tag{4.106}$$

$$E[w_b(t)w_b(t+\tau)] = \sigma_b^2 \delta(\tau) \tag{4.107}$$

and the time-correlated bias is defined by

$$\dot{b}_b(t) = -\frac{1}{\tau_b}b_b(t) + w_{b_b} \tag{4.108}$$

$$E[w_{b_b}(t)] = 0 \tag{4.109}$$

$$E[w_{b_b}(t)w_{b_b}(t+\tau)] = \frac{2\sigma_{b_b}^2}{\tau_b}\delta(\tau) \tag{4.110}$$

4.6   Navigation Estimation

Given the satellite ephemerides, the sensor model and IMU data representing the observer's trajectory, an EKF can be used to estimate the error of an observer's navigation state (position error, velocity error and tilt error).

94

4.6.1 Dynamics Model Description. The IMU provides the system the Δv and $\Delta \theta$ values that, when integrated, will result in the position, velocity, and attitude of the sensor. Therefore from direct integration, the nine navigation states describing position, velocity, and attitude can be calculated. However, due to the stochastic nature of the process, it's necessary to estimate the state. This is accomplished by modeling the true state, $\mathbf{x}_{true}$, as a combination of the IMU integrated state, $\mathbf{x}_{INS}$, with an error state, $\boldsymbol{\delta}\mathbf{x}$.

$$\mathbf{p}_{true} = \mathbf{p}_{INS} + \boldsymbol{\delta}\mathbf{p} \tag{4.111}$$

$$\mathbf{v}_{true} = \mathbf{v}_{INS} + \boldsymbol{\delta}\mathbf{v} \tag{4.112}$$

$$\boldsymbol{\theta}^n_{true} = \mathbf{C}^n_{\tilde{n}}\left(\boldsymbol{\epsilon}\right)\boldsymbol{\theta}^{\tilde{n}}_{INS} \tag{4.113}$$

where the position, $\mathbf{p}$, is described in an ECEF frame of latitude, longitude, and altitude, L, l, h, the velocity, $\mathbf{v}$, is described in a local level North-East-Down frame, and the attitude, $\boldsymbol{\theta}$ is represented by three angles, θ, ϕ, ψ, is a right-handed coordinate frame centered at the vehicle center of mass with the axes going out the vehicle's front, right-side, and down, respectively. The tilt error, $\boldsymbol{\epsilon}$, describes errors in the estimate of the attitude, given by three angles, ϵ_x, ϵ_y, ϵ_z. The states related to the INS can be aggregated in a single vector as

$$\mathbf{x}_{INS} = [L, \ l, \ h, \ v_n, \ v_e, \ v_d, \ \theta, \ \phi, \ \psi]^T \tag{4.114}$$

and an error state vector can be defined as

$$\delta\mathbf{x} = [\delta L, \ \delta l, \ \delta h, \ \delta v_n, \ \delta v_e, \ \delta v_d, \ \epsilon_x, \ \epsilon_y, \ \epsilon_z]^T \tag{4.115}$$

In Eqn. 4.113, $\mathbf{C}^n_{\tilde{n}}$ is the DCM generated from the tilt angles estimated by the Kalman filter, which corrects the integrated INS attitude.

The EKF estimates the error state as it propagates in time according to the Pinson error model [81]. The Pinson error model defines the continuous-time dynamics

95

equations of the error states in the F_P matrix, described in [81], but adapted here to coincide with the order of the states.

$$\mathbf{F}_P = \begin{pmatrix} \mathbf{F}_{pp} & \mathbf{F}_{vp} & \mathbf{F}_{\epsilon p} \\ \mathbf{F}_{pv} & \mathbf{F}_{vv} & \mathbf{F}_{\epsilon v} \\ \mathbf{F}_{p\epsilon} & \mathbf{F}_{v\epsilon} & \mathbf{F}_{\epsilon\epsilon} \end{pmatrix} \tag{4.116}$$

where the subscripts of the matrix $\mathbf{F}_{p,v,\epsilon}$ denote the position, velocity or tilt error states associated in the matrix multiplication. The matrices of $\mathbf{F}_P$ describing the position error dynamics due to the current states are defined as

$$\mathbf{F}_{pp} = \begin{pmatrix} 0 & 0 & \dfrac{-v_N}{R_E^2} \\ v_E \dfrac{\tan(L)}{R_E \cos(L)} & 0 & -\dfrac{v_E}{R_E^2 \cos(L)} \\ 0 & 0 & 0 \end{pmatrix} \tag{4.117}$$

$$\mathbf{F}_{vp} = \begin{pmatrix} \dfrac{1}{R_E} & 0 & 0 \\ 0 & \dfrac{1}{R_E \cos(L)} & 0 \\ 0 & 0 & -1 \end{pmatrix} \tag{4.118}$$

$$\mathbf{F}_{\epsilon p} = \mathbf{0}_{3\times 3} \tag{4.119}$$

The velocity error dynamics as a function of the current state are defined as

$$
\mathbf{F}_{pv} = \begin{pmatrix}
-v_E \dfrac{2\Omega_E \cos(L) + v_E}{R_E \cos^2(L)} & 0 & \dfrac{v_E^2 \tan(L) - v_N v_D}{R_E^2} \\[2ex]
2\Omega_E(v_N \cos(L) - v_D \sin(L)) + \dfrac{v_N v_E}{R_E \cos^2(L)} & 0 & -v_E \dfrac{v_N \tan(L) + v_D}{R_E^2} \\[2ex]
2\Omega_E v_E \sin(L) & 0 & \dfrac{v_N^2 + v_E^2}{R_E^2}
\end{pmatrix}
$$

$$(4.120)$$

$$
\mathbf{F}_{vv} = \begin{pmatrix}
\dfrac{v_D}{R_E} & -2\dfrac{\Omega_E \sin(L) + v_E \tan(L)}{R_E} & \dfrac{v_N}{R_E} \\[2ex]
2\Omega_E \sin(L) + v_E \dfrac{\tan(L)}{R_E} & \dfrac{v_N \tan(L) + v_D}{R_E} & 2\Omega_E \cos(L) + \dfrac{v_E}{R_E} \\[2ex]
-2\dfrac{v_N}{R_E} & -2\Omega_E \cos_L + \dfrac{v_E}{R_E} & 0
\end{pmatrix}
$$

$$(4.121)$$

$$
\mathbf{F}_{\epsilon v} = \begin{pmatrix}
0 & -f_D & f_E \\
f_D & 0 & -f_N \\
-f_E & f_N & 0
\end{pmatrix}
$$

$$(4.122)$$

97

The final components of $\mathbf{F}_P$ describe the tilt error dynamics as a function of the states, defined as

$$\mathbf{F}_{p\epsilon} = \begin{pmatrix} -\Omega_E \sin(L) & 0 & -\dfrac{v_E}{R_E^2} \\[2ex] 0 & 0 & \dfrac{v_N}{R_E^2} \\[2ex] -\Omega_E \cos(L) - \dfrac{v_E}{R_E \cos^2(L)} & 0 & v_E \dfrac{\tan_L}{R_E^2} \end{pmatrix} \quad (4.123)$$

$$\mathbf{F}_{v\epsilon} = \begin{pmatrix} 0 & \dfrac{1}{R_E} & 0 \\[2ex] -\dfrac{1}{R_E} & 0 & 0 \\[2ex] 0 & \dfrac{-\tan(L)}{R_E} & 0 \end{pmatrix} \quad (4.124)$$

$$\mathbf{F}_{\epsilon\epsilon} = \begin{pmatrix} 0 & -\Omega_E \sin(L) - v_E \dfrac{\tan(L)}{R_E} & \dfrac{v_N}{R_E} \\[2ex] \Omega_E \sin(L) + v_E \dfrac{\tan(L)}{R_E} & 0 & \Omega_E \cos(L) + \dfrac{v_E}{R_E} \\[2ex] -\dfrac{v_N}{R_E} & -\Omega_E \cos(L) - \dfrac{v_E}{R_E} & 0 \end{pmatrix}$$

$$(4.125)$$

Combining Eqns. (4.117)-(4.125) to form Eqn. (4.116) provide a way to calculate the transition of the error state in matrix form.

The altimeter and IMU produce samples with FOGM biases, which can be estimated in the filter. Therefore, the error state vector can be augmented to include random variables that represent the time-correlated biases of the altimeter, and the three axes of accelerometers and gyroscopes.

$$\dot{b}_b = -\frac{1}{\tau_b} b_b \quad (4.126)$$

$$\dot{b}_a = -\frac{1}{\tau_a} b_a \quad (4.127)$$

$$\dot{b}_g = -\frac{1}{\tau_g} b_g \quad (4.128)$$

Therefore, the continuous-time matrices for the altimeter, accelerometers, and gyroscopes time-correlated biases are

$$F_{b_b} = -\frac{1}{\tau_b} \tag{4.129}$$

$$\mathbf{F}_{b_a} = I_{3\times3} \cdot -\frac{1}{\tau_a} \tag{4.130}$$

$$\mathbf{F}_{b_g} = I_{3\times3} \cdot -\frac{1}{\tau_g} \tag{4.131}$$

Augmenting the original error state vector with states that estimate the time-correlated biases, results in a new error state vector of

$$\delta\mathbf{x} = [\delta\mathbf{p}, \ \delta\mathbf{v}, \ \boldsymbol{\epsilon}, \ b_b, \ \mathbf{b}_a, \ \mathbf{b}_g]^T \tag{4.132}$$

Combining Eqns. 4.129-4.131 with $\mathbf{F}_P$, from Eqn. 4.116 results in a single dynamics matrix, $\mathbf{F}$.

$$\mathbf{F} = \begin{pmatrix} \mathbf{F}_P & 0 & 0 & \mathbf{0} & \mathbf{0} \\ 0 & F_{b_b} & 0 & \mathbf{0} & \mathbf{0} \\ 0 & 0 & 0 & \mathbf{F}_{b_a} & \mathbf{0} \\ 0 & 0 & 0 & \mathbf{0} & \mathbf{F}_{b_g} \end{pmatrix} \tag{4.133}$$

From this augmented dynamics matrix, the state transition matrix, $\boldsymbol{\Phi}$ can be found using Eqn. 2.13.

To estimate the change in covariance of the error states, additional information must be known about the system. From this information, the noise, $\mathbf{Q}_d$, that is added to each state, according to Eqn. 2.17, can be determined by building the continuous-time matrix $\mathbf{Q}$, from Eqns. 4.96,4.99,4.101,4.104, and 4.110 with its attendant state

distribution matrix, $\mathbf{G}$.

$$\mathbf{Q} = \begin{pmatrix} \mathbf{C}_n^b q_a \mathbf{I}_{3\times3} \mathbf{C}_n^{b\ T} & \mathbf{0} & \mathbf{0} & \mathbf{0} & \mathbf{0} \\ \mathbf{0} & \mathbf{C}_n^b q_g \mathbf{I}_{3\times3} \mathbf{C}_n^{b\ T} & \mathbf{0} & \mathbf{0} & \mathbf{0} \\ \mathbf{0} & \mathbf{0} & \frac{2\sigma_{b_b}^2}{\tau_{b_b}} & \mathbf{0} & \mathbf{0} \\ \mathbf{0} & \mathbf{0} & \mathbf{0} & \frac{2\sigma_{b_a}^2}{\tau_{b_a}}\mathbf{I}_{3\times3} & \mathbf{0} \\ \mathbf{0} & \mathbf{0} & \mathbf{0} & \mathbf{0} & \frac{2\sigma_{b_g}^2}{\tau_{b_g}}\mathbf{I}_{3\times3} \end{pmatrix} \tag{4.134}$$

$$\mathbf{G} = \begin{pmatrix} \mathbf{0}_{3\times3} & \mathbf{0}_{3\times3} & \mathbf{0}_{3\times3} & \mathbf{0}_{3\times3} \\ \mathbf{I}_{3\times3} & \mathbf{0}_{3\times3} & \mathbf{0}_{3\times3} & \mathbf{0}_{3\times3} \\ \mathbf{0}_{3\times3} & \mathbf{I}_{3\times3} & \mathbf{0}_{3\times3} & \mathbf{0}_{3\times3} \\ \mathbf{0}_{1\times3} & \mathbf{0}_{1\times3} & \mathbf{0}_{1\times3} & \mathbf{0}_{1\times3} \\ \mathbf{0}_{3\times3} & \mathbf{0}_{3\times3} & \mathbf{I}_{3\times3} & \mathbf{0}_{3\times3} \\ \mathbf{0}_{3\times3} & \mathbf{0}_{3\times3} & \mathbf{0}_{3\times3} & \mathbf{I}_{3\times3} \end{pmatrix} \tag{4.135}$$

4.6.2 IMU Performance Verification. With the IMU noise values given in Table 4.2, the IMU model's introduction of noise was compared to the expected growth of IMU error described by the Pinson error model. For each grade of IMU, 100 Monte Carlo simulations were run. The trajectory of the observer was identical between runs, thus the true delta-v and delta-theta values describing the motion are the same. Unique to each run is the noise associated with the IMU's process, namely the time-correlated noise in each dimension of the accelerometers and gyroscopes as well as the random walk noise in each dimension. Statistics of the navigation state error are calculated from the Monte Carlo simulations. The difference between the true trajectory and the trajectories generated from integrating the noisy IMU data

determine the navigation error. Specifically, the errors are calculated as

$$\boldsymbol{\epsilon} \mathbf{p} = \mathbf{p}_{true} - \mathbf{p}_{INS} \tag{4.136}$$

$$\boldsymbol{\epsilon} \mathbf{v} = \mathbf{v}_{true} - \mathbf{v}_{INS} \tag{4.137}$$

$$\mathbf{C}_n^{\tilde{n}} = \left(\mathbf{C}_{b,true}^n \mathbf{C}_{\tilde{n},INS}^b \right)^T \tag{4.138}$$

where $\boldsymbol{\epsilon} \mathbf{p}$ is the 3-dimensional position error, $\boldsymbol{\epsilon} \mathbf{v}$ is the 3-dimensional velocity error, $\mathbf{C}_n^{\tilde{n}}$ is the direction cosine matrix representing the tilt error, which for small angles it the matrix cross of the individual component values, $\times \boldsymbol{\epsilon} \boldsymbol{\theta}$.

The mean and standard deviation of the errors are calculated as

$$\boldsymbol{\mu}_p(t_k) = \frac{\sum_{i=1}^{N_{runs}} \boldsymbol{\epsilon} \mathbf{p}_i(t_k)}{N_{runs}} \tag{4.139}$$

$$\boldsymbol{\mu}_v(t_k) = \frac{\sum_{i=1}^{N_{runs}} \boldsymbol{\epsilon} \mathbf{v}_i(t_k)}{N_{runs}} \tag{4.140}$$

$$\boldsymbol{\mu}_\theta(t_k) = \frac{\sum_{i=1}^{N_{runs}} \boldsymbol{\epsilon} \boldsymbol{\theta}_i(t_k)}{N_{runs}} \tag{4.141}$$

$$\boldsymbol{\sigma}_p(t_k) = \left(\frac{\sum_{i=1}^{N_{runs}} \left(\boldsymbol{\epsilon} \mathbf{p}_i(t_k) - \boldsymbol{\mu}_p(t_k) \right)^2}{N_{runs}} \right)^{\frac{1}{2}} \tag{4.142}$$

$$\boldsymbol{\sigma}_v(t_k) = \left(\frac{\sum_{i=1}^{N_{runs}} \left(\boldsymbol{\epsilon} \mathbf{v}_i(t_k) - \boldsymbol{\mu}_v(t_k) \right)^2}{N_{runs}} \right)^{\frac{1}{2}} \tag{4.143}$$

$$\boldsymbol{\sigma} \boldsymbol{\theta}(t_k) = \left(\frac{\sum_{i=1}^{N_{runs}} \left(\boldsymbol{\epsilon} \boldsymbol{\theta}_i(t_k) - \boldsymbol{\mu} \boldsymbol{\theta}(t_k) \right)^2}{N_{runs}} \right)^{\frac{1}{2}} \tag{4.144}$$

Each Monte Carlo simulation has unique errors, but the statistics of all the runs should coincide with the estimated IMU error growth determined by the Pinson error model. The system is modeled such that the errors are zero-mean. In the absence of measurements, the errors of the position, velocity, and tilt error states should grow according to the noise parameters set by the IMU grade specifications. Figure 4.5 shows the horizontal position error results of the Monte Carlo simulations using a tactical grade IMU over a time period of 7 minutes compared to the Kalman filter estimated

Figure 4.5:   North and East dimension of position error and position error covariance as calculated from simulated IMU noise (red) and Kalman filter position error state propagation (blue) for Tactical grade IMU with a single realization from simulated data (green).

error for the same grade of IMU and time period. The solid blue line represents the Kalman filter estimated error mean. Since no measurements were received by the filter through the simulation, the error remained zero throughout. However, the co-variance of the error estimate grows as a function of time for the same reason that no measurements of the state are made and hence the uncertainty of the state estimate grows. The green line in each plot shows the position error from a single Monte Carlo run. The solid red line represents the mean error of the Monte Carlo simulations. It maintains a zero-mean value with slight variations. As the number of runs approaches infinity the mean value of the error approaches zero, so any deviations from zero are a product of the finite number of simulations. The dotted red line represents the ensemble standard deviation of the Monte Carlo simulations. As the figure shows, the ensemble standard deviation matches the estimated standard deviation closely. Differences between the ensemble and estimated standard deviation can also be at-tributed to the finite number of Monte Carlo runs, but not entirely. Another factor that contributes to the Monte Carlo results that doesn't affect the Kalman filter is

Figure 4.6: North and East dimension of velocity error and velocity error covariance as calculated from simulated IMU noise (red) and Kalman filter position error state propagation (blue) for Tactical grade IMU with a single realization from simulated data (green).

the method of integration of the IMU data. The navigation state calculated directly from the IMU is sensitive to the system's knowledge of the local vertical. Without any measurements of the state to correct for errors in vertical position, velocity, and tilt, the drift will not match exactly the estimated error. Often this effect is compensated for by providing the integration method an "aiding altitude", which helps align the local vertical dimensions. In simulation results presented in the following chapters the system uses a barometric altimeter to measure the vertical dimension thus providing the compensation necessary for proper IMU data integration.

From the same Monte Carlo simulations of the tactical grade IMU, Figure 4.6 shows the velocity error results. The ensemble mean and standard deviation of the velocity error states (red solid and dotted lines, respectively) coincide with the same statistics of the estimated velocity error (blue solid and dotted lines). Additionally, a single Monte Carlo velocity error result is shown in green. Figures 4.5 and 4.6 together demonstrate that the Kalman filter as implemented appropriately estimates
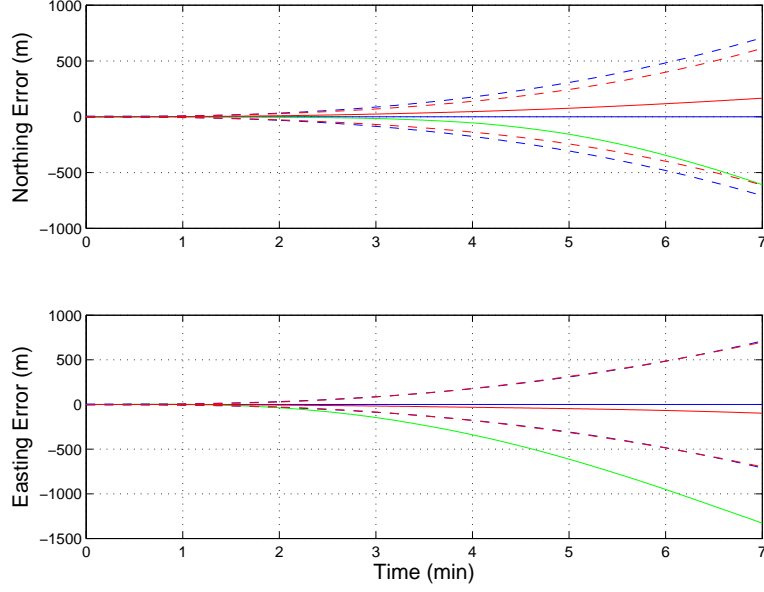
103
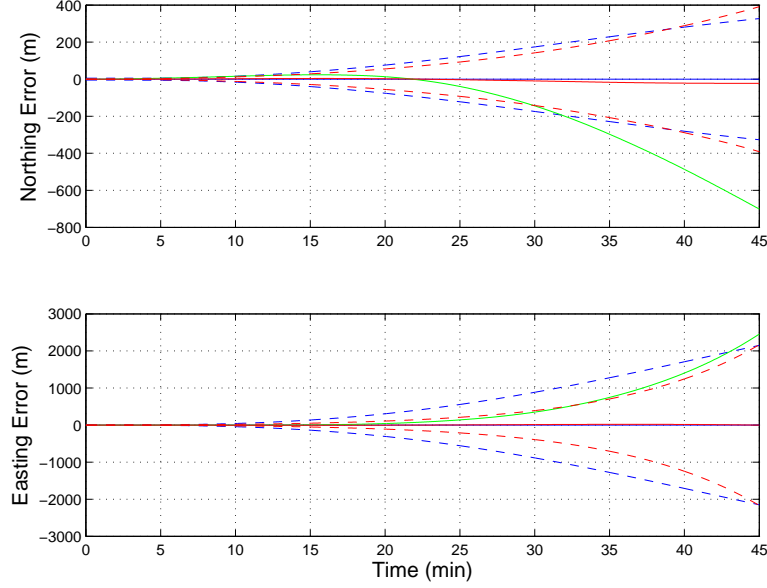
Figure 4.7: North and East dimension of position error and position error covariance as calculated from simulated IMU noise (red) and Kalman filter position error state propagation (blue) for Navigation grade IMU with a single realization from simulated data (green).

the navigation error state using a Pinson error model for a tactical grade IMU. This result allows full system simulations, which will include random noise in star tracker measurements and satellite ephemerides, to rely on the Pinson error model for IMU error modeling rather than using large numbers of Monte Carlo runs to specifically address IMU noise bias.

Figure 4.7 shows the position error results of 100 simulations using a navigation grade IMU over a time period of 45 minutes. Figure 4.8 shows the velocity error results of 100 simulations using a navigation grade IMU over a time period of 45 minutes.

4.6.3 Measurement Model Description. At discrete times, the filter models measurements of the state. There are three measurement types modeled in this work: GPS latitude and longitude position measurements, barometric altimeter altitude measurements, and angles measured from the observer to the imaged satellite. Though a GPS position is not considered an element of this system, a GPS position
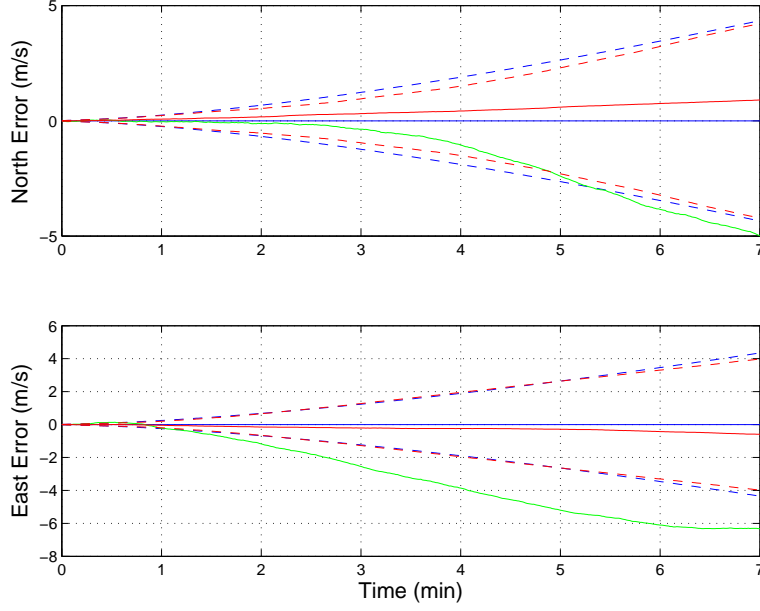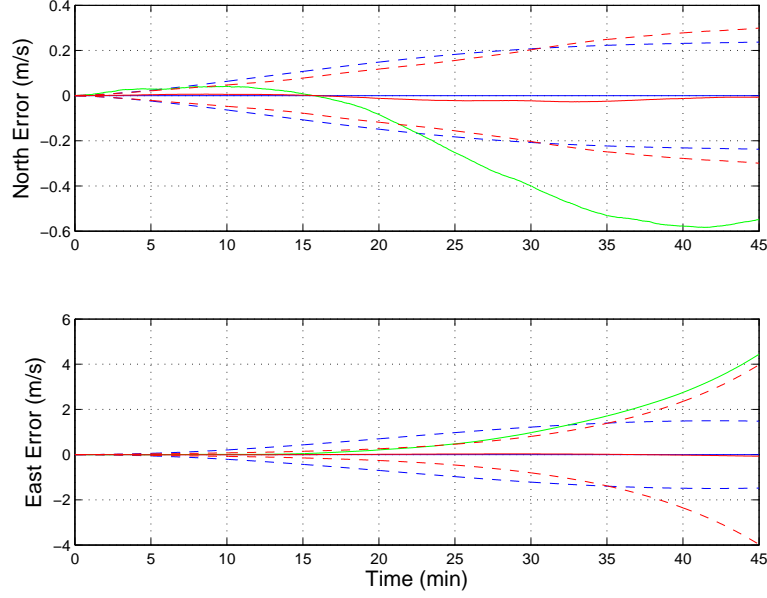
Figure 4.8: North and East dimension of velocity error and velocity error covariance as calculated from simulated IMU noise (red) and Kalman filter position error state propagation (blue) for Navigation grade IMU with a single realization from simulated data (green).

measurement was modeled to simulate a scenario where the observer had an initial position estimate from GPS, but loses the signal and therefore must rely solely on the altimeter and star tracker measurements. The GPS and altimeter measurements are linear combinations of the states described by

$$\mathbf{z}_{gps} = [L, \; l]^T + \boldsymbol{\nu}_{gps} \tag{4.145}$$

$$z_b = h + b_b + \nu_b \tag{4.146}$$

where $\boldsymbol{\nu}_{gps}$ and ν_b are zero-mean AWGN with

$$E[\boldsymbol{\nu}_{gps}(t_i)\boldsymbol{\nu}_{gps}(t_j)] = \sigma_{gps}^2\mathbf{I} \tag{4.147}$$

and

$$E[\nu_b(t_i)\nu_b(t_j)] = \sigma_b^2 \tag{4.148}$$

105

Looking at these equations suitable to Eqn. 2.23, the state mapping to measurement space is

$$\mathbf{H}_{gps} = \begin{bmatrix} 1 & 0 & \mathbf{0}_{1\times14} \\ 0 & 1 & \mathbf{0}_{1\times14} \end{bmatrix} \tag{4.149}$$

$$\mathbf{H}_b = \begin{bmatrix} 0 & 0 & 1 & \mathbf{0}_{1\times6} & 1 & \mathbf{0}_{1\times6} \end{bmatrix} \tag{4.150}$$

The star tracker angle measures are calculated as the right ascension, α_t, and declination, δ_t, in an Earth-centered topological frame given by [84]

$$\mathbf{z}_{st} = \begin{bmatrix} \alpha_t \\ \delta_t \end{bmatrix} + \boldsymbol{\nu}_{st} = \begin{bmatrix} \sin^{-1}\left(\dfrac{p_y}{\sqrt{p_x^2 + p_y^2}}\right) \\ \sin^{-1}\left(\dfrac{p_z}{\rho}\right) \end{bmatrix} + \boldsymbol{\nu}_{st} \tag{4.151}$$

where $\boldsymbol{\nu}_{st}$ is zero-mean AWGN with

$$E[\boldsymbol{\nu}_{st}(t_i)\boldsymbol{\nu}_{st}(t_j)] = \sigma_{st}^2 \mathbf{I} \tag{4.152}$$

and $\mathbf{p}$ is the vector from the observer to the satellite with components $[p_x,\ p_y,\ p_z]$, and ρ is the slant range [84].

$$\mathbf{p} = \mathbf{r}_{sat} - \mathbf{r}_{obs} \tag{4.153}$$

$$\rho = ||\mathbf{p}|| \tag{4.154}$$

These angles are non-linear functions of the state. In order to implement Eqn. 2.21, the angle measure must be linearized around the current state and is

calculated as

$$\mathbf{H}_{st} = \left.\left[\begin{array}{cccc} \dfrac{\partial \alpha_t}{\partial L} & \dfrac{\partial \alpha_t}{\partial l} & \dfrac{\partial \alpha_t}{\partial h} & \mathbf{0}_{1\times 14} \\[2ex] \dfrac{\partial \delta_t}{\partial L} & \dfrac{\partial \delta_t}{\partial l} & \dfrac{\partial \delta_t}{\partial h} & \mathbf{0}_{1\times 14} \end{array} \right]\right|_{\mathbf{x}=\hat{\mathbf{x}}} \tag{4.155}$$

$$\tag{4.156}$$

where the derivation of these equations are found in Appendix A.

These three types of measurements describe both the true system measurements and their relationship to the navigation states. However, those measurements are discrete random processes described generically by Eqn. 2.18. Hence, to model these measurements, their measurement uncertainty is needed.

The GPS, altimeter, and star tracker measurements are modeled with zero-mean AWGN with standard deviations of σ_{gps}, σ_b, and σ_{st}, respectively. The noise in the GPS measures of the latitude and longitude are modeled as uncorrelated. Similarly, the measurement noise in the angle measurements of the star tracker are modeled as uncorrelated. Combined the random variables represent the measurement noise covariance.

$$E[\boldsymbol{\nu}(t_i)\boldsymbol{\nu}(t_j)] = \left[\begin{array}{ccc} \sigma_{gps}^2 \mathbf{I} & 0 & \mathbf{0} \\[1ex] \mathbf{0} & \sigma_b^2 & 0 \\[1ex] \mathbf{0} & 0 & \sigma_{st}^2 \mathbf{I} \end{array} \right] \delta_{ij} \tag{4.157}$$

In this model, the GPS and altimeter measurement random walk noise standard deviation values are set to a 5 m [94] and 0.5 m [78], respectively. The altimeter time-correlated noise used a time constant of 200 for a standard deviation of 20 m. The star tracker measurement standard deviation is calculated as a function of the sensor's specifications, defined in Eqn. 4.76 and shown in Table 4.1.

With the model described using these dynamics and measurement equations, the EKF as described in Section 2.6.1 can be implemented.

4.7   *Summary*

This chapter developed the model to evaluate the performance of integrating a star tracker with an IMU. It developed the ephemeris error simulation, the description of the IMU dynamics, the derivation of star tracker measurement uncertainty and the EKF model components, such as the linearized measurement equations in state space. The next chapter describes the use of this model to evaluate the navigation performance of the integrated model.

V. Simulation Results

$\mathbf{A}$FTER defining the system components and their models, a description of the navigation performance of this system is desired. Among the many variables which contribute to that performance, this model can be used to identify key performance parameters of the system. This chapter implements the model described in Chapter IV and provides the results of simulating the model under several conditions. Those conditions are varied within a range of values and then compared to determine operational curves on which performance can be estimated.

5.1 System Performance Evaluation

Within the several models (satellite orbit, IMU, and star tracker) there are many parameters which contribute to the system's performance. Within the satellite ephemeris simulation, the performance is evaluated as a function of the change in orbital height and ephemeris error. The system performance is also evaluated as a function of the IMU quality. When considering the star tracker, the 3 types of star trackers introduced in Chapter IV are used to compare performance as well as the specific star tracker parameters of FOV, number of pixels in the focal plane array, and limiting magnitude. Additionally, the rate at which the star tracker measurements are made is varied and compared for system performance.

Unless stated explicitly, the default parameters are those reflected in Table 5.1. In most comparisons, both the LEO and MEO cases are considered as well as are both a tactical and navigation grade IMU.

5.1.1 Sample Estimation Results. The Kalman filter estimates the error state of the position, velocity, and tilt in addition to the time-correlated biases of the accelerometers, gyroscopes, and barometric altimeter. The ability of the filter to estimate the true error of the simulation is determined by Eqns 4.136-4.138. A sample position error plot is shown in Figure 5.1. The vertical dimension of the position is aided by both a star tracker measurement and an altimeter measurement. Therefore,

109

Table 5.1:   Default System Parameters for Simulation

Parameter	Value
Orbital Height (LEO)	1000 km
Orbital Height (MEO)	20000 km
Orbital Error	10 m
Number of Satellites Observed (simul)	1
Satellites Observation Method	Highest Elevation
IMU Grade	Navigation
Observation Rate	1 Hz
FOV	10 deg
SNR	2
PSF	0.0787 pixels
N_{pix}	1024 pixels

both the vertical error and the error uncertainty have a different level of accuracy than the horizontal position error. In this scenario, the vertical dimension is bounded by the 20 m altimeter error uncertainty standard deviation, though some variation does occur due to star tracker measurements. In the horizonal position dimensions the error uncertainty increases and decreases throughout the scenario. Each dimension also varies differently. The variability of the uncertainty is due to varying observability of the states by the star tracker measurements. As the system stops measuring one satellite and begins another, the uncertainty decreases abruptly due to the change in geometry between the satellite previously observed and newly observed. Depending on the elevations and azimuths of the satellites with respect to the observer, the North and East position of the observer will be measured differently. This occurs 8 times in this scenario, the times of which are most easily seen in the vertical dimension at approximately $4, 13, 21, 29, 34, 37, 45,$ and 55 minutes into the scenario. Variations of the horizontal position uncertainty that occur between those discrete times are due to changing geometry of the satellite and observer and thus changing observability of the observer's position with a star tracker measurement.

Similarly, the velocity state grows and decreases with the same timing as the position states. Figure 5.2 depicts the velocity estimate error for the same simulation. The timing of the changes in uncertainty is the same, and since the velocity is the

110

Figure 5.1:   Sample System Position Error. An observer's position error is estimated using observations of LEO satellites at 1 Hz over a period of 60 minutes.

derivative of the position, the shape of the three directions of the velocity error follows the shape of the respective three directions of the position error.

The simulation does not integrate the star tracker measurements with an attitude update in the EKF. However, just as an update to the position will lead to corrections in the estimate of the velocity, the tilt error will also be adjusted to account for the updated position. The uncertainty will grow with minor variations due to the effects of the position update reflected through propagation of the state uncertainty, which relates the position error states to the tilt error states using the state transition matrix. Figure 5.3 shows the error in the tilt estimates throughout the simulation for the same run as the position and velocity results previously shown. Note that the tilt error uncertainty in the down direction grows continually because the star tracker measurements give very little information regarding the vertical dimension.

The position, velocity, and tilt error states, combined with the INS solution, describe the navigation solution of the system. The model uses additional states to describe the effects of component time-correlated biases in the accelerometers, gyroscopes, and altimeter. In verifying that the filter appropriately accounts for the

111
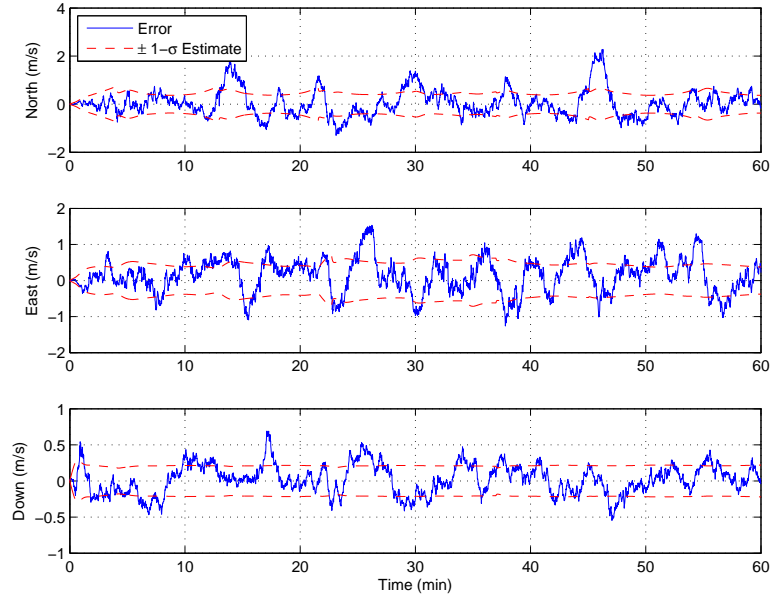
Figure 5.2:   Sample System Velocity Error. An observer's velocity error is estimated using observations of LEO satellites at 1 Hz over a period of 60 minutes. Observability of the position error state improves the velocity error estimate.
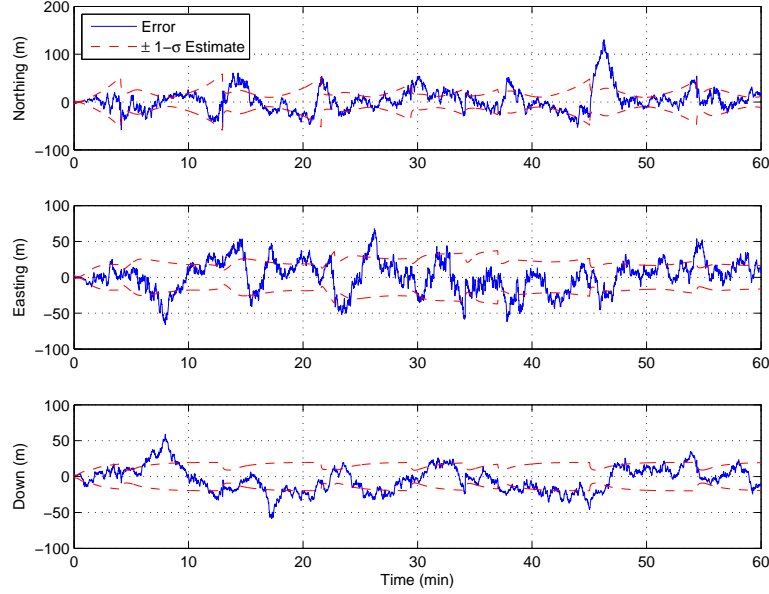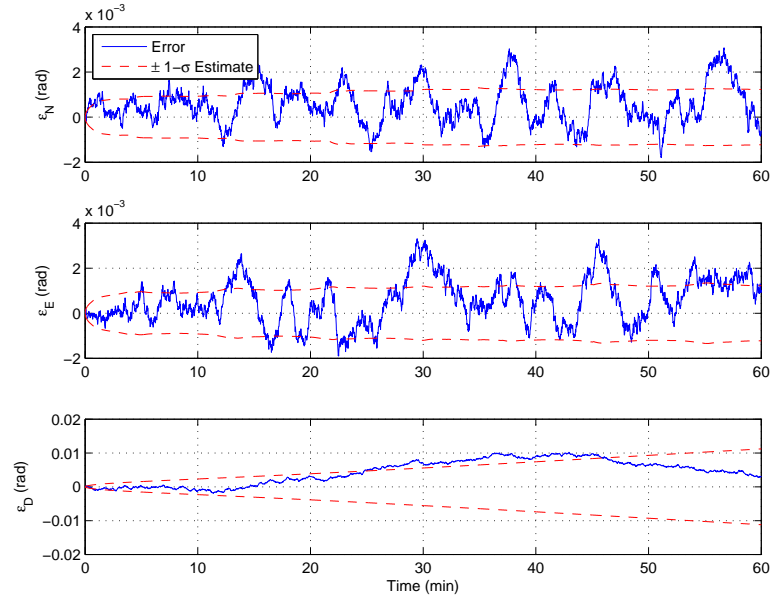

Figure 5.3:   Sample System Tilt Error. An observer's tilt error is estimated using observations of LEO satellites at 1 Hz over a period of 60 minutes. Observability of the position error state improves the tilt error estimate in the North and East direction.
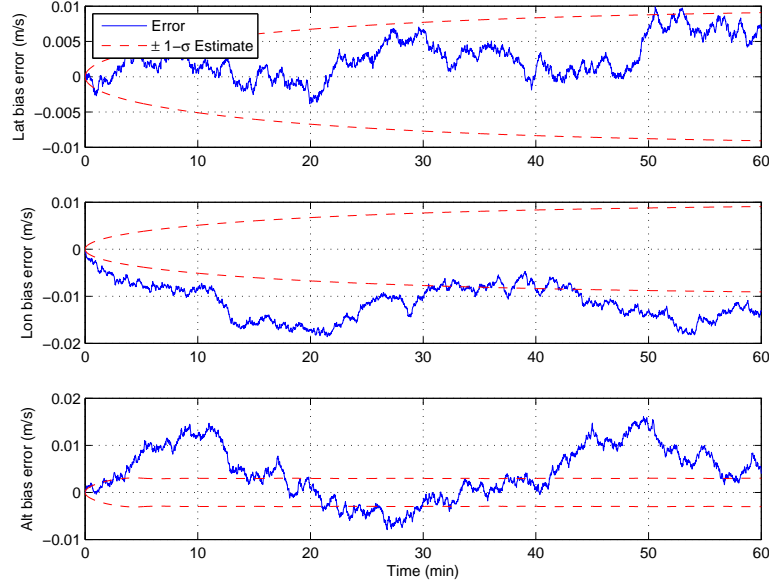
Figure 5.4:   Sample System Accelerometer Time-Correlated Bias Error

system biases, the bias state errors are evaluated as well. First, the accelerometer time-correlated bias state estimates in each dimension are subtracted from their respective simulated accelerometer time-correlated biases, which represent the true bias values. Figure 5.4 shows the accelerometer time-correlated bias error for the same scenario as the previous samples. The bias error in the direction of latitude seems to follow the statistical bounds described by the standard deviation. However, in the direction of longitude, the bias error may be within 2 standard deviations of the mean, but the bias error does not appear zero-mean. As we evaluate the gyroscope bias error in Figure 5.5, the bias in the longitudinal direction appeared non-zero as well, which could cause the accelerometer bias error to be biased.

Figure 5.5 shows the gyroscope time-correlated bias error for the sample simulation. When looking at the gyroscope time-correlated bias errors, the errors in the horizontal dimensions have grown to and maintain values of $2-$ to $3-\sigma$. Because these represent rotations about the horizontal axes, the vertical accelerometer time-correlated bias error also experiences similar growth as previously shown. The vertical
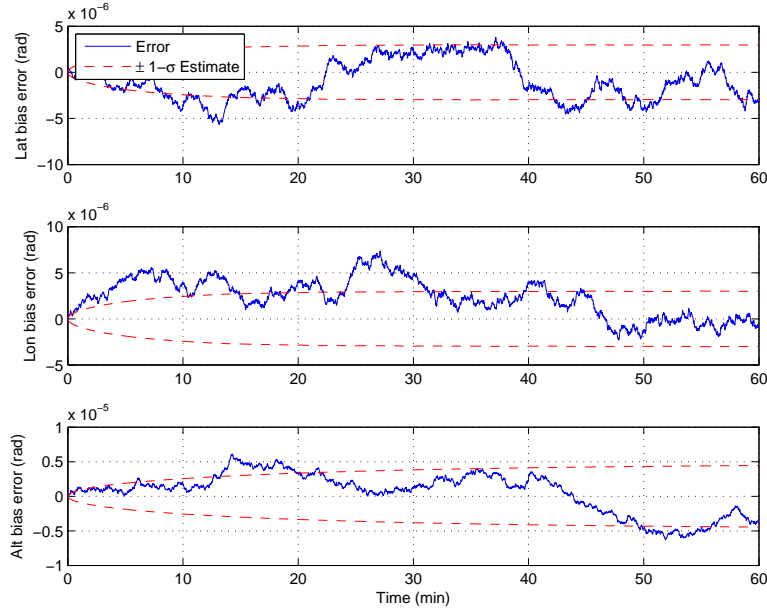
Figure 5.5:   Sample System Gyroscope Time-Correlated Bias Error

dimension gyroscope time-correlated bias error maintains a value within the expected uncertainty.

The barometric altimeter also contains a time-correlated bias, which the system models. The estimated altimeter time-correlated bias values are subtracted from the simulated 'true' altimeter time-correlated bias values to define the estimate error. Figure 5.6 shows the same simulation's altimeter time-correlated bias error. The blue line shows the error value that stays within the uncertainty of the state, shown by the dotted red line. The shape of the uncertainty as it changes in time is similar to that of the vertical position error, because the uncertainty in the time-correlated bias is affected by additional information given of the vertical state. In this case, the star tracker, external to and independent of the altimeter, measures the altitude. This additional information decreases the overall uncertainty of the vertical error state, which in turn improves the filter's ability to estimate the altimeter time-correlated bias. The decrease of the altimeter time-correlated bias uncertainty describes that improvemenft.
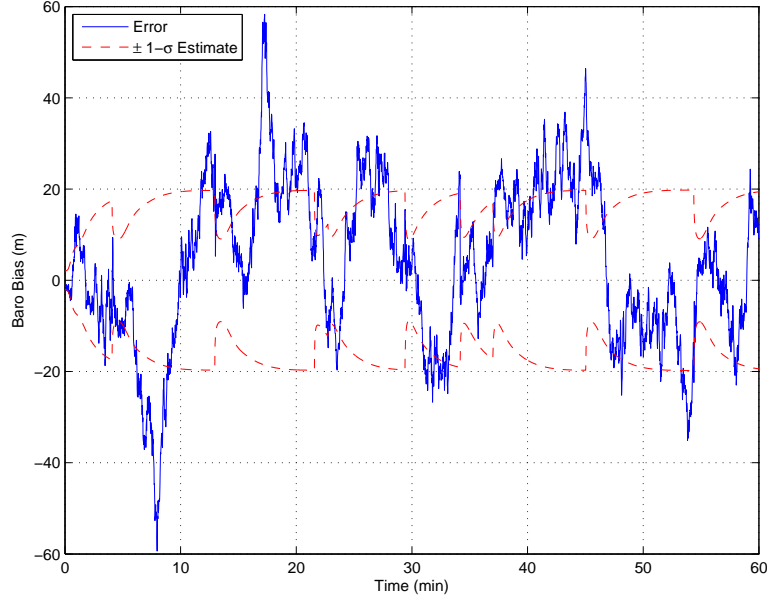
Figure 5.6:   Sample System Altimeter Time-Correlated Bias Error

5.1.2   Performance Metric.   Eqns 4.136-4.138 give a time-sequenced error result of the estimate, but not a good metric for comparison of one simulation to another. A metric to capture the contribution of the star tracker measurements to the navigation performance is a horizontal 2-dimensional distance error. The vertical dimension is not used because the it is additionally aided by the barometric altimeter and is already modeled to be within a certain distance. The root sum square (rss) of the horizontal distance is

$$\epsilon p_{\mathrm{rss}}(t_k) = \sqrt{\epsilon p_N^2(t_k) + \epsilon p_E^2(t_k)} \tag{5.1}$$

Figure 5.7 shows the time sequence of the horizontal distance error from the same data shown in Figure 5.1. This plot shows the sum of the squared error at each time step during the simulation. The rss error is always positive and describes the horizontal distance from a zero error value of the resulting filter error. This rss error results in a time-sequence of distance error metrics, which can be further reduced by addressing the time component. Though the system changes in the simulation (satellite and observer locations, actual measurements made, etc.) the system parameters stay

115
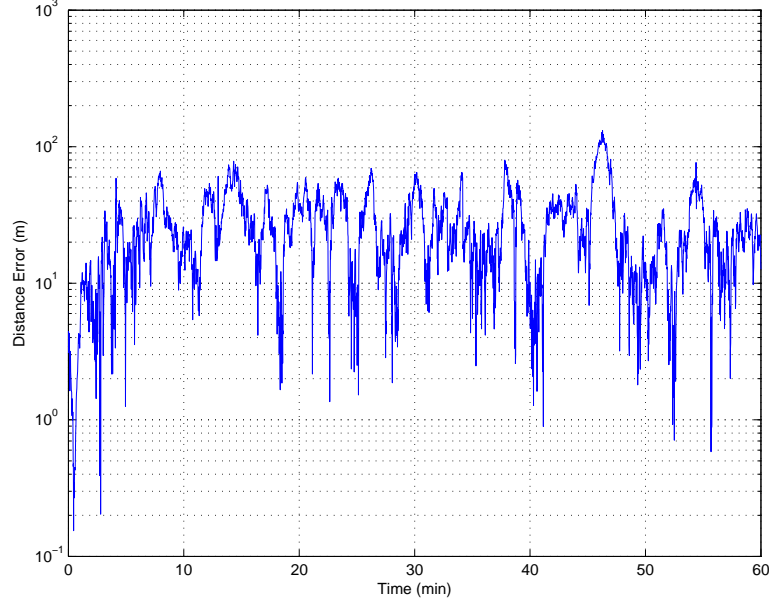
Figure 5.7:   Sample System RSS Error

the same. The time component of the rss error can be accounted for by calculating the cumulative distribution function (CDF) of the rss error. Since the system uses GPS measurements for the first 30 seconds, those error values are not used. As the filter transitions from having GPS measurement to not having them, there is some adjustment time for the state's uncertainty matrix lose the information from GPS measurements contained in the filter estimate as it propagates in time. Therefore, the error values for the 30 seconds after the system "loses" GPS are not used. This time to begin evaluating the system performance is denoted t_0. The CDF, $F(\cdot)$, is calculated from this system as

$$F(\epsilon p_{\mathrm{rss}}) = \frac{N_{\mathrm{valid}}}{N_{\mathrm{results}}} \tag{5.2}$$

where N_{results} is the total number of recorded errors between the final simulation time and t_0 and N_{valid} describes the number of recorded errors over the same time period whose rss error is less than a specified value. Figure 5.8 shows the CDF of the previously shown rss results. What the CDF calculates is the percent of time that the position rss error is below the specified value. When comparing results between

116
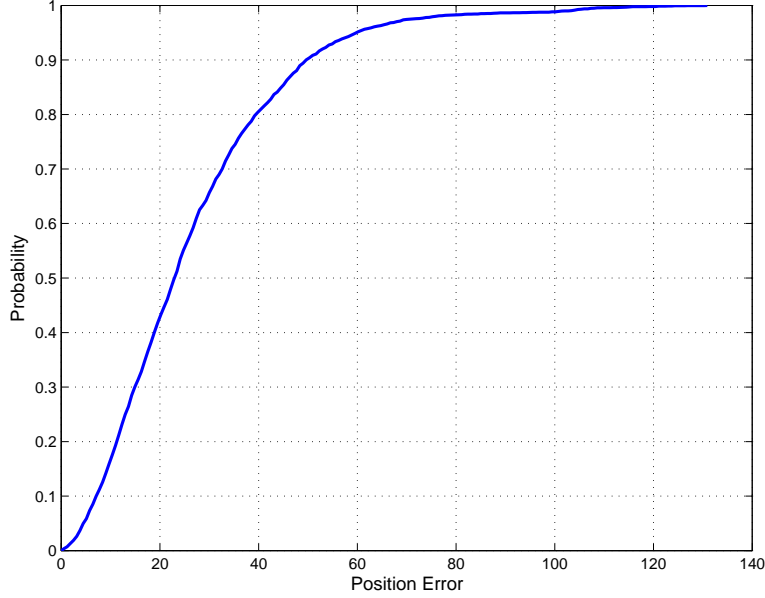
Figure 5.8:   Sample System RSS Error CDF

different simulation parameters, distributions that are further to the left and the top of the plot have less position error, while those to the right and bottom of the plot have more position error. Rather than compare the full distributions a few points of interest can be identified to represent the spread. In performance results presented later in this chapter the CDFs will not be shown fully, but will be represented by an error bar, where the lowest value of the bar is determined by the 0.1 probability value and the highest value is determined by the 0.9 probability value. Additionally, the median value or the 0.5 probability is denoted on the error bar as a point, as shown in Figure 5.9. This description of the performance error derivation is useful when comparing the results of multiple simulations where a parameter of interest has changed the scenario. The rest of this section describes the performance trends calculated by the system with respect to changes in IMU grade, orbital height of observed satellites, star tracker angular accuracy, star tracker update rate, differential site distance from observer, ephemeris error, and satellite selection algorithm.

   5.1.3 IMU Grade Performance.   The system performs as a function of the IMU grade. The tactical grade IMU has larger noise strength values than the
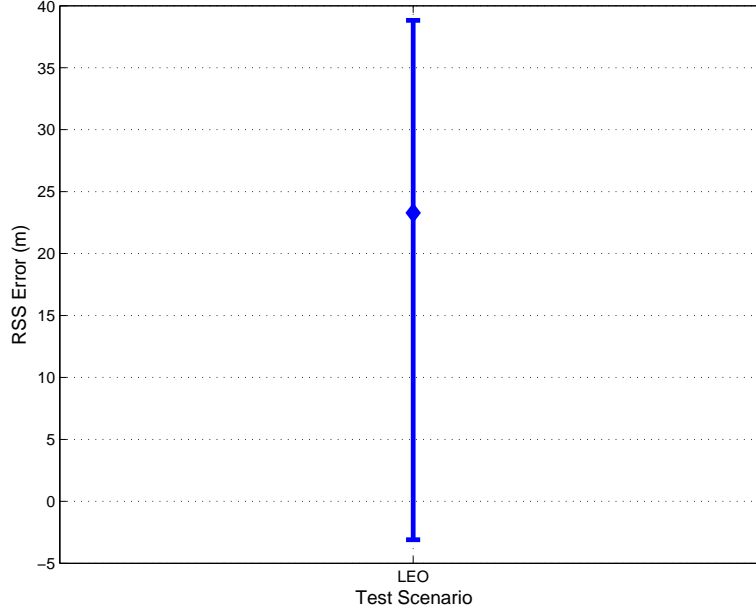
Figure 5.9:   Sample System RSS Performance Errorbar

navigation grade, hence the error in the system due to the IMU, or drift, will be larger for the tactical over the same time intervals. It was shown in Figures 4.5-4.8, how without any measurements to correct for that drift, the two IMU types have continued error growth but at different rates. As the simulation introduces measurements of the navigation state, the drift will be corrected according to the amount of residual in the measurement and the Kalman gain factor of the filter. Because the tactical grade IMU introduces more noise in the system it will have larger errors in position over the same time period or the same amount of position error in a shorter time period than the navigation grade IMU.

The system is simulated using the nominal parameters described in Table 5.1 while varying the IMU grades during different runs. Figure 5.10 depicts the impact of the tactical and navigation IMU grades on the overall system navigation performance. In both orbital height cases depicted, the effect of the IMU grade on the performance is generally as expected. Using the same observation rate of 1 Hz the tactical grade IMU will drift more over that time period than a navigation grade IMU, hence the overall error should be greater. In both the LEO and MEO cases the navigation
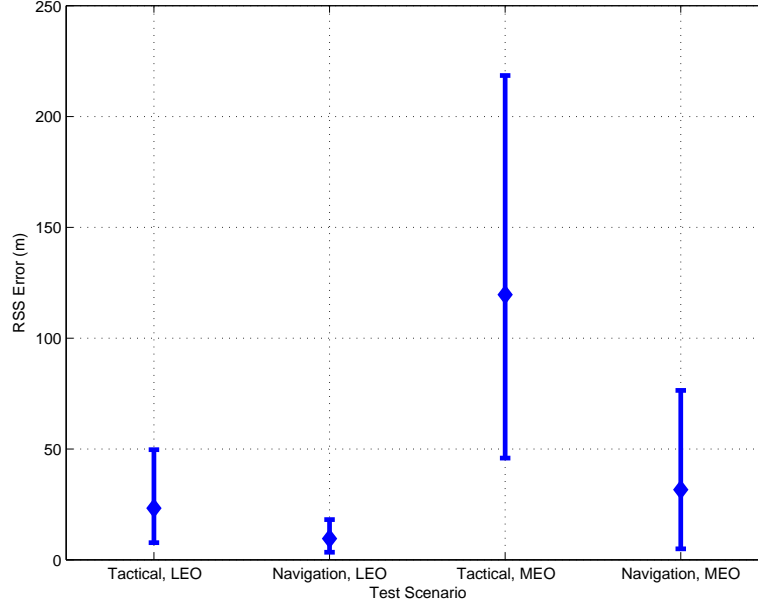
Figure 5.10:   Comparison of Performance Using Tactical and Navigation IMUs

grade IMU has less rss error than the tactical grade. In the specific cases presented in Figure 5.10, the navigation grade IMU reduces the rss error by approximately 50% observing either LEO or MEO satellites.

5.1.4 Satellite Orbit Height.   When comparing the effects of the satellite component of the system, there are two parameters to take into account. The first parameter is the orbital height of the satellites and the second parameter is the ephemeris error. The orbital height parameter affects the filter's distribution of the measurement to the state, specifically changing the **H** matrix and subsequently the Kalman gain, **K**. As the orbital height increases from LEO at 1000 km to MEO at 20000 km or to GEO at 38000 km, the weight of the measurement in the position states is inversely proportional to the slant range (see Eqn. A.14). Therefore, though in simulation the position of the satellite can be known to the same accuracy between orbital heights, but the information available to the states from star tracker measurements decreases with distance from the observer. This affect is logical in that the a star tracker has a finite angle accuracy. The star tracker angle accuracy as it projects along the line of sight away from the star tracker grows to observe a larger physical space. There-
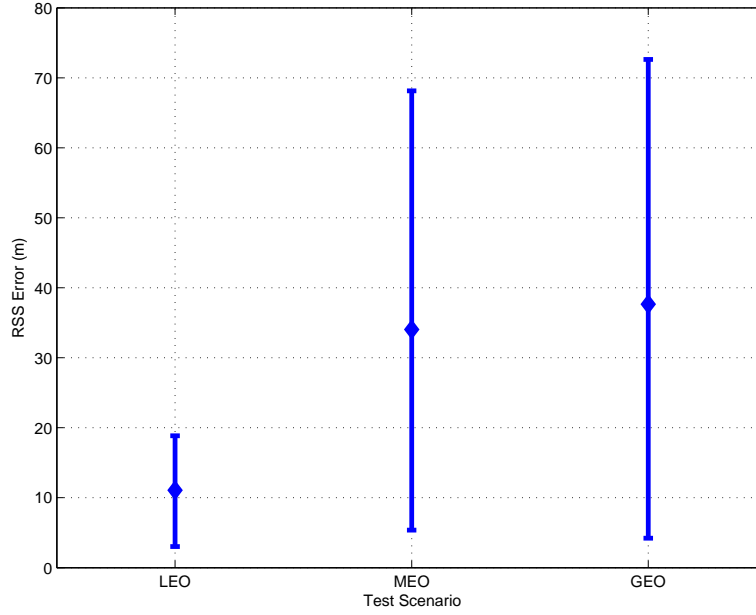
Figure 5.11:   Comparison of Performance Using LEO, MEO, and GEO Satellites

fore, the star tracker will observe a larger region of space at higher altitudes with less ability to distinguish absolute position within that region of the observed object. The additional uncertainty of the observed angle will decrease the amount of information used to improve the navigation position. This becomes evident when looking at Figure 5.11. Geometrically, the space observed over the field of view of the star tracker grows linearly with the distance of the slant range of the observed object from the observer. Hence, it's expected that with the same star tracker angle accuracy the system performance error will decrease directly proportional to the distance to the observed satellite. For example, the MEO satellite orbits at 20000 km should result in a navigation performance of approximately 20/35 of the performance using satellite orbits of 35786 km. Similarly, the comparison of the GEO to LEO performance should be a ratio of approximately 1/35. Figure 5.11 depicts the described trend. This doesn't strictly hold true because the ratio is dependent on the slant range to the objects rather than their orbiting altitudes. The variability of the slant range of objects at a GEO orbit is small compared to the variability of the slant range of LEO objects.

5.1.5 Star Tracker Accuracy Performance.   Besides the IMU and orbital parameters, the system is sensitive to the parameters of the star tracker. The specifications of the star tracker lead to the accuracy of the measurement as described in Section 4.3. In simulation, three different types of star trackers were compared to coincide with the work described in Chapter III. The parameters of each are shown in Table 5.2. The values shown are a subsample of those described in Table 3.3, in order to highlight those parameters that are modeled in the angular uncertainty of the star tracker.

Table 5.2:   Description of Star Tracker Specifications for Simulation

Parameter	Typical Value	Advanced Value	Future Value	Unit	Symbol
Detector					
Aperture Diameter	10	10	10	cm	d_{ap}
Field of View	10	10	10	deg	θ_{FOV}
Number of FPA Pixels	1024	2048	4096	pixels	N_{FPA}
Size of Pixels	13.5	10	10	micron	d_{pixel}
SNR	2	2	2	none	SNR
Derived					
Pixel Resolution	35	17.6	8.8	arcsec	$IFOV$
Focal Length	79	117	235	mm	f
Airy Disk Radius	0.53	1.12	4.44	micron	r_{airy}
Airy Disk Radius	0.079	0.22	0.89	pixel	n_{airy}
Measurement Accuracy	5.153	2.577	1.288	arcsec	σ_{st}

Note that the parameters stated in Table 5.2 do not include the photometric aspects of the observed signal. The amount of signal flux observed changes the signal-to-noise ratio of the measurement, which flux is variable with the star tracker specifications as well as the position of the satellite. In order to constrain the parameter space for simulation the signal-to-noise ratio was set to 2.

The "Typical" star tracker represents a sensor that could be purchased from a vendor as a state of the art system. The "Advanced" star tracker represents a sensor that with little development from vendors could be built in the near future. The

121

"Future" star tracker represents a sensor that would require substantial investment by a developer to build and may not be available in the market for several years. Major distinctions between these three types of star trackers are the size of the focal planes, both in number of pixels along each axis and in the size of the detector elements. The detectors are also distinct in that they have center wavelengths that operate in the visible, 550 nm, near-IR, 780 nm, and mid-wave IR, 1550 nm, for the Typical, Advanced, and Future types, respectively. Those distinctions in physical properties affect the derived parameters of the system, such as the pixel resolution, size of the Airy disk, and measurement accuracy.

Figure 5.12 shows the navigation performance as the angle measurement accuracy changes. Table 5.2 denotes that between each star tracker type is an improvement in angle accuracy of a factor of 2, i.e. the accuracy of the Advanced type is twice as good as the Typical type and the Future type is twice as good as the Advanced type. Hence in each progression, half as much noise is expected in the star tracker measurements or similarly the measurement information is weighted twice as much in the Kalman filter. These changes should be reflected in the overall navigation solution, and Figure 5.12 shows that from Typical to Advanced to Future types, the performance does improve. They also approximately decrease by a factor of 2.

5.1.5.1 *Angle Measurement Update Rate.* A parameter of the star tracker that is not explicitly stated in the specifications is the time interval between measurements, or the update rate using angle measurements. Assuming that a satellite is visible at any given time allows for comparison of the impact of measurement time interval on the navigation performance. In the scenarios tested here, the standard test case was changed such that the star tracker measurements occurred at intervals of 1 sec, 10 sec, 1 min, and 10 min. These intervals represent when one star tracker measurement is received. Being an absolute position update, each individual measurement should result in the same level of accuracy. But between each measurement, the IMU will continue to drift. For longer time intervals between measurements, the
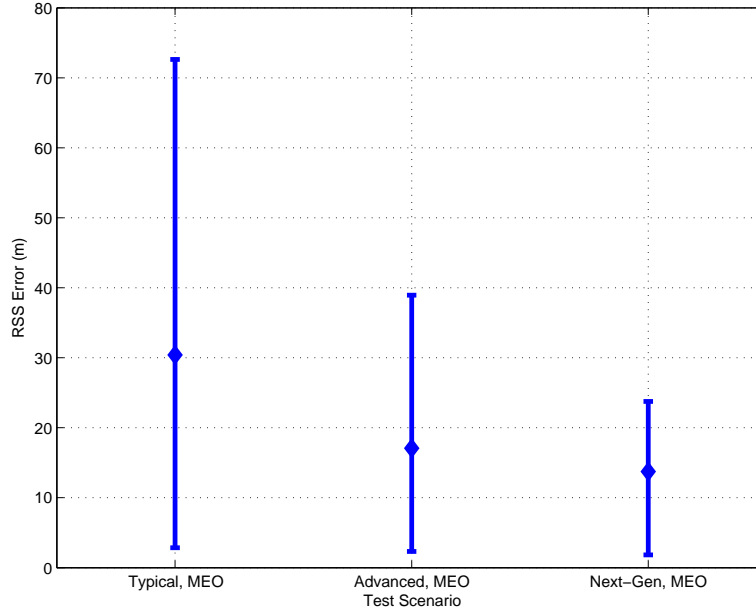
Figure 5.12:   Comparison of Performance Using Typical, Advanced, and Future Star Trackers

drift will be larger making the rss position error larger than shorter time intervals. Figure 5.13 show the horizontal rss error when measuring both LEO and MEO orbits at the stated measurement intervals.

The rss position error increases as the time interval between measurements increases, because there are fewer measurements over the same time period, so the error that is residual from one measurement to the next persists for longer. If many measurements were made simultaneously, then the position error would be greatly reduced, both because the impact of uncorrelated error that exists in each measurement would be diminished and the increased observability of the position by different geometry. However, when one measurement is used the error in that measurement allows some residual position error to propagate until then next measurement. The longer the time interval between measurements the less residual error will be reduced and the longer the residual error persists.

One way to see this result more closely is to compare the covariance of one of the horizontal directions as the interval time changes from 1 sec to 10 min. Figure 5.14

123
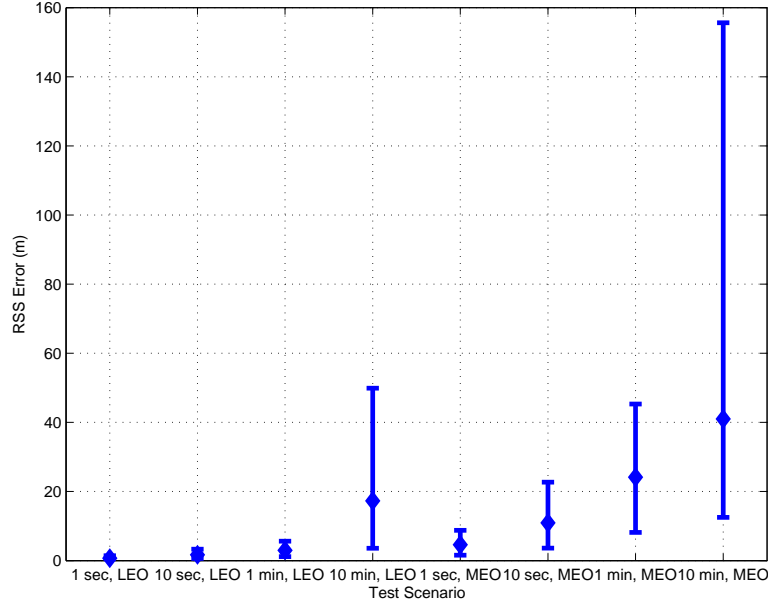
Figure 5.13: Comparison of Performance at Varying Update Intervals, Navigation Grade INS, No Ephemeris Error

shows the $1-\sigma$ values of the covariance for the North direction of the position state when observing a LEO satellite. For the 1, 10, and 60 sec update rates the periodicity of the covariance is due to the geometry of observing the LEO satellites passing overhead. The periodicity of the 10 minute update rate covariance is due only to the covariance decreasing every 10 minutes after receiving a star tracker measurement. Between all the cases, the plot shows that as the interval time increased, the mean of the state covariance increased as well. This is because less information is available regarding the actual position as the measurement interval increases and therefore the uncertainty in that state will increase.

This same result is seen when comparing the position state covariance when observing MEO satellites, as shown in Figure 5.15. Note that the periodicity due to changing satellites does not occur, because at a MEO orbit a satellite is visible for a longer period of time. However, a similar periodicity to that of Figure 5.14 is visible for 10 min update rates due to the availability of a measurement. Because of the greater distance to a satellite in MEO orbit versus LEO orbit, the state covariance is larger. In other words, the same resolution of the star tracker will result in a larger

124
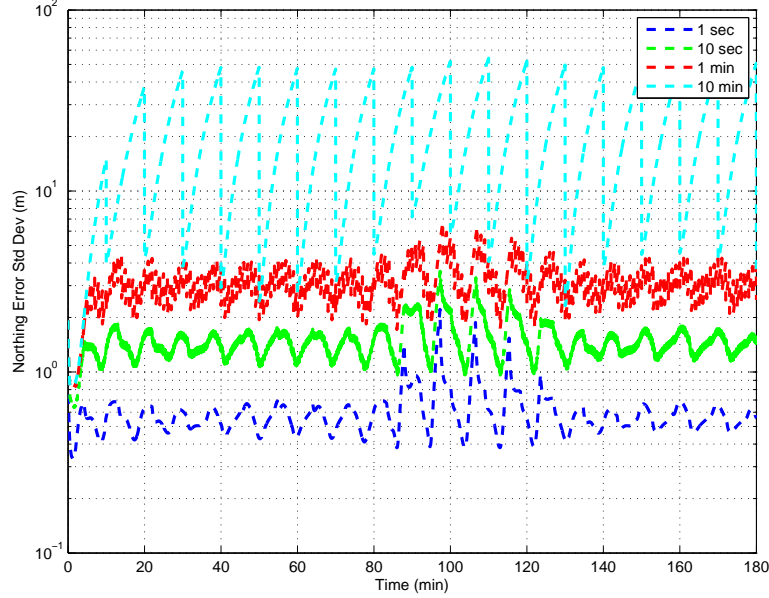
Figure 5.14: Comparison of Position Covariance at Varying Update Intervals Observing a LEO Satellite

covariance, because the area subtended by the measurement is larger at a further distance and hence reflected in the observer's position estimate.

5.1.6 Differential Site Ephemeris Correction. One way to account for the satellite ephemeris error is to estimate the orbital parameters of each observed satellite in the EKF and simultaneously update the ephemeris and observer's position. If the observer's position already has significant error, the updated ephemeris will not be reduced to a level small enough to be of help in further reducing the observer's position error. A better method is to rely on an external measurement of the satellite, which can be used to reduce the ephemeris error directly. In one sense, this is already occurring. The system assumes that the satellite ephemeris was known at some previous time at a known accuracy because some observatory or monitoring station published the ephemeris information. That ephemeris information was used to predict the current satellite position. If a more recent update to that information is available but published in a different manner, the satellite position error could be reduced and a better position estimate of the observer solved.
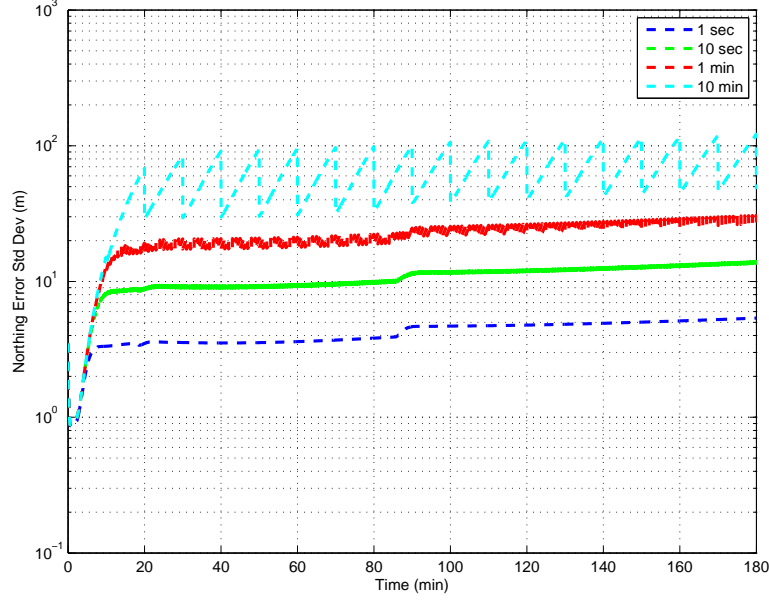
Figure 5.15: Comparison of Position Covariance at Varying Update Intervals Observing a MEO Satellite

In this research, we assumed that a second observing site is available with the same prior published ephemeris information of the satellites and knows its own position exactly. When the second site, offset from the (first) observer's site by some distance, observe's the satellite, it can attribute the residual error in the measurement to satellite position error and not its own position error. This new information about the satellite position error can be provided to the first observer to correct for ephemeris error in its measurement of the satellite. The conversion of the differential site ephemeris error to the observing frame of the first observer requires a transformation of the data. We propose that the satellite ephemeris error measured in the image plane of the differential site observer be projected on the image plane of the first observer. Then, when the first observer measures the satellite using the star tracker, the projected error is directly applied.

First, the differential site's angle residual, $\Delta\theta$, is converted from radians to meters by multiplying it by the slant range, ρ_d to the satellite from the differential

126

site.

$$\boldsymbol{\Delta\theta}_m = \boldsymbol{\Delta\theta} \cdot \rho_d \tag{5.3}$$

where $\boldsymbol{\Delta\theta}_m$ describes the vector in units of meters with components of residual right ascension, $\Delta\alpha_m$, and residual declination, $\Delta\delta_m$.

The reference frame of the differential site image aligns the first dimension, $\mathbf{u}_{1d}$, along the line of sight, the second dimension, $\mathbf{u}_{2d}$, in the direction of right ascension, and the third dimension, $\mathbf{u}_{3d}$, in the direction of declination. The unit vector along the first axis is calculated as

$$\mathbf{u}_{1d} = \frac{\mathbf{p}_d}{\rho_d} \tag{5.4}$$

where $\mathbf{p}_d$ is the Earth-centered vector of the line-of-sight from the differential site to the satellite and ρ_d is the magnitude of that vector. The unit vector along the second axis is the cross of the first dimension with the vector whose only non-zero component is in the negative declination direction.

$$\mathbf{u}_{2\text{temp}} = \mathbf{u}_{1d} \times \begin{pmatrix} 0 & 0 & -1 \end{pmatrix}^T \tag{5.5}$$

$$\mathbf{u}_{2d} = \frac{\mathbf{u}_{2\text{temp}}}{||\mathbf{u}_{2\text{temp}}||} \tag{5.6}$$

The unit vector along the third axis is in the direction of the cross of the first two axes.

$$\mathbf{u}_{3\text{temp}} = \mathbf{u}_{1d} \times \mathbf{u}_{2d} \tag{5.7}$$

$$\mathbf{u}_{3d} = \frac{\mathbf{u}_{3\text{temp}}}{||\mathbf{u}_{3\text{temp}}||} \tag{5.8}$$

These vectors represent the image plane of the differential site measurement reflected in an Earth-centered frame. Then, the angle residual is projected on the plane or-

thogonal to the line of sight to the satellite as

$$\boldsymbol{\Delta}\theta_m^p = \Delta\alpha_m \cdot \mathbf{u}_{2d} + \Delta\delta_m \cdot \mathbf{u}_{3d} \tag{5.9}$$

where the new projected residual angle, $\boldsymbol{\Delta}\theta_m^p$, can be projected onto the observer's image plane. Therefore, the three axes associated with the observer's image plane is calculated similar to that of the differential site in Eqns. 5.4- 5.8. The residual angle is projected onto the unit vectors associated with the observer's right ascension and declination by

$$\boldsymbol{\Delta}\theta_{m,o}^e = \left[\begin{array}{c} \Delta\alpha_{m,o}^e \\ \Delta\delta_{m,o}^e \end{array} \right] = \left[\begin{array}{c} \boldsymbol{\Delta}\theta_m^e \cdot \mathbf{u}_{2o} \\ \boldsymbol{\Delta}\theta_m^e \cdot \mathbf{u}_{3o} \end{array} \right] \tag{5.10}$$

where $\mathbf{u}_{2o}$ and $\mathbf{u}_{3o}$ describe the unit vectors in the plane orthogonal to the line of sight from the observer to the satellite aligned with right ascension and declination, respectively. The final step is to convert the residual values to angular units by

$$\boldsymbol{\Delta}\theta_o = \frac{\boldsymbol{\Delta}\theta_{m,o}^e}{\rho} \tag{5.11}$$

This method converts the measured error in the satellite ephemeris to the measured angle from the estimated observer. To apply it to the observer's measurement of the satellite angle, the converted residual values are added to the estimated satellite angle within the filter. Though some additional error is introduced from the differential site's own measurement error, the correlated error between the two sensors due to satellite ephemeris error can be reduced. The new measurement covariance at the observer, after introducing the corrective factor, is described in Appendix B. If the reference site and the observer are co-located, then the projection between the two images will be the same and the ephemeris error should be mostly removed with only uncorrelated sensor errors remaining in the measurements.
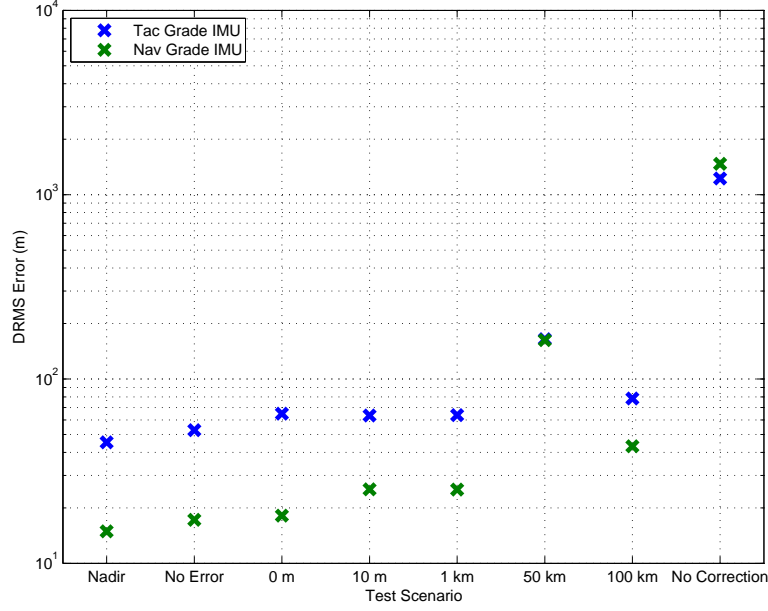
Figure 5.16:   Comparison of Differential Site Baseline Distances When Observing LEO Satellites

Figure 5.16 shows the effects of using a reference site to correct for satellite ephemeris error. The horizontal or 2-dimensional (2-D) distance root mean square (drms) position error is calculated as

$$\epsilon_{\mathrm{drms}} = \sqrt{\frac{\sum\limits_{i=1}^{n}\Big(\epsilon p_N^2(t_i) + \epsilon p_E^2(t_i)\Big)}{n}} \qquad (5.12)$$

where n is the number of time samples in an individual run. This results in a single value for the entire run rather than a time sequence of position errors. Similar to Eqn. (5.2) a CDF is calculated and rather than an error bar as used previously, this figure depicts only the 90% value (or the upper end of the error bar) of the horizontal drms position error for each scenario.

In these scenarios, the satellite ephemeris error simulation parameter was set to 1 km. In this way, random ephemeris errors are generated such that each axis tends to have a standard deviation of 1 km at the end of its availability time window. The system was simulated in 4 different configurations. Between all the cases, the IMU

129

noise, satellite ephemeris error, and measurement noise were identical, where applied. In the first configuration, a satellite was observed directly overhead (at a nadir angle) whose ephemeris was known exactly. Though this is unlikely to occur in the real world, since the satellites will be traveling from horizon to horizon in LEO orbit, the use of this configuration allows for some indication of a lower bound of the horizontal error. Both horizontal directions are equally updated when a satellite is measured at nadir and hence the position error is equally reduced. The leftmost points in the plot show the navigation performance when using this simulated scenario.

The second configuration uses satellites traveling in representative orbits (not at an artificial nadir location), but who still have known ephemerides (i.e., there is no ephemeris error). The points associated with the 'No Error' scenario reflect this configuration. Hence, though the satellites are passing overhead of the observer and some amount of either horizontal direction is being updated with each satellite measurement, the navigation performance is relatively small. Note the vertical axis of the plot is given in decades of values logarithmically.

In the third configuration, the satellite travels in a representative path, the ephemeris error is present, and no reference site provides a correction to the observer's measurement. The rightmost points in the plot show the results of not removing the ephemeris error from the observer's estimate. In this scenario, the accuracy of the navigation solution degrades, increasing the observer's position error by 2 orders of magnitude. With no ability to correct for the ephemeris error, it is passed on to the observer's position estimate.

The fourth configuration applies the reference site measurement of the satellite simultaneous to the observer's measurement of the same satellite. The projected ephemeris error is applied to the observer's measurement prior to calculating the filter update. The reference site was simulated at distances from the observer of 0 m, 10 m, 1 km, 50 km, and 100 km. When the baseline distance between the observer is small, such as when they are 0 m, 10 m , or 1 km apart, the correction greatly reduces

the estimated position error to near the level of if there was no ephemeris error. This is because the two measurements have the same or almost the same view of the satellite. Thus all or most of the angle correction from the reference site will be applied to the observer's measurement. As the distance between the reference site and the observer increases, the observing angles are more different and the measurement correction removes less of the observed ephemeris error, therefore, the horizontal position error increases.

Figure 5.17 shows the same configurations as stated for the LEO cases, but when observing MEO satellites. Because the satellites in LEO orbit are relatively near the Earth's surface, large baseline distances change the amount of ephemeris error the reference site can correct for. In contrast, when observing a satellite at a MEO orbit, even though the baseline distance is large, the change in angle between the two locations when observing the same satellite is very small, and much of the ephemeris error can be removed from any of the modeled reference locations. Additionally, the ratio of the ephemeris error to the satellite's orbital height is much smaller at a MEO orbit than at a LEO orbit, thus the effective angle error is smaller at MEO. These results show that the baseline distance from observer to reference site makes little difference in the estimated position error. The application of the angle correction by a reference site (at any baseline distance) makes a large difference, however, reducing the horizontal position error from approximately 230 m to approximately 90 m in the case of using a navigation grade IMU. A similar reduction of position error occurs for the tactical grade IMU, where 550 m reduces to 220 by applying an angle correction. In both cases, this is a 60% reduction of position error.

5.1.7 *Satellite Selection Algorithm.*   One final aspect of the system which has an effect on system performance, but isn't specific to any single component, is the choice of satellites to observe. Thus far the results have shown the system performance by observing the satellite of highest elevation with respect to the observer at the time of measurement. Observing the highest satellite provides the most information for

131
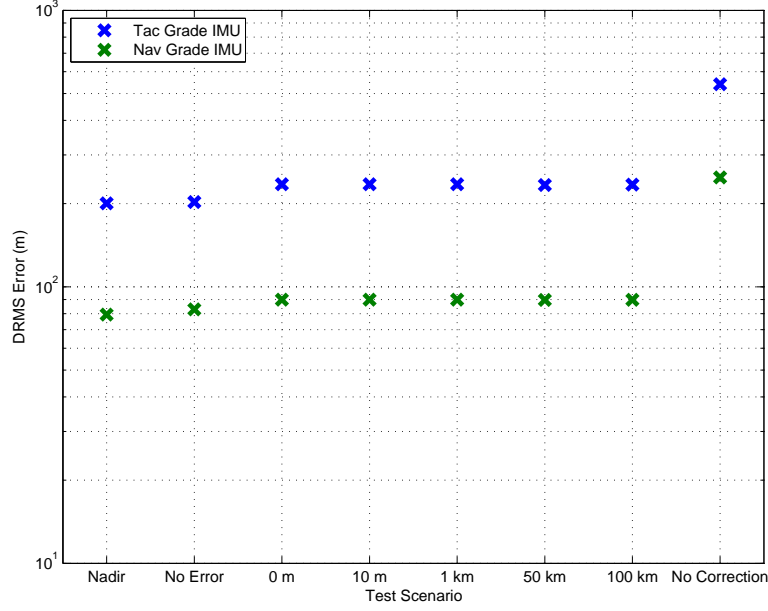
Figure 5.17:   Comparison of Differential Site Baseline Distances When Observing MEO Satellites

both North and East directions of the observer in a single measurement. However, according to the satellite's azimuth with respect to the observer, one of the observer's axes may have more information contributed by the measurement than the other. The algorithm that selects which satellite is observed can be adapted to include multiple simultaneous observations, thereby modeling a sensor that has multiple fields of view or multiple sensors. Another method is to select the satellite of highest elevation then continuously track it until it is below the minimum elevation setting of the star tracker. A third method is to observe the satellite of highest elevation for a specified number of observations, then switch to the next highest elevation satellite, cycling through all visible satellites.

As already stated, the advantage of the first method where the highest elevation satellite at any time is observed, is that the measurement of that satellite will have the most information regarding both North and East directions in the observer's navigation frame. Making a simultaneous measurement of the satellite of next highest elevation will contribute additional information of the observer's state. It is assumed that the noise in the two measurements are uncorrelated and thus when combined

using the EKF, the error will be further reduced. It is also assumed that the two observed satellites will be at different azimuth angles with respect to the observer, such that one measurement will contribute more information in one navigation frame direction than the other. For example, if one satellite is at an azimuth angle of 0 degrees, or directly North, then the noise in the measurement will contribute more in the North direction, and the relative information in the East direction will be larger. For a second satellite at an azimuth angle of 90 degrees, the situation is reversed. The measurement error will contribute more in the East direction than the North and the relative information contribution from the measurement will be larger in the North. This example is explicit when the observer is at the equator and azimuth angles align with an Earth-centered frame of reference. When the observer is not at the equator the principle still holds, but the actual relationship of the information contribution to a specific navigation frame axis will vary. The two leftmost error bars (in Figure 5.18) show the results of using the satellite of highest elevation selection method. As expected, observing two satellites simultaneously improves the navigation performance.

The second method of observing satellites selects the satellite of highest elevation, then continually observes it until it is no longer observable. This is distinctive from the first method in that the observed satellite will have periods of observation where it is not the highest elevation. As such, it's expected that this method will result in a poorer navigation performance than the first. Where the sensor does not have a capability to transition between observable satellites quickly, this may, however, be the applicable method. The increased error of the second method from the first is shown in Figure 5.18. Comparing the results of observing 1 satellite at a time but using methods 1 or 2 show that by using method 1, which satellite is observed will change more often than method 2. Hence, observability of the navigation state will be better both because on average method 1 observations will have higher elevations and because the directional information from the measurements will change more frequently. This latter reason is similar to the improvements seen by simultane-
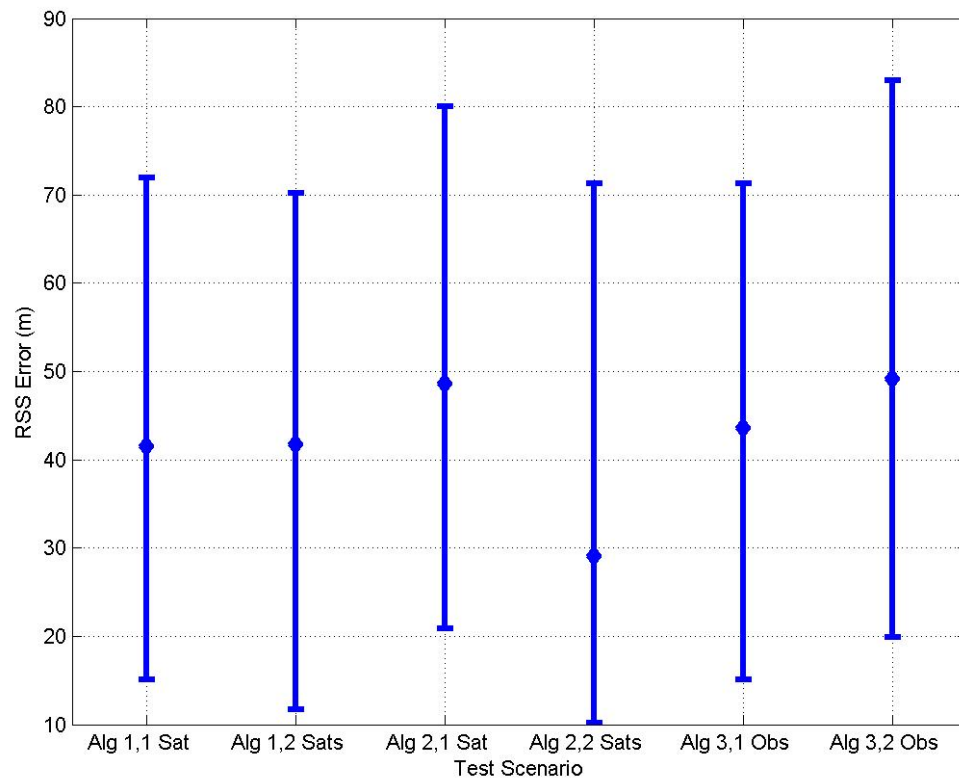
Figure 5.18:   Comparison of Observing Algorithm Performance, No Orbital Errors

ous observations in different azimuth directions, but with some time interval between when the new direction is available. When observing 2 satellite simultaneously, we see improvements from only observing 1 as expected. If observing multiple directions more often seems to reduce position error, a third method may be viable.

The third method assumes that the sensor has a capability to transition between observable satellites, either by slewing the instrument on a gimbal, or by orienting the body of the observer appropriately in a strapdown star tracker case. This third method observes the satellite of highest elevation for a given number of measurements, then switches to the satellite of next highest elevation and continues for all observable satellites. This method is similar, but not identical, to the first method when using multiple simultaneous satellites. In the switching method the observations are sequential rather than simultaneous. Hence, some of the observability in the navigation states is improved by changing azimuth observations, but the observability comes at the expense of larger time intervals between observations of the same satellite. For example, assume one observation has been made to satellite 1. Rather than subsequently observing the same satellite again, the sensor must move to a different angle to switch to a different satellite, make an observation, then switch back to the first. A time interval between the two observations of satellite 1 has been introduced.

In addition, the directional observability comes at the cost of using the highest elevation satellite for all measurements. In an ideal case, where switching between observed satellites doesn't increase the time interval between measurements, observing each satellite once using method 3 should improve the navigation performance compared to observing 1 satellite using method 1. However, the navigation performance will be worse than simultaneous observations of 2 satellites, because of the time intervals between measurements that method 3 incurs. Figure 5.18 shows that when observing 1 satellite, method 3 does have a lower horizontal error than method 1. Observing the same satellite twice before switching, the results of which are shown in the rightmost error bar, seems to have little improvement of the performance. A difference would be seen between observing each satellite once or multiple times if

the system introduced a large time delay between observations due to the need to switch pointing angles. Such delays would cause performance reductions similar to those described in the previous section.

5.2   Summary

This chapter reviewed the results of simulating the system under varying conditions and how those conditions changed the navigation performance results. A sample scenario was presented to show a time-sequence of the errors in position, velocity, and tilt error as well as the error in estimating the time-correlated biases of the accelerometers, gyroscopes, and barometric altimeter.

The system parameters that varied included IMU grade, satellite orbit height, star tracker accuracy, satellite ephemeris error, and the order of satellites observed. As the IMU grade changed from a tactical grade IMU to navigation grade IMU, the rss error decreased when observing satellites in both LEO and MEO orbits.

The results also showed that observing lower orbiting satellites resulted in lower position error than when observing satellites at higher orbits due to the ability to measure a satellite position with the same angular resolution.

When observing satellites at the same orbital height, increasing the angular resolution of the star tracker, thus reducing the noise in satellite measurements, decreases the horizontal position error of the system. In the case of observing MEO satellites, the horizontal position error decreased from 31 m to 17 m median error when the star tracker accuracy improved from 5.1 arcseconds to 2.6 arcseconds. Additional improvement in the position accuracy was shown then the star tracker accuracy improved to 1.3 arcseconds, resulting in a median position error of 13 m.

Increasing the time between star tracker measurements increases the horizontal position error due to persistent residual error in the position estimate and additional IMU drift between measurements.

Introduction of a reference observing site that measured satellite ephemeris error and applied that error to the main observer's estimated satellite measurement significantly reduced the impact of ephemeris error on the navigation solution. When observing MEO satellites, the error was mostly removed. When observing LEO satellites, the effect of the reference site correction terms decreased as the distance from the observer to reference station increased.

Finally, three different algorithms used to select which satellites are observed were compared, and it was shown that higher elevation satellites contributed to lower position error. Depending on the algorithm used, the number of different satellites used either improved or degraded the position accuracy. When observing multiple satellites simultaneously, observing more satellites improved the position estimate accuracy. When sequentially measuring different satellites, switching between two satellites reduced the position estimate accuracy.

This chapter dealt entirely with simulated results. Not all of the configurations described in this chapter can be tested in real-world scenarios. Chapter VI, however, explains how using a representative star tracker system to observe satellites can verify some aspects of the performance model and some additional elements needed when using real imagery.

VI.   Experimental Results

H AVING described several variations of the navigation system in the previous chapter, this chapter compares those simulations to real-world systems. Though full investigation of all the configurations is previously modeled, a comparison can be made between the model's predicted performance and experimental results using a specific set of available ground and orbital systems. This comparison upholds the simulation of the model in a limited set of parameters. For full validation of all the simulated results, multiple sensors and satellite system data would need to be further investigated.

This chapter compares results of the simulated navigation performance with performance based on experimental data. Section 6.1 describes the objectives of the experimental tests and design of the experiment according to components modeled versus real and specific hardware used in collecting data. Section 6.3 presents the data collected on one evening of observations and how it compares to predicted measurements. Section 6.4 presents how the model predicts the overall system to perform using a navigation grade IMU. Finally, section 6.5 presents the navigation performance of the system using the observed satellite data and compares those results to the predicted results.

6.1   Objective of Experimental Tests

The purpose of performing an experiment was to perform a comparison of the results of modeling a star tracker-integrated IMU system with that based on actual images of satellites on a star background. Having collected imagery data of satellites, the star tracker measurement accuracy and the navigation performance as modeled can be confirmed.

The experiment used a simulated IMU and barometric altimeter. The satellites imaged were actual satellites with the navigation performance results presented later in this chapter based on images of GPS satellites. The images were collected using a commercially available telescope and camera provided by the USNO. Observations

Figure 6.1:   Picture of the USNO Celestial Navigation Testbed in Washington, DC

were made on the morning of 13 May, 2014. The experimental setup is described in the next section.

6.1.1 Experimental Design.   The USNO has a facility named the CNTB on location in Washington, DC. As sponsors of this research, they allowed use of the facility as well as access to their professional staff to collect data for this dissertation. The CNTB consists of a telescope and mount, camera, filter wheel, focuser, desktop computer, a GPS receiver, pertinent software, and a domed facility in which shelter it. Figure 6.1 shows the test facility at USNO. Each of these components is described in more detail in the following sections.

Figure 6.2 shows the experimental design of the components. The essential components are captured but the technical interfaces are not detailed though some will be described in later sections.

6.1.2 Telescope, Mount, Test Facility.   The telescope was a PlaneWave Optics 12.5 inch (28 cm). It rested on an Astro Systeme Austria (ASA) Direct Drive
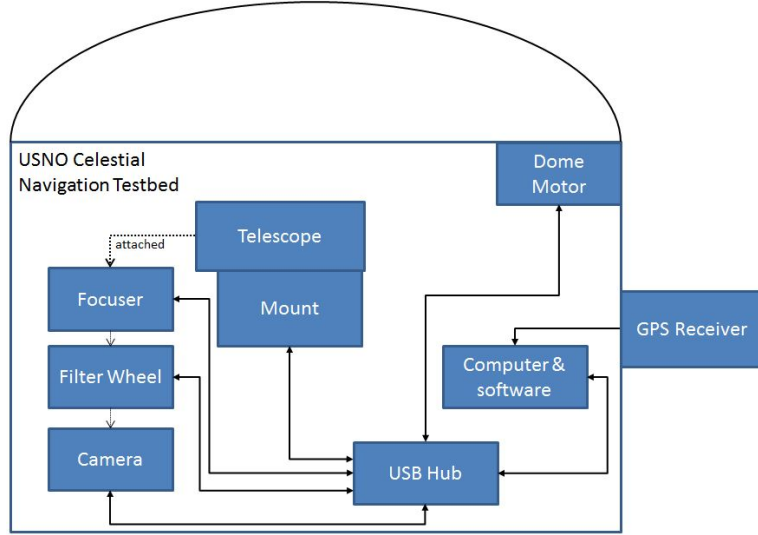
Figure 6.2:   Block Diagram of Experimental Setup at the USNO Navigation Testbed

Mount (DDM)-85 which has the capability to slew 13 degrees per second. Figures 6.3
and 6.4 show the mount and telescope used in this experiment at the CNTB.

6.1.3   Camera.   Figure 6.5 shows the camera used during the experiment. It
is an Apogee CCD camera. It has a target cooling temperature of $-30°$ C, a focal
plane array of 2048×2048 pixels, each with a pitch size of 13.5 microns.

6.1.4   Computer and Software.   The computer was a desktop computer run-
ning Windows 7. The computer platform specifications were not essential since pro-
cessing speed or real-time applications were not under investigation in these tests. Of
more importance are the software programs used to interface and control the compo-
nents. MaximDL [25] software was used to control the camera including setting the
cooling temperature and capturing the images. The telescope mount was controlled
using SkyX [8] software. SkyX showed nominal visible sources to include satellites
given recent Two-Line Element (TLE)s of those satellites. A DomeControl software,
unique to the CNTB, developed specifically for interfacing with the mount control and
the dome motors to control the location of the dome opening such that the telescope
had a clear view of the sky.

140

DDM85 Basic:
Loading capacity 45 kg
(with counterweights 90 kg)

DDM85 Standard:
Loading capacity 65 kg
(with counterweights 130 kg)

DDM85 Premium:
Loading capacity 100 kg
(with counterweights 200 kg)

Used in the field (Basic),
stationary or remotely

USB-Hub, all power and
data connections from
the DEC-axis

DDM85 Premium:
No meridian flip with
client specific pier
necessary

Figure 6.3:   USNO Navigation Testbed Telescope Mount

Figure 6.4:   USNO Navigation Testbed Telescope

Figure 6.5:   USNO Navigation Testbed CCD

6.2   Data Collection

The procedure for collecting satellite angle measurement data consisted of initialization, image capture and storage, and image processing. The result of the data collection is a time sequence of angle measurements of an identified satellite describing the observer-to-satellite angle in right ascension and declination. For ease of use in the EKF the angle is represented in an ECEF reference frame, which is the same as the observer's state estimate.

Specific initialization instructions and procedures for collecting images in the CNTB are listed in Appendix C. The user followed those instructions to calibrate elements of the system and configure the camera control to collect data. The camera controls include integration time, type of filter, number of images collected in sequence, and time interval between images. Another setting used in this collection was an auto-dark feature, which takes a dark (closed-aperture) image prior to opening the aperture to expose the focal plane and automatically subtracts those dark image pixel values from the exposed image, removing the element-wise bias from the data. The images were saved in Flexible Image Transport System (FITS) [67] format by MaximDL. This format recorded the image itself and much of the collection configuration data in the header of the image file. One of those pieces of data is the time at

which the image is taken. MaximDL tags the image with the Universal Time (UT) time based on the computer system time indicating the start time of the exposure.

Once the images are collected, a software tool known as Astromety.net [46] was used to identify the stars in the image and using those stars, produce a binary table of pixel locations of sources in the image and angle values associated with each source. Astrometry.net finds the center of the stars in the image, defines a geometric relationship between four stars, compares that geometric relationship with pre-computed index files based on cataloged star locations, and verifies correct identification by comparing expected star locations from the catalog with additional sources found in the image. Astrometry.net reports [46] to correctly identify stars greater than 99% of the time for images approximately 13×9 arcmin^2 with no false positives and with accuracy to as good as the underpinning catalog files. In this case, the USNO-B1 Catalog [57] was the basis for the index files used for identifying stars. For image sizes smaller than that stated the performance decreases, however, since the system used for the experiment is approximately 35×35 arcmin^2, this tool should perform well.

Once Astrometry.net has processed the images and produced pointing angle information, the data is converted to a Matlab data file for use in the simulation and the pertinent header information, specifically the time of observation is recorded. The final steps in the data collection in preparation for use in the simulation is to convert it into the appropriate frame of reference and correct for refraction. In this case the desired frame of reference was an ECEF frame consistent with the observer's state estimate. Therefore, the angle data, which is given from Astrometry.net in an ECI reference frame, specifically the International Celestial Reference System (ICRS) frame. A Naval Observatory Vector Astrometry Software (NOVAS) [39], [83] routine converted the celestial rectangular coordinates to terrestrial rectangular coordinates by applying earth rotation, polar motion, nutation, and precession. The refraction correction is discussed in Section 6.3.3.

The activities of initialization, collection and data processing occurred prior to running the simulation of the navigation solution. There was no attempt to provide a real-time solution as such a method was outside the scope of this research. Real-time implementation of this navigation algorithm would require additional work and is a possible next-step for this research.

6.3   Model and Experimental Results from 13 May 2014

Using the equipment and the procedures described in the Sections 6.1.1, satellites were observed and recorded on the morning of 13 May 2014. The intent of this specific scenario was to collect data from a single satellite at a MEO orbit over a time period of 30 minutes or more with regular intervals between each image.

6.3.1   Data Collected.   The data was collected for GPS satellite BIIRM-8, which is identified as psuedorandom noise (PRN) 5. This satellite was selected because at the time of collection it had a fairly high elevation with respect to the observer's site and it would be visible for an appropriate period of time. From 0604 to 0618 UT, the camera imaged the satellite. The camera was set to collect with an integration time of 2 seconds every 21 seconds. Over that time period, collected 40 images with a time interval between each image of 21 seconds.

Figure 6.6 shows one of the images collected that evening. The sensor integrated the image over 2 seconds as the mount tracked the satellite. Near the center of the image (inside the circle), the satellite's illumination makes a point Gaussian source. The image of the satellite itself if shown in Figure 6.7. In contrast, the moving telescope over a relatively large integration time creates a streak from each of the stars imaged. In this specific image, 16 stars are easily recognizable and shown as streaks in the image. However, this becomes a problem for the tool used to identify the stars and measure the satellite's pointing angle. Of the 40 images collected on May 13, Astrometry.net identified the sources in 36 images. As Astrometry.net calculated a 'center' of the sources, the location was variable between images.
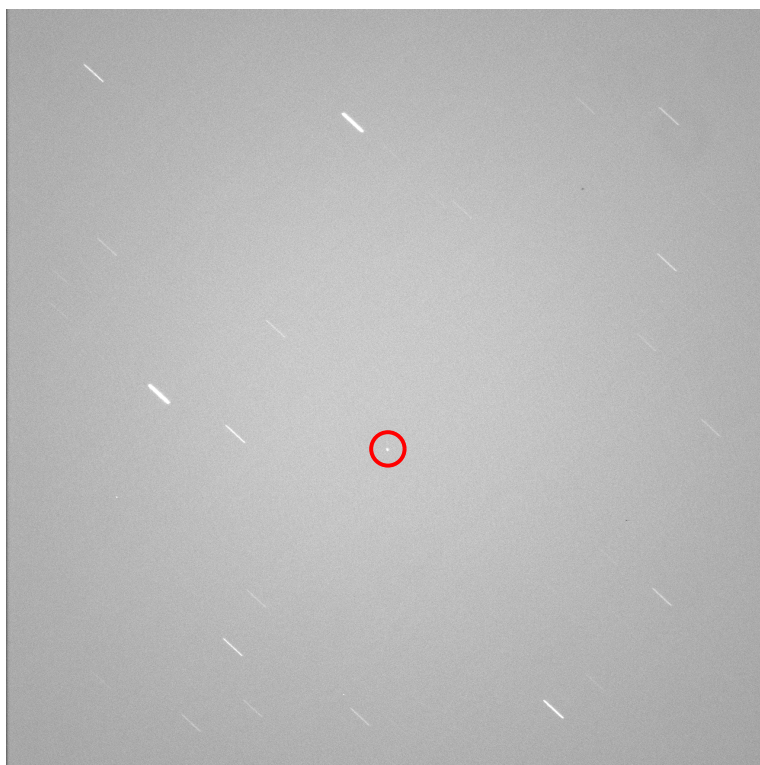
Figure 6.6:   Sample image of a GPS satellite observed at USNO CNTB on 13 May
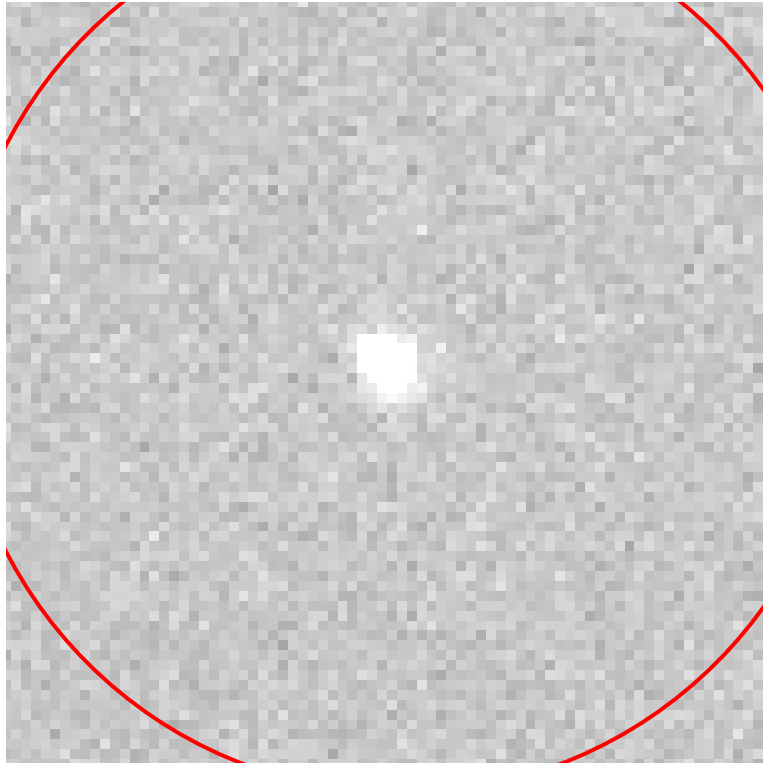2014

Figure 6.7:   Close up Sample image of a GPS satellite observed at USNO CNTB on 13 May 2014

To compensate for Astrometry.net's difficulty centroiding the sources, part of the process was performed by hand. One of the outputs of the Astrometry.net process is a '.corr' file giving the (x, y) pixel location of each source and the corresponding (α, δ) catalog position. By inspecting each image and individually identifying the 'beginning' of each star streak with a 'center' within a few arcseconds, those pixel locations found by hand were matched to the pixel locations in the .corr file, which defined the catalog angle of each star. To measure the satellite angles, two stars were selected to transform the pixel locations from an image frame to right ascension and declination. Then the satellite's pixel locations were interpolated between the star locations. This process calculates nominal satellite angles for each possible star pair in the image. Taking an average of these nominal satellite angles determines the final measured angle.

Figure 6.8 shows the satellite PRN, unique to each satellite, the time of observation, and the images that were correctly processed with Astrometry.net. The blue x's represent the correctly processed images. Generally, there should be a regular measurement time interval of 21 seconds, but note that there are 5 gaps in the sequence. These gaps are denoted in the plot with a red or black circle. The red circles refer to times when images were taken, but Astrometry.net could not identify the stars in those images. The black circle refers to a time delay between when the 20th and 21st images were taken by the system. All the images were of the GPS satellite with PRN 5, describing a continuous tracking of the same object.

6.3.2 Satellite Ephemerides. The GPS satellite positions can be calculated for the day and time of the collected imagery. The global navigation files for the GPS constellation are found at the National Geodetic Survey Continuously Operating Reference Station (CORS) Network website [62]. The global navigation files contain ephemeris information of the satellites that were available on the day of interest. Specifically, the files contain the time of valid ephemeris, the square root of the semi-major axis of the orbit, the eccentricity, the mean anomaly, the inclination, the
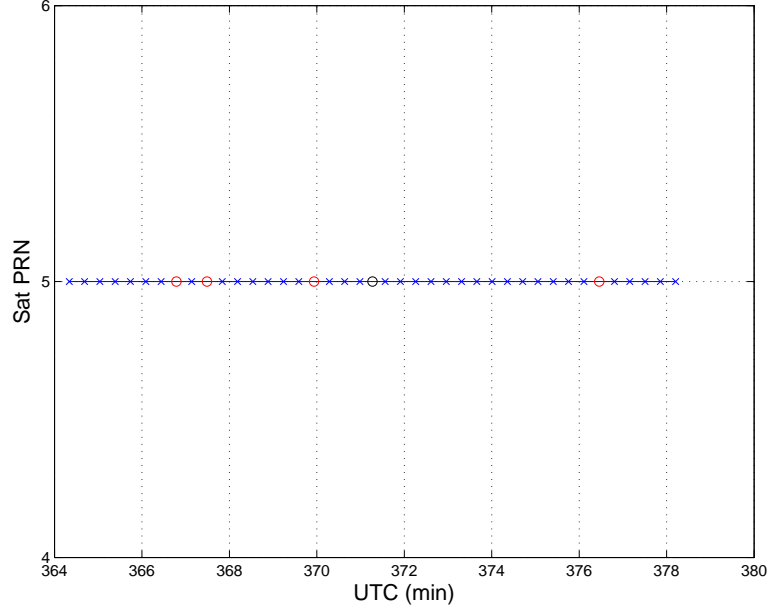
147

Figure 6.8:   Time Sequence of images of a GPS satellite observed at USNO CNTB on 13 May 2014

longitude of the ascending node, the argument of perigee, as well as corrective factors and group delay for the functioning GPS satellites over a time period of 24 hours. The GPS interface specification document, ISS-GPS-200 [64], describes all of the pertinent parameters and how to calculate the satellite position from these parameters.

For the data set of images used from May 13, the satellite positions were calculated as shown in Figure 6.9. This figure shows the position in a polar plot with the angle around the origin being the azimuth of the satellite from the observer and the radius from the origin being the zenith angle of the satellite. As stated earlier, this satellite was chosen for imaging because of it high elevation, which is depicted in this figure, by a low zenith angle, which would give the best observability in both horizontal position dimensions. A later discussion of the calculated angle from a specific observer location will reveal exact values.

6.3.3 Refraction Correction.   The observed angles to the imaged satellite must also be corrected for refraction in order to compare appropriately with the

148
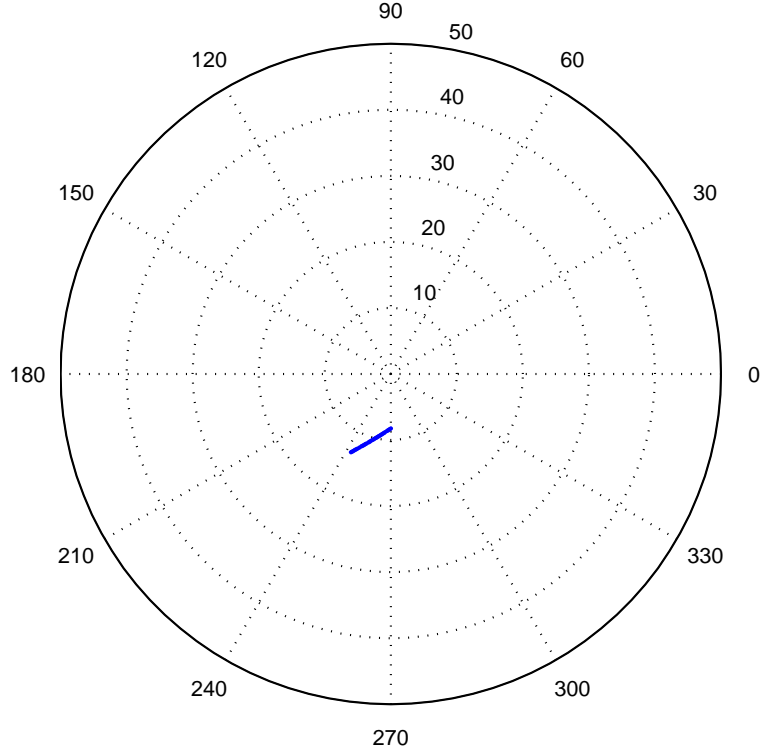
Figure 6.9:   GPS Satellite Position for May 13 Data Set

topocentric pointing angles. The refraction is calculated as [71]

$$R = 1.02 \cot \left(\frac{\phi + 10.3}{\phi + 5.11} \right) \tag{6.1}$$

where ϕ is the true elevation of the observed object from the horizon in degrees. The value R is in units of arcminutes. The refraction as calculated is true for a barometric pressure, P, of 101.0 kPa at a temperature, T, of 10° C. Actual pressure and temperature corrects the refraction by multiplying R by the coefficient c_r defined as [56]

$$c_r = \left(\frac{P}{101} \right) \left(\frac{283}{273 + T} \right) \tag{6.2}$$

$$R' = R c_r \tag{6.3}$$

149

This true atmospheric refraction, R', describes the deviation of the measurement in the direction of the elevation. To apply this refraction amount to the measured angles of right ascension and declination, first the parallactic angle, χ, is calculated which describes the spherical angle between the observer's zenith direction and the Earth pole centered on the observed object. It is calculated as [3]

$$\chi = \sin^{-1}\left(\frac{\cos(L)\sin(HA)}{\sin z_0}\right) \tag{6.4}$$

where L is the observer's latitude in radians, HA is the observer's hour angle in radians, and z_0 is the zenith angle at the object in radians. The zenith angle is found by [3]

$$z_0 = \cos^{-1}\left(\sin(\delta')\sin(L) + \cos(\delta)\cos(L)\cos(HA)\right) \tag{6.5}$$

where δ' is the observed declination of the object in radians.

Having determined the parallactic angle, the refraction can be applied to the observed right ascension, α', and declination, δ', angles as [83]

$$\alpha = \alpha' - R'\sec\delta\sin\chi \tag{6.6}$$

$$\delta = \delta' - R'\cos\chi \tag{6.7}$$

to first order, giving the true right ascension and declination angles.

6.3.4 Comparison of Measurements. Each image was recorded with a time stamp of the collection time represented in UT. The GPS ephemeris information was downloaded from the CORS website in order to calculate the satellite's position at the times of collection, which represent the true satellite positions. One must note that in order to calculate the position of the satellite at the correct time, or the time coincident with the observation, the time provided to the GPS calculation must include an additional 16 seconds, referring to the leap seconds introduced to UT

time since the initiation of GPS. A GPS receiver in the observatory determined the observer's true position. From the true satellite and observer positions, equation 4.151 determines the true pointing angle from the observer the satellite. In order to evaluate measurement accuracy, the calculated pointing angle, represented in polar coordinates of right ascension and declination, was compared to the coordinates measured from the images and astrometric data. Figure 6.10 shows the true right ascension and declination angles in green and the measured angles in blue. Errors will be given later in this section.
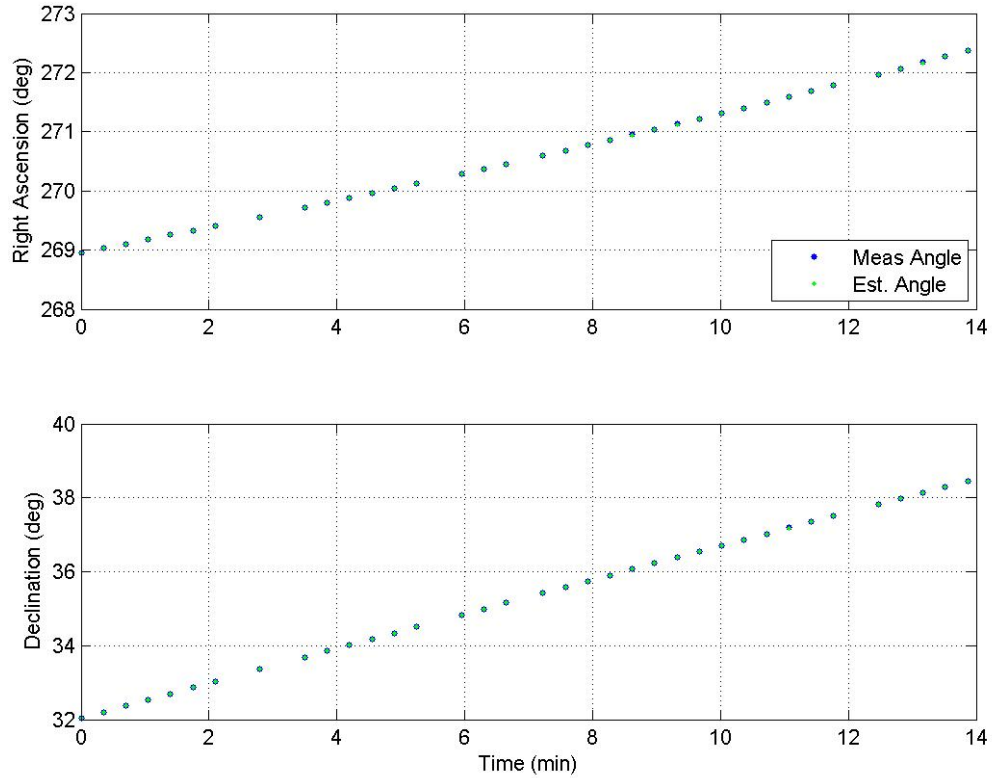

Figure 6.10:   GPS Satellite Expected and Actual Angle Measurements

The top plot shows the trend of the angle increasing in right ascension in time, from approximately 268.8 degrees to 272.3 degrees, indicating motion in a general east-ward direction. Because the observer is known to be stationary, the angle change is due entirely to satellite motion.

The declination increases from approximately 32 degrees to 39 degrees. This angular motion describes a north-ward motion of the satellite. The true and measured declination values agree throughout the observation time. Though the true and measured angles agree as shown by the superposition of the blue and green dots, due to the scale of the plot the accuracy of the measured angles can't be determined with any precision. The difference of the measured and true angles, or angle measurement error, reports the accuracy more precisely. Figure 6.11 shows the difference between the true and measured angles. The top plot shows the error in the right ascension measurement in blue and the bottom plot shows the error in the declination measurement in green. In both plots the mean (solid line) and standard deviation from the mean (dotted line) are shown in red. The error statistics were calculated from the actual error data as shown. To match the model exactly, these errors would have equal statistical means and standard deviations. The measurement errors are modeled as zero-mean with standard deviations calculated as a function of the sensor as discussed in Section 4.3. The model error values are not shown here because they are generated randomly in each simulation, but use the statistics as described. This figure shows that though the standard deviations differ slightly, the angle errors are not zero-mean.

Additionally, it was noted that the errors had a time-varying bias. It was proposed that the image time recorded in the header of the image file, which was based on the hosting computer time could be drifting. To compensate for this drifting clock time, the true observation time, $t_{o}bs$, was modeled as the time of record, t_{rec}, with a linear bias of slope m_t and an initial offset, t_{b0}.

$$t_{obs} = t_{rec} + t_{b0} + m_t \delta t \tag{6.8}$$

where δt describes the time interval between measurements. Finding the time difference between the recorded time and a time that would make the first and last measurement error near zero, an overall time offset can be determined. The time dif-
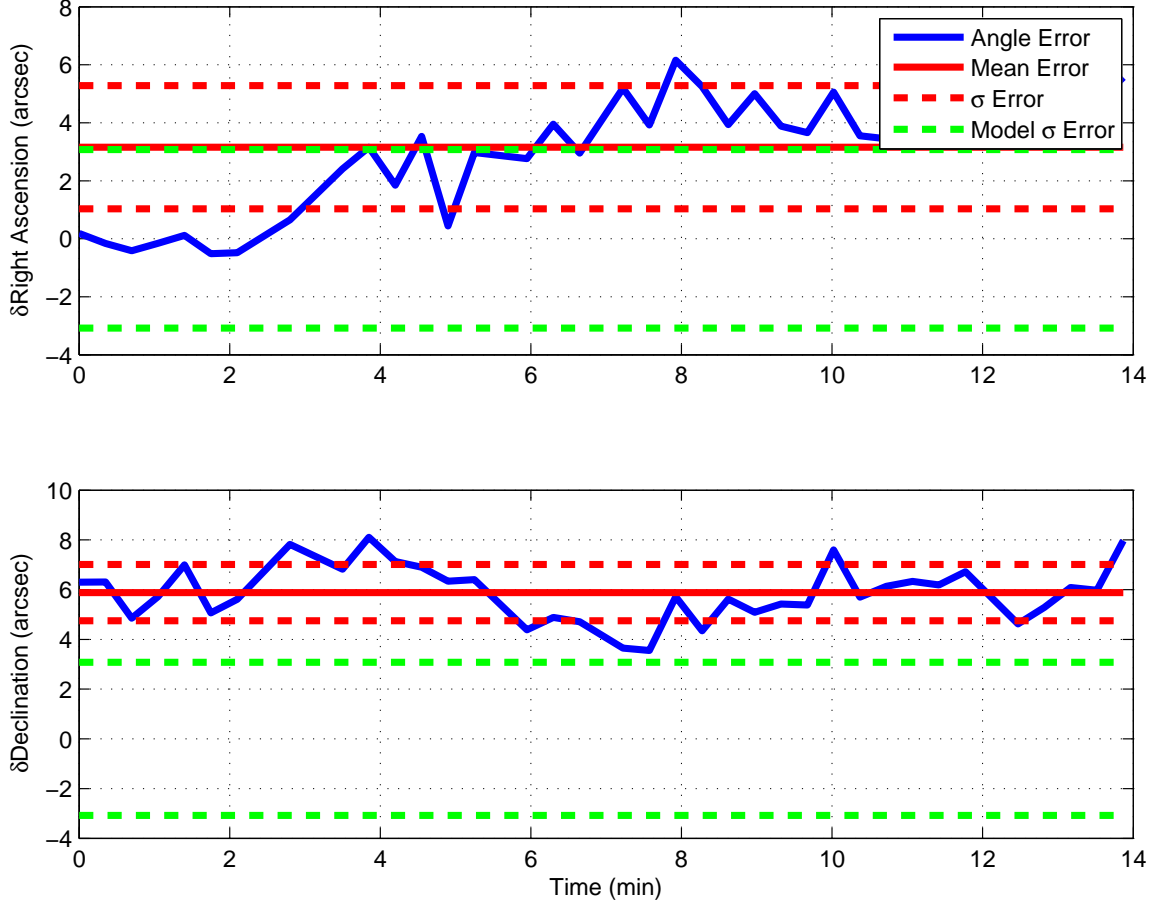
Figure 6.11: Star tracker angle measurement error of observed GPS satellite including bias

ference associated with the first measurement error determines the initial time offset and the change in time difference between the first and last measurement divided by the time interval between them determines the slope of the time drift. In these measurements, the initial offset was 2.17 seconds and the slope was 0.1 ms/s. This slope indicates a system time drift of 8.64 seconds a day, which may be large, but not unreasonable for a computer that has no constant timing synchronization [83]. The slope and initial offset also indicate that the approximately 28 minutes prior to recording the image, the computer clock had been synchronized, which is consistent with the observation procedures on the day of data collection. At the beginning of an observation evening, the computer clock was synchronized with the GPS time reported by

the GPS receiver in the CNTB to within 1 ns. However, this initialization is usually done at the beginning of the observation evening whereas the actual observations are performed minutes to hours later and the computer doesn't continually synchronize. Compensating the time recorded in the image header files with the time offset values results in measurement errors that appear unbiased, as shown in Figure 6.12.
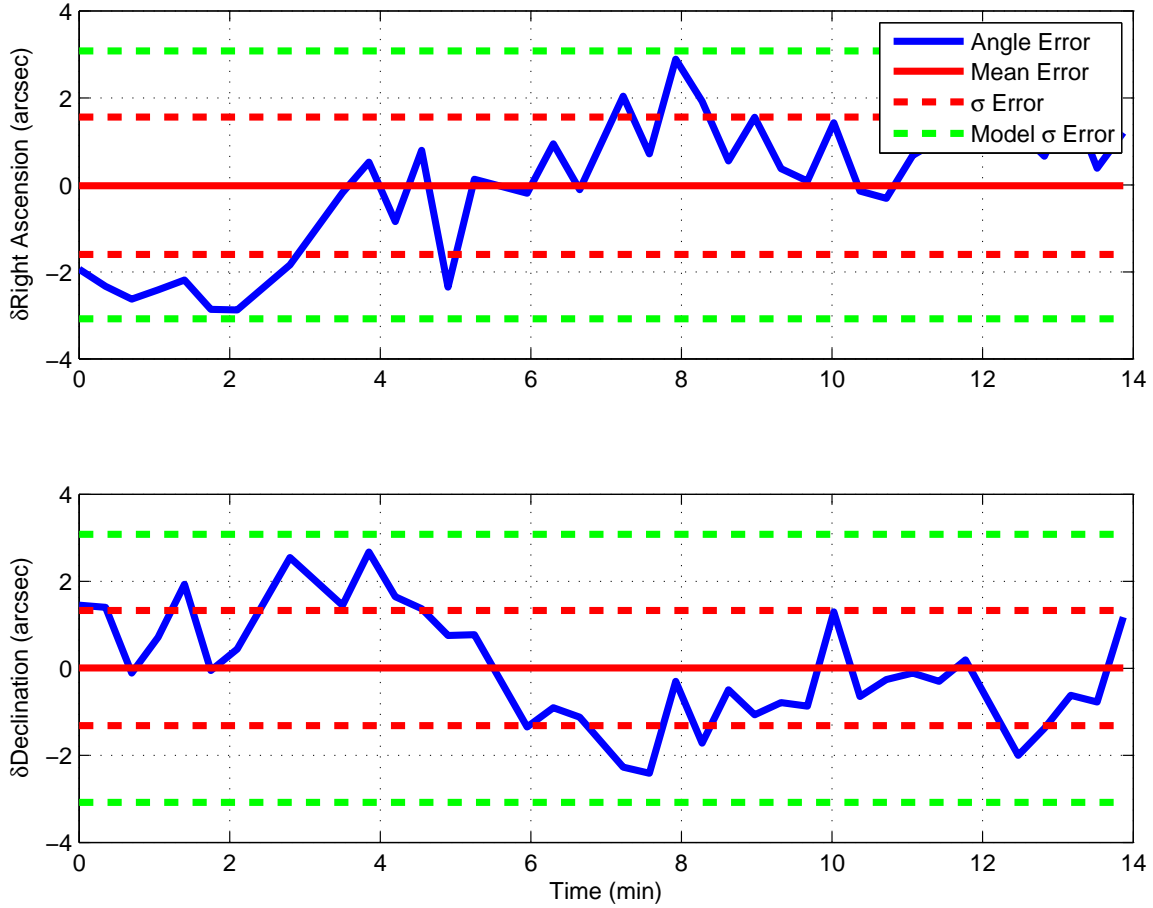
Figure 6.12: Star tracker angle measurement error of observed GPS satellite removing timing bias

In both right ascension and declination, the plots show that the mean is near 0 for either case. In addition, the standard deviation of the error noise is smaller than that predicted by the sensor model. One factor that may contribute to the difference is the estimated number of stars in the field of view. The model predicts that, on average, each image would have 8 stars visible. In the actual images, the number of

154

observed stars are shown in Figure 6.13. In calculating the mean number of stars observed, the 4 images that didn't have successful astrometry data was not used. The plot shows that there is a disparity between the original model and the actual data. The average number of observed stars is 12 per image with the lowest star count of 7 and the highest star count of 27. Adjusting the model to account for the average number of observed stars reduces the standard deviation of the modeled measurement error. Therefore, this star count factor doesn't account for all the difference.

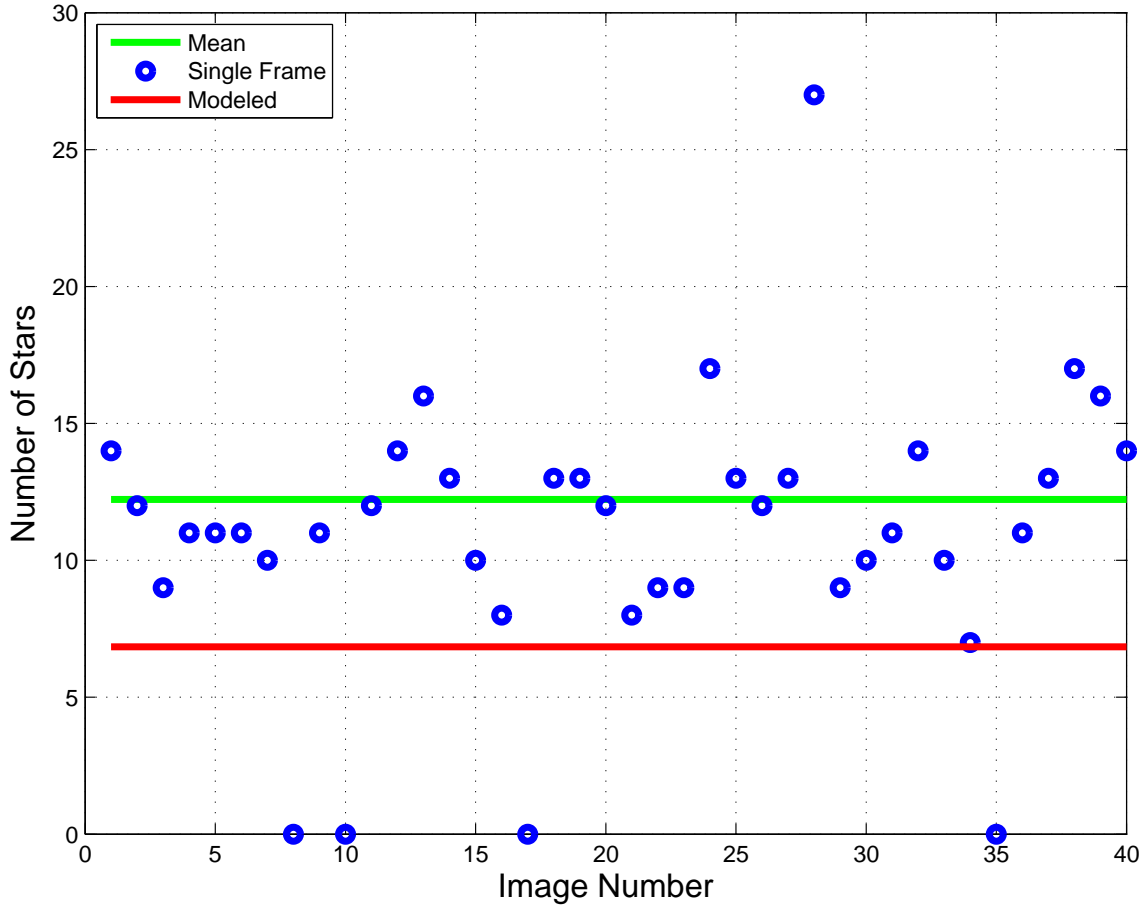Figure 6.13: Number of stars observed in images from 13 May 2014.

By looking at the other components of the angular error model the spot size of the point source on detector and the SNR may contribute to the difference. If the model reflects an SNR of 6.5 in addition to the correct number of stars visible and the width of the spot size is 4.4, then the statistics are much closer as shown in

155

Figure 6.14. The SNR and spot size values described were extracted from the set of satellite observations.
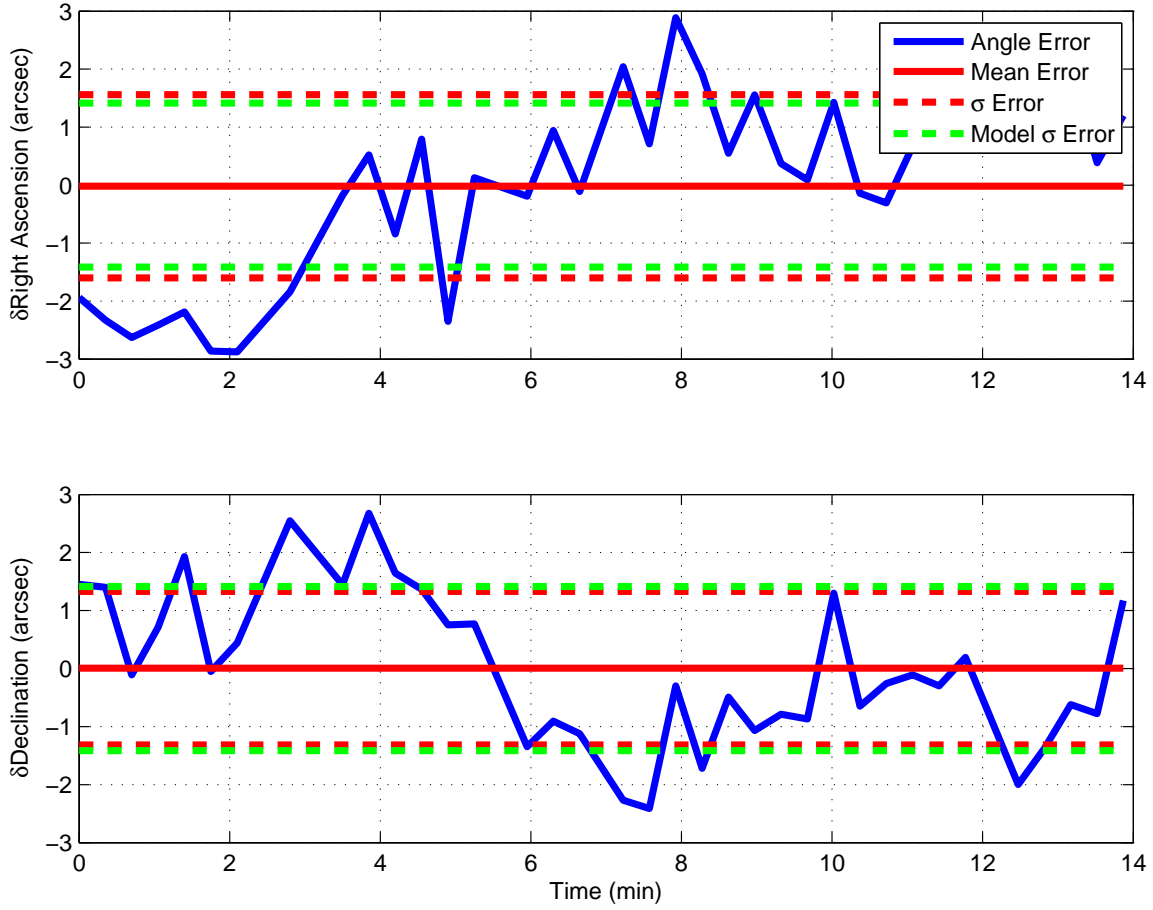
Figure 6.14:   Measurement Error of GPS Imagery with Nominal Adjustments.

6.4   Monte Carlo Model Results

The objective of this chapter is to compare navigation performance using simulated measurements to the performance using real imagery and measurements. To make an equivalent comparison, a scenario consisting of the same satellite geometry, with the same measurement timing, and the navigation grade IMU was run 30 times. In each simulation, the IMU noise, barometer noise, and the star tracker noise was independently generated. The star tracker measurements were calculated from the true satellite and observer's geometry. The barometer measured the altitude at a 1

Hz rate with the same noise parameters as described in Section 4.6.3. GPS measurements occurred for the first 30 seconds the same noise parameters as described in Section 4.6.3. However in the simulations described in this section, the satellite observations didn't begin until 20 minutes into the simulation. Thus, for 19.5 minutes the state estimate only has barometric sensor measurements. When the star tracker measurements begin at the 20 minute mark, the measurements follow the timing interval of the measured data with an average of 20 seconds between measurements. The measurements continue for 14 minutes after which the simulation ends.

The results of the position estimate performance from one run is shown in Figure 6.15. This plot shows that position estimate grows according to the drift rate of the IMU until star tracker measurement become available. The filter appropriately accounts for the star tracker measurements and the position estimate grows slightly between each measurement. In this specific run, the vertical error grows to have an offset of just over 20 m. Though it seems to be a large value, that vertical error is approximately near the standard deviation of the state estimate, denoted by the red dotted line on the plot.

From each of the 30 Monte Carlo simulations, the results were compiled in a manner similar to the previous chapter's methods. Figure 6.16 shows the horizonal position rss errors for all the runs of this scenario. Every color of the plot shows the time-sequenced rss error. For this test, the maximum value of all the runs is approximately 240 m, while the minimum value is less than 10 m. The rss error values show variability across the runs due to the unique IMU process noise in each run, as well as variability within each run due to the random noise in each star tracker measurement. To reduce this performance data for easier comparison, a 2-D drms value for each run was calculated. Only the horizontal dimensions were used in comparing the performance accuracy because the vertical position dimension is additionally aided by the altimeter, whereas we're most interested in the effects of the star tracker measurements.
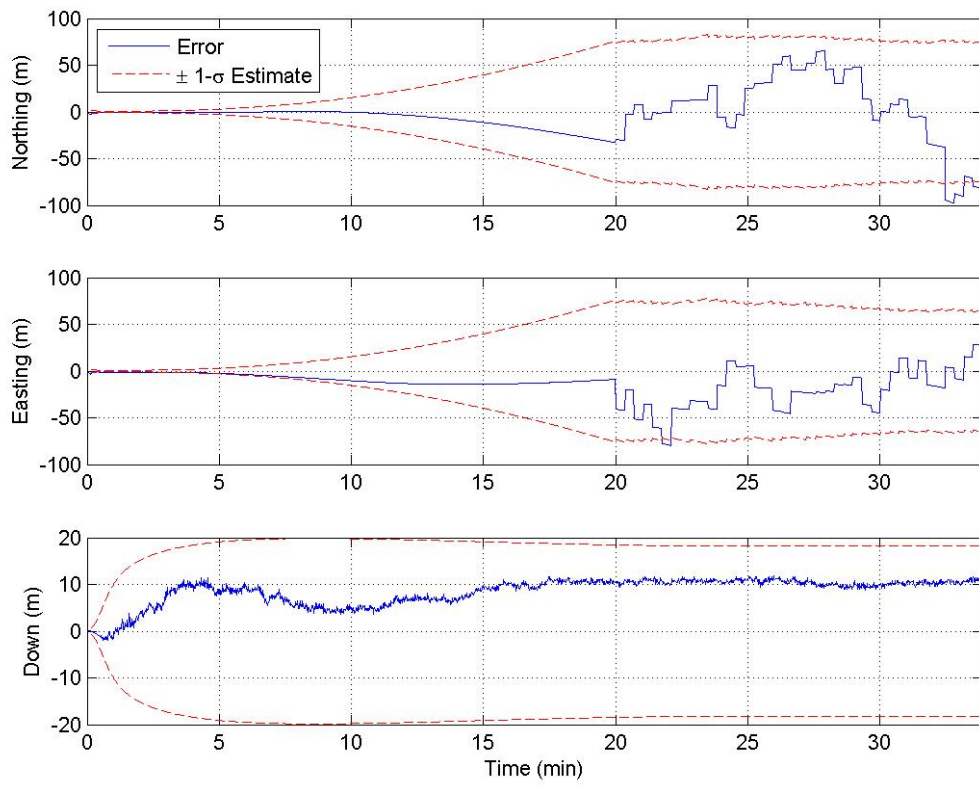
Figure 6.15:   Position Error of One Run from May 13 Simulation
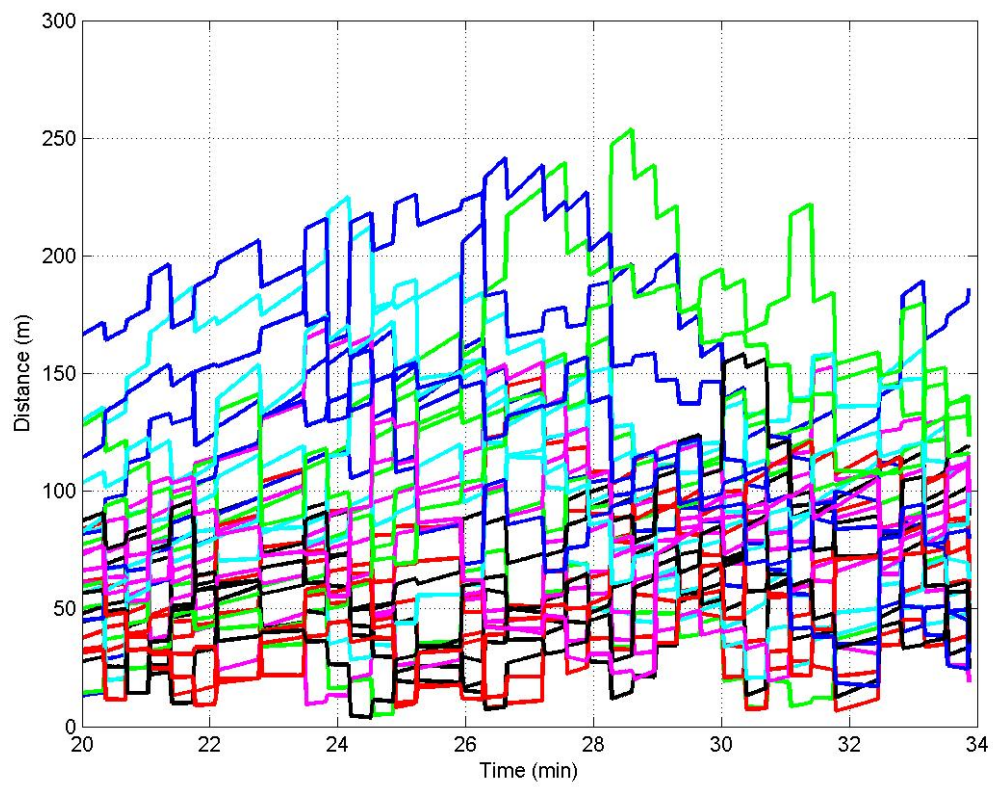
Figure 6.16:   RSS Errors from May 13 Simulations

159
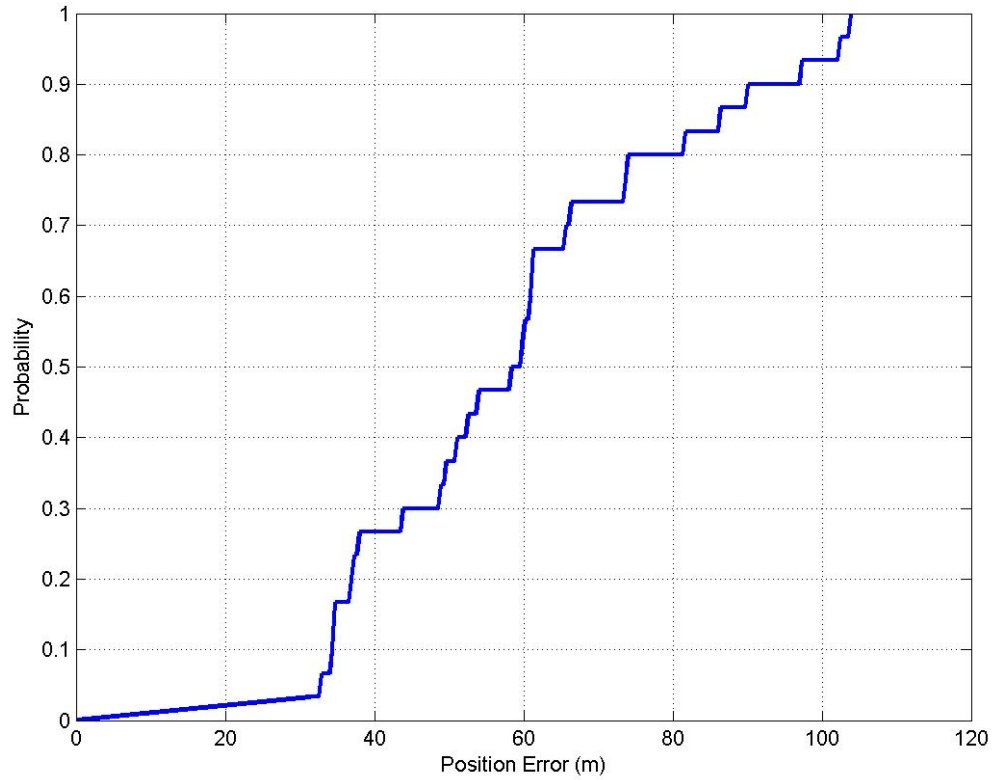
Figure 6.17:   CDF of DRMS Errors from May 13 Simulations

The drms errors from each run were compiled into a single set. The drms error set incorporate the distance error beginning at the first star tracker measurement time to the end of each simulation. From the drms error set a CDF was calculated describing the probability of the drms error to be a certain level of accuracy or better. Figure 6.17 shows the CDF for this scenario with a minimum value near 33 m and a maximum value just over 95 m.

To capture a few values of interest from the plot, Figure 6.18 shows that the distribution of the error has a median value of approximately 55 m, denoted by the dot in the middle of the error bar. The model also calculated that 10% of the time the drms error of the system is less than 34 m, and that 90% of the time the error is less than 76 m.
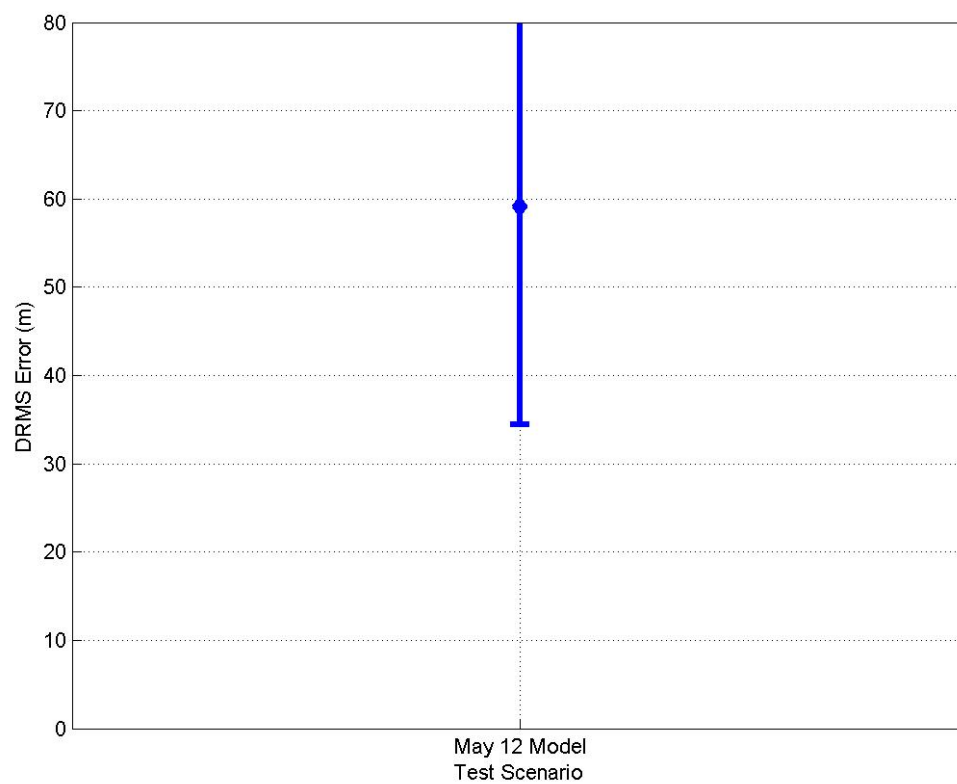
Figure 6.18:   DRMS Error Bar from May 13 Simulations

With the model calculating this level of performance accuracy, the next step is to calculate the performance accuracy using the real imagery and compare it to the results of using simulated measurements.

6.5 Experimental Results

When modeling the navigation solution using the data collected from the telescope, the scenario is the same as that described in the previous section with one exception. Instead of calculating an satellite angle measurement, the model uses the actual angle measurement from the experiment. The IMU noise used in this simulation is independent of that used in the previous simulations, but is based on the same IMU noise model.

Figure 6.19 shows the results of one run of the model incorporating measurements from actual observations. The horizontal position error plots show that with the star tracker measurements the error uncertainty is bounded by the star tracker accuracy imaging an object at MEO orbit. From the standpoint of angular error time distance, the uncertainty in the measurement is approximately 290 m, but when combined in the EKF with a barometric altimeter and an IMU, both the North and East position uncertainty is reduced to under 100 m. This same bounding of the position error in the North and East direction occurs when using modeled measurements as shown previously in Figure 6.15.

The simulation estimates the observer's position using the observed data and calculates the horizonal rss error of the position. Figure 6.20 shows the rss error values for 30 runs. During most of the runs, the error shows a decreasing trend during the time period 26-34 minutes. This trend demonstrates that the more star tracker measurements available the more the error is being reduced with each one, so that the time history of measurements provides a better solution than a single measurement. This should be consistent throughout the whole run, however, over the time period 21-26 minutes, the position error tends to increase for most runs. This unexpected increase could be due to unmodeled errors in the measurements, such
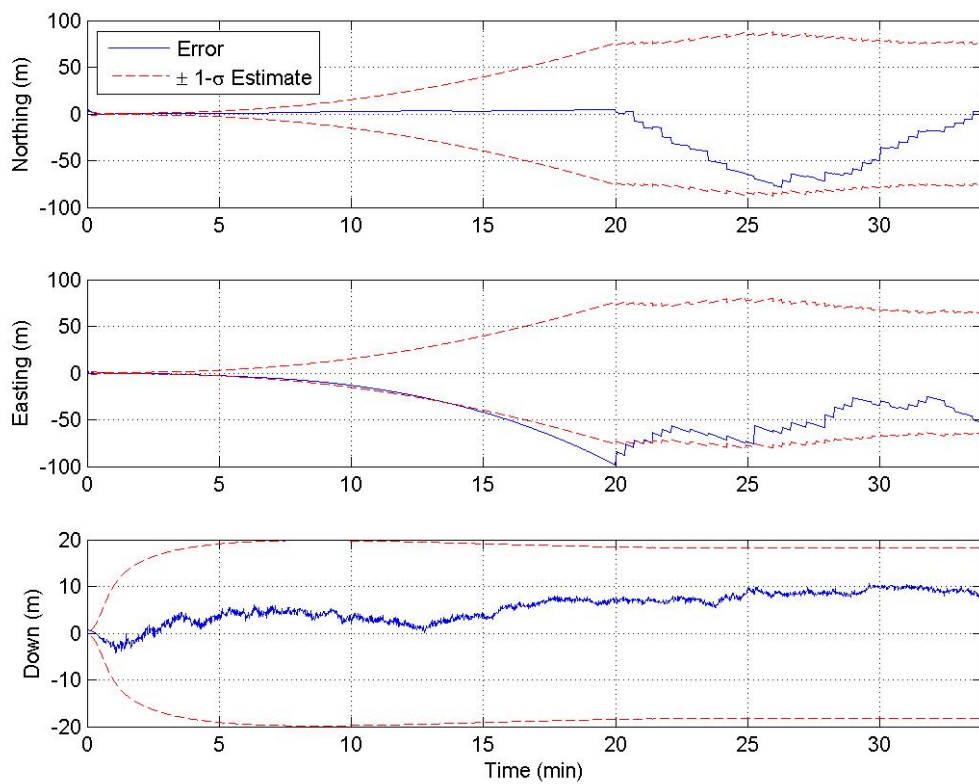
Figure 6.19:   Position Error of One Run from May 13 Using Observations
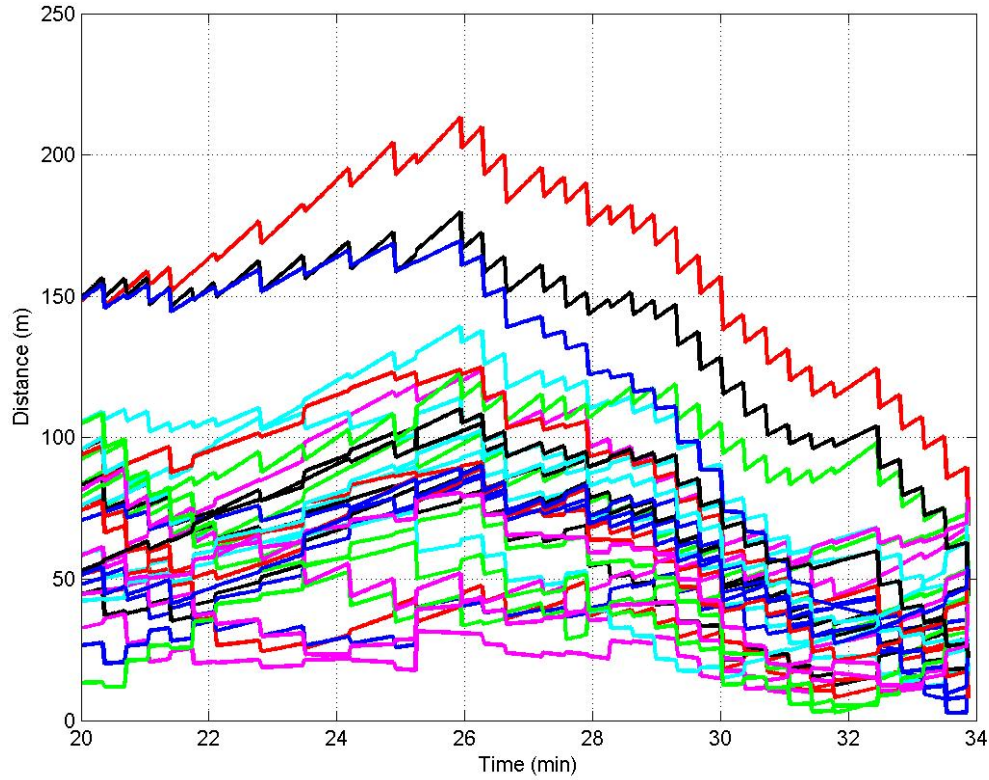
Figure 6.20:   RSS Errors from May 13 Experimental Data

as errors due to centroiding, which were accomplished by inspection. Between each star tracker measurement, the error grows due to the IMU process noise, giving each segment between measurements a positive slope. The largest error among these runs is approximately 240 m and the smallest error is approximately 5 m. The results here are distinct from those in Figure 6.16 in that the errors have less variability within each run. This is due to the smaller process noise in the actual measurements than the noise in the simulated measurements as was shown in Figure 6.12. In addition, the drms errors have similar shapes in the experimental results, which is different than the modeled measurement performance error, because the experimental measurements are not unique between each run. The star tracker measurements between the runs have the same error so the trend when incorporating the measurement in the filter will be similar, but scaled according to the error due to unique IMU noise.

164

To determine the general performance of the system using these measurements a drms value is calculated for each run. Figure 6.21 shows the CDF of the drms errors of the observer's position when using actual measurements in red. The maximum drms value is approximately 105 m and the minimum value is approximately 20 m. The profile differs from the results, shown in green, of the simulations using modeled star tracker measurements. Where the simulated star tracker measurements resulted in an almost linear CDF between 20 and 100 m, the CDF when using actual measurements weights the smaller drms values more than the higher values over the same interval of error. Thus, using the actual measurements results in better performance through smaller drms position error than what is predicted using simulated measurements. This result is expected given that the modeled measurement error standard deviation was larger than the actual measurement error standard deviation. A direct comparison can be shown by first identifying interest points in the CDF.

Figure 6.22 displays the resulting error bars of both cases: using simulated measurements and using actual measurements. The results of the two types of simulations are similar enough to be comparable, and distinct enough to describe the differences. The results indicate that the performance of the simulations based on a simulated star tracker are close to the performance of that using real data, validating in a limited manner the ability of the simulation to predict true performance. The distributions have a similar spread of 10% to 90% values of approximately 40 m. So the model is a fair representation of the actual navigation system.

However, the model should be improved to account for the differences in the results. The median value of the error using simulated measurements is nearer the middle of the errorbar, describing the linear trend of the CDF for those simulations. The median value of the error using the actual measurements is nearer the lower end of the error bar indicating that 50% of the results are lower than half of the error spread. The median value using the real measurements is also near the lower end of the simulated measurement error bar. Therefore, using the real data results in an error significantly lower than that predicted using the simulated data.
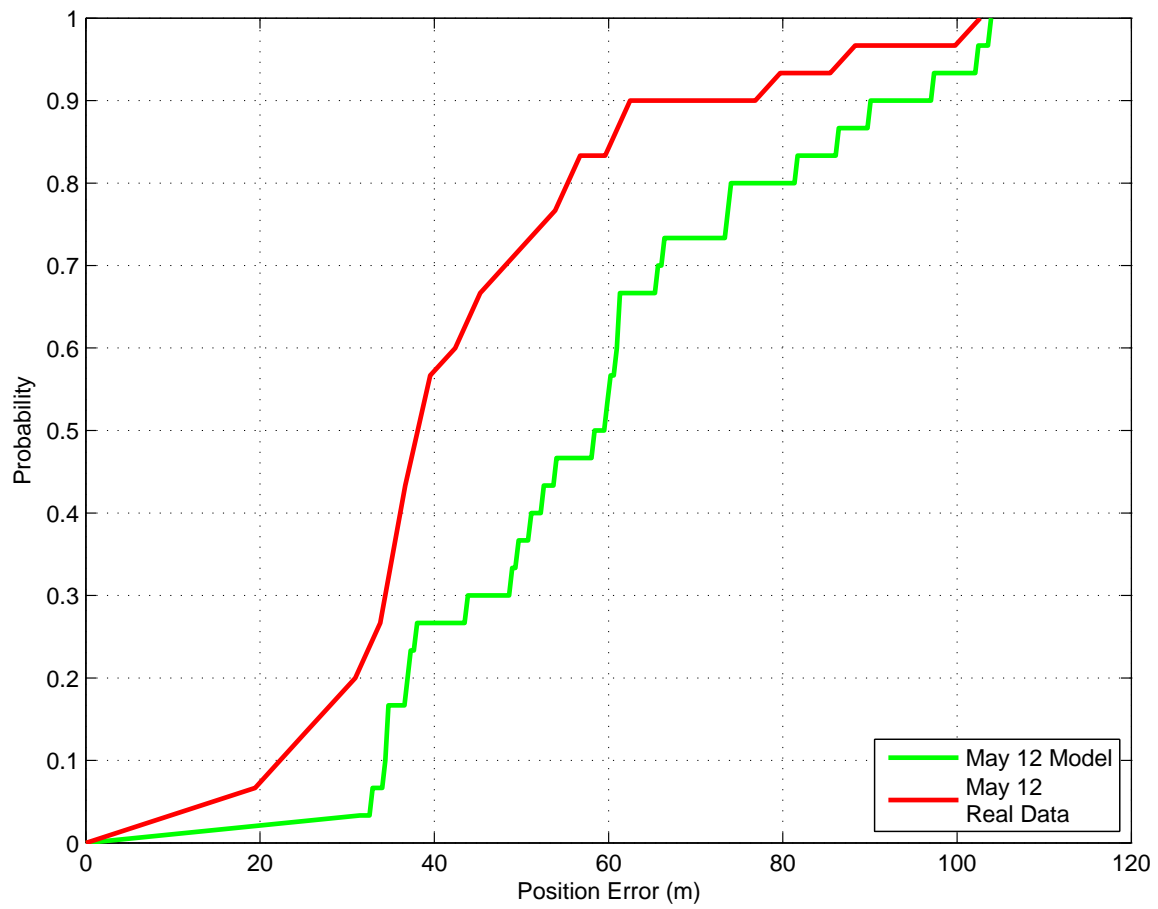
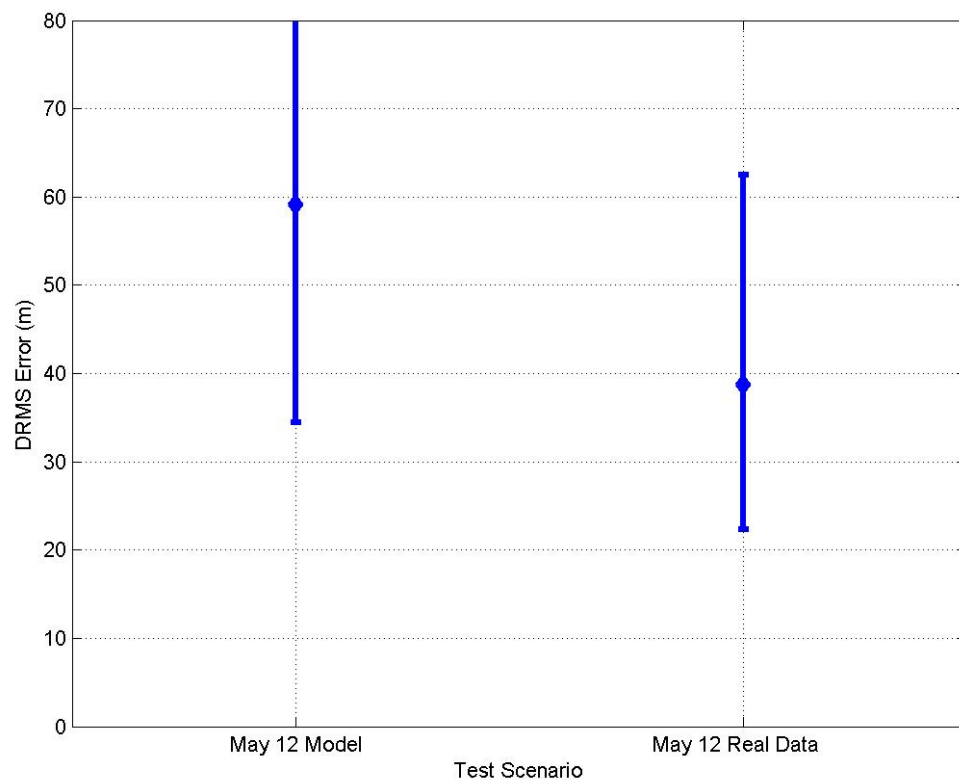Figure 6.21:   CDF of DRMS Errors from May 13 Experimental and Simulated Data

Figure 6.22:   Comparison of Error Bar from May 13

As previously mentioned, this difference is the result of lower noise values in the actual measurements than predicted. Three nominal changes were suggested previously in this chapter. Though having an accurate time stamp of the image was suggested as an addition to the model, it's effect is not shown in Figure 6.22, because the model results are based on a perfect knowledge of time and the experimental data has some residual timing error. Of more impact is the accurate parameter modeling of the sensor leading to SNR calculation, accurate calculation of the centroiding accuracy, which in this research was a set parameter, and finally accurate prediction of the number of observable stars.

The author recommends that to further validate the model, additional observations of satellites be made under different conditions with the same test bed, or alternativly using a different representative star tracker system.

6.6   Summary

This chapter sought to describe the comparison of the simulation results described in the previous chapter and results based on actual imagery. The experiment was described by its processes and components representing expected star tracker measurement capabilities. The actual observations were described and compared to measurements predicted using the simulation with the actual measurements having overall less error than predicted, but consistent with predicted values. Finally, simulations using both simulated measurements and actual measurements showed that the true system followed the predicted model well with overall less position error. The drms errorbars of the predicted performance was confirmed by the performance of the errorbar using real imagery, validating in a limited manner the utility of the simulation.

VII. Conclusion

A summary of the document and the results are discussed here. A discussion of this researches contributions to the body of knowledge are presented. Lastly, a few remarks regarding additional research topics are given and why those topics would be interesting.

7.1 Summary of Document

Chapter I introduced the research objectives, the motivation for this research and the structure of this document. Chapter II described previous related research in star tracker development and application as well as using satellite observations as navigational aids. Chapter II also presented background subject matter regarding state estimation using a Kalman filter, signal and detector properties, and reference frames. Chapter IV presented the integration of the IMU, barometric altimeter, and star tracker in the framework of an EKF. It developed the tightly-integrated model of star tracker measurements and the derivation of their measurement noise based on sensor specifications. The error state estimates using a Pinson error model were shown to agree with the distribution of error state values given the same IMU parameters allowing the overall system simulation to use a Pinson error model to predict position, velocity, and tilt error states.

The power requirements of a light-emitting LEO satellite signal was proposed in Chapter III. The signal power was defined as a function of background noise from sun-scattered light, detector parameters, and satellite parameters. A SNR value of 7 was proposed to determine detectability of the signal. Power values at various operating altitudes and with 3 types of star tracker systems were calculated.

The expected navigation performance using simulation was presented in Chapter V, which was shown to vary as a function of system parameters. Comparisons were made using a standard system configuration with one or two parameters being varied to attribute those parameters effects on the position error. Not surprisingly, the navigation grade IMU was shown to consistently perform better than the tacti-

cal grade IMU decreasing the median position error by 55% in LEO orbits and 75% in MEO orbits. LEO orbiting satellites provided better position measurements than either MEO or GEO orbiting satellites resulting in lower position error estimates. Satellite observation time intervals demonstrated that increasing the delay between measurements reduced the position estimate accuracy, increasing the position error.

Chapter V also presented a new approach to correcting for ephemeris error using a reference site observation. The projection of the reference site measured ephemeris error onto the observer's measured values was presented. The results of simulations described the reduction of position estimate error through the use of this corrective measurement as well as the effect of increasing the distance between the reference site and the observer. Larger distances between the reference site and the observer reduced the applicability of the corrective factor when observing LEO orbiting satellites, but had little to no effect when observing MEO satellites. The simulations also allowed for some discussion of the satellite selection algorithm and the impact of that algorithm on the the navigation solution. The results showed that when observing simultaneous satellites, observing 2 improved the position estimate. However, quickly switching between 2 satellites in sequence after only a few observations resulted in a larger position estimate error than only observing 1 satellite for its availability duration.

After simulating these several scenarios, Chapter VI described the use of a representative star tracker system to capture satellite observations and use them in position estimation. Scenarios were simulated based on the satellite positions to generate expected system performance, which was then compared to the actual measurement accuracy and system performance. The simulated measurements had a position error that was only slightly higher than the error when using actual imagery, demonstrating both agreement of the model and the true system as well as some areas in which the model could be improved to more accurately reflect the true system.

7.2 Summary of Contributions

The main contributions of this work consist of the development of a rigorous performance model of the system integrating an IMU with a star tracker and several other components, identification of many key performance parameters, the application of a reference site corrective measurement, and the definition of the signal requirements for a daytime-visible satellite.

The performance model defines the tight-integration of star tracker measurements of visible satellites in a Kalman filter framework to estimate the observer's position. Though the method of measuring satellites using imagery to estimate an observer's position is not new in this research, the definition of the measurement model with measurement covariance defined by star tracker and other system properties is first described here.

An analysis of several of the key performance parameters of the system and their effects on the navigation performance is described using this rigorous model. Simulations depicting the effects of three satellite selection algorithms were presented, which have not been previously discussed in literature using this suite of sensors.

A method for correcting satellite ephemeris error using a reference site measurement was proposed and simulated to describe the expected reduction in position error when appropriately applied. A derivation of the measurement covariance was presented to accommodate the introduction of a differential measurement in the Kalman filter.

This research also defined the signal properties nominally required for several types of detectors such that satellites could be visible from a near-Earth observer.

These contributions are the elements of this research that have expanded the field of navigation in the application of star tracker integration with a vehicle's navigation system.

7.3 Future Work

In the course of this research it was identified that several aspects could be further investigated and elements of this performance model improved. One improvement to the performance model would be an adaptive definition of the measurement uncertainty. In the definition of the star tracker measurement covariance, the right ascension and declination values are calculated as a function of the signal and the detector properties, and the covariances are identically applied to each dimension. A refinement of this definition could take into account the region of the celestial sphere in which measurements are being taken and the covariance adapted to the non-linear and non-equal distribution of right ascension and declination. The angle subtended by a detector element is not the same in each dimension across the celestial sphere. This refinement should provide a more accurate weighting of the measurement in those dimensions as observations are taken from the celestial equator to the celestial poles.

A second refinement to make the measurement uncertainty adaptive to conditions is to locally calculate expected number of stars visible. In this research, a uniform distribution of stars in the catalog is used to define the measurement uncertainty. However, this value will increase or decrease depending on the locality in the celestial sphere where the measurements are being taken and the density of stars in that locale. This varying parameter will more accurately predict specific configurations of satellite-observer geometries, which were not heavily investigated in this work.

Though three algorithms were developed to identify the satellites to be observed, no effort was made in this research to find an optimal method. Given a specific set of satellites, conditions could be determined regarding either the number and orbital parameters of the satellites or the sequence in which those satellites are observed to minimize the position error of the observer.

Of near-term interest would be to perform additional observations either in a different configuration or using a different sensor. Different configurations, such as observing several satellites in different orbits or testing specific update rates would further refine this model through experimentation. Using a different sensor would allow for further validation of this model, the definition of measurement uncertainty, and ultimately the navigation performance.

Finally, this model could be applied to specific observer trajectories. The trajectories used in this work were generically chosen. In the case of comparing the model to real imagery, the observations were made from a stationary platform. Additional validation can be made comparing the simulated and actual results from a moving platform.

Appendices

Appendix A. Star Tracker Angle Measurement Linearization

In deriving the transformation matrix from error-state space to measurement space, the measurement equations are linearized around a nominal value. This is done by taking the Jacobian of the $\mathbf{h}(\cdot)$ equation vector with respect to the estimated states, then applying the current values of the states where necessary. This process is described by Eqn. 2.23 and is reiterated here.

$$\mathbf{H}[t_{i+1}; \mathbf{x}(t_{i+1}^-)] \triangleq \frac{\partial \mathbf{h}[\mathbf{x}, t_{i+1}]}{\partial \mathbf{x}}\bigg|_{\mathbf{x}=\hat{\mathbf{x}}(t_{i+1}^-)} \tag{A.1}$$

The observer's angular measurement of the satellite is given by Eqn. 4.151, also reiterated here.

$$\alpha = \sin^{-1} \frac{p_y}{\sqrt{p_x^2 + p_y^2}} \tag{A.2}$$

$$\delta = \tan^{-1} \frac{p_z}{\rho} \tag{A.3}$$

where $\mathbf{p}$ is the vector from the observer to the satellite with x, y, and z components and ρ is the slant range from observer to satellite.

$$\mathbf{p} = \begin{bmatrix} p_x \\ p_y \\ p_z \end{bmatrix} = \mathbf{r}_s - \mathbf{r}_o \tag{A.4}$$

$$\rho = \sqrt{p_x^2 + p_y^2 + p_z^2} \tag{A.5}$$

There is one other conversion to take into account at this point. The angular calculations are performed in an ECEF reference frame, yet the error state of observer's position is in a local navigation frame. Therefore, the latitude, longitude, and altitude, with units of radians, radians, and meters, respectively, must be transformed to

175

meters from the center of the Earth. This conversion is given by [23]

$$\mathbf{x}_o^{ecef} = \mathbf{f}(\mathbf{x}_o^n) \tag{A.6}$$

$$= \begin{bmatrix} x \\ y \\ z \end{bmatrix} \tag{A.7}$$

$$= \begin{bmatrix} R\cos(l) \\ R\sin(l) \\ (r_n(1-e^2)+h)\sin(L) \end{bmatrix} \tag{A.8}$$

where the observer's state in the navigation frame, $\mathbf{x}_o^n$, and the coefficients R and r_n are given as [23]

$$\mathbf{x}_o^n = \begin{bmatrix} L & l & h \end{bmatrix}^T \tag{A.9}$$

$$R = (r_n + h)\cos(L) \tag{A.10}$$

$$r_n = \frac{a}{\sqrt{1 - e^2\sin^2(L)}} \tag{A.11}$$

with a and e describing the semimajor axis and the ellipticity of the Earth, respectively.

As such, the measurement equations are more accurately described by

$$\mathbf{H} = \begin{bmatrix} H_{11} & H_{12} & H_{13} & \mathbf{0}_{1\times14} \\ H_{21} & H_{22} & H_{23} & \mathbf{0}_{1\times14} \end{bmatrix} \tag{A.12}$$

$$= \begin{bmatrix} \frac{\partial\alpha}{\partial L} & \frac{\partial\alpha}{\partial l} & \frac{\partial\alpha}{\partial h} & \mathbf{0}_{1\times14} \\ \frac{\partial\delta}{\partial L} & \frac{\partial\delta}{\partial l} & \frac{\partial\delta}{\partial h} & \mathbf{0}_{1\times14} \end{bmatrix} \tag{A.13}$$

Each of these elements of the **H** matrix are described individually here.

$$\frac{\partial \alpha}{\partial \delta L} = \frac{\partial}{\partial \delta L}\left(\sin^{-1}\left(\frac{p_y}{\sqrt{p_x^2 + p_y^2}}\right)\right) \tag{A.14}$$

$$= \left(1 - \left(\frac{p_y}{\sqrt{p_x^2 + p_y^2}}\right)^2\right)^{-1/2}\left[\frac{(\frac{\partial}{\partial \delta L}p_y)\sqrt{p_x^2 + p_y^2} - p_y\frac{\partial}{\partial \delta L}\sqrt{p_x^2 + p_y^2}}{\left(\sqrt{p_x^2 + p_y^2}\right)^2}\right] \tag{A.15}$$

$$\frac{\partial \alpha}{\partial \delta l} = \frac{\partial}{\partial \delta l}\left(\sin^{-1}\left(\frac{p_y}{\sqrt{p_x^2 + p_y^2}}\right)\right) \tag{A.16}$$

$$= \left(1 - \left(\frac{p_y}{\sqrt{p_x^2 + p_y^2}}\right)^2\right)^{-1/2}\left[\frac{(\frac{\partial}{\partial \delta l}p_y)\sqrt{p_x^2 + p_y^2} - p_y\frac{\partial}{\partial \delta l}\sqrt{p_x^2 + p_y^2}}{\left(\sqrt{p_x^2 + p_y^2}\right)^2}\right] \tag{A.17}$$

$$\frac{\partial \alpha}{\partial \delta h} = \frac{\partial}{\partial \delta h}\left(\sin^{-1}\left(\frac{p_y}{\sqrt{p_x^2 + p_y^2}}\right)\right) \tag{A.18}$$

$$= \left(1 - \left(\frac{p_y}{\sqrt{p_x^2 + p_y^2}}\right)^2\right)^{-1/2}\left[\frac{(\frac{\partial}{\partial \delta h}p_y)\sqrt{p_x^2 + p_y^2} - p_y\frac{\partial}{\partial \delta h}\sqrt{p_x^2 + p_y^2}}{\left(\sqrt{p_x^2 + p_y^2}\right)^2}\right] \tag{A.19}$$

$$\frac{\partial \delta}{\partial \delta L} = \frac{\partial}{\partial \delta L}\left(\sin^{-1}\left(\frac{p_z}{\rho}\right)\right) \tag{A.20}$$

$$= \left(1 - \left(\frac{p_z}{\rho}\right)^2\right)^{-1/2}\left[\frac{(\frac{\partial}{\partial \delta L}p_z)\rho - p_z\frac{\partial}{\partial \delta L}\rho}{\rho^2}\right] \tag{A.21}$$

$$\frac{\partial \delta}{\partial \delta l} = \frac{\partial}{\partial \delta l}\left(\sin^{-1}\left(\frac{p_z}{\rho}\right)\right) \tag{A.22}$$

$$= \left(1 - \left(\frac{p_z}{\rho}\right)^2\right)^{-1/2}\left[\frac{(\frac{\partial}{\partial \delta l}p_z)\rho - p_z\frac{\partial}{\partial \delta l}\rho}{\rho^2}\right] \tag{A.23}$$

$$\frac{\partial \delta}{\partial \delta h} = \frac{\partial}{\partial \delta h}\left(\sin^{-1}\left(\frac{p_z}{\rho}\right)\right) \tag{A.24}$$

$$= \left(1 - \left(\frac{p_z}{\rho}\right)^2\right)^{-1/2}\left[\frac{(\frac{\partial}{\partial \delta h}p_z)\rho - p_z\frac{\partial}{\partial \delta h}\rho}{\rho^2}\right] \tag{A.25}$$

These require subsequent partial derivatives of the observer to satellite vector and the slant range. The partial derivatives of the components of the observer to satellite

vector are presented first.

$$\frac{\partial p_x}{\partial \delta L} = \frac{\partial}{\partial \delta L} (x_s - x_o) \tag{A.26}$$

$$= 0 - \frac{\partial}{\partial \delta L} (R \cos(l + \delta l)) \tag{A.27}$$

$$= -\left(\frac{\partial}{\partial \delta L} R\right) \cos(l + \delta l) - R \left(\frac{\partial}{\partial \delta L} \cos(l + \delta l)\right) \tag{A.28}$$

$$= -\frac{\partial R}{\partial \delta L} \cos(l + \delta l) \tag{A.29}$$

$$\frac{\partial p_x}{\partial \delta l} = \frac{\partial}{\partial \delta l} (x_s - x_o) \tag{A.30}$$

$$= 0 - \frac{\partial}{\partial \delta l} (R \cos(l + \delta l)) \tag{A.31}$$

$$= -\left(\frac{\partial}{\partial \delta l} R\right) \cos(l + \delta l) - R \left(\frac{\partial}{\partial \delta l} \cos(l + \delta l)\right) \tag{A.32}$$

$$= -\frac{\partial R}{\partial \delta l} \cos(l + \delta l) + R \sin(l + \delta l) \tag{A.33}$$

$$\frac{\partial p_x}{\partial \delta h} = \frac{\partial}{\partial \delta h} (x_s - x_o) \tag{A.34}$$

$$= 0 - \frac{\partial}{\partial \delta h} (R \cos(l + \delta l)) \tag{A.35}$$

$$= -\left(\frac{\partial}{\partial \delta h} R\right) \cos(l + \delta l) - R \left(\frac{\partial}{\partial \delta h} \cos(l + \delta l)\right) \tag{A.36}$$

$$= -\frac{\partial R}{\partial \delta h} \cos(l + \delta l) \tag{A.37}$$

$$\frac{\partial p_y}{\partial \delta L} = \frac{\partial}{\partial \delta L} (y_s - y_o) \tag{A.38}$$

$$= 0 - \frac{\partial}{\partial \delta L} (R \sin(l + \delta l)) \tag{A.39}$$

$$= - \left(\frac{\partial}{\partial \delta L} R \right) \sin(l + \delta l) - R \left(\frac{\partial}{\partial \delta L} \sin(l + \delta l) \right) \tag{A.40}$$

$$= - \frac{\partial R}{\partial \delta L} \sin(l + \delta l) \tag{A.41}$$

$$\frac{\partial p_y}{\partial \delta l} = \frac{\partial}{\partial \delta l} (y_s - y_o) \tag{A.42}$$

$$= 0 - \frac{\partial}{\partial \delta l} (R \sin(l + \delta l)) \tag{A.43}$$

$$= - \left(\frac{\partial}{\partial \delta l} R \right) \sin(l + \delta l) - R \left(\frac{\partial}{\partial \delta l} \sin(l + \delta l) \right) \tag{A.44}$$

$$= - R \cos(l + \delta l) \tag{A.45}$$

$$\frac{\partial p_y}{\partial \delta h} = \frac{\partial}{\partial \delta h} (y_s - y_o) \tag{A.46}$$

$$= 0 - \frac{\partial}{\partial \delta h} (R \sin(l + \delta l)) \tag{A.47}$$

$$= - \left(\frac{\partial}{\partial \delta h} R \right) \sin(l + \delta l) - R \left(\frac{\partial}{\partial \delta h} \sin(l + \delta l) \right) \tag{A.48}$$

$$= - \frac{\partial R}{\partial \delta h} \sin(l + \delta l) \tag{A.49}$$

$$\frac{\partial p_z}{\partial \delta L} = \frac{\partial}{\partial \delta L}(z_s - z_o) \tag{A.50}$$

$$= 0 - \frac{\partial}{\partial \delta L}\left((r_n(1 - e^2) + h + \delta h)\sin(L + \delta L)\right) \tag{A.51}$$

$$= -\left(\frac{\partial}{\partial \delta L}(r_n(1 - e^2) + h + \delta h)\right)\sin(L + \delta L) - (r_n(1 - e^2) + h + \delta h)\left(\frac{\partial}{\partial \delta L}\sin(L + \delta L)\right) \tag{A.52}$$

$$= -\left(\frac{\partial}{\partial \delta L}(r_n(1 - e^2)) + 0\right)\sin(L + \delta L) - (r_n(1 - e^2) + h + \delta h)\cos(L + \delta L) \tag{A.53}$$

$$= -\frac{\partial r_n}{\partial \delta L}(1 - e^2)\sin(L + \delta L) - (r_n(1 - e^2) + h + \delta h)\cos(L + \delta L) \tag{A.54}$$

$$\frac{\partial p_z}{\partial \delta l} = \frac{\partial}{\partial \delta l}(z_s - z_o) \tag{A.55}$$

$$= 0 - \frac{\partial}{\partial \delta l}\left((r_n(1 - e^2) + h + \delta h)\sin(L + \delta L)\right) \tag{A.56}$$

$$= -\left(\frac{\partial}{\partial \delta l}(r_n(1 - e^2) + h + \delta h)\right)\sin(L + \delta L) - (r_n(1 - e^2) + h + \delta h)\left(\frac{\partial}{\partial \delta l}\sin(L + \delta L)\right) \tag{A.57}$$

$$= -\left(\frac{\partial}{\partial \delta l}(r_n(1 - e^2)) + 0\right)\sin(L + \delta L) \tag{A.58}$$

$$= -\frac{\partial r_n}{\partial \delta l}(1 - e^2)\sin(L + \delta L) \tag{A.59}$$

$$\frac{\partial p_z}{\partial \delta h} = \frac{\partial}{\partial \delta h}(z_s - z_o) \tag{A.60}$$

$$= 0 - \frac{\partial}{\partial \delta h}\left((r_n(1 - e^2) + h + \delta h)\sin(L + \delta L)\right) \tag{A.61}$$

$$= -\left(\frac{\partial}{\partial \delta h}(r_n(1 - e^2) + h + \delta h)\right)\sin(L + \delta L) - (r_n(1 - e^2) + h + \delta h)\left(\frac{\partial}{\partial \delta h}\sin(L + \delta L)\right) \tag{A.62}$$

$$= -\left(\frac{\partial}{\partial \delta h}(r_n(1 - e^2)) + 1\right)\sin(L + \delta L) \tag{A.63}$$

$$= -\left(\frac{\partial r_n}{\partial \delta h}(1 - e^2) + 1\right)\sin(L + \delta L) \tag{A.64}$$

Now the partial derivatives of the slant range can be derived using Eqn. 4.154.

$$\frac{\partial \rho}{\partial \delta L} = \frac{\partial}{\partial \delta L}\sqrt{(x_s - x_o)^2 + (y_s - y_o)^2 + (z_s - z_o)^2} \tag{A.65}$$

$$= \frac{1}{2\rho}\left[\frac{\partial}{\partial \delta L}(x_s - x_o)^2 + \frac{\partial}{\partial \delta L}(y_s - y_o)^2 + \frac{\partial}{\partial \delta L}(z_s - z_o)^2\right] \tag{A.66}$$

$$= \frac{1}{2\rho}\left[2(x_s - x_o)\frac{\partial}{\partial \delta L}(x_s - x_o) + 2(y_s - y_o)\frac{\partial}{\partial \delta L}(y_s - y_o) + 2(z_s - z_o)\frac{\partial}{\partial \delta L}(z_s - z_o)\right] \tag{A.67}$$

$$= \frac{1}{\rho}\left[p_x\frac{\partial p_x}{\partial \delta L} + p_y\frac{\partial p_y}{\partial \delta L} + p_z\frac{\partial p_z}{\partial \delta L}\right] \tag{A.68}$$

$$\frac{\partial \rho}{\partial \delta l} = \frac{1}{\rho}\left[p_x\frac{\partial p_x}{\partial \delta l} + p_y\frac{\partial p_y}{\partial \delta l} + p_z\frac{\partial p_z}{\partial \delta l}\right] \tag{A.69}$$

$$\frac{\partial \rho}{\partial \delta h} = \frac{1}{\rho}\left[p_x\frac{\partial p_x}{\partial \delta h} + p_y\frac{\partial p_y}{\partial \delta h} + p_z\frac{\partial p_z}{\partial \delta h}\right] \tag{A.70}$$

Additionally, the partial derivatives are needed of the slant range projected onto the x-y plane, which are analogous to the results of Eqns. A.65-A.70.

$$\frac{\partial}{\partial \delta L}\sqrt{p_x^2 + p_y^2} = \frac{1}{2\sqrt{p_x^2 + p_y^2}}\left[\frac{\partial}{\partial \delta L}p_x^2 + \frac{\partial}{\partial \delta L}p_y^2\right] \tag{A.71}$$

$$= \frac{1}{2\sqrt{p_x^2 + p_y^2}}\left[2p_x\frac{\partial p_x}{\partial \delta L} + 2p_y\frac{\partial p_y}{\partial \delta L}\right] \tag{A.72}$$

$$= \frac{1}{\sqrt{p_x^2 + p_y^2}}\left[p_x\frac{\partial p_x}{\partial \delta L} + p_y\frac{\partial p_y}{\partial \delta L}\right] \tag{A.73}$$

$$\frac{\partial}{\partial \delta l}\sqrt{p_x^2 + p_y^2} = \frac{1}{\sqrt{p_x^2 + p_y^2}}\left[p_x\frac{\partial p_x}{\partial \delta l} + p_y\frac{\partial p_y}{\partial \delta l}\right] \tag{A.74}$$

$$\frac{\partial}{\partial \delta h}\sqrt{p_x^2 + p_y^2} = \frac{1}{\sqrt{p_x^2 + p_y^2}}\left[p_x\frac{\partial p_x}{\partial \delta h} + p_y\frac{\partial p_y}{\partial \delta h}\right] \tag{A.75}$$

The final unknown values to solve for are the partial derivatives of the ECEF conversion coefficients with respect to the error states.

$$\frac{\partial r_n}{\partial \delta L} = \frac{\partial}{\partial \delta L} \left[\frac{a}{\sqrt{1 - e^2 \sin^2(L + \delta L)}} \right] \tag{A.76}$$

$$= \frac{\frac{\partial a}{\partial \delta L} \sqrt{1 - e^2 \sin^2(L + \delta L)} - a \frac{\partial}{\partial \delta L} \sqrt{1 - e^2 \sin^2(L + \delta L)}}{1 - e^2 \sin^2(L + \delta L)} \tag{A.77}$$

$$= \frac{0 - a \frac{1}{2}(1 - e^2 \sin^2(L + \delta L))^{-1/2} \frac{\partial}{\partial \delta L}(1 - e^2 \sin^2(L + \delta L))}{1 - e^2 \sin^2(L + \delta L)} \tag{A.78}$$

$$= -\frac{a(-e^2) \frac{\partial}{\partial \delta L} \sin^2(L + \delta L))}{2 \left(1 - e^2 \sin^2(L + \delta L)\right)^{3/2}} \tag{A.79}$$

$$= -\frac{a(-e^2) \frac{\partial}{\partial \delta L} \sin^2(L + \delta L))}{2 \left(1 - e^2 \sin^2(L + \delta L)\right)^{3/2}} \tag{A.80}$$

$$= \frac{ae^2(2 \sin(L + \delta L) \cos(L + \delta L))}{2 \left(1 - e^2 \sin^2(L + \delta L)\right)^{3/2}} \tag{A.81}$$

$$= \frac{ae^2 \sin(L + \delta L) \cos(L + \delta L))}{\left(1 - e^2 \sin^2(L + \delta L)\right)^{3/2}} \tag{A.82}$$

$$\frac{\partial r_n}{\partial \delta l} = \frac{\partial}{\partial \delta l} \left[\frac{a}{\sqrt{1 - e^2 \sin^2(L + \delta L)}} \right] = 0 \tag{A.83}$$

$$\frac{\partial r_n}{\partial \delta h} = \frac{\partial}{\partial \delta h} \left[\frac{a}{\sqrt{1 - e^2 \sin^2(L + \delta L)}} \right] = 0 \tag{A.84}$$

$$\tag{A.85}$$

$$\frac{\partial R}{\partial \delta L} = \frac{\partial}{\partial \delta L}(r_n + h + \delta h)\cos(L + \delta L) \tag{A.86}$$

$$= \left(\frac{\partial}{\partial \delta L}(r_n + h + \delta h)\right)\cos(L + \delta L) + (r_n + h + \delta h)\left(\frac{\partial}{\partial \delta L}\right)\cos(L + \delta L) \tag{A.87}$$

$$= \frac{\partial r_n}{\partial \delta L}\cos(L + \delta L) - (r_n + h + \delta h)\sin(L + \delta L) \tag{A.88}$$

$$\frac{\partial R}{\partial \delta l} = \frac{\partial}{\partial \delta l}(r_n + h + \delta h)\cos(L + \delta L) \tag{A.89}$$

$$= \left(\frac{\partial}{\partial \delta l}(r_n + h + \delta h)\right)\cos(L + \delta L) + (r_n + h + \delta h)\left(\frac{\partial}{\partial \delta l}\right)\cos(L + \delta L) \tag{A.90}$$

$$= \frac{\partial r_n}{\partial \delta L}\cos(L + \delta L) + 0 \tag{A.91}$$

$$= 0 \tag{A.92}$$

$$\frac{\partial R}{\partial \delta h} = \frac{\partial}{\partial \delta h}(r_n + h + \delta h)\cos(L + \delta L) \tag{A.93}$$

$$= \left(\frac{\partial}{\partial \delta h}(r_n + h + \delta h)\right)\cos(L + \delta L) + (r_n + h + \delta h)\left(\frac{\partial}{\partial \delta h}\right)\cos(L + \delta L) \tag{A.94}$$

$$= \frac{\partial r_n}{\partial \delta h}\cos(L + \delta L) + \cos(L + \delta L) + 0 \tag{A.95}$$

$$= \cos(L + \delta L) \tag{A.96}$$

Appendix B. Projection of Differential Covariance

When projecting the measurement noise generated by the differential site's image sensor onto the observer's image plane, the uncertainty is transformed. This appendix derives the calculation of the projection of the measurement uncertainty as described in 2.19.

The transformation described in Section 5.1.6 is reiterated here in relation to measurement covariance rather than the ephemeris error as previously described. The differential site's angular measurement of the satellite position is calculated using 4.151 with the appropriate position and slant range values applied and expressed as $\mathbf{z}_d$.

$$\mathbf{z}_d = \mathbf{h}\left(\mathbf{x}_d, \mathbf{x}_{sat} + \boldsymbol{\delta}\mathbf{x}_{sat}\right) + \mathbf{v}_d \tag{B.1}$$

$$\mathbf{z}_d = \mathbf{h}\left(\mathbf{x}_d, \mathbf{x}_{sat}\right) + \boldsymbol{\Delta\theta}_d + \mathbf{v}_d \tag{B.2}$$

$$\mathbf{r}_d = \mathbf{z}_{d,true} - \mathbf{z}_d \tag{B.3}$$

$$= \boldsymbol{\Delta\theta}_d + \mathbf{v}_d \tag{B.4}$$

$$= \begin{bmatrix} \Delta\alpha_d \\ \Delta\delta_d \end{bmatrix} + \mathbf{v}_d \tag{B.5}$$

where $\boldsymbol{\Delta\theta}_d$ describes the angular error assumed to be due to the satellite ephemeris error. The measurement uncertainty of the differential site is given by

$$E\left[\mathbf{v}_d\mathbf{v}_d^T\right] = \mathbf{R}_d\boldsymbol{\delta}_{ij} \tag{B.6}$$

$$= \begin{bmatrix} \sigma_{d,\alpha}^2 & 0 \\ 0 & \sigma_{d,\delta}^2 \end{bmatrix} \delta_{ij} \tag{B.7}$$

where the measurement noise in the right ascension, $\sigma_{d,\alpha}$, and the measurement noise in the declination, $\sigma_{d,\delta}$ are shown to be uncorrelated, and δ_{ij} is the Kroenicker delta function. However, the transformation that projects the satellite ephemeris error will cause the noise to become correlated in the observer's image plane. This result is shown later in the appendix.

Similar to the measurement from the differential site, the observer's angular measurement is described by

$$\mathbf{z}_o = \mathbf{h}\left(\mathbf{x}_o, \mathbf{x}_{sat} + \boldsymbol{\delta}\mathbf{x}_{sat}\right) + \mathbf{v}_o \tag{B.8}$$

$$\mathbf{z}_o = \mathbf{h}\left(\mathbf{x}_o, \mathbf{x}_{sat}\right) + \boldsymbol{\Delta\theta}_o + \mathbf{v}_o \tag{B.9}$$

Here, the measurement error given by the differential site's residual can be applied to the observer's measurement through the transformation. However, the measurement correction received from that differential site also has sensor noise, which must now be accounted for in the Kalman filter uncertainty. The observer's measurement is then rewritten as

$$\mathbf{z}_o = \mathbf{h}\left(\mathbf{x}_o, \mathbf{x}_{sat}\right) + \mathrm{T}\left(\boldsymbol{\Delta\theta}_d + \mathbf{v}_d\right) + \mathbf{v}_o \tag{B.10}$$

It can be shown that the $T(\cdot)$ operator is linear, therefore superposition applies

$$\mathrm{T}\left(\boldsymbol{\Delta\theta}_d + \mathbf{v}_d\right) = \mathrm{T}\left(\boldsymbol{\Delta\theta}_d\right) + \mathrm{T}\left(\mathbf{v}_d\right) \tag{B.11}$$

and the transformed angle errors in the measurement equation of the EKF become

$$\mathbf{z}_o = \mathbf{h}\left(\mathbf{x}_o, \mathbf{x}_{sat}\right) + \mathrm{T}\left(\boldsymbol{\Delta\theta}_d\right) + \mathrm{T}\left(\mathbf{v}_d\right) + \mathbf{v}_o \tag{B.12}$$

where

$$E\left[\mathbf{v}_{o,i}\mathbf{v}_{o,j}^T\right] = \mathbf{R}_o \delta_{ij} \tag{B.13}$$

is known, but

$$E\left[\mathrm{T}\left(\mathbf{v}_{d,i}\right)\mathrm{T}\left(\mathbf{v}_{d,j}\right)^T\right] = \mathbf{R}_{Td}\delta_{ij} \tag{B.14}$$

must be solved for.

185

The transformation operator, $T(\cdot)$, describes the process of projecting the differential residual value onto the image plane of the observer.

The satellite ephemeris error and differential sensor error is projected onto a set of unit vectors, $[\mathbf{u}_{los,d}, \mathbf{u}_{\alpha,d}, \mathbf{u}_{\delta,d}]$, in the differential site's image plane orthogonal to the line of sight from the differential site to the satellite. These vectors are in an ecef frame, thus the angular measurement is converted to units of meters, $(\boldsymbol{\Delta\theta}_d^e, \ \mathbf{v}_d^e)$ using the slant range, ρ_d.

$$\boldsymbol{\Delta\theta}_d^e = \rho_d \left(\Delta\alpha_d \mathbf{u}_{\alpha,d} + \Delta\delta_d \mathbf{u}_{\delta,d} \right) \tag{B.15}$$

$$\mathbf{v}_d^e = \rho_d \left(v_{\alpha,d} \mathbf{u}_{\alpha,d} + v_{\delta,d} \mathbf{u}_{\delta,d} \right) \tag{B.16}$$

The vector describing the direction of the image plane in the right ascension is determined by finding the cross product of the line of sight vector and the negative z-axis of the ecef frame. The vector in the declination direction is the cross product of the line of sight vector and this new right ascension vector. All three vectors are normalized to unit length.

$$\mathbf{u}_{los,d} = \frac{\mathbf{p}_d}{\rho_d} \tag{B.17}$$

$$\mathbf{u}_{\alpha,d} = \frac{\mathbf{u}_{los,d} \times [0, 0, -1]^T}{\left| \mathbf{u}_{los,d} \times [0, 0, -1]^T \right|} \tag{B.18}$$

$$\mathbf{u}_{\delta,d} = \frac{\mathbf{u}_{los,d} \times \mathbf{u}_{\alpha,d}}{\left| \mathbf{u}_{los,d} \times \mathbf{u}_{\alpha,d} \right|} \tag{B.19}$$

A similar set of vector is determined for the image plane associated with the observer to satellite line of sight, $\mathbf{p}_o$.

$$\mathbf{u}_{los,o} = \frac{\mathbf{p}_o}{\rho_o} \tag{B.20}$$

$$\mathbf{u}_{\alpha,o} = \frac{\mathbf{u}_{los,o} \times [0, 0, -1]^T}{\left| \mathbf{u}_{los,o} \times [0, 0, -1]^T \right|} \tag{B.21}$$

$$\mathbf{u}_{\delta,o} = \frac{\mathbf{u}_{los,o} \times \mathbf{u}_{\alpha,d}}{\left| \mathbf{u}_{los,o} \times \mathbf{u}_{\alpha,o} \right|} \tag{B.22}$$

Having established the new right ascension and declination direction vectors of the observer's image plane, the ecef vector describing the satellite ephemeris error can be projected onto those vectors using the dot product of the error onto the new unit vector axes.

$$\Delta\boldsymbol{\theta}_o^e = \begin{bmatrix} \Delta\boldsymbol{\theta}_d^e \cdot \mathbf{u}_{\alpha,o} \\ \Delta\boldsymbol{\theta}_d^e \cdot \mathbf{u}_{\delta,o} \end{bmatrix} \tag{B.23}$$

$$\mathrm{T}(\mathbf{v}_d)^e = \begin{bmatrix} \mathbf{v}_d^e \cdot \mathbf{u}_{\alpha,o} \\ \mathbf{v}_d^e \cdot \mathbf{u}_{\delta,o} \end{bmatrix} \tag{B.24}$$

Using Eqn. B.15 and Eqn. B.16 these become

$$\Delta\boldsymbol{\theta}_o^e = \begin{bmatrix} \left(\rho_d \left(\Delta\alpha_d \mathbf{u}_{\alpha,d} + \Delta\delta_d \mathbf{u}_{\delta,d}\right)\right) \cdot \mathbf{u}_{\alpha,o} \\ \left(\rho_d \left(\Delta\alpha_d \mathbf{u}_{\alpha,d} + \Delta\delta_d \mathbf{u}_{\delta,d}\right)\right) \cdot \mathbf{u}_{\delta,o} \end{bmatrix} \tag{B.25}$$

$$= \rho_d \begin{bmatrix} \Delta\alpha_d \left(\mathbf{u}_{\alpha,d} \cdot \mathbf{u}_{\alpha,o}\right) + \Delta\delta_d \left(\mathbf{u}_{\delta,d} \cdot \mathbf{u}_{\alpha,o}\right) \\ \Delta\alpha_d \left(\mathbf{u}_{\alpha,d} \cdot \mathbf{u}_{\delta,o}\right) + \Delta\delta_d \left(\mathbf{u}_{\delta,d} \cdot \mathbf{u}_{\delta,o}\right) \end{bmatrix} \tag{B.26}$$

and

$$\mathrm{T}(\mathbf{v}_d)^e = \begin{bmatrix} \rho_d \left(v_{\alpha,d} \mathbf{u}_{\alpha,d} + v_{\delta,d} \mathbf{u}_{\delta,d}\right) \cdot \mathbf{u}_{\alpha,o} \\ \rho_d \left(v_{\alpha,d} \mathbf{u}_{\alpha,d} + v_{\delta,d} \mathbf{u}_{\delta,d}\right) \cdot \mathbf{u}_{\delta,o} \end{bmatrix} \tag{B.27}$$

$$= \rho_d \begin{bmatrix} v_{\alpha,d} \left(\mathbf{u}_{\alpha,d} \cdot \mathbf{u}_{\alpha,o}\right) + v_{\delta,d} \left(\mathbf{u}_{\delta,d} \cdot \mathbf{u}_{\alpha,o}\right) \\ v_{\alpha,d} \left(\mathbf{u}_{\alpha,d} \cdot \mathbf{u}_{\delta,o}\right) + v_{\delta,d} \left(\mathbf{u}_{\delta,d} \cdot \mathbf{u}_{\delta,o}\right) \end{bmatrix} \tag{B.28}$$

Finally, to express the transformed correction in the proper units, radians, the values are divided by the slant range from the observer to the satellite.

$$\Delta\boldsymbol{\theta}_o = \frac{\rho_d}{\rho_o} \begin{bmatrix} \Delta\alpha_d \left(\mathbf{u}_{\alpha,d} \cdot \mathbf{u}_{\alpha,o}\right) + \Delta\delta_d \left(\mathbf{u}_{\delta,d} \cdot \mathbf{u}_{\alpha,o}\right) \\ \Delta\alpha_d \left(\mathbf{u}_{\alpha,d} \cdot \mathbf{u}_{\delta,o}\right) + \Delta\delta_d \left(\mathbf{u}_{\delta,d} \cdot \mathbf{u}_{\delta,o}\right) \end{bmatrix} \tag{B.29}$$

$$\mathrm{T}(\mathbf{v}_d) = \frac{\rho_d}{\rho_o} \begin{bmatrix} v_{\alpha,d} \left(\mathbf{u}_{\alpha,d} \cdot \mathbf{u}_{\alpha,o}\right) + v_{\delta,d} \left(\mathbf{u}_{\delta,d} \cdot \mathbf{u}_{\alpha,o}\right) \\ v_{\alpha,d} \left(\mathbf{u}_{\alpha,d} \cdot \mathbf{u}_{\delta,o}\right) + v_{\delta,d} \left(\mathbf{u}_{\delta,d} \cdot \mathbf{u}_{\delta,o}\right) \end{bmatrix} \tag{B.30}$$

The angle correction, $\boldsymbol{\Delta\theta}_o$, can be added to the observer's measurement directly, however to make use of the transformed measurement uncertainty the covariance matrix must be calculated.

The covariance of the transformed differential measurement uncertainty in the observer's image plane is calculated using Eqn. B.14.

$$E\left[\mathrm{T}\left(\mathbf{v}_{d,i}\right)\mathrm{T}\left(\mathbf{v}_{d,j}\right)^T\right](1,1) = E\left[\left(\frac{\rho_d}{\rho_o}\right)^2\left(v_{\alpha,d}^2\left(\mathbf{u}_{\alpha,d}\cdot\mathbf{u}_{\alpha,o}\right)^2 + \right.\right.$$

$$v_{\delta,d}^2\left(\mathbf{u}_{\delta,d}\cdot\mathbf{u}_{\alpha,o}\right)^2 +$$

$$2v_{\alpha,d}v_{\delta,d}\left(\mathbf{u}_{\alpha,d}\cdot\mathbf{u}_{\alpha,o}\right)\left(\mathbf{u}_{\delta,d}\cdot\mathbf{u}_{\alpha,o}\right)\left.\right)\right] \tag{B.31}$$

$$E\left[\mathrm{T}\left(\mathbf{v}_{d,i}\right)\mathrm{T}\left(\mathbf{v}_{d,j}\right)^T\right](1,2) = E\left[\left(\frac{\rho_d}{\rho_o}\right)^2\left(v_{\alpha,d}^2\left(\mathbf{u}_{\delta,d}\cdot\mathbf{u}_{\alpha,o}\right)\left(\mathbf{u}_{\alpha,d}\cdot\mathbf{u}_{\delta,o}\right) + \right.\right.$$

$$v_{\alpha,d}v_{\delta,d}\left(\mathbf{u}_{\delta,d}\cdot\mathbf{u}_{\alpha,o}\right)\left(\mathbf{u}_{\alpha,d}\cdot\mathbf{u}_{\delta,o}\right) +$$

$$v_{\alpha,d}v_{\delta,d}\left(\mathbf{u}_{\alpha,d}\cdot\mathbf{u}_{\alpha,o}\right)\left(\mathbf{u}_{\delta,d}\cdot\mathbf{u}_{\delta,o}\right) +$$

$$v_{\delta,d}^2\left(\mathbf{u}_{\delta,d}\cdot\mathbf{u}_{\alpha,o}\right)\left(\mathbf{u}_{\delta,d}\cdot\mathbf{u}_{\delta,o}\right)\left.\right)\right] \tag{B.32}$$

$$E\left[\mathrm{T}\left(\mathbf{v}_{d,i}\right)\mathrm{T}\left(\mathbf{v}_{d,j}\right)^T\right](2,1) = E\left[\mathrm{T}\left(\mathbf{v}_{d,i}\right)\mathrm{T}\left(\mathbf{v}_{d,j}\right)^T\right](1,2) \tag{B.33}$$

$$E\left[\mathrm{T}\left(\mathbf{v}_{d,i}\right)\mathrm{T}\left(\mathbf{v}_{d,j}\right)^T\right](1,1) = E\left[\left(\frac{\rho_d}{\rho_o}\right)^2\left(v_{\alpha,d}^2\left(\mathbf{u}_{\alpha,d}\cdot\mathbf{u}_{\delta,o}\right)^2 + v_{\delta,d}^2\left(\mathbf{u}_{\delta,d}\cdot\mathbf{u}_{\delta,o}\right)^2 + \right.\right.$$

$$2v_{\alpha,d}v_{\delta,d}\left(\mathbf{u}_{\alpha,d}\cdot\mathbf{u}_{\delta,o}\right)\left(\mathbf{u}_{\delta,d}\cdot\mathbf{u}_{\delta,o}\right)\left.\right)\right] \tag{B.34}$$

Since, the only random processes in the expected value operation are those associated with the angle correction, so the equations become

$$E\left[\mathrm{T}\left(\mathbf{v}_{d,i}\right)\mathrm{T}\left(\mathbf{v}_{d,j}\right)^T\right](1,1) = \left(\frac{\rho_d}{\rho_o}\right)^2\left[E\left[v_{\alpha,d}^2\right]\left(\mathbf{u}_{\alpha,d}\cdot\mathbf{u}_{\alpha,o}\right)^2 + E\left[v_{\delta,d}^2\right]\left(\mathbf{u}_{\delta,d}\cdot\mathbf{u}_{\alpha,o}\right)^2 + \right.$$
$$\left. 2E\left[v_{\alpha,d}v_{\delta,d}\right]\left(\mathbf{u}_{\alpha,d}\cdot\mathbf{u}_{\alpha,o}\right)\left(\mathbf{u}_{\delta,d}\cdot\mathbf{u}_{\alpha,o}\right)\right] \tag{B.35}$$

$$E\left[\mathrm{T}\left(\mathbf{v}_{d,i}\right)\mathrm{T}\left(\mathbf{v}_{d,j}\right)^T\right](1,2) = \left(\frac{\rho_d}{\rho_o}\right)^2\left[E\left[v_{\alpha,d}^2\right]\left(\mathbf{u}_{\delta,d}\cdot\mathbf{u}_{\alpha,o}\right)\left(\mathbf{u}_{\alpha,d}\cdot\mathbf{u}_{\delta,o}\right) + \right.$$
$$E\left[v_{\alpha,d}v_{\delta,d}\right]\left(\mathbf{u}_{\delta,d}\cdot\mathbf{u}_{\alpha,o}\right)\left(\mathbf{u}_{\alpha,d}\cdot\mathbf{u}_{\delta,o}\right) +$$
$$E\left[v_{\alpha,d}v_{\delta,d}\right]\left(\mathbf{u}_{\alpha,d}\cdot\mathbf{u}_{\alpha,o}\right)\left(\mathbf{u}_{\delta,d}\cdot\mathbf{u}_{\delta,o}\right) +$$
$$\left. E\left[v_{\delta,d}^2\right]\left(\mathbf{u}_{\delta,d}\cdot\mathbf{u}_{\alpha,o}\right)\left(\mathbf{u}_{\delta,d}\cdot\mathbf{u}_{\delta,o}\right)\right] \tag{B.36}$$

$$E\left[\mathrm{T}\left(\mathbf{v}_{d,i}\right)\mathrm{T}\left(\mathbf{v}_{d,j}\right)^T\right](2,1) = E\left[\mathrm{T}\left(\mathbf{v}_{d,i}\right)\mathrm{T}\left(\mathbf{v}_{d,j}\right)^T\right](1,2) \tag{B.37}$$

$$E\left[\mathrm{T}\left(\mathbf{v}_{d,i}\right)\mathrm{T}\left(\mathbf{v}_{d,j}\right)^T\right](1,1) = \left(\frac{\rho_d}{\rho_o}\right)^2\left[E\left[v_{\alpha,d}^2\right]\left(\mathbf{u}_{\alpha,d}\cdot\mathbf{u}_{\delta,o}\right)^2 + E\left[v_{\delta,d}^2\right]\left(\mathbf{u}_{\delta,d}\cdot\mathbf{u}_{\delta,o}\right)^2 + \right.$$
$$\left. 2E\left[v_{\alpha,d}v_{\delta,d}\right]\left(\mathbf{u}_{\alpha,d}\cdot\mathbf{u}_{\delta,o}\right)\left(\mathbf{u}_{\delta,d}\cdot\mathbf{u}_{\delta,o}\right)\right] \tag{B.38}$$

The covariance of the differential site measurement noise is known, therefore, the final version of this process is

$$E\left[\mathrm{T}\left(\mathbf{v}_{d,i}\right)\mathrm{T}\left(\mathbf{v}_{d,j}\right)^T\right](1,1) = \left(\frac{\rho_d}{\rho_o}\right)^2\left[\sigma_{\alpha,d}^2\left(\mathbf{u}_{\alpha,d}\cdot\mathbf{u}_{\alpha,o}\right)^2 + \sigma_{\delta,d}^2\left(\mathbf{u}_{\delta,d}\cdot\mathbf{u}_{\alpha,o}\right)^2\right] \tag{B.39}$$

$$E\left[\mathrm{T}\left(\mathbf{v}_{d,i}\right)\mathrm{T}\left(\mathbf{v}_{d,j}\right)^T\right](1,2) = \left(\frac{\rho_d}{\rho_o}\right)^2\left[\sigma_{\alpha,d}^2\left(\mathbf{u}_{\delta,d}\cdot\mathbf{u}_{\alpha,o}\right)\left(\mathbf{u}_{\alpha,d}\cdot\mathbf{u}_{\delta,o}\right) + \right.$$
$$\left. \sigma_{\delta,d}^2\left(\mathbf{u}_{\delta,d}\cdot\mathbf{u}_{\alpha,o}\right)\left(\mathbf{u}_{\delta,d}\cdot\mathbf{u}_{\delta,o}\right)\right] \tag{B.40}$$

$$E\left[\mathrm{T}\left(\mathbf{v}_{d,i}\right)\mathrm{T}\left(\mathbf{v}_{d,j}\right)^T\right](2,1) = E\left[\mathrm{T}\left(\mathbf{v}_{d,i}\right)\mathrm{T}\left(\mathbf{v}_{d,j}\right)^T\right](1,2) \tag{B.41}$$

$$E\left[\mathrm{T}\left(\mathbf{v}_{d,i}\right)\mathrm{T}\left(\mathbf{v}_{d,j}\right)^T\right](1,1) = \left(\frac{\rho_d}{\rho_o}\right)^2\left[\sigma_{\alpha,d}^2\left(\mathbf{u}_{\alpha,d}\cdot\mathbf{u}_{\delta,o}\right)^2 + \sigma_{\delta,d}^2\left(\mathbf{u}_{\delta,d}\cdot\mathbf{u}_{\delta,o}\right)^2\right] \tag{B.42}$$

This transformation can be reduced to a linear matrix multiplier, $\mathbf{W}$, which when left multiplied to the differential site's measurement correction produces the

observer's measurement correction.

$$\mathbf{W}\boldsymbol{\Delta\theta}_d = \frac{\rho_d}{\rho_o} \begin{bmatrix} (\mathbf{u}_{\alpha,d} \cdot \mathbf{u}_{\alpha,o}) & (\mathbf{u}_{\delta,d} \cdot \mathbf{u}_{\alpha,o}) \\ (\mathbf{u}_{\alpha,d} \cdot \mathbf{u}_{\delta,o}) & (\mathbf{u}_{\delta,d} \cdot \mathbf{u}_{\delta,o}) \end{bmatrix} \begin{bmatrix} v_{r,\alpha} \\ v_{r,\delta} \end{bmatrix} \tag{B.43}$$

The covariance of the differential site when projected on the observer's image plane is found by the left and right multiply by $\mathbf{W}$.

$$E\left[(\mathbf{W}\mathbf{v}_d)(\mathbf{W}\mathbf{v}_d)^T \right] = \mathbf{W}E\left[\mathbf{v}_d\mathbf{v}_d^T \right] \mathbf{W}^T \tag{B.44}$$

Appendix C.   Image Capture Procedures

This appendix records the experimental setup and procedures for the USNO's CNTB, which was used for the research presented in Chapter VI.

3.1   Experimental Setup

Two figures describe the experimental setup for data collection at the CNTB. Figure C.1 describes the hardware used within the observatory and Figure C.2 describes the software hosted on the main computer at the observatory used in running the observatory and taking observations.

The hardware components of the CNTB consist of the host computer, a GPS receiver, the dome motor and controls, and the overall optical system containing the telescope, mount, focuser, filter wheel, and camera or CCD focal plane. The computer hosts the software that controls the optical system and the dome as well as interfaces between all the hardware components.

3.2   Experimental Procedures

The following sequence was followed to initialize the equipment and software. These steps also include the use of the software to run the camera, capturing images as desired. This is intended to record the process of preparing for observation and provide visual aids to others who would repeat the process.

1. Turn on the Powerstrip (on mount base)

   - Pause while system powers up, wait until clicking/beeping on camera and mount are completed

2. Open Autoslew Program, Autoslew window shown in Figure C.3

   - Move telescope to home position "1", where the telescope body is pointed in the zenith direction. Use "west" and "north" buttons in Autoslew to move telescope to position.
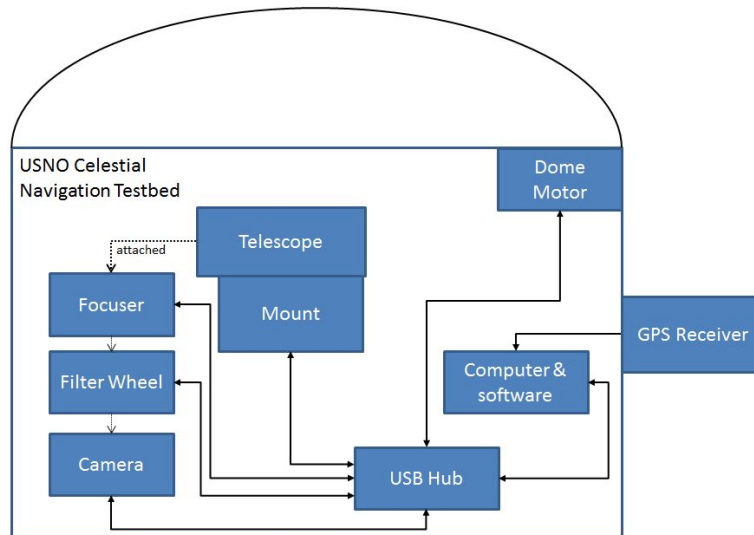
Figure C.1:   Hardware Components of CNTB
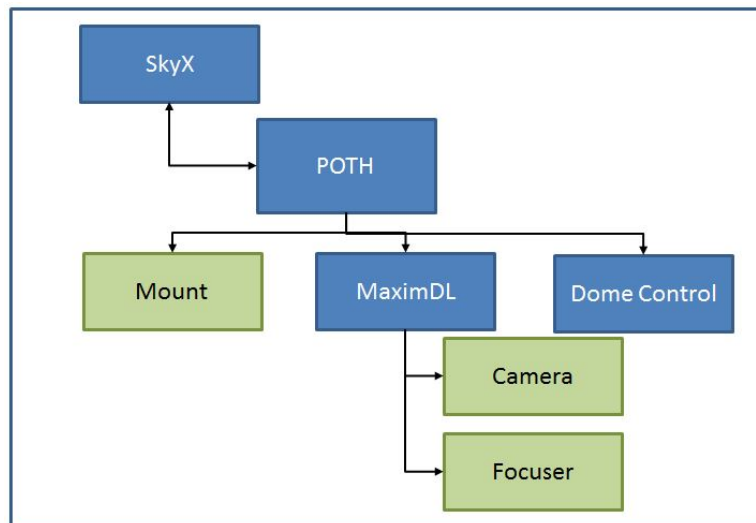

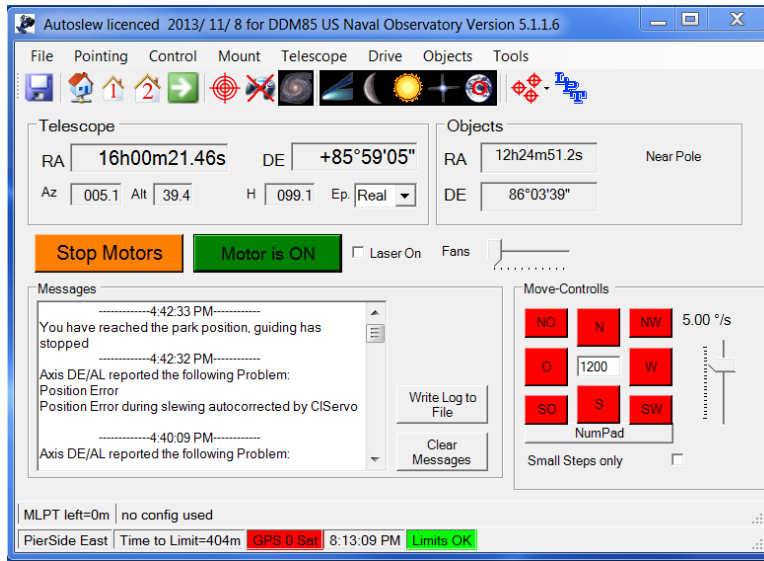Figure C.2:   Software Components of CNTB

Figure C.3:   Main Window of Autoslew Software

- Set "Home" icon in order to align mount

- Test "Home 1" and "Home 2" icons for proper slewing

3. Open MaximDL program, MaximDL window shown in Figure C.4

- Under the View Menu, select Camera Control, Setup tab (Figure C.5), then Connect, and turn Cooler "On".

- Under Observatory Control (Figure C.6), select POTH Hub Connect and wait for flashing ASCOM indicator. Check default values for Autoslew in the menu.

- In ASCOM window (POTH), shown in Figure C.7, select Connect Dome, then Go to 90. When the dome has rotated to the right location, then Go to 210. These two commands reset the dome control sensor such that the controller now knows that the dome opening is aligned.

- In View Observatory Control, select Connect Focuser and Start PW13 (Figure C.8). Verify connection to focuser.

4. Open SkyX (shown in Figure C.9)

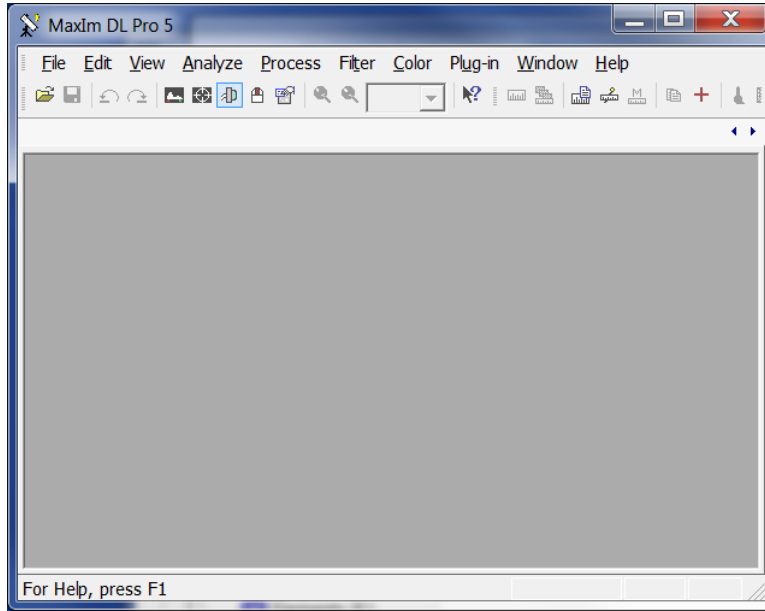- In Telescope menu (Figure C.10), select Connect.

193

Figure C.4:   Main Window of MaximDL Software

5. Load TLE files [33], published in [44], of desired satellites or constellations into SkyX (see Figure C.11.

6. Select a satellite from the Main SkyX window and verify correct tracking using Track Satellite Window (Figure C.12).

7. Capture image using MaximDL using the Exposure tab of the Camera Control window (see Figure C.13).

   - Use 'Single' radial button to take a single image, using other fields to designate desired exposure time, 'Seconds', and filter type, 'Filter Wheel'.

   - Sequence of images is captured using 'Continuous' radial button, with similar settings.

   - If variety of settings are desired, 'Autosave' radial button can establish tailored sequence of images with fields including filter type, exposure time, number of times to repeat that setting, and delay between successive images. The autosave configuration window is shown in Figure C.14. Ad-
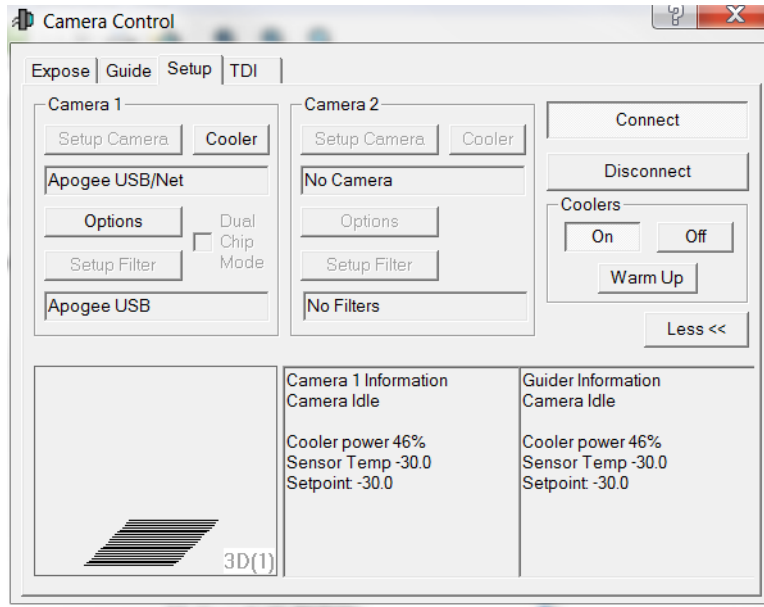
194

Figure C.5:   Camera Control Window of MaximDL Software

ditionally, image file name conventions can be established in this window.

- Use 'Start' and 'Stop' buttons to begin or end image or image sequence capture.
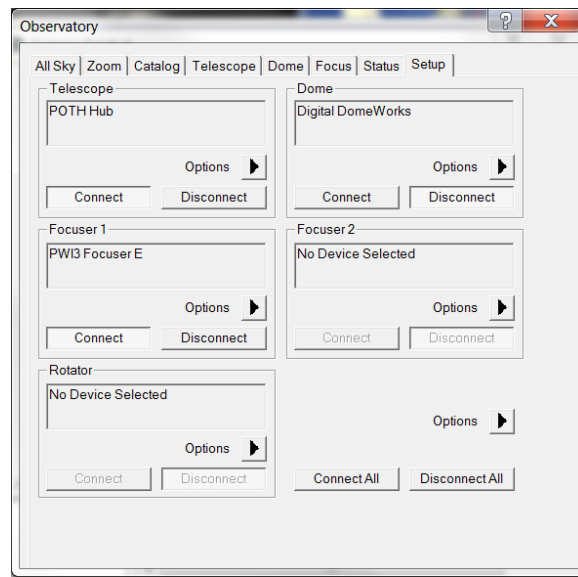
Figure C.6:   Observatory Control Window of MaximDL Software
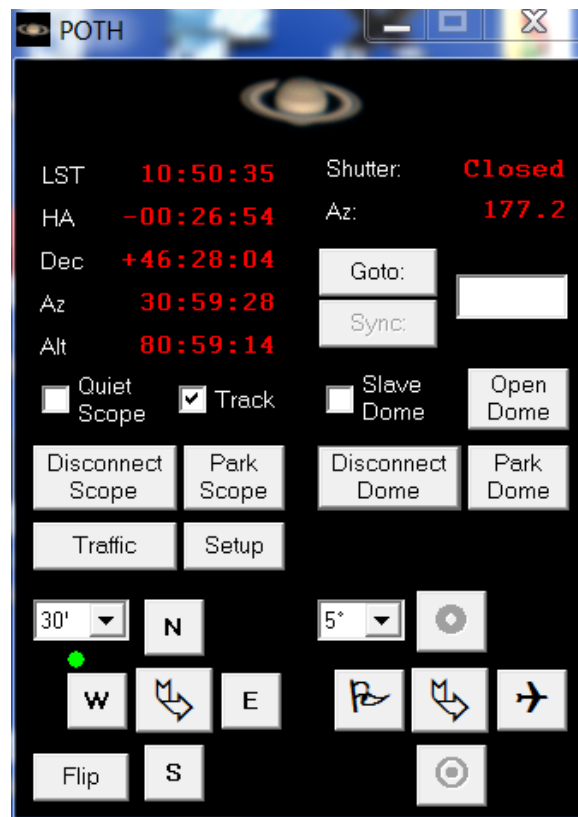

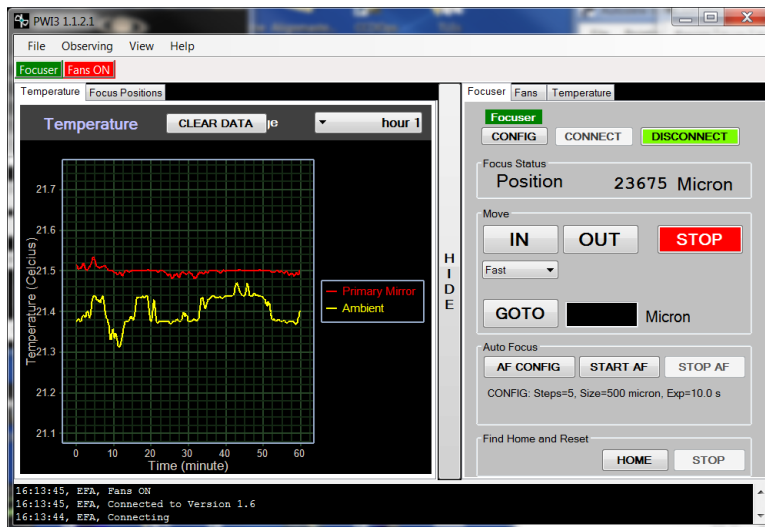Figure C.7:   Main Window of POTH Software

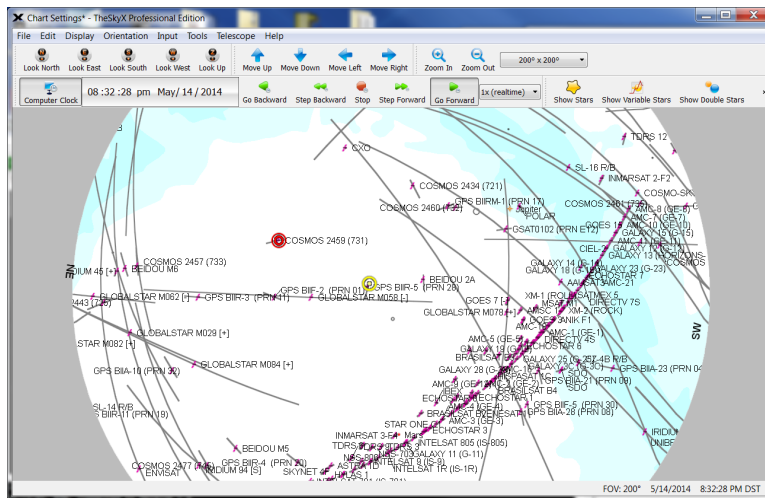Figure C.8:   Control Window of Focuser Software

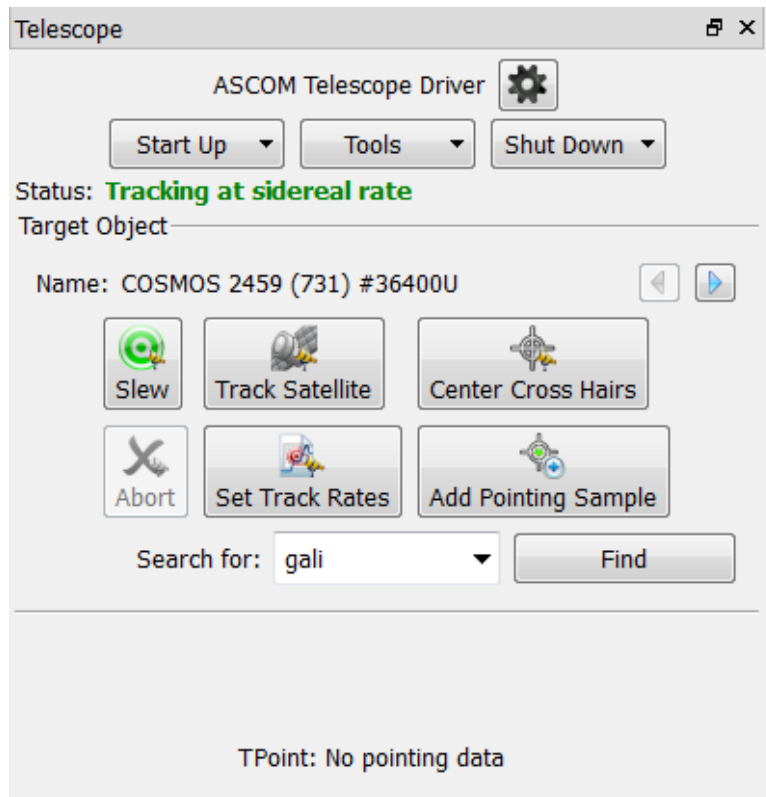Figure C.9:   Main Window of SkyX Software

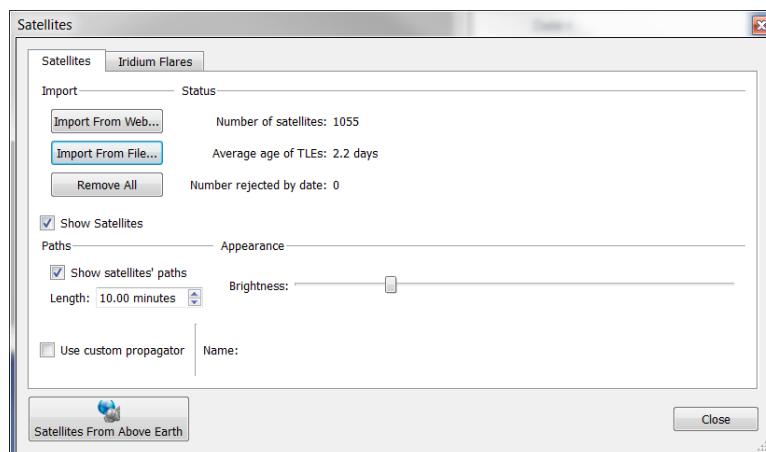Figure C.10:   Telescope Window of SkyX Software

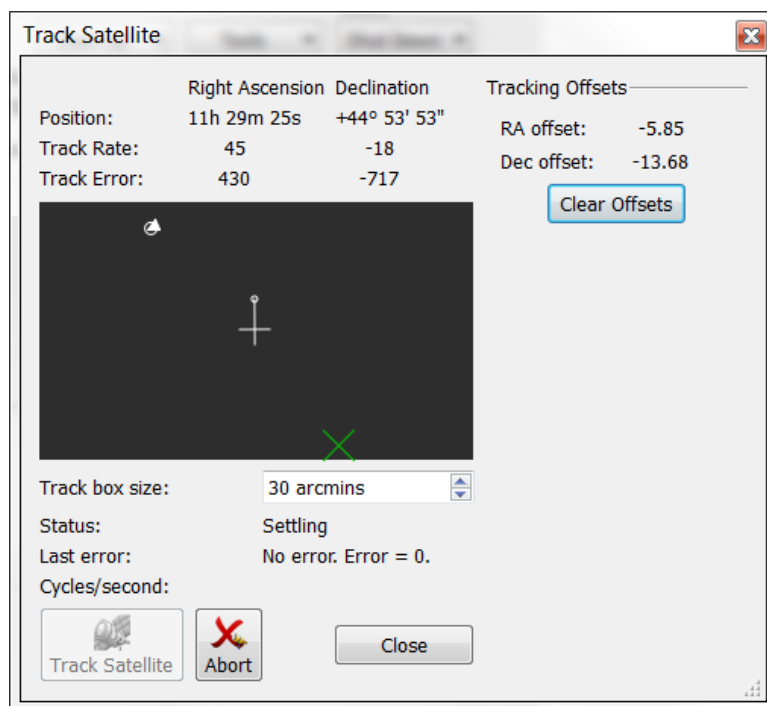Figure C.11:   TLE Load Window of SkyX Software
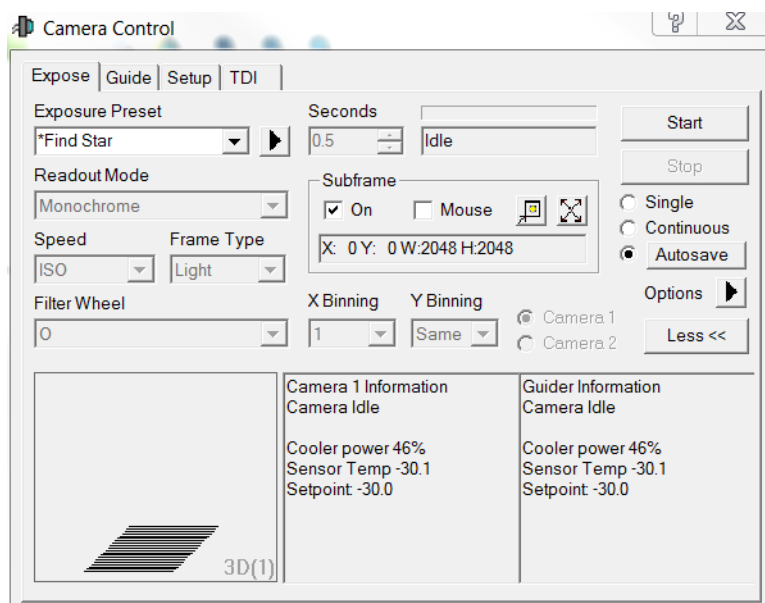
Figure C.12:   Satellite Tracking Window of SkyX Software

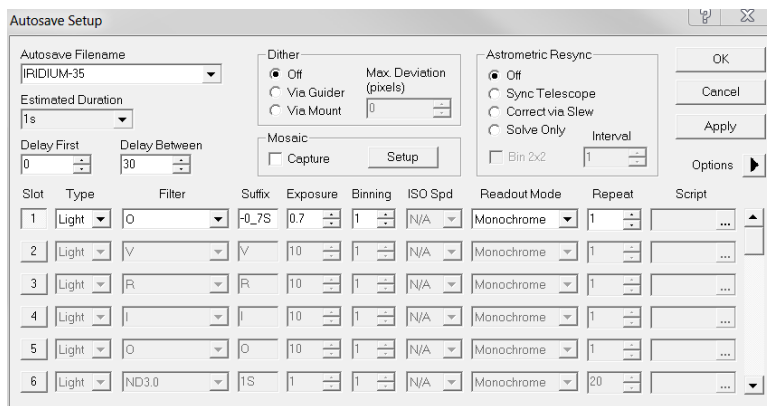Figure C.13:   Exposure Window of MaximDL Software

199

Figure C.14: Autosave Window of Maxim Software for Image Capture Configuration

Bibliography

1. Allen, C. W. *Astrophysical Quantities*. The Athlone Press, 4 Gower Street, London wc1, 3rd edition, 1981.

2. Alonso, Roberto, John L Crassidis, and John L Junkins. "Vision-based relative navigation for formation flying of spacecraft". *AIAA Guidance, Navigation, and Control Conference and Exhibit, Denver, CO*. 2000.

3. van Altena, William F. *Astrometry for Astrophysics: Methods, Models, and Applications*. Cambridge University Press, Nov 2012.

4. Bate, Roger R., Donald D. Mueller, and Jerry E. White. *Fundamentals of Astrodynamics*. Dover Publications, Inc., New York, 1971.

5. Battin, Richard H. *An Introduction to the Mathematics and Methods of Astrodynamics*. AIAA Education Series, New York, 2nd edition, 1999.

6. Belen'kii, Mikhail, Tim Brinkley, Louis Cuellar, Kevin Hughes, and Allen Tannenbaum. *Daytime Electronic Stellar Imager*. Final report, Space and Naval Warfare Center, 4301 Pacific Highway, San Diego CA 92110, February 2003. Work performed by Trex Enterprises Corporation, 10455 Pacific Center Court, San Diego, CA 92121 under Contract N00039-02-C-2205.

7. Biretta, J. A., Chris Burrows, Jon Holtzman, Chris Burrows, Jon Holtzman, Inge Heyer, Mark Stevens, Sylvia Baggett, Stefano Casertano, Mark Clampin, Andrew Fruchter, Harry Ferguson, Ron Gilliland, Shireen Gonzaga, Richard Griffiths, Steve Hulbert, Anton Koekemoer, John Krist, John MacKenty, Matt McMaster, Keith Noll, Christopher O'Dea, Adam Riess, Susan Rose, Al Schultz, Massimo Stiavelli, Anatoly Suchkov, Jean Surdej, Michael Wiggs, and Brad Whitmore. *WFPC2 Instrument Handbook*. STScI, Baltamore, 5.0 edition, 2000.

8. Bormanis, Andre and Woodrow W. Grizzle III. *TheSkyX Professional and Serious Astronomer Edition User Guide*. Software Bisque, Incorporated, Golden, CO, December 2014.

9. Bowditch, Nathaniel. *The American Practical Navigator*. 9. Defense Mapping Agency Hydrographic/Topographic Center, Bethesda, MD, 1995.

10. Canciani, Aaron. *Integration of Cold Atom Interferometry INS with Other Sensors*. Technical report, DTIC Document, 2012.

11. Chen, SY. "Kalman filter for robot vision: a survey". *Industrial Electronics, IEEE Transactions on*, 59(11):4409–4420, 2012.

12. Cheng, Yang and Malcolm D. Shuster. "Robustness and Accuracy of the QUEST Algorithm". *AAS*, 7:41–61, July 2012.

13. Chobotov, Vladimir A. *Orbital Mechanics*. AIAA, 1801 Alexander Bell Drive, Reston, VA 20191, 3rd edition, 2003. Used for min number of satellites in constellation equation.

14. Clohessy, W. H. and R. S. Wiltshire. "Terminal Guidance System for Satellite Rendezvous". *Journal of the Aerospace Sciences*, 27(9):653–658, 1960.

15. Cole, Craig L and John L Crassidis. *Fast star pattern recognition using spherical triangles*. Ph.D. thesis, State University of New York at Buffalo, 2004.

16. Crassidis, John L., Roberto Alonso, and John L. Junkins. "Optimal Attitude and Position Determination from Line-of-Sight Measurements". *The Journal of the Astronautical Sciences*, 48(2-3):391–408, April-Sept 2000.

17. Department of Defense. "STELLAR Technical Goals". BAA-11-15-PKM, Dec 2010.

18. Dereniak, Eustace L. and G. Boreman. *Infrared Detectors and Systems*. Wiley-Interscience, 1996.

19. Driggers, Ronald G., Paul Cox, and Timothy Edwards. *Introduction to Infrared and Electro-Optical Systems*. Artech House, Inc., 685 Canton St., Norwood, MA 02062, 1999.

20. Dugan, Z. "Stellar Distributions as a Function of I-band Magnitude". *American Astronomical Society Meeting Abstracts*, volume 214 of *American Astronomical Society Meeting Abstracts*, 603.02. December 2009.

21. El-Sheimy, Naser, Sameh Nassar, and Ahoelmagd Noureldin. "Wavelet denoising for IMU alignment". *Aerospace and Electronic Systems Magazine, IEEE*, 19(10):32–39, 2004.

22. Enright, John, Doug Sinclair, C. Cordell Grant, Geoff McVittie, and Tom Dzamba. "Toward Star Tracker Only Attitude Estimation". *Proceedings of the AIAA/USU Conference on Small Satellites, Mission Enabling Technologies 1*, SSC10-X-3. Ryerson University, Sinclair Interplanetary, University of Toronto, August 2010.

23. Farrell, James L. *Integrated Aircraft Navigation*. Academic Press, Inc., San Diego, CA, 1976.

24. Funge, Alistair D. *Daytime Detection of Space Objects*. Master's thesis, Air Force Institute of Technology, 2950 Hobson Way, Wright-Patterson AFB, OH, March 2005.

25. George, Doug, Garland Sharratt, Eric Benson, Hilderic Browne, Chris Creery, Owen Lawrence, Adam Robichaud, Paul Boltwood, Pat Browne, RoseAnne Mussar, and John Waring. *MaxIm DL*. Diffraction Limited, 1997-2013.

26. Grumman, Northrop. "LN-120G Specification Sheet". vendor website, Jan 2013.

27. Guier, William H and George C Weiffenbach. "Theoretical analysis of Doppler radio signals from earth satellites". 1958.

28. Guier, William H. and George C. Weiffenbach. "Genesis of Satellite Navigation". *Johns Hopkins APL Technical Digest*, 18(1):14–17, 1998.

29. Hecht, Eugene. *Optics*. Pearson Education, Inc. and Addison Wesley, San Francisco, CA, 2002.

30. Hejduk, M. D. "Specular and Diffuse Components in Spherical Satellite Photometric Modeling", 2011. A.i. solutions, Inc.

31. Hill, George W. "Researches in Lunar Theory". *American Journal of Mathematics*, 1:5–26, 1878.

32. Hoffleit, D. and Jr. W.H.Warren. "The Bright Star Catalog, 5th Revised Edition (Preliminary Version)", 1991.

33. Hoots, Felix R. and Ronald L. Roehrich. *Models for Propagation of NORAD Element Sets*. Technical Report 3, Aerospace Defense Center, Peterson AFB, CO, December 1980.

34. Huang, Yangming, Arne Vestergarrd Olesen, Meiping Wu, and Kaidon Zhang. "SGA-WZ: A New Strapdown Airborne Gravimeter". *Sensors*, 12(7):9336–9348, 2012.

35. Iyengar, S. S., C. C. Jorgensen, S. V. N. Rao, and C. R. Weisbin. "Robot navigation algorithms using learned spatial graphs". *Robotica*, 4(2):93–100, 1986.

36. Janesick, James R. *Scientific Charge-Coupled Devices*, volume PM83. SPIE Press, January 2001.

37. Jørgensen, John Leif. *In Orbit Performance of a Fully Autonomous Star Tracker*. ESTEC/ESA, 1999.

38. Junkins, John L, Declan C Hughes, Karim P Wazni, and Vatee Pariyapong. "Vision-based navigation for rendezvous, docking, and proximity operations". *22nd Annual AAS Guidance and Control Conference, Breckenridge, CO*, 99–021. Citeseer, 1999.

39. Kaplan, G. H., J. A. Hughes, P. K. Seidelmann, C. A. Smith, and B. D. Yallop. "Mean and apparent place computations in the new IAU system. III - Apparent, topocentric, and astrometric places of planets and stars". *Astronomical Journal*, 97:1197–1210, Apr 1989.

40. Kaplan, George H. "Angles-Only Navigation: Position and Velocity Solution from Absolute Triangulation". *Navigation*, 58(3):187–201, Fall 2011.

41. Kaptuch, James A. *Skymark Selection Algorithm for a Space-Based Navigational Concept*. Master's thesis, Massachusetts Institute of Technology, Sep 2002.

42. Kauffman, Kyle. *Radar Based Navigation in Unknown Terrain*. Ph.D. thesis, Air Force Institute of Technology, 2012.

43. Keller, John. "Air Force seeds to prop-up lagging U.S. space star tracker manufacturing capability". website, Feb 2013.

44. Kelso, T. S. "http://www.celestrak.com/". website, 2014.

45. Laboratory, Air Force Geophysics. *Handbook of Geophysics and the Space Environment*. National Technical Information Service, 5285 Port Royal Road, Springfield, VA 22161, 4th edition, 1985.

46. Lang, D., D. W. Hogg, K. Mierle, M. Blanton, and S. Roweis. "Astrometry.net: Blind astrometric calibration of arbitrary astronomical images". *Astronomical Journal*, 137:1782–2800, 2010. ArXiv:0910.2233.

47. Lee, S, GG Ortiz, and JW Alexander. "Star tracker-based acquisition, tracking, and pointing technology for deep-space optical communications". *Interplanetary Network Progress Report*, 42(161):42–161, 2005.

48. Lerner, G.M. "Three-Axis Attitude Determination". *Spacecraft Attitude Determination and Control*, 420–488, 1978.

49. Liebe, Carl C. "Accuracy Performance of Star Trackers–A Tutorial". *IEEE Transactions on Aerospace adn Electronic Systems*, 38(2):587–599, April 2002.

50. Liebe, C.C. "Star trackers for attitude determination". *Aerospace and Electronic Systems Magazine, IEEE*, 10(6):10–16, 1995. ISSN 0885-8985.

51. Liebe, C.C., L. Alkalai, G. Domingo, B. Hancock, D. Hunter, J. Mellstrom, I. Ruiz, C. Sepulveda, and B. Pain. "Micro APS based star tracker". *Aerospace Conference Proceedings, 2002. IEEE*, volume 5, 5–2285–5–2299 vol.5. 2002.

52. Liebe, C.C., E.W. Dennison, B. Hancock, R.C. Stirbl, and B. Pain. "Active pixel sensor (APS) based star tracker". *Aerospace Conference, 1998 IEEE*, volume 1, 119–127 vol.1. 1998. ISSN 1095-323X.

53. Maybeck, Peter S. *Stochastic Models, Estimation, and Control Volume 2*. AP, New York, 1982.

54. Maybeck, Peter S. *Stochastic Models, Estimation, and Control Volume 1*. Navtech, Virginia, 1994.

55. McGuffin, John T. "Terrain referenced navigation electromagnetic-gravitational correlation", December 21 1993. US Patent 5,272,639.

56. Meeus, Jean. *Astronomical Algorithms*. Willman-Bell, Inc., Richmond, VA, 2nd edition, 1999.

57. Monet, D. G., S. E. Levine, B. Canzian, H. D. Ables, A. R. Bird, C. C. Dahn, H. H. Guetter, H. C. Harris, A. A. Henden, S. K. Leggett, H. F. Levison, C. B. Luginbuhl, J. Martini, A. K. B. Monet, J. A. Munn, J. R. Pier, A. R. Rhodes,

B. Riepe, S. Sell, R. C. Stone, F. J. Vrba, R. L. Walker, G. Westerhout, R. J. Brucato, I. N. Reid, W. Schoening, M. Hartley, M. A. Read, and S. B. Tritton. "The USNO-B Catalog". *Astronomical Journal*, 125:984–993, February 2003.

58. Mortari, Daniele. "Search-less algorithm for star pattern recognition". *Journal of Astronautical Sciences*, 45(2):179–194, 1997.

59. Mortari, Daniele, John L Junkins, and M Samaan. "Lost-in-space pyramid algorithm for robust star pattern recognition". *Guidance and Control 2001*, 49–68. 2001.

60. Mortari, Daniele and Beny Neta. "K-vector range searching techniques". *Paper AAS 00-128 of the 10th Annual AIAA/AAS Space Flight Mechanics Meeting, Clearwaters, FL*. 2000.

61. Mortari, Daniele and Andrea Romoli. "StarNav III: A Three Fields of View Star Tracker". *IEEEAC*, 47–57, 2002.

62. National Geodetic Survey. "http://geodesy.noaa.gov/CORS/data.shtml".

63. National Solar Observatory. "Magnitude", 2008.

64. Navstar GPS Joint Program Office. *ISS-GPS-200D, Navstar GPS Space Segment/Navigation User Interfaces*. Technical report, Headquarters, Space and Missile Systems Center, Navstar GPS Joint Program Office, El Segundo, CA, December 2004.

65. Palmer, James M. and Barbara G. Grant. *The Art of Radiometry*. SPIE Press, P.O. Box 10, Bellingham, WA 98227, 2010.

66. Payne, Craig M. *Principles of Naval Weapon Systems*. Naval Institute Press, 2nd edition, Feb 2010.

67. Pence, W. D., L. Chiappetti, C. G. Page, R. A. Shaw, and E. Stobie. "Definition of the Flexible Image Transport System (FITS)". *Astronomy & Astrophysics*, 524(A42):1–40, November 2010.

68. Petovello, Mark G. *Real-time integration of a tactical-grade IMU and GPS for high-accuracy positioning and navigation*. 2003.

69. au Rousseau, G. Lamy, J. Bostel, and B. Mazari. "Star Recognition Algorithm for APS Star Tracker: Oriented Angles". *IEEE A&E Systems Magazine*, 27–31, February 2005.

70. Rufino, Giancarlo and Domenico Accardo. "Enhancement of the centroiding algorithm for star tracker measurement refinement". *Acta Astronautica*, 53:135–147, 2003.

71. Sæmundsson, T. "Atmospheric Refraction". *Sky and Telescope*, 72:70, Jul 1986.

72. Saint-Pe, Olivier, Michael Breart de Boisanger, Franck Larnaudie, Michel Tulet, Robert Davancens, Pierre Magnan, and Philippe Martin Gonthier. *The CMOS*

Breakthrough for Space Optical Detection: Recent Advances and Short Term Perspectives. Final report, EADS Astrium, 31 Avenue des cosmonautess 31402 Toulouse Cedex 4 France, July 2005. See also ADM001791, Potentially Disruptive Technologies and Their Impact in Space Programs Held in Marseille, France on 4-6 July 2005.

73. Serway, Raymond A. and R. J. Beichner. *Physics for Scientists and Engineers*. Harcourt, New York, 2000.

74. Shanks, Joe. "Sensor Modeling Basics". unpublished, May 2011.

75. Shockley, Jeremiah A. *Ground Vehicle Navigation Using Magnetic Field Variation*. Ph.D. thesis, Air Force Institute of Technology, 2012.

76. Shockley, Jeremiah A. and John F. Raquet. "Three-Axis Magnetometer Navigation in Suburban Areas". *Proceedings of the 25th International Technical Meeting of The Satellite Division of the Institute of Navigation (ION GNSS 2012)*, 1607–1618. Nashville, TN, September 2012.

77. Shucker, Brian. "Ground-Based Prototype of CMOS Navigational Star Camera for Small Satellite Applications". *15th AIAA/USU Conference on Small Satellites*, 1–11. University of Arizona, University of Arizona, Tucson, AZ 85721.

78. Sokolovic, Vlada, Goran Dikic, and Rade Stancic. "Adaptive Error Damping in the Vertical Channel of the INS/GPS/Baro-Altimeter Integrated Navigation System". *Scientific Technical Review*, 64(2):14–20, 2014.

79. Sukkarieh, Salah, Eduardo M Nebot, and Hugh F Durrant-Whyte. "A high integrity IMU/GPS navigation loop for autonomous land vehicle applications". *Robotics and Automation, IEEE Transactions on*, 15(3):572–578, 1999.

80. Tappe, Jack, Jae Jun Kim, Albert Jordan, and Brij Agrawal. "Star Tracker Attitude Estimation for an Indoor Ground-Based Spacecraft Simulator". *AIAA Modeling and Simulation Technologies Conference*, volume 6270, 1–19. American Institute of Aeronautics and Astronautics, August 2011.

81. Titterton, D. and J. Weston. *Strapdown Intertial Navigation Technology*. Peter Peregrinus Ltd, United Kingdom, 1997.

82. Truesdale, Nicholas A., Kevin J. Dinkel, Zach J.B. Dischner, Jed H. Diller, and Eliot F. Young. "DayStar: Modeling and test results of a balloon-borne daytime star tracker". *Aerospace Conference, 2013 IEEE*, 1–12. 2013. ISSN 1095-323X.

83. Urban, Sean E. and P. Kenneth Seidelmann. *Explanatory Supplement to the Astronomical Almanac*. University Science Books, Mill Valley, CA, 3rd edition, 2013.

84. Vallado, David A. *Fundamentals of Astrodynamics and Applications*, volume 21. Microcosm Press and Springer, Hawthorne, CA and New York, New York, third edition, 2007.

85. Vaníček, P. and M. Omerbašic. "Does a navigation algorithm have to use a Kalman filter?" *Canadian aeronautics and space journal*, 1999.

86. Veth, Michael and John Raquet. *Fusion of Low-Cost Imaging and Intertial Sensors for Navigation*. Technical report, Air Force Institute of Technology, 2007.

87. Veth, Michael J. *Fusion of Imaging and Inertial Sensors for Navigation*. Ph.D. thesis, Air Force Institute of Technology, 2006.

88. Veth, Michael J. and John F. Raquet. "Stochastic Constraints for Robust Image Correspondence Search". *IEEE Transactions on Aerospace Electronic Systems, Publication forthcoming*.

89. Walker, John G. "Satellite Constellations". *Journal of the British Interplanetary Society*, 37:559–571, 1984.

90. Werner, Benjamin A, Sundar Raman, and Lionel Jacques Garin. "Method for Seamless Transition from Urban Outdoor Environments to Indoor Navigation", March 14 2013. US Patent 20,130,065,604.

91. White, R. L. and R. B. Gounley. *Satellite Autonomous Navigation with SHAD*. Technical Report CSDL-R-1982, The Charles stark Draper Laboratory, Inc., 555 Technology Square, Cambridge MA, April 1987.

92. Wie, Bong, H Weiss, and A Arapostathis. "Quarternion feedback regulator for spacecraft eigenaxis rotations". *Journal of Guidance, Control, and Dynamics*, 12(3):375–380, 1989.

93. Willhite, Weldon Barry. *An Analysis of ICBM Navigation Using Optical Observations of Existing Space Objects*. Master's thesis, Massachusetts Institute of Technology, May 2004.

94. William J. Hughes Technical Center. *Global Positioning System Standard Positioning Service Performance Analysis Report*. Technical Report 86, NTSB/WAAS Test and Evaluation Team, Atlantic City, NJ, Jun 2014.

95. Yadid-Pecht, Orly, Christopher Clark, Bedabrata Pain, Craig Staller, and Eric Fossum. "Wide Dynamic Range APS Star Tracker". *SPIE Proceedings*, 2654:82–92, March 1996.

REPORT DOCUMENTATION PAGE

Form Approved
OMB No. 0704–0188

1. REPORT DATE *(DD–MM–YYYY)*	2. REPORT TYPE	3. DATES COVERED *(From — To)*
26–03–2015	Doctoral Dissertation	Oct 2012 — Mar 2015

4. TITLE AND SUBTITLE

Modeling Navigation System Performance of a Satellite-Observing Star Tracker Tightly Integrated with an Inertial Measurement Unit

5a. CONTRACT NUMBER

5b. GRANT NUMBER

5c. PROGRAM ELEMENT NUMBER

6. AUTHOR(S)

Pierce, Scott J., Maj, USAF

5d. PROJECT NUMBER

n/a

5e. TASK NUMBER

5f. WORK UNIT NUMBER

7. PERFORMING ORGANIZATION NAME(S) AND ADDRESS(ES)

Air Force Institute of Technology
Graduate School of Engineering and Management (AFIT/EN)
2950 Hobson Way
WPAFB OH 45433-7765

8. PERFORMING ORGANIZATION REPORT NUMBER

AFIT-ENG-DS-15-M-260

9. SPONSORING / MONITORING AGENCY NAME(S) AND ADDRESS(ES)

United States Naval Observatory (Bryan Dorland)
3450 Massachusetts Avenue, NW
Washington, DC 20392-5420
(202-762-0134, bryan.dorland@us.navy.mil)

10. SPONSOR/MONITOR'S ACRONYM(S)

USNO

11. SPONSOR/MONITOR'S REPORT NUMBER(S)

12. DISTRIBUTION / AVAILABILITY STATEMENT

DISTRIBUTION STATEMENT A. APPROVED FOR PUBLIC RELEASE; DISTRIBUTION IS UNLIMITED.

13. SUPPLEMENTARY NOTES

This material is declared a work of the U.S. Government and is not subject to copyright protection in the United States.

14. ABSTRACT

This dissertation evaluates a navigation system using satellite observations from a star tracker tightly-integrated with an inertial measurement unit (IMU) and a barometric altimeter using an extended Kalman filter. The star tracker measurement accuracy of a satellite is derived. Several system configurations are simulated comparing the performance of the estimate with respect to system parameters of the IMU, and star tracker, as well as comparing performance when providing a remote sensor satellite ephemeris error correction. Experimental observations are used to evaluate the model performance. Additionally, power requirements were calculated for a satellite signal operating in imaging bands, such that a Low Earth Orbiting satellite constellation could be detected during the day. This type of signal would make it possible to operate the star tracker integrated navigation system in GPS-degraded environments with similar duration and comparable accuracy of GPS.

15. SUBJECT TERMS

Kalman filter, satellite observation, image-aided navigation, star tracker

16. SECURITY CLASSIFICATION OF:			17. LIMITATION OF ABSTRACT	18. NUMBER OF PAGES	19a. NAME OF RESPONSIBLE PERSON
a. REPORT	b. ABSTRACT	c. THIS PAGE			John Raquet
U	U	U	UU	222	19b. TELEPHONE NUMBER *(include area code)* (937) 255–3636, ext 4580; john.raquet@afit.edu

Standard Form 298 (Rev. 8–98)
Prescribed by ANSI Std. Z39.18